# Spectroscopic investigations of [FeFe] hydrogenases and related model systems

Inaugural dissertation

for the attainment of the title of doctor
in the Faculty of Mathematics and Natural Sciences
at the Heinrich Heine University Düsseldorf

presented by

**Agnieszka Adamska-Venkatesh**
from Żnin (Poland)

Düsseldorf, November 2014

from the Max Planck Institute for Chemical Energy Conversion

Published by permission of the
Faculty of Mathematics and Natural Sciences at
Heinrich Heine University Düsseldorf

Supervisor: Prof. Dr. Wolfgang Lubitz
Co-supervisor: Prof. Dr. Rainer Weinkauf

Date of the oral examination: 15.04.2015

## Declaration

The work in this thesis is set out in five self-contained chapters. Each of the chapters forms a journal article. A brief introduction into this research field and theoretical approaches, as well as description of main experimental techniques, is presented. The summary section contains a general review on each of the journal articles.

The investigations detailed in this thesis were carried out jointly with other co-authors. Their contributions to this thesis include:

- Biological sample preparation and biochemical analysis by J. Siebel (chapters 3 – 5), Prof. T. Happe research group (chapters 1 – 4) and Prof. Fontecave research group (chapter 2).
- Synthetic complexes preparation by K. Weber (chapter 4) and Prof. Fontecave research group (chapter 2, 3 and 5).
- EPR measurements by Dr. S. Gambarelli and Dr. G. Bergren (chapter 2).
- DFT calculations by Dr. J. -M. Mouesca (chapter 2).

All other work in this thesis is my own

Agnieszka Adamska-Venkatesh

## Abstract

[FeFe] Hydrogenases are metalloenzymes which catalyze the oxidation of $H_2$ as well as the reduction of protons to form $H_2$. Understanding their catalytic mechanism and biosynthesis pathway as well as their electronic and geometrical structure is of great interest for biotechnology where they serve as models for the development of hydrogen conversion catalysts in renewable energy systems. The algal [FeFe] hydrogenase from *Clamydomonas reinhardtii* (CrHydA1) is a particularly convenient system for studying hydrogenase function since it contains only the active site and no additional iron-sulfur clusters which occur as electron transport pathway components in bacterial hydrogenases. The active site is referred to as the "H-cluster" and consists of a "classical" [4Fe-4S] cluster connected via a protein cysteine side group to a unique $[2Fe]_H$ sub-cluster containing CO and $CN^-$ ligands as well as bridging dithiolate ligand.

In this thesis, combined EPR, FTIR and electrochemical methods were used to study the active site of the [FeFe] hydrogenase from *Clamydomonas reinhardtii*. The following topics were addressed:

- The super reduced state of the H-cluster ($H_{sred}$) which only seems to be stable as resting state in CrHydA1 was characterized by EPR spectroscopy in combination with FTIR. These studies identified $H_{sred}$ as a $[4Fe\text{-}4S]^{1+}Fe^{I}Fe^{I}$ configuration which is two steps reduced relative to the active oxidized state $H_{ox}$. Protein Film Electrochemistry (PFE) experiments indicated involvement of the super reduced state in the catalytic cycle. We proposed a new catalytic cycle in which the reduction of a substrate proton to a terminal hydride occurs in one step.
- The biosynthesis of the H-cluster was studied by FTIR and EPR methods supplemented by DFT calculations. It was shown that three mimic complexes of the $[2Fe]_H$ sub-cluster can bind to the [4Fe-4S] cluster of HydF (one of the maturases involved in the biosynthesis of the H-cluster) and then can be transferred to apo

[FeFe] hydrogenase. The apo [FeFe] hydrogenase could be fully activated only with the mimic complex containing a bridging amine function in the dithiolate ligand confirming its postulated role in the catalytic mechanism.

- Subsequent biochemical experiments combined with EPR and FTIR showed that the apo [FeFe] hydrogenase can be activated also directly by the mimic complex, i.e. without assistance of HydF, and that the H-cluster obtained in this way is spectroscopically undistinguishable from the native one.
- FTIR spectroelectrochemistry was used to study the redox behavior of CrHydA1 in the presence and absence of extrinsic CO for the active semisynthetic H-cluster as well as for one of the non-active variants. Two new redox states were identified in which the $[4Fe\text{-}4S]_H$ sub-cluster was in the reduced state. This finding strongly supports a model in which the $[4Fe\text{-}4S]_H$ sub-cluster is actively participating in the redox transitions occurring during the catalytic cycle of the enzyme.
- Multi-frequency HYSCORE and ENDOR studies were performed on a hybrid enzyme maturated with a non-natural H-cluster in which the bridging amine function was replaced by an inert $CH_2$ group. The $CN^-$ ligands of this hybrid H-cluster were labeled with $^{13}C$ and $^{15}N$. These studies provided detailed information on how the spin density is distributed over both $CN^-$ ligands. The detailed data on the relative orientation of the $^{13}C$ and $^{15}N$ magnetic interaction tensors allowed us to propose that the g-axis frame of the H-cluster in the $H_{ox}$ state adopts the local symmetry of the $[2Fe]_H$ sub-cluster.

## Zusammenfassung

[FeFe]-Hydrogenasen sind Metalloenzyme, die die Oxidation von Wasserstoff sowie die Reduktion von Protonen zu Wasserstoff katalysieren. Das Verständnis des katalytischen Mechanismus und der Biosynthese von Hydrogenasen sowie ihrer elektronischen und geometrischen Struktur ist von großem Interesse für biotechnologische Prozesse. Hydrogenasen dienen als Modelle für die Entwicklung von Wasserstoff-umsetzenden Katalysatoren basierend auf erneuerbaren Energiequellen.

Die aus Algen stammende [FeFe]-Hydrogenase aus dem Organismus *Clamydomonas reinhardtii* (CrHydA1) ist für die Untersuchung von Hydrogenasen besonders gut geeignet, da sie ausschließlich das aktive Zentrum und keine weiteren Eisen-Schwefel-Cluster enthält, welche für den Elektronentransport in von Bakterien abstammenden Hydrogenasen verantwortlich sind. Das aktive Zentrum wird als „H-Cluster“ bezeichnet und besteht aus einem „klassischen“ [4Fe-4S]-Cluster, verbunden über den Schwefel einer Cystein-Gruppe mit der ungewöhnlichen $[2Fe]_H$-Untereinheit, welche CO und $CN^-$ Liganden sowie einen verbrückenden Dithiolat-Liganden enthält.

In der vorliegenden Arbeit wurde das aktive Zentrum der [FeFe]-Hydrogenase von *Clamydomonas reinhardtii* mit einer Kombination von EPR- und FTIR-spektroskopischen sowie elektrochemischen Methoden untersucht. Folgende Fragestellungen wurden dabei untersucht:

- Der „super-reduzierte“ Zustand des H-Clusters ($H_{sred}$), der scheinbar nur in Algenenzymen als stabiler Verweilzustand existiert, wurde mittels EPR-Spektroskopie in Kombination mit FTIR-Spektroskopie untersucht. Die durchgeführte Analyse identifiziert $H_{sred}$ als $[4Fe\text{-}4S]^{1+}Fe^{I}Fe^{I}$ Zustand, welcher gegenüber dem aktiven oxidierten Zustand $H_{ox}$ um zwei Redoxstufen reduziert ist. Proteinfilmelektrochemie (PFE) Experimente deuten auf die Beteiligung des „super-reduzierten“ Zustandes im katalytischen Zyklus hin. Ein neuer katalytischer Zyklus

wurde basierend auf diesen Ergebnissen vorgeschlagen, in dem die Reduktion des Substrats zum terminalen Hydrid in einem Schritt vollzogen wird.

- Die Biosynthese des H-Clusters wurde mittels EPR- und FTIR-Spektroskopie untersucht und die Analyse durch DFT-Rechnungen unterstützt. Es wurde gezeigt, dass drei freie Modellkomplexe der $[2Fe]_H$-Untereinheit an den [4Fe-4S]-Cluster von HydF, einer für die Biosynthese des H-Clusters relevanten Maturase, binden und anschließend an die apo-[FeFe]-Hydrogenase transferiert werden können. Die apo-[FeFe]-Hydrogenase konnte in vollem Umfang nur mit einem Modellkomplex aktiviert werden, der eine Amin-Gruppe in der Dithiolat-Brücke enthält. Dieses Ergebnis bestätigt die Rolle der Amin-Base im katalytischen Mechanismus.
- Anschließende biochemische Experimente in Kombination mit EPR- und FTIR-Spektroskopie zeigten, dass die apo-[FeFe]-Hydrogenase auch auf direktem Wege ohne die Beteiligung der HydF-Maturase mit einem Modellkomplex aktiviert werden konnte. Der so erhaltene H-Cluster ist von dem nativen System spektroskopisch nicht unterscheidbar.
- FTIR Spektroelektrochemie wurde eingesetzt, um das Redoxverhalten von CrHydA1 mit dem aktiven semi-synthetischen H-Cluster und den inaktiven Derivaten in Gegenwart und in Abwesenheit von zugeführtem CO zu untersuchen. Zwei neue Redoxzustände wurden identifiziert, in denen der [4Fe-4S]-Cluster reduziert vorliegt. Dieses Ergebnis unterstützt die These, dass der [4Fe-4S]-Cluster an den Redoxübergängen im katalytischen Zyklus des Enzyms aktiv beteiligt ist.
- Multi-Frequenz HYSCORE und ENDOR Untersuchungen wurden am Hybridenzym durchgeführt, welches mit einem nicht-natürlichen H-Cluster maturiert wurde. Dieses enthält statt einer Amin-Funktion in der Dithiolat-Brücke eine $CH_2$-Gruppe. Die $CN^-$ Liganden dieses Hybrid-Clusters wurden mit $^{13}C$- und $^{15}N$-Isotopen markiert. Diese Studien erlaubten einen detaillierten Einblick in die Verteilung der Spindichte

über beide $CN^-$ Liganden. Die Analyse der relativen Orientierung der $^{13}C$ und $^{15}N$ Hyperfeintensoren erlaubte die Annahme, dass das g-Achsensystem des H-Clusters im $H_{ox}$ Zustand die lokale Symmetrie der $[2Fe]_H$-Untereinheit einnimmt.

## Acknowledgments

The work presented in this thesis could not come to existence without support from the following people to whom I would like to express my gratitude:

- Prof. Dr. Wolfgang Lubitz, first for an opportunity to learn advanced EPR methods during my master studies, in one of the best EPR centers in the world and then, for giving me the opportunity to do my research in his group in Max Planck Institute for Chemical Energy Conversion, for discussions and allowing me to develop as a scientist.
- Prof. Dr. Rainer Weinkauf for agreeing to be the second reviewer of this thesis.
- Dr. Edward Reijerse for his supervision, endless discussions, support and patience, especially during correcting all the manuscripts and the thesis.
- Dr. Alexey Silakov and Dr. Olaf Rüdiger for introducing me to the "hydrogenase world" and increasing my knowledge about magnetic resonance techniques as well as introducing me to the wonderful world of electrochemistry and FTIR. I am very thankful for all the discussions and help.
- Dr. Camilla Lambertz, Julian Esselborn, Danuta Krawietz and Dr. Martin Winkler and Prof. Dr. Thomas Happe (from Ruhr-University Bochum) for long term and fruitful collaboration, amazing quality samples, discussions and letting me realize that maybe biochemistry is not entirely black magic.
- Dr. Gustav Berggren, Dr. Trevor Simmons, Dr. Vincent Artero and Prof. Dr. Marc Fontecave (from CEA) for a successful collaboration and providing both protein samples and chemical compounds.
- Judith Siebel and Dr. Katharina Weber not only for samples, abstract translation to german, but also for sharing the wall between offices and all the laughter.
- Ania Nalepa for endless discussions about our projects and life and especially all the hugs and support during the rough times.

- Gudrun Klihm, Leslie Curell and Frank Reikowski for their technical support in the EPR and FTIR labs.
- Stephan Syring and Siegfried Klihm for their help in improving of the FTIR equipment.
- Birgit Deckers for her help when pictures were not pretty enough, and Rita Gröver, who always had a helping hand.
- All my coworkers in the Max Planck Institute for their smaller and bigger help during my studies and for being there after working hours. Especially I would like to thank Dr. Özlen Erdem for bringing some culture to my life and all the concerts.
- Last but not the least my parents and brother Piotr for their constant support, even when many unexpected choices had to be made and my husband Dr. Prasanna Venkatesh Rangadurai for his care, encouragement and understanding.

## Table of Contents

## List of Abbreviations

| | |
|---|---|
| $b_6f$ | cytochrome $b_6f$ |
| CpI | [FeFe] hydrogenase from *Clostridium pasteurianum* |
| CrHydA1 | [FeFe] hydrogenase from *Clamydomonas reinhardtii* |
| CV | cyclic voltammetry |
| CW | continuous wave |
| DdH | [FeFe] hydrogenase from *Desulfovibrio desulfuricans* |
| DET | direct electron transfer |
| DFT | density functional theory |
| *E. coli* | *Escherichia coli* |
| ENDOR | electron nuclear double resonance |
| EPR | electron paramagnetic resonance |
| ESE | electron spin echo |
| ESEEM | electron spin echo envelope modulation |
| EXAFS | extended X-ray absorption fine structure |
| FID | free-induction decay |
| FTIR | Fourier transform infrared |
| GTP | guanosine-5-triphosphate |
| HYSCORE | hyperfine sublevel correlation spectroscopy |
| IR | infrared |
| MW | microwave |
| NMR | nuclear magnetic resonance |
| PC | plastocyanin |

| | |
|---|---|
| PCET | proton coupled electron transfer |
| PetF | [2Fe-2S] ferredoxin PetF |
| PFE | protein film electrochemistry |
| PGE | pyrolytic graphite edge |
| PQ | plastoquinone |
| PSI | photosystem I |
| PSII | photosystem II |
| QM/MM | quantum mechanics/molecular mechanics |
| RF | radiofrequency |
| ROS | reactive oxygen species |
| SAM | S-adenosylmethionine |

# I. Introduction

Energy sources had, have and will have great influence on politics and the economy of the world. Together with the increase of population and economic development, energy demand is increasing. Nowadays, most of the energy is produced from non-renewable sources like oil, coal and gas. Despite considerable pressure on the development of green energy sources, in 2012, only 9% of the total consumed energy was produced from renewable sources. On the other hand, energy rich hydrogen, which upon combustion, produce only water as a byproduct, is hardly utilized at all, though NASA, since the 1970s, has demonstrated the use of liquid hydrogen to propel space shuttles and rockets into space. Over the past 40-45 years, many methods of hydrogen production were developed. However none of them are efficient and cheap enough to change the market. That is why it is important to look at nature for inspiration and find out how some microorganisms use hydrogen in their metabolic processes, since this involves hydrogen splitting and also hydrogen formation/generation.

Metalloenzymes called hydrogenases are found in the wide range of microorganisms from archaea, bacteria to some of the eukaryotes[1-4]. This is one of the oldest enzymes found in nature and it reversibly catalyzes the seemingly simple reaction of molecular hydrogen conversion into protons and electrons[1, 2]:

$$H_2 \rightleftharpoons 2H^+ + 2e^- \quad (1.1)$$

Microbes produce $H_2$ to dispose the excess of reducing equivalents created during fermentative metabolism or as a byproduct of nitrogenase activity[2]. Other $H_2$ production mechanisms are connected to anoxic photosynthetic dark reactions[2, 5, 6]. In unicellular green algae like *Chlamydomonas reinhardtii*, dihydrogen ($H_2$) is produced by a hydrogenase in the chloroplast from electrons delivered to it by photosystem I via a plant type ferredoxin (see figure 1.1)[7-9].

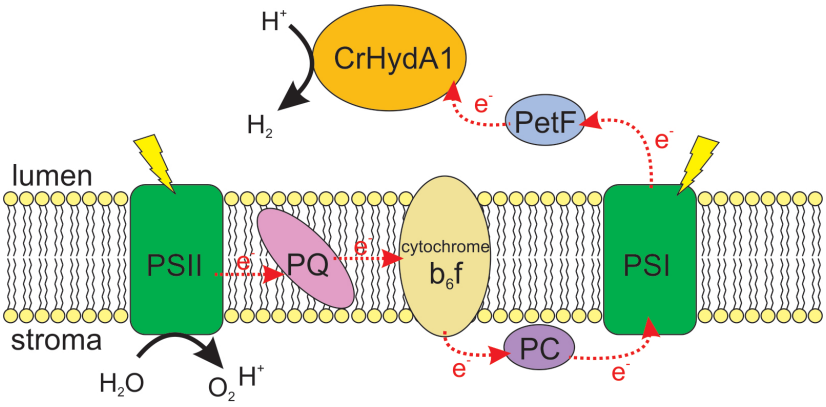


**Figure 1.1.** Schematic representation of the light reaction and electron transfer to the [FeFe] hydrogenase in green algae. PQ is plastoquinone, PC plastocyanin, PetF [2Fe-2S]-ferredoxin, PSI photosystem I and PSII photosystem II.

Hydrogenases are found in various locations in microorganisms and have different functions and compositions. Hydrogenases can be classified into three groups, depending on the metal composition of their active site[3]:

(1) [NiFe] hydrogenases containing a hetero-nuclear nickel-iron bimetallic site as well as the related subclass of [NiFeSe] hydrogenases where the one of the cysteine residues is substituted by a selenocysteine[10];

(2) [FeFe] hydrogenases with a unique 6 Fe cluster, which is described in more detail below and

(3) [Fe] hydrogenase, also called iron-sulfur-cluster-free hydrogenases, containing only one iron atom surrounded by a distorted square or an octahedral ligation shell depending on the enzymatic state (see figure 1.2)[11].

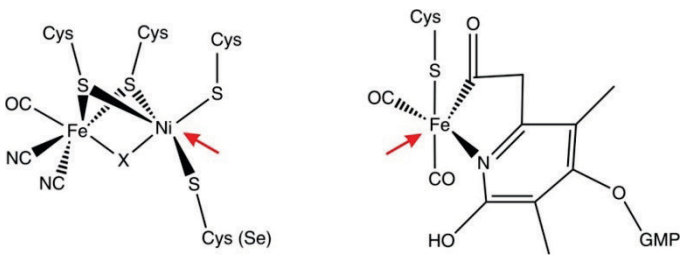


**Figure 1.2**. Schematic representation of the active sites of the [NiFe] (left) and [Fe] (right) hydrogenases. In the [NiFeSe] subclass Se is located in one of the Cys of the Ni atom. The red arrows indicate the open coordination sites.

The present study is focused on the characterization of [FeFe] hydrogenases, which are the most active hydrogenases in hydrogen production.

## 1.1. Structure of [FeFe] hydrogenases and its active site

Until this day crystal structures of only two holo [FeFe] hydrogenases and one apo [FeFe] hydrogenase were obtained (all of them are shown in the figure 1.3)[12-17]. The first structure was published in 1998 with a resolution of 1.8 Å, for the cytoplasmic [FeFe] hydrogenase from the bacteria *Clostridium pasteurianum* (referred to as CpI)[12]. It was found that this 64 kDa monomeric enzyme contains 20 Fe atoms arranged into 5 distinct [Fe-S] clusters. One year later, the structure of heterodimeric [FeFe] hydrogenase from *Desulfovibrio desulfuricans* (referred to as DdH) was resolved with a resolution of 1.6 Å[14]. The bigger subunit (46 kDa) contains 12 Fe atoms creating 3 [Fe-S] clusters, while the smaller subunit (14kDa) does not contain any iron. The active site is rather unusual and contains 6 Fe atoms[12, 14]. The rest of the Fe atoms are arranged in [4Fe-4S] clusters and a [2Fe-2S] cluster, as is the case in CpI, that are within the distance of approximately 11 Å from each other and create an electron transfer pathway from the surface of the enzyme to the active site. More recently, in 2010, the crystal structure of unmaturated [FeFe] hydrogenase from *Chlamydomonas reinhardtii* (CrHydA1) was published[17]. In this relatively small monomeric enzyme, the active site is localized near the surface and no extra [FeS] clusters were identified. It is interesting that despite many groups attempting to crystalize the active form of CrHydA1, none of them have been successful until this day.

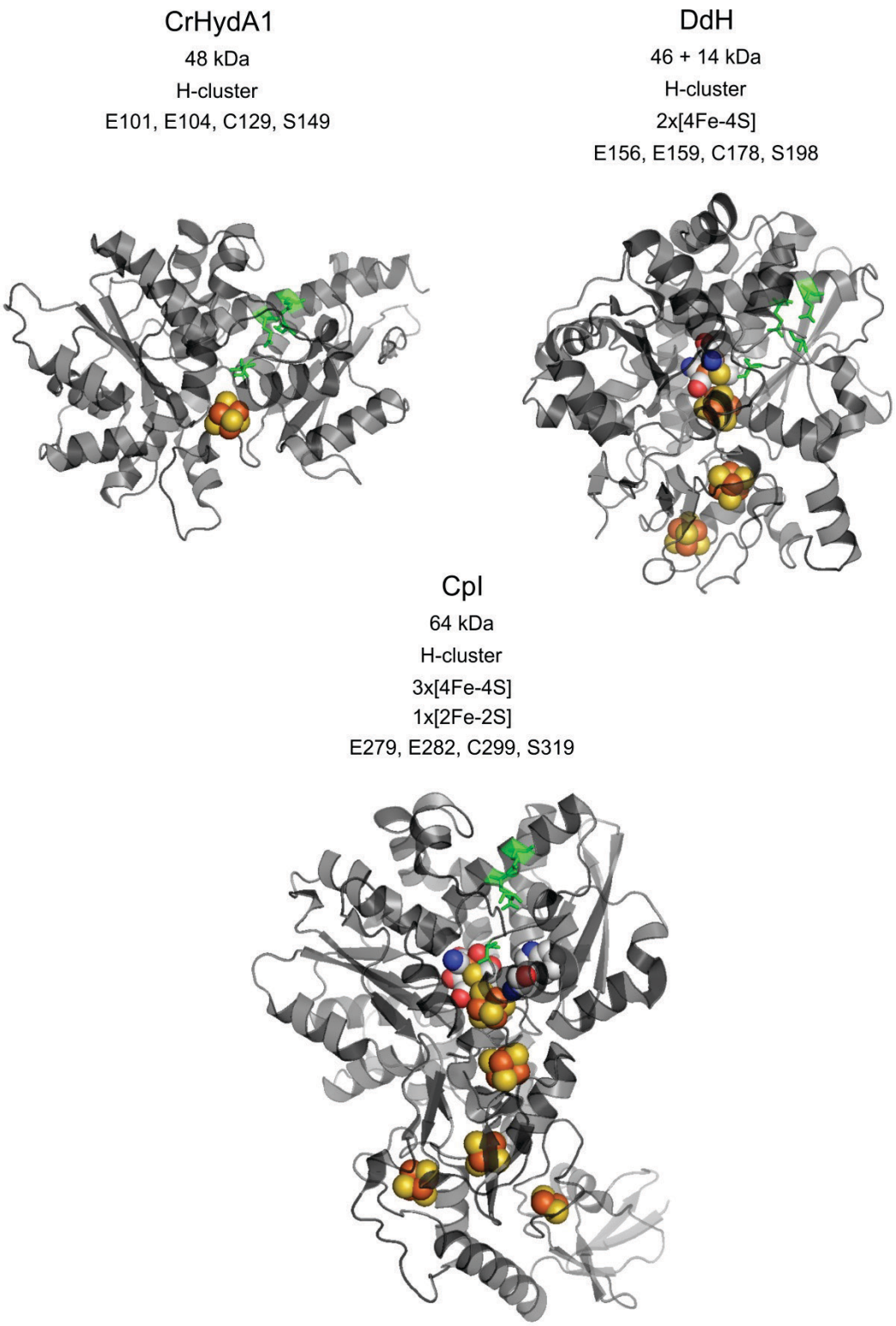


**Figure 1.3.** Three available structures of [FeFe] hydrogenases from *Chlamydomonas reinhardtii* (PDB 3LX4)[17] (unmaturated form), *Desulfovibrio desulfuricans* (PDB 1HFE)[14] and *Clostridium pasteurianum* (PDB 3C8Y)[16]. Iron-sulfur clusters involved in electron transfer are indicated as spheres and amino acids involved in the $H^+$ transfer in green. Above the structures molecular masses of each protein as well as number and type of the iron-sulfur clusters and amino acids involved in the $H^+$ transfer are indicated.

The active site of [FeFe] hydrogenases is called the H-cluster (see figure 1.4) and it is almost identical in the two available X-ray structures[12-16]. This 6 Fe cluster is built up from a typical [4Fe-4S] cluster and attached via a cysteine sulfur to a diiron center [2Fe]. Combined crystallographic data and FTIR studies show that both Fe ions in the $[2Fe]_H$ sub-cluster are coordinated by two terminal CO and $CN^-$ ligands which are keeping these ions in low oxidation and spin states[15]. Additionally, there are two bridging motifs namely a bridging CO ligand and a dithiolate group. In the crystal structures (with resolution 1.6 and 1.8 Å), the central atom of this dithiolate group could not be uniquely identified and at first was assigned as a carbon[12, 14]. However, in following studies, it was also proposed to be an oxygen or nitrogen atom[16, 18, 19]. The first experimental evidence for a nitrogen atom was delivered by $^{14}N$ HYSCORE spectroscopy[20]. This assignment was recently unambiguously confirmed by the results presented in this thesis[21, 22]. The iron, distal to the $[4Fe\text{-}4S]_H$ sub-cluster ($Fe_d$) has an open coordination site, which is most likely the substrate binding site.

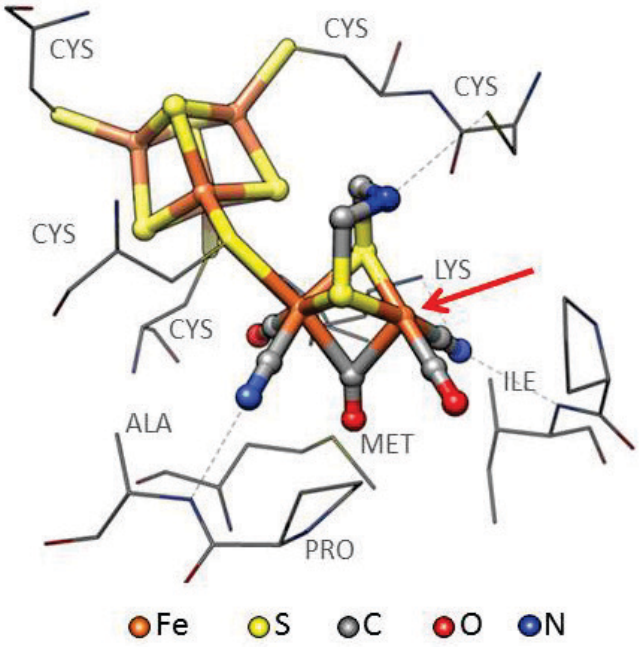


**Figure 1.4.** Structure of the active site of [FeFe] hydrogenases with marked hydrogen bonds of the ligands to the surrounding amino acids. The red arrow indicates the open coordination site.

It is noteworthy that the diiron part of the active site is bound to the protein only by one covalent bound (described above). Furthermore, the $CN^-$ ligands as well as the amino group in the bridging dithiol bridgehead, create hydrogen bonds with the amino acids in the protein pocket conserved in the [FeFe] hydrogenases (see figure 1.4). It was shown in EPR studies that the hydrogen bonding is particularly strong between the distal $CN^-$ ligand and lysine[20]. The importance of conserved amino acids surrounding the H-cluster was also demonstrated. Upon single mutation of any amino acid creating a hydrogen bond with the diiron part of the active site, the integrity and activity is strongly influenced[23].

The crystal structures also reveal the presence of hydrophobic channels from the active site to the surface which allows for gas transfer[14, 24]. Molecular dynamic simulations performed on CpI and DdH show that there are three gas accessible channels serving as a pathway for hydrogen gas as well as oxygen and carbon monoxide[25].

The structures of CpI and DdH investigated with QM/MM methods and amino acid exchange studies of CrHydA1 show that the highly conserved cysteine located next to the nitrogen from the dithiol bridge is the first amino acid in the proton transfer pathway[26, 27]. Then the proton is transferred to the surface of the enzyme by two glutamic acid as well as by serine (see figure 1.3)[28, 29].

## 1.2. Maturation of [FeFe] hydrogenases

The mechanism of H-cluster assembly in [FeFe] hydrogenases is still not completely understood[1, 30-32]. By looking at the structure of this cluster, two well distinguished sub-clusters can be identified, one being a typical [4Fe-4S] cluster and the second is an unusual diiron cluster. It was shown that during heterogenic overexpression of CrHydA1 in the *Escherichia coli* system, the obtained enzyme is not active[33]. It turned out that the cubane part is assembled while the $[2Fe]_H$ sub-cluster is missing[17]. This means that the

[4Fe-4S] cluster is synthesized by the standard iron/sulfur cluster machinery which is also present in *E. coli*[34].

Three accessory proteins namely HydE, HydF and HydG, responsible for synthesis and insertion of the diiron part have been identified already ten years ago, but information about their structures and functions is still rather limited[35-37]. In many co-expression studies it was shown that all of these proteins are needed to maturate CrHydA1[32, 38, 39]. This is in contradiction to a cell-free system study suggesting that HydF may be optional in hydrogenase maturation[40]. On the other hand, it turned out that in all cell-free activation assays the addition of an *E. coli* protein cell lysate was essential[40, 41]. This suggests that all the proteins involved in the maturation are still not identified.

HydE and HydG are homologs containing a $CX_3CX_2C$ motif characteristic for the radical S-adenosylmethionine (SAM) family of enzymes[42, 43]. These proteins contain an N-terminal [4Fe-4S] cluster with an open binding site for SAM. HydE and HydG also contain a binding motif for an accessory iron sulfur cluster, [2Fe-2S] in HydE and [4Fe-4S] in HydG[44-46]. A recent study indicated that while SAM binds to the N-terminal cluster of HydG, tyrosine could interact with the C-terminal [4Fe-4S] cluster[47]. It is now generally accepted that upon a SAM initiated radical reaction, the CO and $CN^-$ ligands of the H-cluster are generated along with deoxyadenosine and *p*-cresol[39, 45]. A recent rapid freeze quench and spectroscopic study demonstrated that the generated CO and $CN^-$ are transferred together with the Fe ion from the C-terminal [4Fe-4S] cluster to the unmaturated CrHydA1, being the precursors of the diiron part of the H-cluster[48]. There is no information about the synthesis of the dithiolate bridge available and since the function of HydE is not known, it is assumed that this enzyme might be responsible for this step.

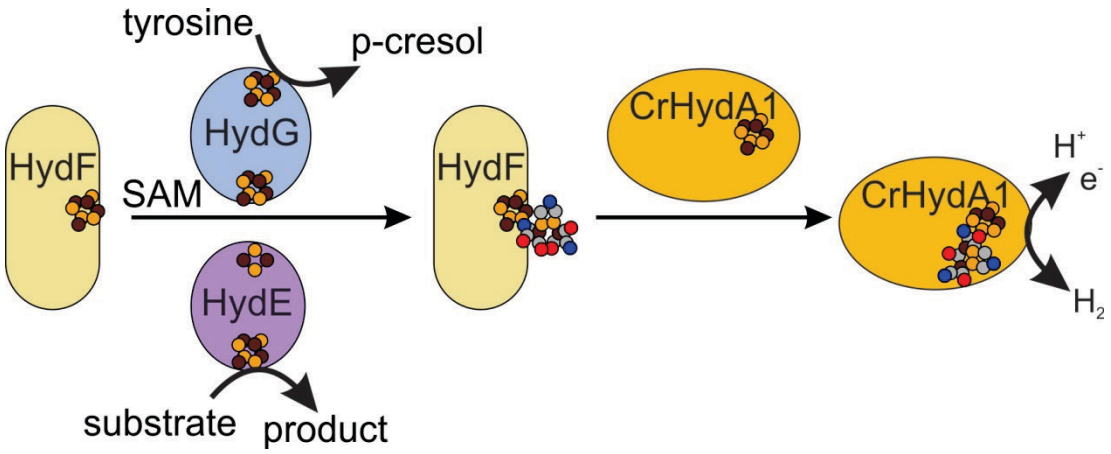


**Figure 1.5.** Schematic mechanism of maturation of [FeFe] hydrogenase, where HydG and Hyd E synthetize precursor of the active site and HydF transfers and assembles it to unmaturated hydrogenase.

The crystal structure of apo HydF from *Thermotoga neapolitana* has been obtained with 3.0 Å resolution[49]. It confirmed the presence of an N-terminal domain containing a GTP-binding pocket as well as a C-terminal domain containing the [4Fe-4S] cluster binding site[50]. Three cysteines and one histidine are located at the surface of the enzyme indicating that the [4Fe-4S] cluster is exposed at the surface. It was shown with various methods that HydF prepared in the presence of HydE and HydG, carries the precursor of the diiron sub-cluster of the H-cluster and can activate unmaturated [FeFe] hydrogenase[38, 51, 52]. It was therefore postulated that HydF acts as a transferase for the precursor of the $[2Fe]_H$ sub-cluster and facilitates its insertion into the [FeFe] hydrogenase. Based on the available crystal structures of unmaturated CrHydA1 and fully assembled CpI, it was postulated that [FeFe] hydrogenases have a special channel for the insertion of the diiron part of the H-cluster which closes after maturation of the enzyme[12, 13, 16, 17]. This hypothesis is, however, still not confirmed and the exact mechanism of precursor insertion by HydF is still an open question.

## 1.3. Redox states of the H-cluster

During the catalytic process of hydrogen conversion, the iron centers in the active site of [FeFe] hydrogenases change their oxidation states. Based on several spectroscopic

methods, namely FTIR, FTIR spectroelectrochemistry, EPR (Electron Paramagnetic Resonance) and Mössbauer spectroscopy, various characteristic states of the H-cluster have been identified[53].

Two inactive oxidized states of the H-cluster called $H_{inact}^{air}$ and $H_{trans}$ were observed in aerobically purified DdH[54, 55]. However, those inactive states were not observed in any anaerobically purified hydrogenases such as CpI and CrHydA1[53]. Both iron atoms in the "overoxidized" inactive $[2Fe]_H$ sub-cluster states are in the ($Fe^{II}$) configuration and therefore EPR silent[54]. In the $H_{inact}^{air}$ state, the $[4Fe\text{-}4S]_H$ sub-cluster is oxidized and therefore also does not show an EPR signal[54]. Upon one electron reduction ($E_m$=-92 mV at pH 8.0) $H_{trans}$ is generated[55]. In this process the $[4Fe\text{-}4S]_H$ part is reduced (1+) and shows a characteristic $[4Fe\text{-}4S]^+$ S=1/2 EPR signal with g=(2.06, 1.96, 1.89)[54].

In the next step, under gentle reductive conditions e.g. through $H_2$ exposure, $H_{trans}$ from DdH is irreversibly converted ($E_m$=-301 mV at pH 8.0) into the active oxidized state ($H_{ox}$)[55]. In some spectroelectrochemical experiments the Nernst curve was consistent with a two electron process, although it is not clear, if electrons are flowing during this process[55]. In any case, the $H_{trans}$ and $H_{ox}$ state of the H-cluster are iso-electronic. Apart from DdH the $H_{ox}$ state is also present in isolated samples of CpI and CrHydA1 and, in fact, in all known [FeFe] hydrogenases. The $H_{ox}$ state, can also be induced from the more reduced states of the enzyme by oxidation with thionine or, simply, by flashing with argon[54, 56]. The FTIR spectra of $H_{ox}$ in the CO and $CN^-$ stretch region of the various [FeFe] hydrogenases are virtually identical[1]. There is a characteristic signal present for the bridging CO around 1800 $cm^{-1}$. Also the EPR signals look very similar for all the [FeFe] hydrogenases. In this state, the diiron part of the H-cluster exists in a mixed valence ($Fe^{I}Fe^{II}$) paramagnetic (S=1/2) state with g=(2.10, 2.04, 2.00) while the $[4Fe\text{-}4S]_H$ sub-cluster is oxidized (2+) and EPR silent[1, 54, 57-60].

Upon further one electron reduction ($E_m$ around -400 mV at pH 8.0), the active reduced state ($H_{red}$) is generated[55, 61]. It is believed that reduction takes place in the $[2Fe]_H$

sub-cluser resulting in an antiferromagnetically coupled $Fe^{I}Fe^{I}$ configuration which is EPR silent[1, 53]. In the FTIR spectra obtained for CrHydA1 all signals are shifted to lower wavenumbers confirming the reduction of Fe ions in the diiron part[61]. A different situation is observed in DdH where the signal from the bridging CO is lost (the bridging CO ligand becomes terminal and is bound to the distal iron of the $[2Fe]_H$ sub-cluster) and the whole spectrum is rearranged[55].

The $H_{red}$ can, in principle, be further reduced to a so-called "super reduced" state ($H_{sred}$ ). This process was first observed for DdH at very low potentials ($E_m$=-540 mV at pH 8.0 but this transition was "incomplete and irreversible" and was resulting in the destruction of the enzyme[55]. A stable $H_{sred}$ was obtained for CrHydA1 at much higher potential ($E_m$=-460 mV at pH 8.0) but has an FTIR spectrum very similar to the one obtained for $H_{red}$ from DdH[61, 62]. It is postulated that [FeFe] hydrogenases containing additional [4Fe-4S] clusters, the super reduced state is not stabilized because electron redistribution to F-clusters is thermodynamically favorable and a superposition of the $H_{red}$ and $H_{sred}$ is observed. In small hydrogenases like CrHydA1 which contain only the H-cluster all the redox states can be observed and stabilized.

The $H_{sred}$ state is expected to be EPR active (S=1/2). Hence, there are two possibilities for the electronic structure of the H-cluster in the $H_{sred}$ state: either the binuclear site is further reduced to $Fe^{0}Fe^{I}$ or the $[4Fe\text{-}4S]^{2+}$ sub-cluster is reduced to $[4Fe\text{-}4S]^{+}$. The results presented in this thesis solved this dilemma. It was shown that occurrence of the $H_{sred}$ state, as identified by FTIR, is correlated with a paramagnetic species consistent with a reduced $[4Fe\text{-}4S]_H$ cluster (see results presented in this thesis)[62]. It was also postulated that this species is catalytically active and participates in the reaction mechanism of all [FeFe] hydrogenases[62].

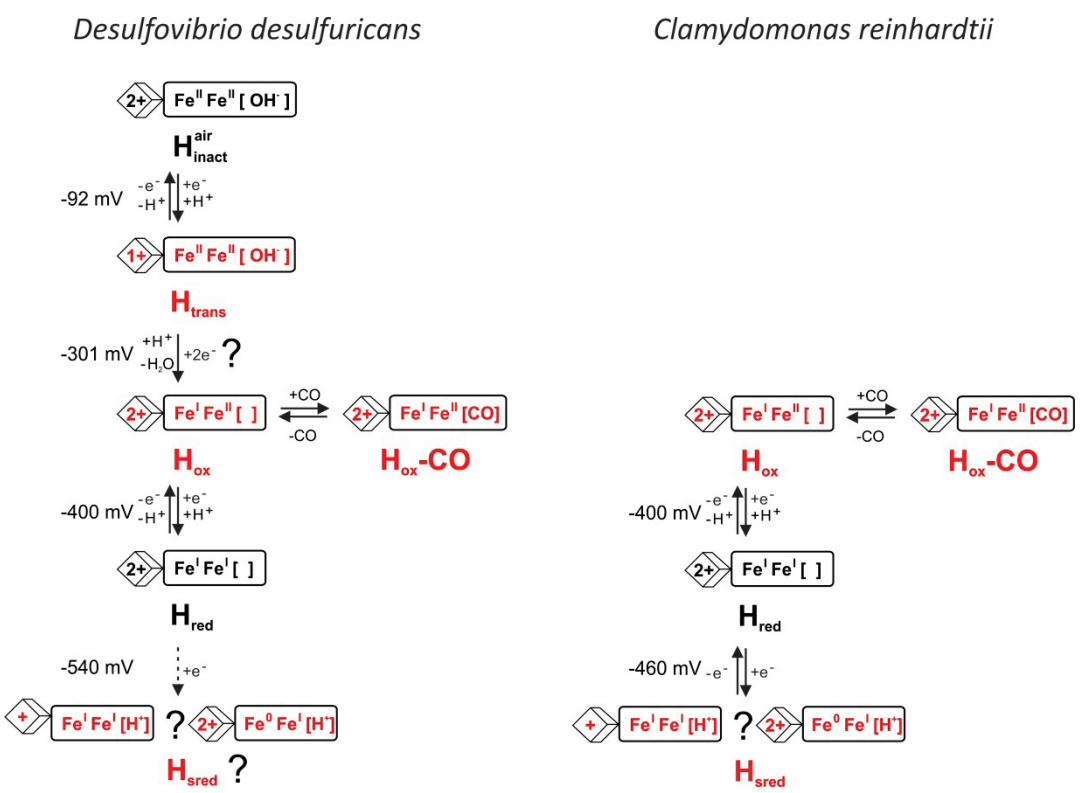


**Figure 1.6.** Oxidation states of the iron ions in the diiron and $[4Fe\text{-}4S]_H$ sub-clusters observed in two different [FeFe] hydrogenases in different redox states observed experimentally (without including knowledge presented in this thesis) as well as relationship between these states and the transition potentials measured at pH 8.0. Redox states observed in the EPR are marked in red and EPR silent states in black. Question marks represent uncertainty in the knowledge.

The active site of the active enzyme can be inhibited by CO which generates the $H_{ox}$-CO state[1, 13, 63]. Again, for this state, both EPR and FTIR signals are very similar for all the [FeFe] hydrogenases[1]. The electronic structure of $H_{ox}$-CO is similar to that of $H_{ox}$ and is characterized by a mixed valence ($Fe^IFe^{II}$) $[2Fe]_H$ sub-cluster in combination with an oxidized $[4Fe\text{-}4S]_H$ sub-cluster[1]. The EPR (S=1/2) signal is axial with g=(2.052, 2.007, 2.007)[54, 58, 64]. The signal from $H_{ox}$-CO is often observed in samples exposed to light and/or oxygen. In this case, the CO ligands dissociated from the destroyed H-cluster are captured by H-clusters that are still intact. This process is referred to as "cannibalization"[54, 55].

It is shown in the work presented in this thesis that upon one electron reduction ($E_m$=-470 mV at pH 8.0) of $H_{ox}$-CO from CrHydA1, a reduced CO inhibited state is generated ($H_{'red'}$-CO). The FTIR spectra of both these states are only slightly shifted with respect to each

other, but the electronic structure cannot be consistent to either $H_{ox}$-CO or $H_{red}$. It was therefore postulated that reduction takes place on the $[4Fe\text{-}4S]_H$ sub-cluster and results in an EPR silent species.

### 1.4. [FeFe] hydrogenases activity

[FeFe] hydrogenases are the most active group amongst all hydrogenases concerning *in vivo* hydrogen production[65, 66]. Of course, there are significant differences in the turnover rate obtained for [FeFe] hydrogenases from different organisms[65]. However, also differences in protein preparation methods and activity assays cause variability in the reported activity values between different groups. In the pioneering experiments performed on [FeFe] hydrogenase from *Chlamydomonas eugametos* reduced methylviologen was used as electron mediator[67]. This procedure in combination with gas chromatography is currently the most commonly used method for determination of hydrogen production[65]. Usually, the activity of the enzymes is given in µmol $H_2$ per minute per mg of enzyme, which can be converted into turnovers per second. Different [FeFe] hydrogenases can produce hundreds to thousands of $H_2$ molecules per second.

Another good method to study enzyme activity as well as inactivation and reactivation events is protein film electrochemistry (PFE) where the enzyme is attached to an electrode and the enzyme activity is observed as an electrical current[68, 69]. However, with this method it is very difficult to determine the turnover rate of the enzyme due to low coverage of the enzyme what prevents its determination. Also one does not observe specific redox states but rather activity of the enzyme at certain potentials.

In the simplest and most common PFE experiment, called cyclic voltammetry (CV), three regions of potential for nearly all [FeFe] hydrogenases are observed (see figure 1.7)[68, 69]. At low potentials hydrogen production is dominating. When the current crosses the zero line, at the thermodynamic potential for $H^+$ reduction, hydrogen production and

oxidation activity are equal. Then the $H_2$ oxidation process becomes dominant until at very high potentials under 1 bar $H_2$ the enzyme starts to inactivate and the current drops.

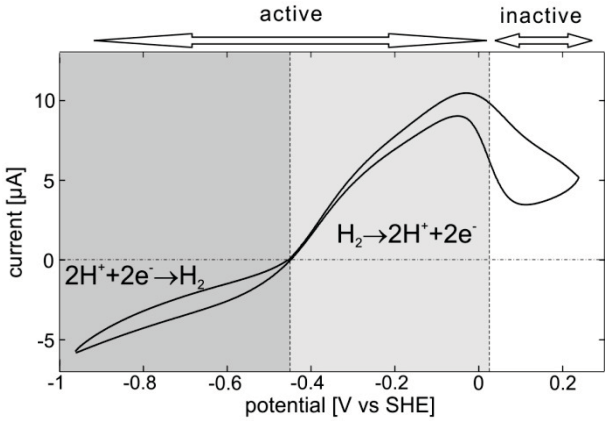


**Figure 1.7.** Typical cyclic voltammogram obtained for CrHydA1 adsorbed at the pyrolytic graphite electrode.

The PFE is a very useful method for the observation of inhibition and/or destruction of the enzyme[70]. For example, CO inhibition was studied in immaculate detail using PFE[1, 71-73]. It was observed that when the active enzyme is exposed to CO gas the catalytic current drops almost immediately. After removing the CO from the electrochemical cell the current slowly recovers. It was concluded from the detailed potential dependence on CO inhibition that at high potentials CO inhibition is complete and fully reversible while at low potentials it exhibits some irreversibility.

Since the emergence of hydrogenases is estimated at 2-4 billion years ago and at that time oxygen was not present in the atmosphere, it is not surprising that [FeFe] hydrogenases are extremely oxygen sensitive[1]. It was nicely demonstrated that in the presence of even very small amounts of oxygen, the activity of the enzyme immediately drops and does not recover[74, 75]. The mechanism of $O_2$ inactivation is not fully understood. However, important insight was obtained from extended X-ray absorption fine structure (EXAFS) spectroscopy[76]. It was proposed that oxygen was damaging the $[4Fe\text{-}4S]_H$ cluster of the H-cluster rather than the diiron center and in the proposed mechanism $O_2$ would first bind to the distal iron atom in the H-cluster, where it would be partially reduced to form a

reactive oxygen species (ROS) that could migrate the short distance to damage the $[4Fe\text{-}4S]_H$ cluster[76].

## 1.5. Proposed catalytic mechanisms

Based on available knowledge about the structure of the H-cluster as well as the active redox states different mechanisms of the hydrogen evolution and oxidation were considered[19, 53, 77-82].

As mentioned previously, the central atom in the ditholate bridge could not be uniquely identified in the crystal structure of CpI and DdH. Depending on the type of atom two main hypotheses based on DFT calculations were discussed. If the dithiolate group contains carbon, which cannot act as a base, it is most probable that heterolitic splitting occurs via formation of a bridging hydride and protonation of one of the bridging sulfurs of the dithiol moiety[79, 82]. On the other hand, if in the dithiolate bridge an oxygen atom would be present, heterolitic splitting would proceed via the ether group[16]. The experimental evidences presented in this thesis unambiguously demonstrate that a nitrogen atom is present in the dithiolate bridge. Therefore, these mechanisms are no longer under consideration.

Based on the two known redox states ($H_{ox}$ and $H_{red}$) several mechanisms involving proton coupled electron transfer (PCET) steps were proposed[53]. These would lead to additional transient states; for example, $Fe^{II}Fe^{II}[H^-]$ and $Fe^{II}Fe^{I}[H_2]$. In these mechanisms only the diiron part of the H-cluster was involved in the hydrogen conversion and the $[4Fe\text{-}4S]_H$ sub-cluster remained in its oxidized form through the catalytic cycle.

In this thesis it is proposed that also a third active state ($H_{sred}$) is involved in the catalytic cycle which infers that the $[4Fe\text{-}4S]_H$ cluster is an integral part of the H-cluster donating or accepting electrons. In the proposed mechanism (in this thesis) the amine group in the dithiolate bridge bends over to the open coordination site and accepts or donates a proton from a transient hydride bound to this site[62]. In the literature, there is still discussion

on the involvement of the $H_{sred}$ in the catalytic cycle[83]. Also the presence of alternative double reduced intermediates was proposed[84]. However, clear experimental evidence for these intermediates has not been shown up to date.

# II. Theory and experimental methods

This chapter introduces the theoretical principles of EPR and FTIR spectroscopies as well as electrochemistry and the application of these methods in the structural and mechanistic studies of [FeFe] hydrogenases.

## 2.1. EPR spectroscopy

In electron paramagnetic resonance (EPR) spectroscopy, the magnetic spin transitions of systems with one or more unpaired electrons are observed. Information about the electronic structure of a paramagnetic molecule is obtained through magnetic parameters which describe electron spin and nuclear spin interactions with the applied magnetic field and with each other[85]. The EPR spectra can be interpreted using the effective spin Hamiltonian approach where the full Hamiltonian is replaced by effective Hamiltonian containing only spin operators.

### *2.1.1. Spin Hamiltonian*

The concept of the spin Hamiltonian was developed and described by Abragam and Bleaney and represents an empirical rather than a full physical model[85]. The spin Hamiltonian has to accurately parameterize and describe the interactions observed in the EPR spectra. To fully understand the properties of the studied system, the obtained parameters have to be interpreted using theoretical calculations.

Due to the electron spin interaction with the external magnetic field as well as the internal couplings with neighboring electrons or nuclear magnetic moments, the spin Hamiltonian can be split into different terms describing different types of interactions[85-88]. Below only those interactions will be discussed that are directly related to the presented studies. In this case the spin Hamiltonian $H_0$ includes the following terms:

$$H_0 = H_{EZ} + H_{NZ} + H_{HF} + H_{NQ} \quad (2.1)$$

where $H_{EZ}$ is the electron Zeeman interaction, $H_{NZ}$ the nuclear Zeeman interaction, $H_{HF}$ the hyperfine interaction between electron spins and nuclear spins, and $H_{NQ}$ the nuclear quadrupole interaction for spins with nuclear spin quantum number larger than ½.

### *2.1.2. Zeeman interactions*

The interaction between electron spin and external magnetic field is described by the electron Zeeman interaction. The spin Hamiltonian for a free electron in an external magnetic field $B_0$ is expressed as:

$$H_{EZ} = g_e \beta_e B_0 \widehat{\boldsymbol{S}} \tag{2.2}$$

where $\beta_e$ is the Bohr magneton, $\widehat{\boldsymbol{S}}$ is the electron spin operator of the unpaired electron(s) and $g_e$ is g value for unpaired electron. For a simple case of $S = 1/2$, the application of the $B_0$ results in a splitting to two energy levels because spin S can be oriented either parallel or antiparallel to $B_0$ (see figure 2.1). These two states are characterized by magnetic quantum numbers $m_s = \pm 1/2$. Then, assuming that $B_0$ is directed along the z-axis, the energy is:

$$E_{ms} = g_e \beta_e B_0 m_s \tag{2.3}$$

and the energy required for this transition is:

$$\Delta E = g_e \beta_e B_0 \tag{2.4}$$

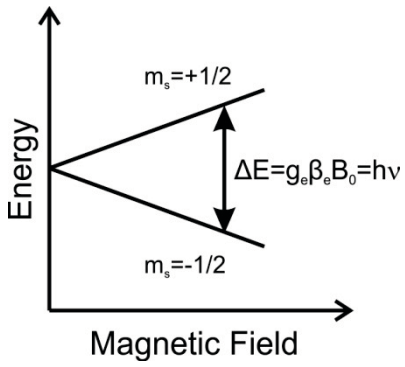


**Figure 2.1.** Energy level scheme for S=1/2 system. An EPR transition is observed when the resonance condition is fulfilled.

However, in most of the systems the Zeeman interaction does not only depend on the angle between the effective spin vector $\vec{\boldsymbol{S}}$ and $\vec{\boldsymbol{B}}_{\boldsymbol{0}}$ but also on the angle between $\vec{\boldsymbol{B}}_{\boldsymbol{0}}$ and

the axes defined by the local symmetry of the magnetic complex. Then this part of the spin Hamiltonian will change its form to:

$$H_{EZ} = \beta_e \vec{\boldsymbol{B}}_{\boldsymbol{0}} \cdot \boldsymbol{g} \cdot \hat{\boldsymbol{S}} \tag{2.5}$$

The $\boldsymbol{g}$ (pseudo) tensor is represented by a 3x3 matrix which can be transformed to a diagonal form via rotation to the principal axes frame. These diagonal elements are called the principal $g$ values. With the help of the Euler angles, the orientation of the principal axes with respect to the laboratory frame can be described.

The nuclear Zeeman term describes the interaction between the nuclear spin $\vec{\boldsymbol{I}}$ and $\vec{\boldsymbol{B}}_{\boldsymbol{0}}$:

$$H_{NZ} = -g_n \beta_n \vec{\boldsymbol{B}}_{\boldsymbol{0}} \cdot \hat{\boldsymbol{I}} \tag{2.6}$$

where $g_n$ is the nuclear g factor, a constant depending on the type of the nuclei and $\beta_n$ is the nuclear magneton.

### *2.1.3. Hyperfine interactions*

The hyperfine interaction between the electron spin and a nuclear spin is described by the following spin Hamiltonian:

$$H_{HF} = \hat{\boldsymbol{S}} \cdot \boldsymbol{A} \cdot \hat{\boldsymbol{I}} \tag{2.7}$$

where $\boldsymbol{A}$ is the hyperfine tensor, which can be split into isotropic and anisotropic terms. The isotropic term is described by the Fermi contact interaction:

$$H_{FC} = A_{iso} \hat{\boldsymbol{S}} \cdot \hat{\boldsymbol{I}} = \left(\frac{2}{3}\frac{\mu_0}{h} g_e \beta_e g_n \beta_n |\Psi_0(0)|^2\right) \cdot \hat{\boldsymbol{S}} \cdot \hat{\boldsymbol{I}} \tag{2.8}$$

where $A_{iso}$ is the isotropic coupling constant and $|\Psi_0(0)|^2$ is the spin density at the nucleus. The electron-nuclear dipole-dipole coupling is an important contribution to the anisotropic part represents and is given by:

$$H_{DD} = \hat{\boldsymbol{S}} \cdot \boldsymbol{A_{dd}} \cdot \hat{\boldsymbol{I}} = \frac{\mu_0}{4\pi h} g_e \beta_e g_n \beta_n \left[\frac{(3\hat{\boldsymbol{S}}\cdot\vec{\boldsymbol{r}})(\vec{\boldsymbol{r}}\cdot\hat{\boldsymbol{I}})}{r^5} - \frac{\hat{\boldsymbol{S}}\cdot\hat{\boldsymbol{I}}}{r^3}\right] \tag{2.9}$$

where $\vec{\boldsymbol{r}}$ is the vector connecting the electron and nuclear spin and $\boldsymbol{A_{dd}}$ is the dipolar coupling tensor, which is typically traceless and symmetric.

The Fermi contact interactions in general describe the interaction of the nuclear spin with the electron spin from atomic s-orbitals. When the unpaired electron is located in a p-, d- or f-orbital, the isotropic hyperfine coupling can also be significant due to configuration interactions or spin polarization[86, 89].

### *2.1.4. Nuclear quadrupole interactions*

Nuclei with spin I≥1 are characterized by a non-spherical charge distribution of the nucleus giving rise to a nuclear electronic quadrupole moment $Q$. The interaction of this charge distribution with the electric field gradient around the nucleus caused by the surrounding has to be considered and is given by the following spin Hamiltonian:

$$H_{NQ} = \hat{\boldsymbol{I}} \cdot \boldsymbol{P} \cdot \hat{\boldsymbol{I}} \tag{2.10}$$

where $\boldsymbol{P}$ is the traceless nuclear quadrupole tensor. In its principal axes system, the spin Hamiltonian can be expanded:

$$H_{NQ} = P_x \hat{\boldsymbol{I}}_x^2 + P_y \hat{\boldsymbol{I}}_y^2 + P_z \hat{I}_z^2 = \frac{3}{2}\frac{e^2qQ}{h \cdot 2I(2I-1)}\left[\left(\hat{\boldsymbol{I}}_z^2 - \frac{1}{3}I(I+1) + \frac{1}{3}\eta\left(\hat{\boldsymbol{I}}_x^2 - \hat{\boldsymbol{I}}_y^2\right)\right)\right] \tag{2.11}$$

where $eq$ is the electric field gradient and

$$\eta = \frac{P_x - P_y}{P_z} \tag{2.12}$$

$\eta$ is the asymmetry parameter with $|P_z| \geq |P_y| \geq |P_x|$ and $0 \leq \eta \leq 1$. The largest value of the quadrupole tensor is given by:

$$P_z = \frac{e^2qQ}{h \cdot 2I(2I-1)} \tag{2.13}$$

The quadrupole tensor is usually expressed in terms of two parameters $K = \frac{e^2qQ}{4h}$ and $\eta$.

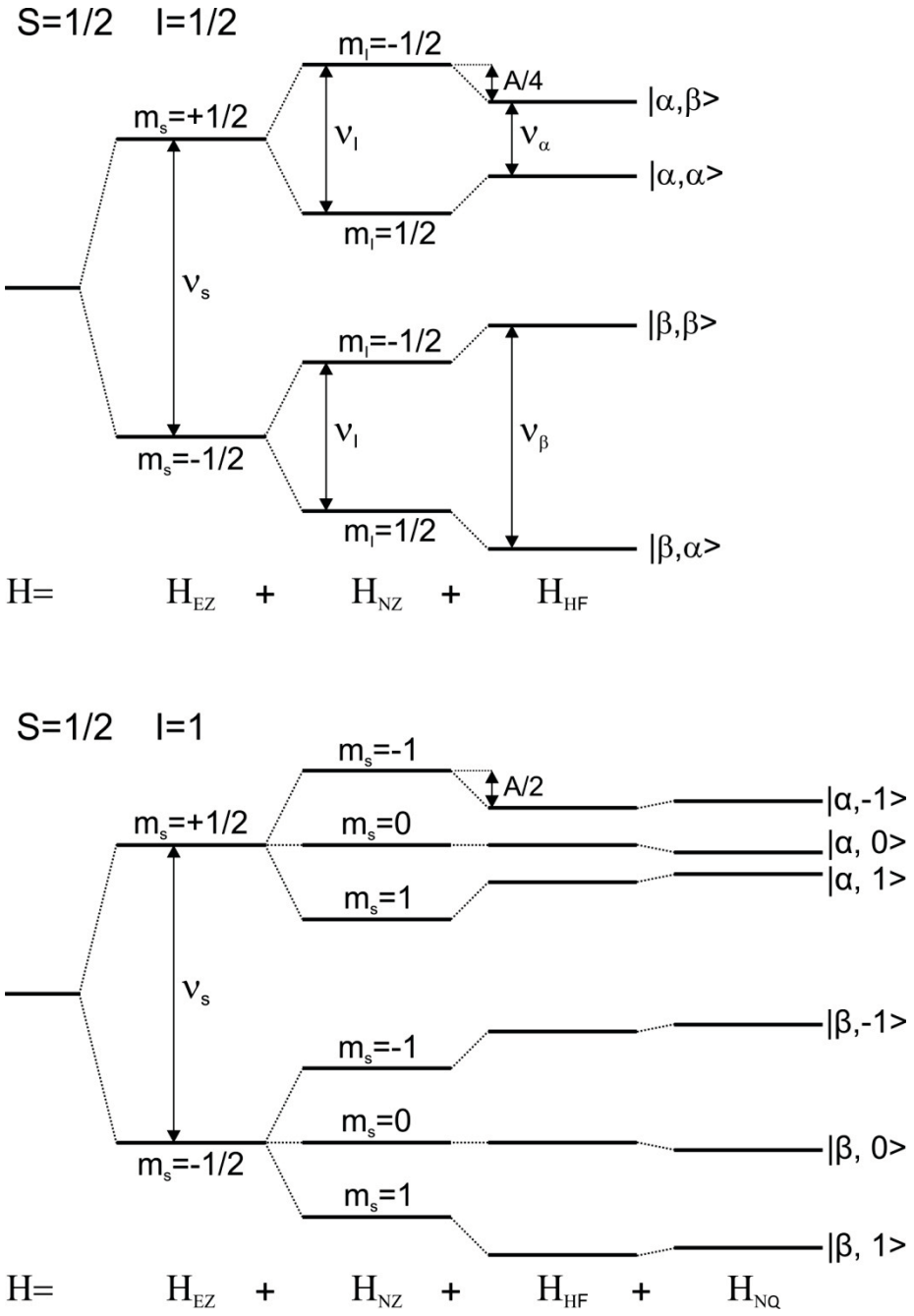


**Figure 2.2.** Energy level scheme for S=1/2 and I=1/2 (top) and S=1/2 and I=1 (bottom) systems, where $\alpha$ = 1/2 and $\beta$ = -1/2.

### *2.1.5. Measurement of EPR spectra*

To detect an EPR transition, the resonance condition as described in equation 2.4 has to be fulfilled. To find EPR transitions, the external magnetic field is scanned while the microwave frequency is kept fixed. Often, to better understand a system measurements at more than one microwave frequency have to be performed. The most common frequency

bands are referred to as X-, Q- and W-band with center frequencies 9.5, 34 and 95 GHz, respectively.

EPR methods can be divided into two groups, namely continuous wave (CW) and pulse EPR methods. The CW EPR experiment as well as two basic pulse methods (free-induction decay (FID) and two pulse electron spin echo (2-pulse ESE)) give similar spectral information. In the CW experiment, the first harmonic of the signal (first derivative) is obtained when the modulated magnetic field is being continuously linearly swept. In the above mentioned pulse methods the absorption spectrum is detected which is a response of the spin system to one or more microwave (MW) pulses.

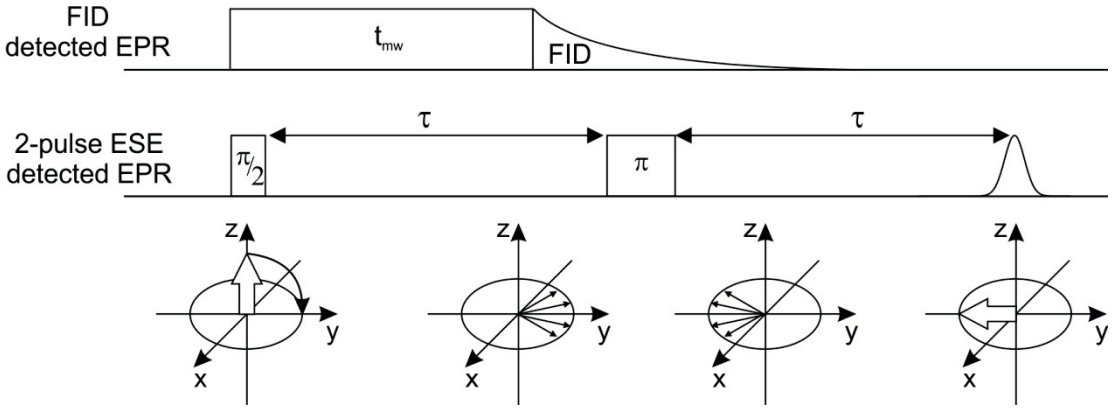


**Figure 2.3.** FID detected and 2-pulse ESE detected EPR pulse sequence and the vector model of Hahn echo formation[90]. In the 2-pulse ESE detected experiment the first π/2 MW pulse turns the magnetization vector by 90° and immediately the spins start to precess. After time τ a second π MW pulse is applied which reverses precession and after time τ the spins refocus and an electron spin echo is observed.

In the FID detected EPR experiment one soft (long) π/2 MW pulse is applied generating an FID signal approximately of the same length as the excitation pulse (see figure 2.3). The signal can be detected only after the instrumental dead time and can be very weak. This signal is integrated and recorded as a function of the swept magnetic field generating an absorption type EPR signal very similar to the integrated CW EPR spectrum.

In the 2-pulse ESE detected EPR experiment, a primary spin echo is generated using "hard" non-selective MW pulses (see figure 2.3). The echo signal is integrated and recorded

as a function of the swept magnetic field, again generating a signal similar to a CW EPR spectrum. However, the EPR spectra obtained by this method can be distorted due to field dependent modulations originating from interactions with the nuclear spins (see description of the ESEEM experiment).

In all these experiments the MW power has to be optimized and relaxation effects have to be taken into account. In the continuous wave experiments, a higher MW power can be used to obtain a higher sensitivity but it can also lead to saturation of the signal. This happens if the MW power, which is proportional to the rate of absorption, is higher than the relaxation rate of the electron spins. In the pulse methods the MW power has to be matched with the length of the pulses to obtain a true 90° and 180° nutation angle. Also the total length of the pulse sequence and its repetition time has to be adjusted to the relaxation properties of the studied system. Fast relaxation prevents long pulse experiments but on the other hand fast relaxation allows fast repetition of the sequence. Metallo-protein samples are measured usually at low temperatures (10 K – 30 K) to slow down relaxation and increase the population difference between the spin levels.

A frozen solution is considered as a powder sample with all possible orientations of the studied system along $B_0$. Since, in case of g-anisotropy, the resonance condition and, therefore, the line position in the EPR spectrum depends on the orientation of the spin system along $B_0$, the obtained spectrum under this condition will be assembled from all possible EPR spectra in all possible orientations. Three typical line shapes of EPR spectra of frozen solutions dependent on the anisotropy of the g-tensor are shown in figure 2.4.

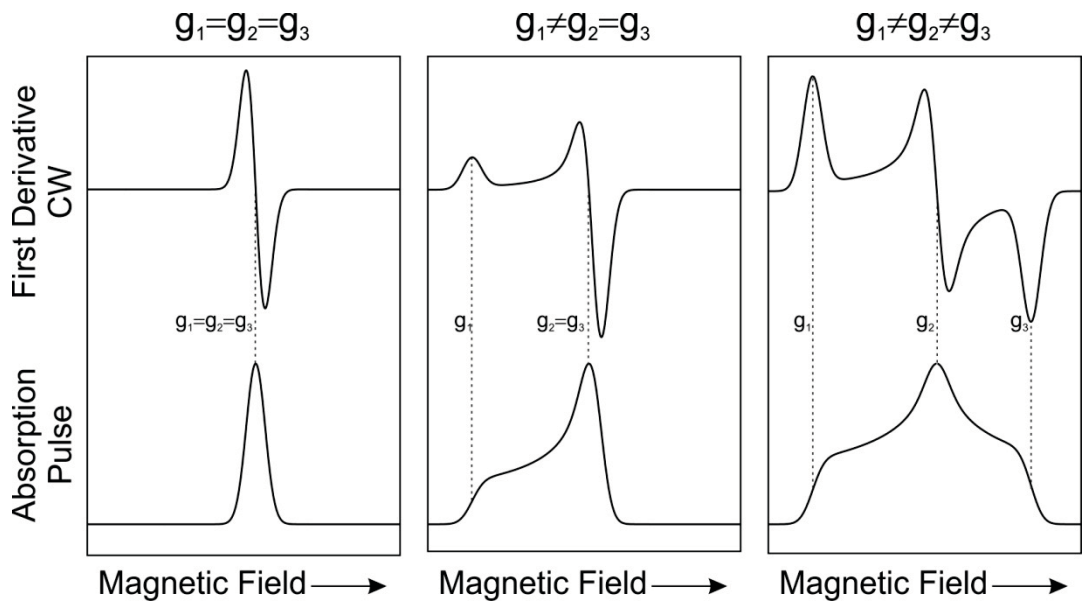


**Figure 2.4.** Absorption and first derivative spectra observed in case of isotropic ($g_1=g_2=g_3$), axial ($g_1\neq g_2=g_3$ or $g_1=g_2\neq g_3$) and rhombic ($g_1\neq g_2\neq g_3$) g-tensor.

Besides the g-tensor, also information about the hyperfine interaction can be obtained from the simple spectra (see figure 2.5). However, if hyperfine splitting's are smaller than the inhomogeneous EPR linewidth these interactions cannot be resolved in the field swept spectra and more advanced pulse techniques like electron nuclear double resonance (ENDOR), electron spin echo envelope modulation (ESEEM) or hyperfine sublevel correlation spectroscopy (HYSCORE) have to be applied to access these small interactions. With these techniques the nuclear transition frequencies are indirectly detected through EPR transitions (see below).

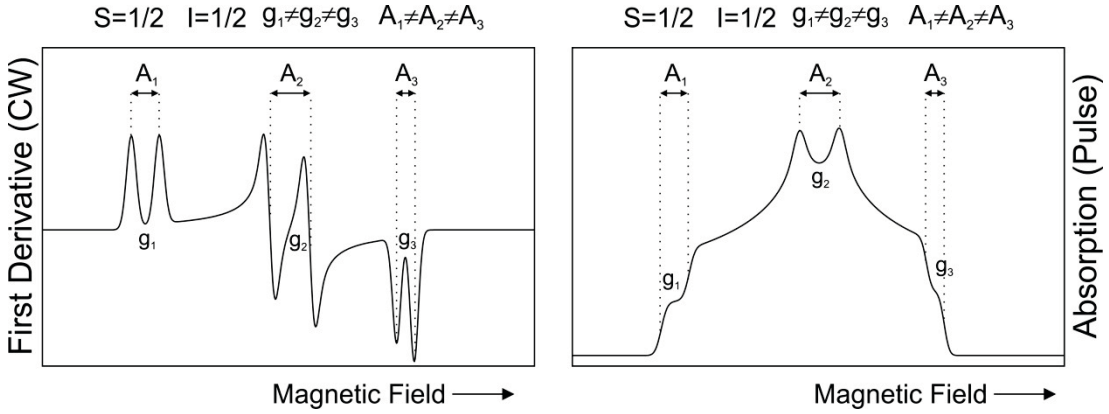


**Figure 2.5.** Absorption and first derivative spectra observed for the S=1/2 and I=1/2 system in case of rhombic g-tensor and A-tensor.

### *2.1.6. ENDOR*

The two most popular pulse ENDOR techniques are due to Davies and Mims[88, 91, 92]. The corresponding pulse sequences and energy diagrams are shown in figure 2.6. In both techniques MW and radiofrequency (RF) pulses are used and they rely on transfer of electron spin to nuclear spin polarization.

In the Davies ENDOR sequence during the preparation period one selective MW π pulse inverts the spin population of a single EPR transition and creates a hole in the EPR spectrum. Then, the following RF π pulse applied during the mixing period induces an NMR transition and the nuclear spin polarization is changed. This effect is usually detected by measuring the changes in intensity of the ESE after a sequence of two MW pulses. This technique is especially suited to detect large hyperfine interactions because of the dependence on the first MW $\pi$ pulse selectivity. In this experiment weak couplings can be suppressed due to excitations of both electronic transitions by the first inversion pulse.

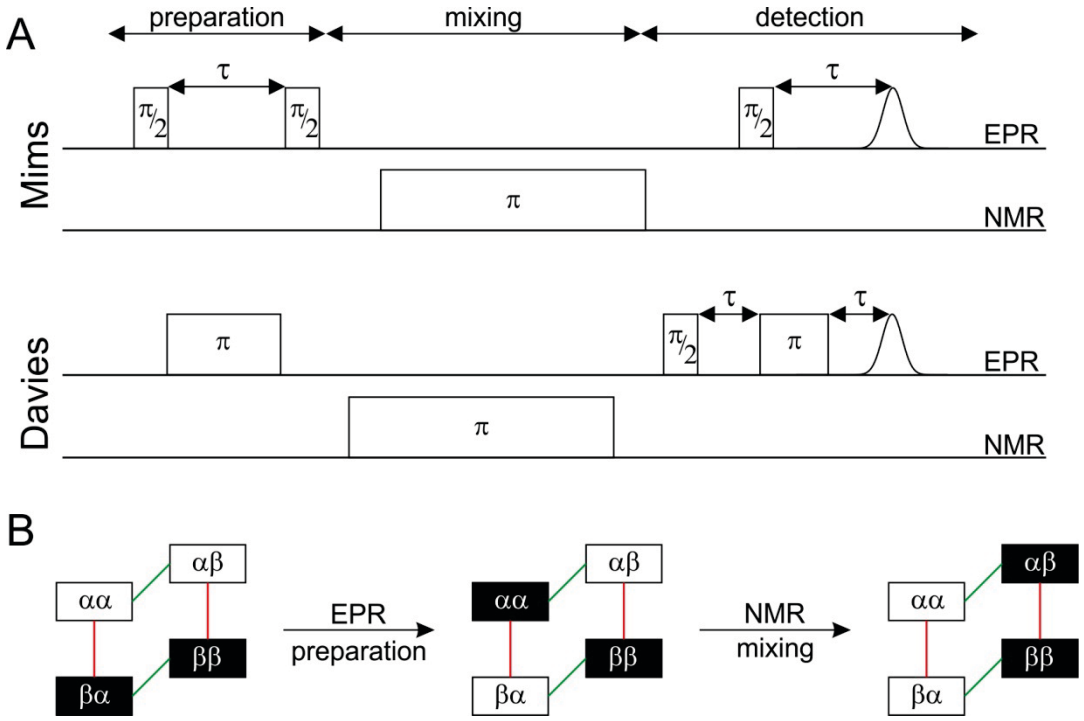


**Figure 2.6.** A: Pulse sequences for Mims ENDOR and Davies ENDOR experiments. B: Energy level scheme for the S=1/2 and I=1/2 system and its changes during the Davies ENDOR experiment. Transitions exited by MW pulses are marked in red and by RF pulses in green.

The Mims ENDOR sequence is based on the 3 pulse stimulated echo sequence with 3 non selective MW π/2 pulses. In the preparation part two pulses separated by τ create a periodic polarization pattern depending on τ. Then, similar to Davies ENDOR, in the mixing period an RF π pulse is applied to change the nuclear spin polarization which is then detected after the third MW π/2 pulse. This method is more sensitive because short MW pulses can be used and thereby excite more spins. However, in the Mims ENDOR spectrum, blind spots could appear at frequencies determined by the first pulse interval given by τ=2πn/A, where n=1,2,…etc. This is why this method is mostly used for small couplings where the blind spots are not distorting the measured couplings.

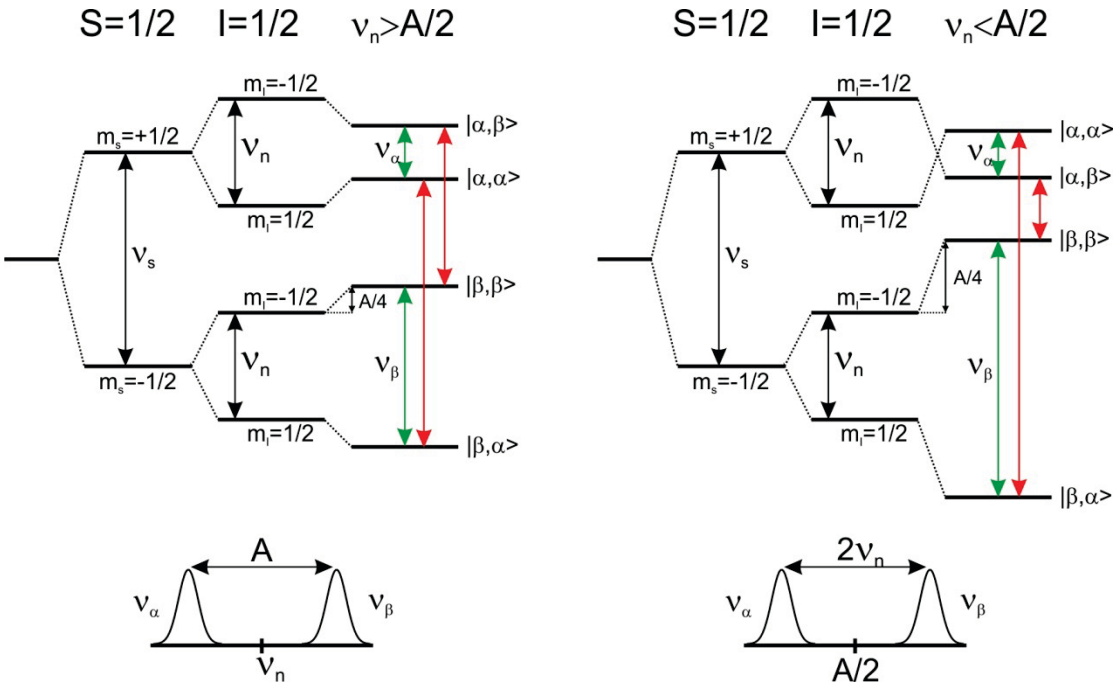


**Figure 2.7.** Energy level schemes for S=1/2 and I=1/2 and the ENDOR spectra in case of weak hyperfine coupling (left) and strong hyperfine coupling (right), where $\alpha$ = 1/2 and $\beta$ = -1/2. $\nu_\alpha$ and $\nu_\beta$ are nuclear spin transitions indicated by green arrows, and electron spin transitions are indicated by red arrows.

In all ENDOR experiments, the radio frequency is usually scanned, while the field position and other parameters are kept constant. The echo intensity is measured and a characteristic signal shown in figure 2.7 is recorded where the frequencies fulfill in the simplest case of the isotropic hyperfine constant $a$ the following equation:

$$\nu_{ENDOR} = \left|\nu_n \pm \frac{A}{2}\right| \quad (2.14)$$

In case of weak hyperfine couplings, when half of the hyperfine coupling is smaller than the nuclear Larmor frequency, the resonance lines are split by the hyperfine coupling constant and centered around the nuclear Larmor frequency. The opposite situation happens in case of strong hyperfine coupling, when $A/2 > \nu_n$, in which case the lines are separated by $2\nu_n$ around a frequency equal to $A/2$. For nuclei $I > 1/2$ quadrupole couplings can cause an additional splitting.

### *2.1.7. ESEEM and HYSCORE*

Another technique used for studying small hyperfine and quadrupole interactions does not require RF pulses and is referred to as Electron Spin Echo Envelop Modulation or "ESEEM"[88, 93, 94]. It takes advantage from the fact that the observed spin echo which decays with time due to relaxation effects is also influenced by coupling of the electrons spins to nearby nucleus causing its modulation with transition frequencies of interacting nuclear spins.

In the most popular 3 pulse ESEEM technique during the preparation period, similar to Mims ENDOR, two MW $\pi/2$ pulses separated by $\tau$ invert the electron spin population (see figure 2.8) creating polarization along the z-axis as well as nuclear coherence. Then after evolution time T, a third MW $\pi/2$ pulse is applied, which converts the electron polarization and nuclear coherence, and the stimulated echo is observed after time $\tau$. In this experiment, the intensity of the echo is measured as a function of T (T is increased during experiment). A one dimensional frequency spectrum is obtained by subtraction of the decay of the spin echo and Fourier Transformation of the obtained time domain spectrum. It is possible to record the 3-pulse ESEEM spectrum as a function of the magnetic field thus obtaining a 2D spectrum providing information about the A-tensor principal values and, in favorable cases, the Euler angles.

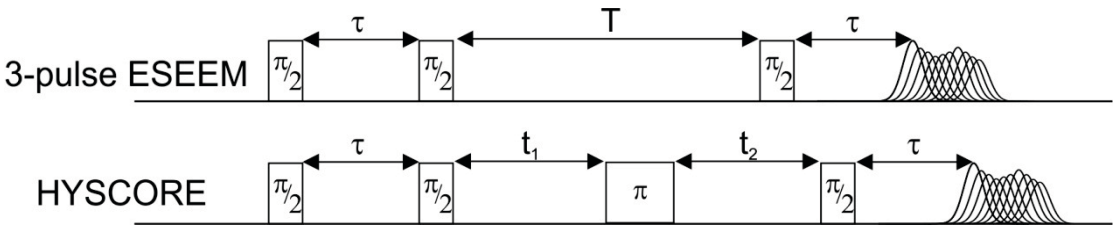


**Figure 2.8.** Pulse sequences for 3-pulse ESEEM and HYSCORE experiments.

HYSCORE is a 2D method based on 3-pulse ESEEM with an additional mixing π pulse during the long waiting time T which interchanges the nuclear spin coherence between the two electron spin manifolds (see figure 2.8). The 2D spectrum is obtained by varying $t_1$ and $t_2$ independently. In case of weak hyperfine coupling ($A/2 < \nu_n$) cross peaks are observed in the first (++) quadrant of the spectra and in case of strong hyperfine coupling ($A/2 > \nu_n$) peaks appear in the second (+-) quadrant (see figure 2.9). The expansion into the second dimension simplifies the interpretation of the complicated spectra because cross peaks are observed between frequencies of the same nucleus. Although, additional autocorrelation peaks can appear along diagonal as a result of non-ideal π inversion pulse.

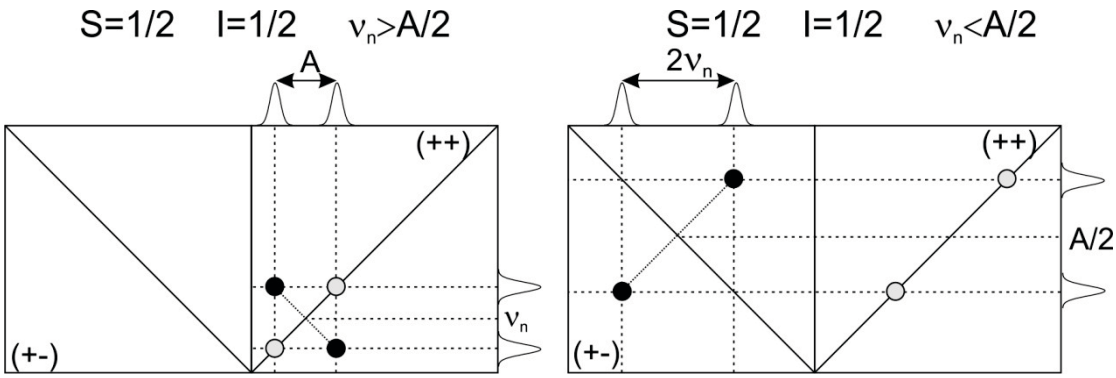


**Figure 2.9.** Schematic representation of HYSCORE spectra for S=1/2 and I=1/2 in case of weak hyperfine coupling (left) and strong hyperfine coupling (right).

Spectra obtained by both these methods depend on the τ separation time and similarly to Mims ENDOR exhibit blind spots behavior. For $\omega_{\alpha\beta}=2\pi n/\tau$ where n=0,1,2,... the blind spots suppress the signal . This is why usually spectra for a few different τ values are recorded in order to identify and detect all modulation signals.

## 2.2. FTIR spectroscopy

Infrared (IR) spectroscopy is a very common tool used by chemists to identify and describe chemical compounds. It takes advantage of the fact that the electromagnetic radiation in the IR range has a frequency close to the frequency of molecular vibrations which are characteristic for the structure of the molecule. It is a useful method in the analyses of the structure as well as the interaction of molecules with their surroundings.

### *2.2.1. Vibrations of a diatomic molecule*

The simplest physical model illustrating vibrations of a diatomic molecule would be two masses ($m_1$ and $m_2$) representing two nuclei attached to two ends of a spring with force constant $k$ representing the strength of the bond between the two atoms[95]. The vibration of the two nuclei occurs only along the spring. Under assumption that one nucleus does not change position the movement of the second one can be described as harmonic oscillations by Hooke's law[95]:

$$\nu_{vib} = \frac{1}{2\pi}\sqrt{\frac{k}{\mu}} \tag{2.15}$$

where $\nu_{vib}$ is a frequency of the vibration and $\mu$ is the reduced mass which can be calculated from the following equation:

$$\mu = \frac{m_1 m_2}{m_1 + m_2} \tag{2.16}$$

The potential curve for this diatomic molecule is presented in the figure 2.10 where the energy of vibration $E_{\mathrm{v}}$ is given by eigenvalues:

$$E_{\mathrm{v}} = h\,\nu_{vib}\left(\mathrm{v} + \frac{1}{2}\right) \tag{2.17}$$

where v is vibrational quantum number that can have the values 0, 1, 2 …

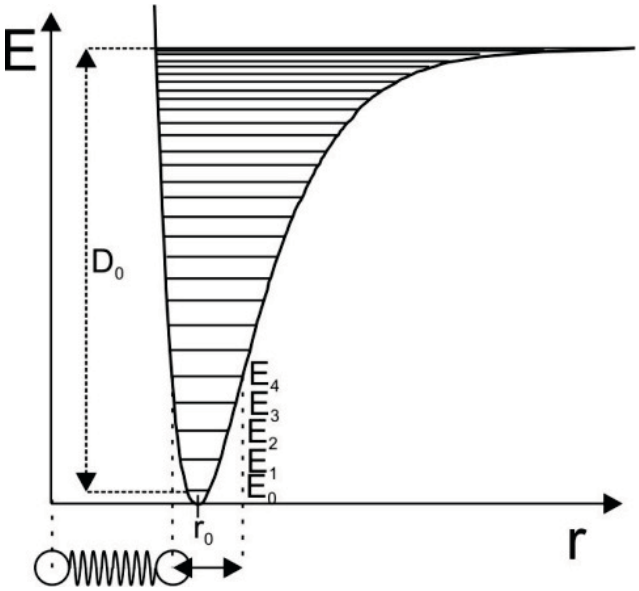


**Figure 2.10.** Schematic representation of a diatomic molecule as inharmonic oscillator vibrating at energy level $E_4$ and the representation of potential energy levels. $D_0$ is the dissociation energy and $r_0$ is the bond length.

### *2.2.2. Vibrations of a polyatomic molecule*

In a polyatomic molecule the situation is much more complicated. Here, all nuclei perform their own harmonic oscillations. However, any of these complicated vibrations of the molecule may be represented as a superposition of a few "normal" vibrations (normal modes). For a nonlinear molecule (like the diiron sub-cluster of the H-cluster) with N atoms 3N-6 normal vibrations can be distinguished. These normal vibrations are independent from each other but involve simultaneous vibrations of different part of the molecule.

Two groups of normal vibrations can be distinguished: stretching and bending (see figure 2.11). The stretching vibration is associated with a motion of atoms causing a change in the length of a bond which can be further classified as symmetric or anti-symmetric. The bending vibrations occur when the bond angle between two atoms or a group of atoms change in relation to the rest of the molecule.

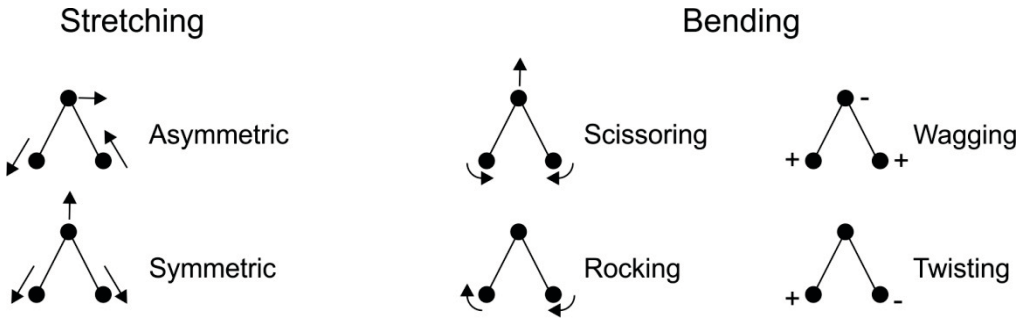


**Figure 2.11.** Schematic representation of different types of vibrations in polyatomic molecule. Arrows shows the direction of the vibration and + and – represent movement of the atom outside the plane.

### *2.2.3. Interaction of molecule with light – Absorption in the infrared*

When light passes through a molecule, an oscillating electric dipole is created. Only a net change in the dipole moment of a molecule, which is caused by vibration or rotation within a molecule, can cause the absorption of IR radiation. If the frequency of the radiation matches the vibrational frequency of the molecule then radiation will be absorbed, causing a change in the amplitude of molecular vibration. As a consequence of the absorption of electromagnetic radiation which matches the normal vibrations of the poly atomic molecule, the IR spectrum can be obtained.

### *2.2.4. FTIR spectroscopy-Interferometer and interferogram*

The principle of the fourier transform infrared experimental techniques is based on the Michelson interferometer[96]. As shown in the figure 2.12, light from a polychromatic infrared source (“glow bar”) is split on the beam splitter and 50% of the light is reflected towards the fixed mirror and 50% towards the moving mirror. Then, light is reflected back from both mirrors to the beam splitter and subsequently goes through the sample to the detector. During the measurement the moving mirror moves continuously forward and backward changing its distance to the beam splitter. This difference in the distance of both mirrors is known as optical retardation ($\delta$). The detector records the signal for each mirror position (as a function of retardation) and a digital plot of light intensity versus the mirror

position called interferogram is produced. Then, using a mathematical method called Fourier transformation, the interferogram can be represented by the integral:

$$I(\delta) = \int_{-\infty}^{+\infty} B(\bar{\nu})cos(2\pi\bar{\nu}\delta)d\bar{\nu} \quad (2.18)$$

which is one-half of a cosine Fourier transform pair, the other being:

$$B(\bar{\nu}) = \int_{-\infty}^{+\infty} I(\delta)cos(2\pi\bar{\nu}\delta)d\,\delta \quad (2.19)$$

$I(\delta)$ information in the interferogram is converted to a $B(\bar{\nu})$ plot of intensity versus wavenumber $(\bar{\nu})$ (frequency). The band positions in the FTIR spectrum obtained in this way are presented as wavenumbers $(\bar{\nu})$ in units of $cm^{-1}$. This signal corresponds to the frequency at which the sample absorbed the IR radiation and the unit is proportional to the energy of the vibration.

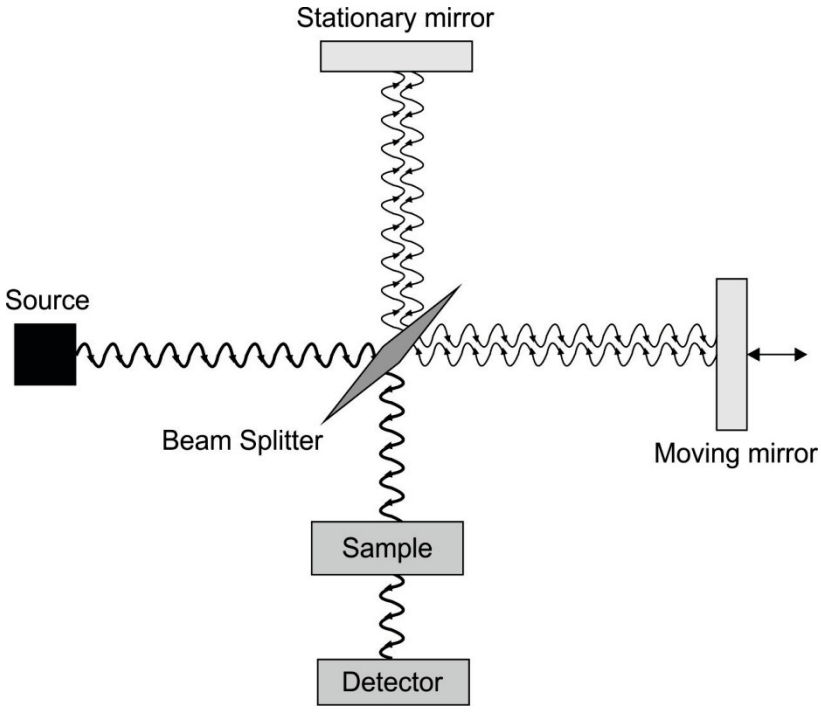


**Figure 2.12.** Schematic representation of the Michelson interferometer as an integral part of FTIR spectrometer.

### *2.2.5. Methods of sampling*

The basic procedures for infrared measurements can be divided in transmission and reflectance modes. In contrast to transmission infrared in the reflectance mode the infrared energy does not pass through the sample but is reflected from its surface. In transmission

infrared spectroscopy, only the fraction of the IR radiation which is not absorbed by the sample can be detected. This is why it is crucial (especially for water samples) to measure a proper background. Even then, the signals in certain regions of the spectra cannot be detected because water absorbs all the infrared radiation in these ranges. From the Beer-Lambert law the amount of light transmitted by a sample can be related to its thickness and concentration[96, 97]:

$$A = \varepsilon \cdot c \cdot l \tag{2.20}$$

where $A$ is absorbance, $\varepsilon$ is the molar absorptivity, $c$ is concentration of the sample and $l$ is the path length (thickness of the sample).

### *2.2.6. FTIR spectroscopy in the studies of [FeFe] hydrogenases*

The low oxidation states of the iron atoms in the active site of the [FeFe] hydrogenases are stabilized by carbonyl and cyanide groups. The IR stretching vibrations of those diatomic molecules occur in a region free from other vibrations. The free $\nu_{CO}$ stretch (2155 $cm^{-1}$) in these complexes is shifted to lower frequencies and can be commonly observed in the range 2100-1800 $cm^{-1}$, whereas free $\nu_{CN}$ (2080 $cm^{-1}$) is shifted to higher frequencies (2200-2000 $cm^{-1}$). In general, $CN^-$ is a better $\sigma$-donor and poorer $\pi$-acceptor than CO. Thus, the $\nu_{CN}$ of the complexes are generally higher than the value for free $CN^-$, whereas the opposite prevails for the CO complexes[95].

In the active site of the [FeFe] hydrogenases the CO and $CN^-$ ligands are very sensitive to the change in the oxidation state of the iron atoms as well as changes in their interactions with the surrounding. This is why unique spectra for each redox state of the active site can be observed. Also changes in the hydrogen bonds or in the degree of freedom of ligands strongly influence the recorded spectra. Figure 2.13 presents FTIR band positions observed for different states of the active site of [FeFe] hydrogenases of three different organisms and the influence of single mutation next to the active site on these spectra.

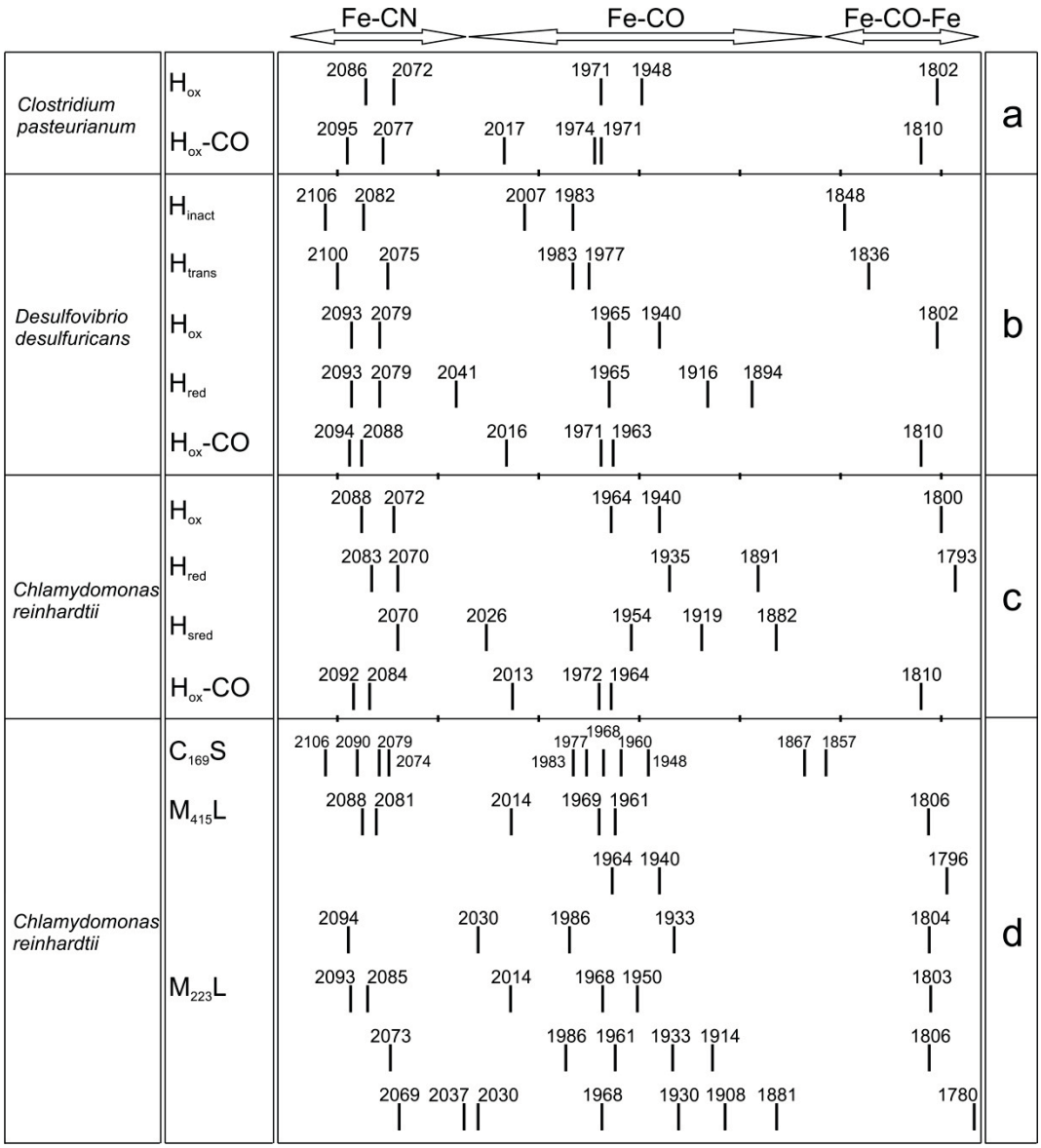


**Figure 2.13.** Overview of FTIR bands positions observed for different states of the H-cluster of [FeFe] hydrogenases from different native and genetically modified organisms: a) *Clostridium pasterianum*[98], b) *Desulfovibrio desulfuricans*[55], c) *Chlamydomonas reinhardtii*[61] and d) genetically modified *Chlamydomonas reinhardtii*[99].

## 2.3. Protein electrochemistry

Electrochemistry is a common method used for studying chemical reactions which take place at the interface of an electrode. These reactions involve electric charges moving between the electrodes and the electrolyte or ionic species in a solution. Direct electron transfer to proteins was first shown in the 1970's and opened the way for detailed studies of biological reactions[100-102]. Electrochemistry is commonly used to understand the kinetics and energetics of biological electron transfer processes as well as reactions coupled to the redox transitions.

### *2.3.1.* Redox thermodynamics: the Nernst equation

A situation where the redox mixture contains oxidized and reduced forms of two species can be represented by the equations below:

$$ox_1 + red_2 \rightleftharpoons red_1 + ox_2 \tag{2.21}$$

where $ox_1$ and $red_1$ represents the first species in oxidized and reduced states. Analogously $ox_2$ and $red_2$ represents the second species in oxidized and reduced states. The free energy of the reaction ($\Delta_r G$) is given by:

$$\Delta_r G = \Delta_r G^0 + RTln\frac{[red_1][ox_2]}{[ox_1][red_2]} \tag{2.22}$$

where $R$ is equal to 8.314 $\frac{J}{K*mol}$ and is the universal gas constant, $T$ is the temperature and $\Delta_r G^0$ is the standard free energy of the reaction. Equilibrium is reached when $\Delta_r G$=0 and the equilibrium constant ($K_{eq}$) is represented as:

$$K_{eq} = \frac{[red_1][ox_2]}{[ox_1][red_2]} = exp\left(-\frac{\Delta_r G^0}{RT}\right) \tag{2.23}$$

During the reaction, $ox_2$ is reduced and takes electrons from $red_1$. Hence the reaction can be represented as the sum of two half-reactions:

$$ox_1 + ne^- = red_1 \tag{2.24}$$

and

$$red_2 = ox_2 + ne^- \tag{2.25}$$

The redox potential ($E$) of the redox couple of each of the half-reactions is given by the Nernst equation:

$$E = E^0 + \frac{RT}{nF} ln \frac{[ox]}{[red]} = E^0 + 2.303 \frac{RT}{nF} log \frac{[ox]}{[red]} \quad (2.26)$$

where $E^0$ is the standard redox potential of the redox couple $ox/red$ also known as the midpoint potential, $F$ is Faraday's constant (96485 $\frac{C}{mol}$) and $n$ is a number of transferred electrons. In an electrochemical cell only the difference between two electrodes can be measured and electrons are going to flow in the direction of the electrode with lower potential until equilibrium will be achieved:

$$K_{eq} = \frac{[red_1][ox_2]}{[ox_1][red_2]} = exp\left(-\frac{nF}{RT}(E_2^0 - E_1^0)\right) \quad (2.27)$$

and since reduction potentials and free energies are linked and $\Delta_r G^0 = -RTlnK_{eq}$, the standard free energy of the reaction can be given as:

$$\Delta_r G^0 = -nF(\Delta E^0) \quad (2.28)$$

The Nernst equation can be used to determine the direction in which a redox reaction will proceed spontaneously. Also from the Nernst curve, as shown in figure 2.14, the number of transferred electrons and $E^0$ can be determined. The Nernst curve is obtained after allowing the system to equilibrate with the electrode at the different potentials. The ratio $[ox]/[red]$ is determined usually by spectroscopic methods. Often the concentrations of $ox$ and $red$ are measured as function of electrode potential and the data are fitted with:

$$[red] = \frac{1}{1+exp\left(\frac{nF}{RT}(E-E^0)\right)} \quad (2.29)$$

$$[ox] = \frac{exp\left(\frac{nF}{RT}(E-E^0)\right)}{1+exp\left(\frac{nF}{RT}(E-E^0)\right)} \quad (2.30)$$

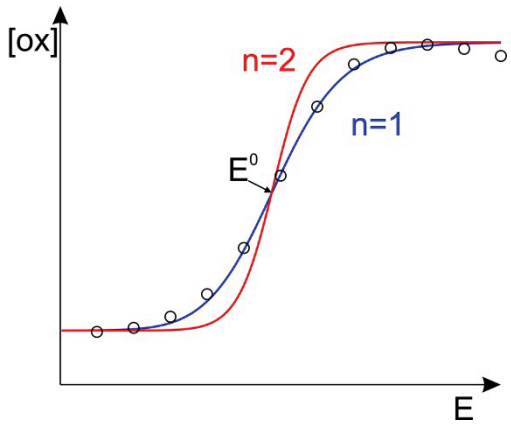


**Figure 2.14.** The experimental points created the Nernst curve (○). Simulations are shown for one (blue) and two (red) electron transitions.

### *2.3.2.* Protein Film Electrochemistry

Protein film electrochemistry (PFE) is used for dynamic studies of redox enzymes immobilized on an the electrode which plays the role of its redox partner as electron donor or acceptor[103]. In this technique, electron transfer processes are no longer limited by protein diffusion to the electrode. Therefore quantitative thermodynamic and kinetic information can be obtained in real time from very small samples.

The native properties of the protein must be preserved upon immobilization and a fast electron exchange between protein and electrode has to occur to establish direct electron transfer (DET). To fulfill the second requirement, the redox center or one of the redox cofactors in the enzyme has to be exposed to the surface and oriented in the direction of the electrode so that the distance between this center and the electrode allows electron tunneling 20 A according to Marcus theory[104].

There are many methods of protein attachment to the electrode and a number of different electrode materials can be used[103, 105]. In the work presented in this dissertation different [FeFe] hydrogenases were adsorbed or covalently attached to a highly oriented pyrolytic graphite edge (PGE) electrode[106]. Proteins easily adsorb on such electrodes (see figure 2.15 A). However, random orientation of the protein on the electrode does not guarantee DET on all the immobilized proteins. Alternatively, the surface of the PGE

electrodes can be modified by creating a monolayer to which the protein can be covalently attached[107, 108]. Depending on the surface charge of the protein around the most exposed redox cofactor, the electrode can be modified with different diazonium functional groups to obtain a positively or negatively charged surface on the electrode (see figure 2.15 B and C).

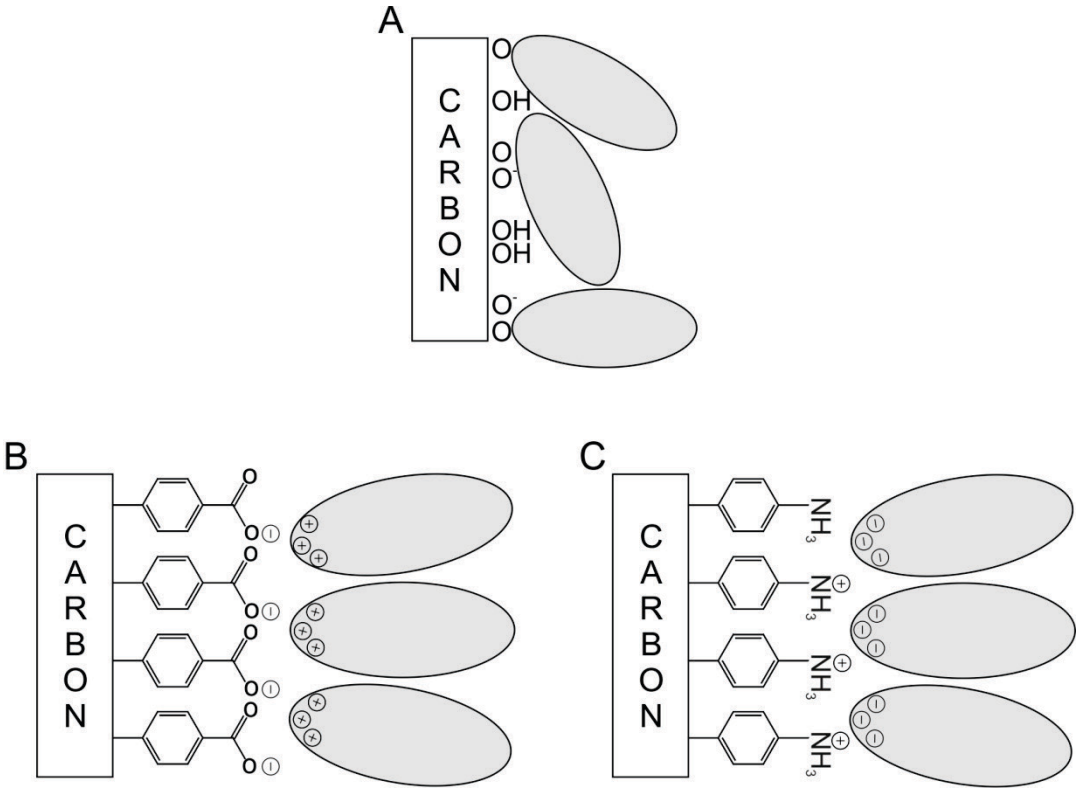


**Figure 2.15.** Schematic representation of proteins attached to the electrodes in PFE: A) protein adsorbed to PGE electrode, B) protein covalently bound to PGE electrode modified with 4-benzoicacidiazonium salt C) protein covalently bound to PGE electrode modified with 4-nitrobenzenediazonium salt. The local charges of the aminoacid residues in the proximity of the most surface exposed electron relay redox moiety in the protein are also indicated.

Figure 2.16 shows a standard three electrode cell used for PFE studies in this dissertation. The working electrode with the immobilized enzyme is commonly rotated to avoid substrate diffusion limitation. The reference electrode is usually placed in a side arm linked to the main compartment by a capillary to keep it at room temperature. A third electrode called counter electrode is used to compensate the potential applied on the working electrode and avoid passing current through the reference electrode. Temperature, pH and gases are strictly controlled in the electrochemical cell.

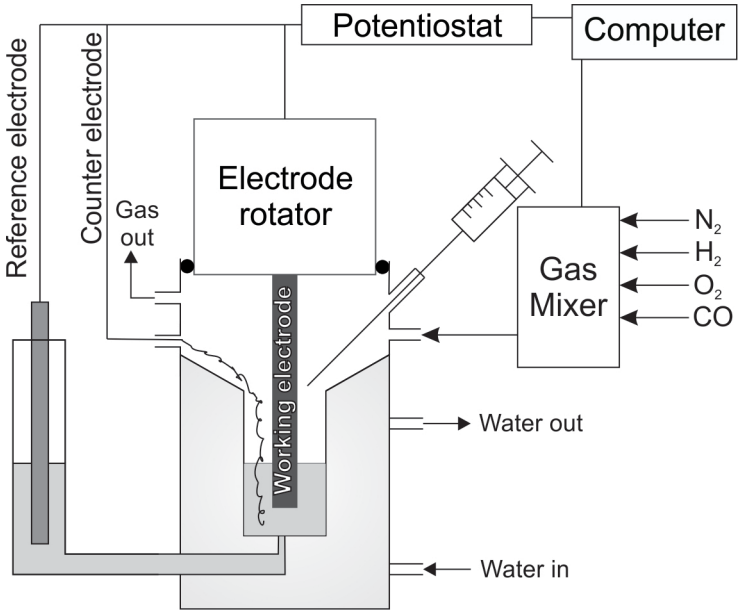


**Figure 2.16.** Schematic representation of the set-up used for PFE experiments.

In the experiments, a potentiostat controls the potential of the working electrode and measures the current flowing between working electrode and counter. Two main experiments called cyclic voltammetry (CV) and chronoamperometry are used to study the electrocatalytic behavior of the enzyme[109, 110].

In a CV experiment, the potential is swept at a constant given rate (scan rate given in $\frac{V}{s}$) between two potential limiting values (see figure 2.17 left panel). For a protein adsorbed on an electrode with one redox active center where a reversible electron transfer reaction takes place, the CV would contain a pair of current peaks (see figure 2.17 A left panel). The positive current peak would be registered while sweeping the potential to higher values while redox center is being oxidized and the negative peak is observed during a potential sweep to lower values during reduction of the redox center. The average of the peak positions gives the midpoint potential of the reaction ($E^0$) and the area under the peaks ($S$) is directly related to the number of active sites:

$$S = nFA\Gamma\nu \tag{2.31}$$

where $n$ is the number of transferred electrons, $F$ is Faraday's constant ($\frac{C}{mol}$), $A$ is the electrode surface area ($cm^2$), $\Gamma$ coverage of the electrode ($\frac{mol}{cm^2}$) and $\nu$ is the scan rate ($\frac{V}{s}$).

The catalytic properties of the enzyme are observed after adding substrate to the solution. The shape of the CV ideally changes to a sigmoidal shown in the figure 2.17 B left panel (or for [FeFe] hydrogenases figure 1.7) due to the constantly occurring catalytic process. The observed current ($i$) at a certain potential where catalytic activity is measured can be directly related to the turnover frequency ($k_{cat}$) of the enzyme:

$$i = nFA\Gamma k_{cat}. \tag{2.32}$$

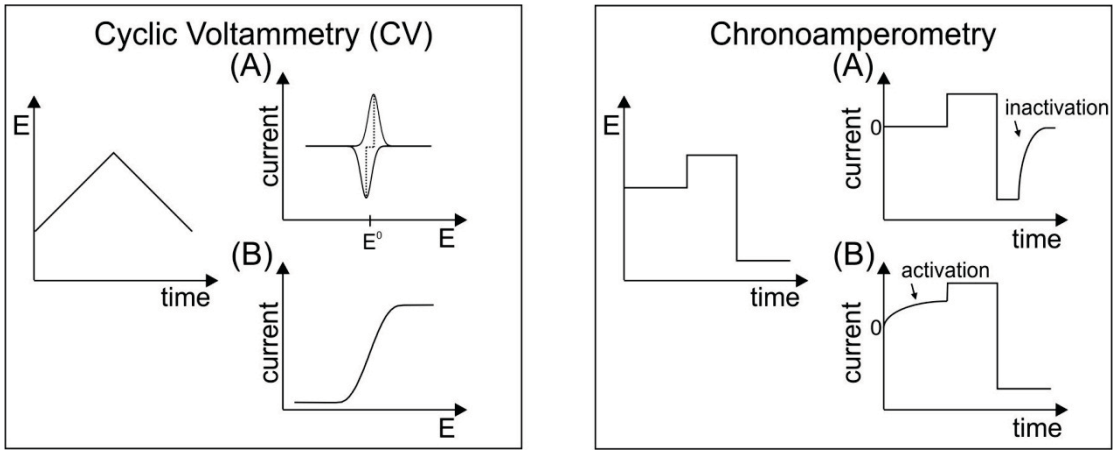


**Figure 2.17.** Plots explaining the two main experimental techniques used in PFE. In the left part of each panel changes in the potential applied during each experiment are shown over time. Diagram A) in the cyclic voltammetry panel shows the non-turnover signal while in the B) signal obtained after introduction of substrate. Diagrams A) and B) in the chronoamperometry panel show the situation when at specific potential protein is inhibited or activated.

In a chronoamperometry experiment, current is monitored as a function of time when the potential is kept constant or changed in consecutive steps (see figure 2.17 right panel). In this experiment the time and potential dependencies are separated. During measurements at constant potential the activity can be monitored and the enzyme can be exposed to external inhibitors, for example CO in case of [FeFe] hydrogenases, or inactivation and reactivation processes can be triggered by the electrode potential.

## 2.4. Spectroelectrochemistry

In the FTIR electrochemical experiment, FTIR spectra are measured for a series of the potentials adjusted and stabilized in an electrochemical three electrode cell based on design shown in figure 2.18[111]. The sample is loaded on a semitransparent (70 % transparency) gold mesh which together with a platinum foil counter and Ag/AgCl reference electrode completes a three electrode system (see figure 2.18). The outer cavity of the cell is filled with buffer/salt solution and closed between two $CaF_2$ windows. The IR radiation passes through the cell (like in the typical transmission mode) and IR spectra are recorded.

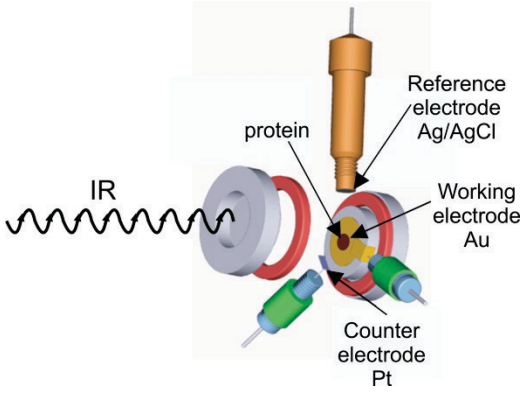


**Figure 2.18.** Schematic representation of cell used in FTIR electrochemistry.

It is very common to use mediators in such solution electrochemistry set-up. Unfortunately, not all enzymes are stable in their presence and in many cases they cannot be used which significantly increases the stabilization time to reach equilibrium with the electrode. However, using a very thin spectroelectrochemical cell and a high surface working electrode leads to relatively fast equilibration of the system.

From the obtained FTIR spectra the ratio $[ox]/[red]$ is determined and data are processed by fitting to the Nernst equation as described in the section 2.3.1. In case of three species in the redox mixture (number of the redox states usually observed for CrHydA1) equations 2.29 and 2.30 are replaced (under the assumption that $n$ is the same for each electron transition) by:

$$[sred] = \frac{1}{1+exp\left(\frac{nF}{RT}\left(E-E_2^0\right)\right)+exp\left(\frac{nF}{RT}\left(2E-E_1^0-E_2^0\right)\right)} \quad (2.33)$$

,

$$[red] = \frac{exp\left(\frac{nF}{RT}\left(E-E_2^0\right)\right)}{1+exp\left(\frac{nF}{RT}\left(E-E_1^0\right)\right)+exp\left(\frac{nF}{RT}\left(2E-E_1^0-E_2^0\right)\right)} \quad (2.34)$$

and

$$[ox] = \frac{exp\left(\frac{nF}{RT}\left(2E-E_1^0-E_2^0\right)\right)}{1+exp\left(\frac{nF}{RT}\left(E-E_1^0\right)\right)+exp\left(\frac{nF}{RT}\left(2E-E_1^0-E_2^0\right)\right)} \quad (2.35)$$

# III. Summary

This chapter contains an overview of the academic work done during my doctoral studies. It includes five journal articles which are already published. My contribution to each study is listed below together with the short description of each article:

## *3.1. Identification and Characterization of the "Super-Reduced" State of the H-Cluster in [FeFe] Hydrogenase: A New Building Block for the Catalytic Cycle?*

Published in Angewandte Chemie International Edition, 2012 Vol. 51 (46), pp 11458-11462.

- I prepared samples in different redox states
- I performed all the FTIR experiments and the data analysis
- I performed all the EPR experiments and the data simulation
- I performed all the PFE experiments
- I was largely involved in the production of the manuscript

C. Lambertz provided all the biological samples.

The catalytic mechanism of the reversible conversion of protons and electrons to molecular hydrogen by [FeFe] hydrogenases is not yet fully understood. The proposed models are based on the two redox states of the H-cluster: $H_{ox}$ (active oxidized) and $H_{red}$ (active reduced) which were identified in many known [FeFe] hydrogenases using FTIR, EPR and Mössbauer spectroscopy. The FTIR spectroelectrochemical studies of bacterial [FeFe]

hydrogenase from *Desulfovibrio desulfuricans* (DdH) provided the first indication of the existence of an additional redox state, i.e. the super reduced state $H_{sred}$. However, the transition from $H_{red}$ to $H_{sred}$ appears to be incomplete and irreversible in DdH. In algal [FeFe] hydrogenase from *Clamydomonas reinhardtii* (CrHydA1), however, $H_{sred}$ can be stabilized and the transition from $H_{red}$ to $H_{sred}$ is fully reversible. The study of the electronic structure of the $H_{sred}$ state and its relevance to the catalytic cycle are presented in this work.

The FTIR spectra corresponding to the different redox states were well known but the EPR of the $H_{sred}$ state had not been identified yet. This EPR spectrum could differentiate between the $[4Fe\text{-}4S]^{2+}Fe^{I}Fe^{0}$ and the $[4Fe\text{-}4S]^{1+}Fe^{I}Fe^{I}$ configuration. FTIR and EPR samples were prepared simultaneously and studied at low temperatures. It was shown that with the increase of the FTIR signal characteristic for $H_{sred}$ a broad EPR signal also appeared. The obtained spectral parameters of this signal allowed assigning it to the reduced [4Fe-4S] cluster and favor the $[4Fe\text{-}4S]^{1+}Fe^{I}Fe^{I}$ configuration. This result also shows that the $[4Fe\text{-}4S]_{H}$ cluster is an essential part of the H-cluster involved in the electron transfer.

The presence of the super reduced state in the catalytically active samples as well as its full reversibility into the $H_{red}$ state and further into the $H_{ox}$ state, allowed the conclusion that $H_{sred}$ is active and involved in the catalytic cycle. The PFE experiments performed on bacterial and algal [FeFe] hydrogenases did not show inactivation of the enzymes at the low potentials where $H_{sred}$ is accumulated thus confirming its involvement in the catalytic cycle.

Based on these results, the catalytic cycle shown below was formulated and it was proposed that $H_{sred}$ is involved in the reaction cycle of all [FeFe] hydrogenases but only in algal enzymes it is stabilized as resting state due to the lack of F-clusters, which in bacterial enzymes immediately reoxidize $H_{sred}$ to $H_{red}$.

### *3.2. Biomimetic assembly and activation of [FeFe]-hydrogenases*

Published in Nature, 2013 Vol. 499 (7456), pp 66-69.

- I performed all the FTIR experiments and the data analysis
- I was involved in the production of the manuscript

G. Berggren and T. R. Simmons provided synthetic complexes; G. Berggren, C. Lambertz and J. Esselborn contributed to maturation experiments; G. Berggren and S. Gambarelli performed EPR experiments; J.-M. Mouesca did DFT calculations.

The biosynthesis of the H-cluster is not well understood. It is postulated that proteins known as HydE and HydG synthesize the binuclear part of the H-cluster and an additional protein HydF transfers it to the apo [FeFe] hydrogenase which contains only the $[4Fe\text{-}4S]_H$ cluster. In this work this hypothesis is tested by attempting to bind different mimics of the bi-nuclear sub-cluster to HydF which contains a surface exposed [4Fe-4S] cluster. Since the nature of the bridgehead atom in the dithiol ligand was still not uniquely identified (either carbon, oxygen, or nitrogen), all three options were explored.

The combined FTIR and EPR experiments proved that all three mimic complexes ("pdt", "adt", and "odt") can bind to the HydF from *Thermatoga maritima*. Moreover, the obtained FTIR spectra showed close resemblance to the one obtained previously for HydF prepared in the presence of HydE and HydG suggesting that the mimic complexes are indeed very similar to the proposed precursor of the diiron sub-cluster. Further detailed EPR analysis combined with DFT calculations showed that isomerization of one of the $CN^-$ ligands takes place and the mimic complexes bind to the [4Fe-4S] cluster in the HydF through the carbon atom. The HydF proteins, however, did not show any hydrogenase activity.

In the next step the three mimic complexes were transferred from HydF to the apo [FeFe] hydrogenase from *Clamydomonas reinhardtii* by simple mixing these two proteins. The FTIR signals showed that all of the mimic complexes maturated the apo enzyme but only the one carrying the adt bridge showed all the active states of the H-cluster. This was confirmed by activity tests performed for all the hybrid enzymes and it was concluded that fully active [FeFe] hydrogenase can be obtained only by maturation with the mimic complex containing the azadithiolate (adt) bridge.

It is clearly shown in this work that to obtain full enzymatic activity not only both parts of the H-cluster have to be present (the HydF with bound mimic complexes is not active) but also the proper protein environment is necessary. In addition this procedure provides a simple biotechnological tool for producing active [FeFe] hydrogenases since the apo protein can be easily expressed in *E. coli*.

### *3.3. Spontaneous activation of [FeFe]-hydrogenases by an inorganic [2Fe] active site mimic*

Published in Nature Chemical Biology, 2013 Vol. 9 (10), pp 607-609.

- I performed all the FTIR experiments and the data analysis
- I performed all the EPR experiments and the data simulation
- I was involved in the production of the manuscript

J. Esselborn, C. Lambertz, J. Noth and J. Siebel provided biological samples and performed biochemical experiments; G. Berggren and T. R. Simmons provided synthetic complexes.

In this work the biosynthesis of active [FeFe] hydrogenases described above (see 3.2.) was taken one step further. It was shown that without the presence of any additional proteins the mimic complex can spontaneously maturate apo [FeFe] hydrogenases containing only the $[4Fe\text{-}4S]_H$ sub-cluster of the active site. Using the mimic complex containing the azadithiolate bridge full activity was obtained for algal (*Clamydomonas reinhardtii*) and bacterial (*Clostridium pasteurianum* and *Megasphaera elsdenii*) enzymes. This is not trivial, since the active site in these bacterial [FeFe] hydrogenases is buried deep inside the protein and they contain more than one [4Fe-4S] cluster. This would suggest that the protein recognizes the mimic complex and triggered by specific interactions directs it inside.

During this spontaneous maturation process one of the CO ligands in the mimic complex is released and the H-cluster is formed. The FTIR and EPR spectra indicate that all active states can be observed in “as is” samples. Furthermore, the enzyme can be inhibited by external CO. The FTIR signals originating from the bridging CO ligand indicate that a

change of the ligand geometry has to occur. The rhombic EPR signal and the FTIR signal originating from the $H_{sred}$ state also clearly indicate that a covalent bond between mimic complex and the $[4Fe\text{-}4S]_H$ cluster has to be created resulting in a native-like H-cluster.

These results, significantly simplify active [FeFe] hydrogenase preparations in larger amounts. The “semisynthetic” protocol also provides a new route for the synthetic chemist by demonstrating that a poor catalyst inserted in the right protein environment can lead to a great performance. Moreover, isotope labeling of the H-cluster precursor outside the protein allows spectroscopic experiments which could not be done before. Also, many changes (for example ligand substitutions) can be introduced to mimic complexes and their interactions with the protein environment can be observed. For spectroscopic experiments facilitated specific isotope labeling will become feasible.

### *3.4. New redox states observed in [FeFe] hydrogenases reveal redox coupling within the H-cluster.*

Published in Journal of American Chemical Society, 2014 Vol. 136 (32), pp 11339-11346.

- I performed all the FTIR electrochemistry experiments and the data analysis
- I performed all the FTIR experiments and the data analysis
- I performed all the EPR experiments and data simulations
- I was largely involved in the production of the manuscript

D. Krawietz and J. Siebel provided biological samples; K. Weber provided synthetic compounds.

Knowledge of the possible redox states of the enzyme as well as its electronic structure is very important in the study of its catalytic cycle. The potential range in which different redox states appear is also crucial for the enzyme's performance and its interactions with electron donors/acceptors. The semisynthetic active [FeFe] hydrogenase showed full activity and all active states were observed. However, more detailed experiments had to be performed to confirm that the semisynthetic enzyme is indistinguishable from the wild type. In addition, studies of inactive but intact modified H-clusters (like the one containing a $CH_2$ group in the bridging motive instead of NH) can provide information on redox states that cannot be stabilized in the active enzyme.

FTIR spectroelectrochemistry is the perfect technique to study the redox behavior of [FeFe] hydrogenases since the CO and $CN^-$ ligands are sensitive to the change in the oxidation state of the iron ions. The experiments showed that for an active semisynthetic

enzyme, the active states $H_{ox}$, $H_{red}$ and $H_{sred}$ are present in the same potential range as in the native system and are separated by two reversible one electron transitions. It is interesting that at high potentials, in contrast to PFE experiments, the active site is disrupted and an inactive oxidized CO inhibited ($H_{ox}$-CO) state appears. The sample in this state is stable and upon reductive titration revealed a new reduced CO inhibited state ($H_{'red'}$-CO) which can be further reduced to the active $H_{sred}$ state. Based on small changes in the FTIR spectra, the potential range and detailed studies involving light induced $^{13}CO$ scrambling it is concluded that reduction between two CO inhibited states takes place on the $[4Fe\text{-}4S]_H$ sub-cluster and the $H_{'red'}$-CO state is in the $[4Fe\text{-}4S]^{+}Fe^{I}Fe^{II}$ configuration. These results also show that a CO inhibited sample can be activated through the $H_{sred}$ state.

FTIR spectroelectrochemistry experiments on the inactive semisynthetic enzyme containing a $CH_2$ group in the dithiolate bridge revealed two stable redox states (oxidized and reduced) separated by a reversible one electron transition. FTIR spectra obtained for both the states strongly resemble that of the $H_{ox}$ state of the native enzyme. For the oxidized sample EPR spectra were obtained that were identical of those of the $H_{ox}$ state of the native hydrogenase. This suggests that this form can be described as a $[4Fe\text{-}4S]^{2+}Fe^{I}Fe^{II}$ configuration. Similar as in the case of CO inhibited states of the active hydrogenase, the IR signals show only a slight shift between both redox states which would suggest that the reduction occurs on the $[4Fe\text{-}4S]_H$ sub-cluster.

For both newly identified redox states in [FeFe] hydrogenases the redox potential of the binuclear part is lowered by changes of the active site (such as blocking the open coordination site by a CO ligand or preventing the proton flow by modification of the bridging motif) and causes reduction of the $[4Fe\text{-}4S]_H$ sub-cluster while the binuclear part remains in the mixed valence state. This study demonstrates the strong redox coupling between the two parts of the H-cluster and confirms that the $[4Fe\text{-}4S]_H$ sub-cluster is also redox active and as such an integral part of the H-cluster participating in the catalytic cycle.

### *3.5. Artificially maturated [FeFe] hydrogenase from Chlamydomonas reinhardtii: HYSCORE and ENDOR study of a non-natural H-cluster*

Published in Physical Chemistry Chemical Physics, 2015 Vol.17 (7), pp 5421-5430.

- I was involved in samples preparation
- I performed all the FTIR experiments and data analysis
- I performed all the EPR experiments and data simulations
- I was largely involved in the production of the manuscript

J. Siebel provided all biological samples; T. Simmons provided synthetic compounds.

An analysis of the electronic structure of the oxidized [FeFe] hydrogenase from *Clamydomonas reinhardtii* maturated with the non-natural biomimetic complex $[Fe_2(CO)_4(CN)_2(pdt)]^{2-}$ in which the bridging amine is replaced by a $CH_2$ group is reported in this work. This inactive semisynthetic hydrogenase in its oxidized state strongly resembles the native $H_{ox}$ state where the EPR signal originates from the mixed valence $Fe^{I}Fe^{II}$ state of the binuclear sub-cluster. Taking advantage of the readily available isotope labeled biomimetic complex as well as the possibility to obtain a single specific redox state, multi-frequency HYSCORE and ENDOR studies of $^{13}C$ and $^{15}N$ labeled $CN^-$ ligands in the non-natural H-cluster were performed.

The hyperfine couplings of the $^{13}C$ nuclei were detected using X-band and Q-band ENDOR spectroscopy. This study revealed that the spin density is distributed over both $CN^-$ ligands but is predominantly localized on the $^{13}C$ nuclei bound to the distal Fe. Determination of the relative orientation of the hyperfine tensor with respect to the g

tensor made it possible to relate the orientation of the strongly coupled $CN^-$ ligand to the crystal structure.

HYSCORE spectra obtained for the sample labeled with $^{15}N$ at the $CN^-$ ligands at X-band and Q-band could be simultaneously simulated with one set of parameters showing that significant spin density is distributed over one and not both nitrogen atoms. The obtained hyperfine tensor and its orientation was further used to simulate the $^{14}N$ HYSCORE spectra with $^{14}N$ in the $CN^-$ ligands confirming the previously obtained nuclear quadrupole couplings.

The obtained results show that the oxidized [FeFe] hydrogenase maturated with the non-natural biomimetic complex in which the bridging amine is replaced by a $CH_2$ group is a very good model system to study the native $H_{ox}$ state. Furthermore, a detailed analysis of the obtained data and available crystal structures of [FeFe] hydrogenases allowed a first estimation of the g tensor orientation relative to the molecular axes in the active site of this enzyme.

## Reference List


1. Lubitz, W., Ogata, H., Rüdiger, O., and Reijerse, E. (2014) Hydrogenases, *Chemical Reviews 114*, 4081-4148.

2. Cammack, R. F., M.; Robson, R. (2001) *Hydrogen as a Fuel: Learning from Nature*, Taylor & Francis, London.

3. Vignais, P. M., and Billoud, B. (2007) Occurrence, classification, and biological function of hydrogenases: An overview, *Chemical Reviews 107*, 4206-4272.

4. Vignais, P. M., Billoud, B., and Meyer, J. (2001) Classification and phylogeny of hydrogenases, *Fems Microbiology Reviews 25*, 455-501.

5. Gaffron, H. (1939) Reduction of Carbon Dioxide with Molecular Hydrogen in Green Algae, *Nature 143*, 204-205.

6. Gaffron, H. (1940) The oxyhydrogen reaction in green algae and the reduction of carbon dioxide in the dark, *Science 91*, 529-530.

7. Stuart, T. S., and Gaffron, H. (1972) The Gas Exchange of Hydrogen-adapted Algae as Followed by Mass Spectrometry, *Plant Physiology 50*, 136-140.

8. Stuart, T. S., and Gaffron, H. (1972) The Mechanism of Hydrogen Photoproduction by Several Algae II. The Contribution of Photosystem II *Planta 106*, 101-112.

9. Winkler, M., Kuhlgert, S., Hippler, M., and Happe, T. (2009) Characterization of the Key Step for Light-driven Hydrogen Evolution in Green Algae, *Journal of Biological Chemistry 284*, 36620-36627.

10. Volbeda, A., Charon, M.-H., Piras, C., Hatchikian, E. C., Frey, M., and Fontecilla-Camps, J. C. (1995) Crystal structure of the nickel-iron hydrogenase from *Desulfovibrio gigas*, *Nature 373*, 580-587.

11. Shima, S., Pilak, O., Vogt, S., Schick, M., Stagni, M. S., Meyer-Klaucke, W., Warkentin, E., Thauer, R. K., and Ermler, U. (2008) The Crystal Structure of [Fe]-Hydrogenase Reveals the Geometry of the Active Site, *Science 321*, 572-575.

12. Peters, J. W., Lanzilotta, W. N., Lemon, B. J., and Seefeldt, L. C. (1998) X-ray Crystal Structure of the Fe-Only Hydrogenase (CpI) from *Clostridium pasteurianum* to 1.8 Angstrom Resolution, *Science 282*, 1853-1858.

13. Lemon, B. J., and Peters, J. W. (1999) Binding of Exogenously Added Carbon Monoxide at the Active Site of the Iron-Only Hydrogenase (CpI) from *Clostridium pasteurianum*, *Biochemistry 38*, 12969-12973.

14. Nicolet, Y., Piras, C., Legrand, P., Hatchikian, C. E., and Fontecilla-Camps, J. C. (1999) *Desulfovibrio desulfuricans* iron hydrogenase: the structure shows unusual coordination to an active site Fe binuclear center, *Structure with Folding & Design 7*, 13-23.

15. Nicolet, Y., de Lacey, A. L., Vernede, X., Fernandez, V. M., Hatchikian, E. C., and Fontecilla-Camps, J. C. (2001) Crystallographic and FTIR Spectroscopic Evidence of Changes in Fe Coordination Upon Reduction of the Active Site of the Fe-Only Hydrogenase from *Desulfovibrio desulfuricans*, *Journal of the American Chemical Society 123*, 1596-1601.

16. Pandey, A. S., Harris, T. V., Giles, L. J., Peters, J. W., and Szilagyi, R. K. (2008) Dithiomethylether as a Ligand in the Hydrogenase H-Cluster, *Journal of the American Chemical Society 130*, 4533-4540.

17. Mulder, D. W., Boyd, E. S., Sarma, R., Lange, R. K., Endrizzi, J. A., Broderick, J. B., and Peters, J. W. (2010) Stepwise [FeFe]-hydrogenase H-cluster assembly revealed in the structure of $HydA^{\Delta EFG}$, *Nature 465*, 248-251.

18. Nicolet, Y., Cavazza, C., and Fontecilla-Camps, J. C. (2002) Fe-only hydrogenases: structure, function and evolution, *Journal of Inorganic Biochemistry 91*, 1-8.

19. Siegbahn, P. E. M., Tye, J. W., and Hall, M. B. (2007) Computational Studies of [NiFe] and [FeFe] Hydrogenases, *Chemical Reviews 107*, 4414-4435.

20. Silakov, A., Wenk, B., Reijerse, E., and Lubitz, W. (2009) $^{14}N$ HYSCORE investigation of the H-cluster of [FeFe] hydrogenase: evidence for a nitrogen in the dithiol bridge, *Physical Chemistry Chemical Physics 11*, 6592-6599.

21. Berggren, G., Adamska, A., Lambertz, C., Simmons, T., Esselborn, J., Atta, M., Gambarelli, S., Mouesca, J. M., Reijerse, E., Lubitz, W., Happe, T., Artero, V., and Fontecave, M. (2013) Biomimetic assembly and activation of [FeFe]-hydrogenases, *Nature 499*, 66-70.

22. Esselborn, J., Lambertz, C., Adamska-Venkatesh, A., Simmons, T., Berggren, G., Noth, J., Siebel, J., Hemschemeier, A., Artero, V., Reijerse, E., Fontecave, M., Lubitz, W., and Happe, T. (2013) Spontaneous activation of [FeFe]-hydrogenases by an inorganic [2Fe] active site mimic, *Nature Chemical Biology 9*, 607-609.

23. Knörzer, P., Silakov, A., Foster, C. E., Armstrong, F. A., Lubitz, W., and Happe, T. (2012) Importance of the Protein Framework for Catalytic Activity of [FeFe] -Hydrogenases, *Journal of Biological Chemistry 287*, 1489-1499.

24. Montet, Y., Amara, P., Volbeda, A., Vernede, X., Hatchikian, E. C., Field, M. J., Frey, M., and Fontecilla-Camps, J. C. (1997) Gas access to the active site of Ni-Fe hydrogenases probed by X-ray crystallography and molecular dynamics, *Nature Structural Biology 4*, 523-526.

25. Hong, G., and Pachter, R. (2012) Inhibition of Biocatalysis in [Fe-Fe] Hydrogenase by Oxygen: Molecular Dynamics and Density Functional Theory Calculations, *ACS Chemical Biology 7*, 1268-1275.

26. Hong, G., Cornish, A. J., Hegg, E. L., and Pachter, R. (2011) On understanding proton transfer to the biocatalytic $[Fe\text{-}Fe]_H$ sub-cluster in [Fe-Fe] $H_2$ ases: QM/MM MD simulations, *Biochimica et Biophysica Acta - Bioenergetics 1807*, 510-517.

27. Long, H., King, P. W., and Chang, C. H. (2014) Proton Transport in *Clostridium pasteurianum* [FeFe] Hydrogenase I: A Computational Study, *Journal of Physical Chemistry B 118*, 890-900.

28. Cornish, A. J., Gaertner, K., Yang, H., Peters, J. W., and Hegg, E. L. (2011) Mechanism of Proton Transfer in [FeFe]-Hydrogenase from *Clostridium pasteurianum*, *Journal of Biological Chemistry 286*, 38341-38347.

29. Ginovska-Pangovska, B., Ho, M.-H., Linehan, J. C., Cheng, Y., Dupuis, M., Raugei, S., and Shaw, W. J. (2014) Molecular dynamics study of the proposed proton transport pathways in [FeFe]-hydrogenase, *Biochimica et Biophysica Acta - Bioenergetics 1837*, 131-138.

30. Mulder, D. W., Shepard, E. M., Meuser, J. E., Joshi, N., King, P. W., Posewitz, M. C., Broderick, J. B., and Peters, J. W. (2011) Insights into [FeFe]-Hydrogenase Structure, Mechanism, and Maturation, *Structure 19*, 1038-1052.

31. Nicolet, Y., and Fontecilla-Camps, J. C. (2012) Structure-Function Relationships in [FeFe]-Hydrogenase Active Site Maturation, *Journal of Biological Chemistry 287*, 13532-13540.

32. Shepard, E. M., Mus, F., Betz, J. N., Byer, A. S., Duffus, B. R., Peters, J. W., and Broderick, J. B. (2014) [FeFe]-Hydrogenase Maturation, *Biochemistry 53*, 4090-4104.

33. Voordouw, G., Hagen, W. R., Krüse-Wolters, K. M., van Berkel-Arts, A., and Veeger, C. (1987) Purification and characterization of *Desulfovibrio vulgaris* (Hildenborough) hydrogenase expressed in *Escherichia coli European Journal of Biochemistry 162*, 31-36.

34. Mulder, D. W., Ortillo, D. O., Gardenghi, D. J., Naumov, A. V., Ruebush, S. S., Szilagyi, R. K., Huynh, B., Broderick, J. B., and Peters, J. W. (2009) Activation of HydA(Delta EFG) Requires a Preformed [4Fe-4S] Cluster, *Biochemistry 48*, 6240-6248.

35. Posewitz, M. C., King, P. W., Smolinski, S. L., Zhang, L. P., Seibert, M., and Ghirardi, M. L. (2004) Discovery of Two Novel Radical S-Adenosylmethionine Proteins Required for the Assembly of an Active [Fe] Hydrogenase, *Journal of Biological Chemistry 279*, 25711-25720.

36. Posewitz, M. C., King, P. W., Smolinski, S. L., Smith, R. D., Ginley, A. R., Ghirardi, M. L., and Seibert, M. (2005) Identification of genes required for hydrogenase activity in *Chlamydomonas reinhardtii*, *Biochemical Society Transactions 33*, 102-104.

37. Meyer, J. (2007) [FeFe] hydrogenases and their evolution: a genomic perspective, *Cellular and Molecular Life Sciences 64*, 1063-1084.

38. Czech, I., Silakov, A., Lubitz, W., and Happe, T. (2010) The FeFe -hydrogenase maturase HydF from *Clostridium acetobutylicum* contains a CO and $CN^-$ ligated iron cofactor, *FEBS Letters 584*, 638-642.

39. McGlynn, S. E., Shepard, E. M., Winslow, M. A., Naumov, A. V., Duschene, K. S., Posewitz, M. C., Broderick, W. E., Broderick, J. B., and Peters, J. W. (2008) HydF as a scaffold protein in [FeFe] hydrogenase H-cluster biosynthesis, *FEBS Letters 582*, 2183-2187.

40. Kuchenreuther, J. M., Britt, R. D., and Swartz, J. R. (2012) New Insights into [FeFe] Hydrogenase Activation and Maturase Function, *Plos One 7*, e45850.

41. Kuchenreuther, J. M., George, S. J., Grady-Smith, C. S., Cramer, S. P., and Swartz, J. R. (2011) Cell-free H-cluster Synthesis and [FeFe] Hydrogenase Activation: All Five CO and $CN^-$ Ligands Derive from Tyrosine, *PLoS One 6*, e20346.

42. Rubach, J. K., Brazzolotto, X., Gaillard, J., and Fontecave, M. (2005) Biochemical characterization of the HydE and HydG iron-only hydrogenase maturation enzymes from *Thermatoga maritima*, *FEBS Letters 579*, 5055-5060.

43. Sofia, H. J., Chen, G., Hetzler, B. G., Reyes-Spindola, J. F., and Miller, N. E. (2001) Radical SAM, a novel protein superfamily linking unresolved steps in familiar biosynthetic pathways with radical mechanisms: functional characterization using new analysis and information visualization methods, *Nucleic Acids Research 29*, 1097-1106.

44. Pilet, E., Nicolet, Y., Mathevon, C., Douki, T., Fontecilla-Camps, J. C., and Fontecave, M. (2009) The role of the maturase HydG in [FeFe]-hydrogenase active site synthesis and assembly, *FEBS Letters 583*, 506-511.

45. Shepard, E. M., Duffus, B. R., George, S. J., McGlynn, S. E., Challand, M. R., Swanson, K. D., Roach, P. L., Cramer, S. P., Peters, J. W., and Broderick, J. B. (2010) [FeFe]-Hydrogenase Maturation: HydG-Catalyzed Synthesis of Carbon Monoxide, *Journal of the American Chemical Society 132*, 9247-9249.

46. Nicolet, Y., Rubach, J. K., Posewitz, M. C., Amara, P., Mathevon, C., Atta, M., Fontecave, M., and Fontecilla-Camps, J. C. (2008) X-ray structure of the [FeFe]-hydrogenase maturase HydE from *Thermotoga maritima*, *Journal of Biological Chemistry 283*, 18861-18872.

47. Kuchenreuther, J. M., Myers, W. K., Stich, T. A., George, S. J., NejatyJahromy, Y., Swartz, J. R., and Britt, R. D. (2013) A Radical Intermediate in Tyrosine Scission to the CO and $CN^-$ Ligands of FeFe Hydrogenase, *Science 342*, 472-475.

48. Kuchenreuther, J. M., Myers, W. K., Suess, D. L. M., Stich, T. A., Pelmenschikov, V., Shiigi, S. A., Cramer, S. P., Swartz, J. R., Britt, R. D., and George, S. J. (2014) The HydG Enzyme Generates an $Fe(CO)_2(CN)$ Synthon in Assembly of the FeFe Hydrogenase H-Cluster, *Science 343*, 424-427.

49. Cendron, L., Berto, P., D'Adamo, S., Vallese, F., Govoni, C., Posewitz, M. C., Giacometti, G. M., Costantini, P., and Zanotti, G. (2011) Crystal Structure of HydF Scaffold Protein Provides Insights into [FeFe]-Hydrogenase Maturation, *Journal of Biological Chemistry 286*, 43944-43950.

50. Brazzolotto, X., Rubach, J. K., Gaillard, J., Gambarelli, S., Atta, M., and Fontecave, M. (2006) The [Fe-Fe]-hydrogenase maturation protein HydF from *Thermotoga maritima* is a GTPase with an iron-sulfur cluster, *Journal of Biological Chemistry 281*, 769-774.

51. Czech, I., Stripp, S., Sanganas, O., Leidel, N., Happe, T., and Haumann, M. (2011) The [FeFe]-hydrogenase maturation protein HydF contains a H-cluster like [4Fe4S]-2Fe site, *FEBS Letters 585*, 225-230.

52. Shepard, E. M., McGlynn, S. E., Bueling, A. L., Grady-Smith, C. S., George, S. J., Winslow, M. A., Cramer, S. P., Peters, J. W., and Broderick, J. B. (2010) Synthesis of the 2Fe subcluster of the [FeFe]-hydrogenase H cluster on the HydF scaffold, *Proceedings of the National Academy of Sciences of the United States of America 107*, 10448-10453.

53. Lubitz, W., Reijerse, E., and van Gastel, M. (2007) [NiFe] and [FeFe] hydrogenases studied by advanced magnetic resonance techniques, *Chemical Reviews 107*, 4331-4365.

54. Albracht, S. P. J., Roseboom, W., and Hatchikian, E. C. (2006) The active site of the [FeFe]-hydrogenase from *Desulfovibrio desulfuricans*. 1. Light sensitivity and magnetic hyperfine interactions as observed by electron paramagnetic resonance, *Journal of Biological Inorganic Chemistry 11*, 88-101.

55. Roseboom, W., de Lacey, A. L., Fernandez, V. M., Hatchikian, E. C., and Albracht, S. P. J. (2006) The active site of the [FeFe]-hydrogenase from *Desulfovibrio desulfuricans*. II. Redox properties, light sensitivity and CO-ligand exchange as observed by infrared spectroscopy, *Journal of Biological Inorganic Chemistry 11*, 102-118.

56. Hagen, W. R., van Berkel-Arts, A., Krüse-Wolters, K. M., Dunham, W. R., and Veeger, C. (1986) EPR of a novel high-spin component in activated hydrogenase from *Desulfovibrio vulgaris* (Hildenborough), *FEBS Letters 201*, 158-162.

57. Silakov, A., Reijerse, E. J., Albracht, S. P. J., Hatchikian, E. C., and Lubitz, W. (2007) The Electronic Structure of the H-Cluster in the [FeFe]-Hydrogenase from *Desulfovibrio desulfuricans:* A Q-band $^{57}$Fe-ENDOR and HYSCORE Study, *Journal of the American Chemical Society 129*, 11447-11458.

58. Kamp, C., Silakov, A., Winkler, M., Reijerse, E. J., Lubitz, W., and Happe, T. (2008) Isolation and first EPR characterization of the [FeFe]-hydrogenases from green algae, *Biochimica et Biophysica Acta-Bioenergetics 1777*, 410-416.

59. Pereira, A. S., Tavares, P., Moura, I., Moura, J. J. G., and Huynh, B. H. (2001) Mossbauer characterization of the iron-sulfur clusters in Desulfovibrio vulgaris hydrogenase, *Journal of the American Chemical Society 123*, 2771-2782.

60. Popescu, C. V., and Munck, E. (1999) Electronic structure of the H cluster in [Fe]-hydrogenases, *Journal of the American Chemical Society 121*, 7877-7884.

61. Silakov, A., Kamp, C., Reijerse, E., Happe, T., and Lubitz, W. (2009) Spectroelectrochemical Characterization of the Active Site of the [FeFe] Hydrogenase HydA1 from *Chlamydomonas reinhardtii*, *Biochemistry 48*, 7780-7786.

62. Adamska, A., Silakov, A., Lambertz, C., Rüdiger, O., Happe, T., Reijerse, E., and Lubitz, W. (2012) Identification and Characterization of the "Super-Reduced" State of the H-Cluster in [FeFe] Hydrogenase: A New Building Block for the Catalytic Cycle?, *Angewandte Chemie - International Edition 51*, 11458-11462.

63. Pierik, A. J., Hulstein, M., Hagen, W. R., and Albracht, S. P. J. (1998) A low-spin iron with CN and CO as intrinsic ligands forms the core of the active site in [Fe]-hydrogenases, *European Journal of Biochemistry 258*, 572-578.

64. Silakov, A., Reijerse, E. J., Albracht, S. P., Hatchikian, E., Claude, and Lubitz, W. (2007) The electronic structure of the H-cluster in the [FeFe]-hydrogenase from Desulfovibrio desulfuricans: A Q-band Fe-57-ENDOR and HYSCORE study, *Journal of the American Chemical Society 129*, 11447-11458.

65. Stripp, S. T., and Happe, T. (2009) How algae produce hydrogen-news from the photosynthetic hydrogenase, *Dalton Transactions*, 9960-9969.

66. Hatchikian, E. C., Forget, N., Fernandez, V. M., Williams, R., and Cammack, R. (1992) Further Characterization of the [Fe]-Hydrogenase from Desulfovibrio-Desulfuricans Atcc-7757, *European Journal of Biochemistry 209*, 357-365.

67. Abeles, F. B. (1964) Cell-free Hydrogenase from Chlamydomonas, *Plant Physiology 39*, 169-176.

68. Vincent, K. A., Parkin, A., and Armstrong, F. A. (2007) Investigating and exploiting the electrocatalytic properties of hydrogenases, *Chemical Reviews 107*, 4366-4413.

69. Pershad, H. R., Duff, J. L. C., Heering, H. A., Duin, E. C., Albracht, S. P. J., and Armstrong, F. A. (1999) Catalytic Electron Transport in *Chromatium vinosum* [NiFe]-Hydrogenase: Application of Voltammetry in Detecting Redox-Active Centers and Establishing That Hydrogen Oxidation Is Very Fast Even at Potentials Close to the Reversible $H^+/H_2$ Value, *Biochemistry 38*, 8992-8999.

70. Armstrong, F. A., Belsey, N. A., Cracknell, J. A., Goldet, G., Parkin, A., Reisner, E., Vincent, K. A., and Wait, A. F. (2009) Dynamic electrochemical investigations of hydrogen oxidation and production by enzymes and implications for future technology, *Chemical Society Reviews 38*, 36-51.

71. Wait, A. F., Brandmayr, C., Stripp, S. T., Cavazza, C., Fontecilla-Camps, J. C., Happe, T., and Armstrong, F. A. (2011) Formaldehyde-A Rapid and Reversible Inhibitor of Hydrogen Production by [FeFe]-Hydrogenases, *Journal of the American Chemical Society 133*, 1282-1285.

72. Baffert, C., Bertini, L., Lautier, T., Greco, C., Sybirna, K., Ezanno, P., Etienne, E., Soucaille, P., Bertrand, P., Bottin, H., Meynial-Salles, I., De Gioia, L., and Leger, C. (2011) CO Disrupts the Reduced H-Cluster of [FeFe] Hydrogenase. A Combined DFT and Protein Film Voltammetry Study, *Journal of the American Chemical Society 133*, 2096-2099.

73. Foster, C. E., Kramer, T., Wait, A. F., Parkin, A., Jennings, D. P., Happe, T., McGrady, J. E., and Armstrong, F. A. (2012) Inhibition of [FeFe]-Hydrogenases by Formaldehyde and Wider Mechanistic Implications for Biohydrogen Activation, *Journal of the American Chemical Society 134*, 7553-7557.

74. Vincent, K. A., Parkin, A., Lenz, O., Albracht, S. P. J., Fontecilla-Camps, J. C., Cammack, R., Friedrich, B., and Armstrong, F. A. (2005) Electrochemical definitions of $O_2$ sensitivity and oxidative inactivation in hydrogenases, *Journal of the American Chemical Society 127*, 18179-18189.

75. Baffert, C., Demuez, M., Cournac, L., Burlat, B., Guigliarelli, B., Bertrand, P., Girbal, L., and Leger, C. (2008) Hydrogen-activating enzymes: Activity does not correlate with oxygen sensitivity, *Angewandte Chemie-International Edition 47*, 2052-2054.

76. Stripp, S. T., Goldet, G., Brandmayr, C., Sanganas, O., Vincent, K. A., Haumann, M., Armstrong, F. A., and Happe, T. (2009) How oxygen attacks [FeFe] hydrogenases from photosynthetic organisms, *Proceedings of the National Academy of Sciences of the United States of America 106*, 17331-17336.

77. Bruschi, M., Greco, C., Kaukonen, M., Fantucci, P., Ryde, U., and De Gioia, L. (2009) Influence of the [2Fe](H) Subcluster Environment on the Properties of Key Intermediates in the Catalytic Cycle of [FeFe] Hydrogenases: Hints for the Rational Design of Synthetic Catalysts, *Angewandte Chemie-International Edition 48*, 3503-3506.

78. Liu, Z. P., and Hu, P. (2002) Mechanism of $H_2$ metabolism on Fe-only hydrogenases, *Journal of Chemical Physics 117*, 8177-8180.

79. Zhou, T. J., Mo, Y. R., Liu, A. M., Zhou, Z. H., and Tsai, K. R. (2004) Enzymatic mechanism of Fe-only hydrogenase: Density functional study on H-H making/breaking at the diiron cluster with concerted proton and electron transfers, *Inorganic Chemistry 43*, 923-930.

80. Fan, H. J., and Hall, M. B. (2001) A capable bridging ligand for Fe-only hydrogenase: Density functional calculations of a low-energy route for heterolytic cleavage and formation of dihydrogen, *Journal of the American Chemical Society 123*, 3828-3829.

81. Bruschi, M., Fantucci, P., and De Gioia, L. (2002) DFT Investigation of Structural, Electronic, and Catalytic Properties of Diiron Complexes Related to the $[2Fe]_H$ Subcluster of Fe-Only Hydrogenases, *Inorganic Chemistry 41*, 1421-1429.

82. Bruschi, M., Fantucci, P., and De Gioia, L. (2003) Density Functional Theory Investigation of the Active Site of [Fe]-Hydrogenases: Effects of Redox State and Ligand Characteristics on Structural, Electronic, and Reactivity Properties of Complexes Related to the $[2Fe]_H$ Subcluster, *Inorganic Chemistry 42*, 4773-4781.

83. Hajj, V., Baffert, C., Sybirna, K., Meynial-Salles, I., Soucaille, P., Bottin, H., Fourmond, V., and Leger, C. (2014) FeFe hydrogenase reductive inactivation and implication for catalysis, *Energy & Environmental Science 7*, 715-719.

84. Mulder, D. W., Ratzloff, M. W., Shepard, E. M., Byer, A. S., Noone, S. M., Peters, J. W., Broderick, J. B., and King, P. W. (2013) EPR and FTIR Analysis of the Mechanism of $H_2$ Activation by [FeFe]-Hydrogenase HydA1 from *Chlamydomonas reinhardtii*, *Journal of the American Chemical Society 135*, 6921-6929.

85. Abragam, A., and Bleaney, B. (1970) *Electron Paramagnetic Resonance of Transition Ions, by A. Abragam and B. Bleaney*, Oxford Uniwersity Press.

86. Atherton, N. M. (1993) *Principles of electron spin resonance*, Ellis Horwood.

87. Rudowicz, C., and Misra, S. K. (2001) Spin-Hamiltonian formalisms in electron magnetic resonance (EMR) and related spectroscopies, *Applied Spectroscopy Reviews 36*, 11-63.

88. Schweiger, A., and Jeschke, G. (2001) *Principles of Pulse Electron Paramagnetic Resonance*, Oxford University Press.

89. McGarvey, B. R. (1967) The Isotropic Hyperfine Interaction, *Journal of Physical Chemistry 71*, 51-66.

90. Hahn, E. L. (1950) Spin Echoes, *Physical Review 80*, 580-594.

91. Mims, W. B. (1965) Pulsed Endor Experiments, *Proceedings of the Royal Society of London Series a-Mathematical and Physical Sciences 283*, 452-457.

92. Davies, E. R. (1974) A new pulse endor technique, *Physics Letters A A 47*, 1-2.

93. Rowan, L. G., Hahn, E. L., and Mims, W. B. (1965) Electron-Spin-Echo Envelope Modulation, *Physical Review 137*, A61-A71.

94. Mims, W. B. (1972) Envelope Modulation in Spin-Echo Experiments, *Physical Review B-Solid State 5*, 2409-2419.

95. Nakamoto, K. (1977) *Infrared and Raman Spectra of Inorganic and Coordination Compounds: Applications in coordination, organometallic, and bioinorganic chemistry*, John Wiley & Sons, New York.

96. Griffiths, P. R., and De Haseth, J. A. (1986) *Fourier Transform Infrared Spectrometry*, John Wiley & Sons, New York.

97. Stuart, B. H. (2004) *Infrared Spectroscopy: Fundamentals and Applications*, John Wiley & Sons, New York.

98. Chen, Z. J., Lemon, B. J., Huang, S., Swartz, D. J., Peters, J. W., and Bagley, K. A. (2002) Infrared studies of the CO-inhibited form of the Fe-only hydrogenase from *Clostridium pasteurianum* I: Examination of its light sensitivity at cryogenic temperatures, *Biochemistry 41*, 2036-2043.

99. Knörzer, P., Silakov, A., Foster, C. E., Armstrong, F. A., Lubitz, W., and Happe, T. (2012) Importance of the Protein Framework for Catalytic Activity of [FeFe]-Hydrogenases, *Journal of Biological Chemistry 287*, 1489-1499.

100. Eddowes, M. J., and Hill, H. A. O. (1977) Novel method for the investigation of the electrochemistry of metalloproteins: cytochrome c, *Journal of the Chemical Society-Chemical Communications*, 771-772.

101. Yeh, P., and Kuwana, T. (1977) REVERSIBLE ELECTRODE-REACTION OF CYTOCHROME C, *Chemistry Letters*, 1145-1148.

102. Niki, K., Yagi, T., Inokuchi, H., and Kimura, K. (1979) Electrochemical Behavior of Cytochrome $c_3$ of *Desulfovibrio vulgaris*, Strain Miyazaki, on the Mercury Electrode, *Journal of the American Chemical Society 101*, 3335-3340.

103. Hammerich, O., and Ulstrup, J. (2007) *Bioinorganic Electrochemistry*, Springer.

104. Marcus, R. A., and Sutin, N. (1985) Electron transfers in chemistry and biology, *Biochimica Et Biophysica Acta 811*, 265-322.

105. Lojou, E. (2011) Hydrogenases as catalysts for fuel cells: Strategies for efficient immobilization at electrode interfaces, *Electrochimica Acta 56*, 10385-10397.

106. Engstrom, R. C., and Strasser, V. A. (1984) Characterization of electrochemically pretreated glassy carbon electrodes, *Analytical Chemistry 56*, 136-141.

107. Schneider, T. W., and Buttry, D. A. (1993) Electrochemical quartz crystal microbalance studies of adsorption and desorption of self-assembled monolayers of alkyl thiols on gold, *Journal of the American Chemical Society 115*, 12391-12397.

108. Rüdiger, O., Abad, J. M., Hatchikian, E. C., Fernandez, V. M., and De Lacey, A. L. (2005) Oriented immobilization of *Desulfovibrio gigas* hydrogenase onto carbon electrodes by covalent bonds for nonmediated oxidation of $H_2$, *Journal of the American Chemical Society 127*, 16008-16009.

109. Bard, A. J., and Faulkner, L. R. (2000) *Electrochemical Methods: Fundamentals and Applications*, John Wley & Sons, New York.

110. Compton, R. G., and Banks, C. E. (2011) *Understanding Voltammetry*, Imperial College Press, London.

111. Moss, D., Nabedryk, E., Breton, J., and Mantele, W. (1990) Redox-Linked Conformational-Changes in Proteins Detected by A Combination of Infrared-Spectroscopy and Protein Electrochemistry - Evaluation of the Technique with Cytochrome *C*, *European Journal of Biochemistry 187*, 565-572.

## Journal articles

This section consists of five research articles mentioned above in the format as they are accepted or submitted to corresponding scientific journal.

http://onlinelibrary.wiley.com/doi/10.1002/anie.201204800/abstract?issn=1433-7851

Angewandte Communications

[FeFe] Hydrogenase Mechanism

DOI: 10.1002/anie.201204800

# Identification and Characterization of the "Super-Reduced" State of the H-Cluster in [FeFe] Hydrogenase: A New Building Block for the Catalytic Cycle?**

*Agnieszka Adamska, Alexey Silakov,* Camilla Lambertz, Olaf Rüdiger, Thomas Happe, Edward Reijerse,* and Wolfgang Lubitz**

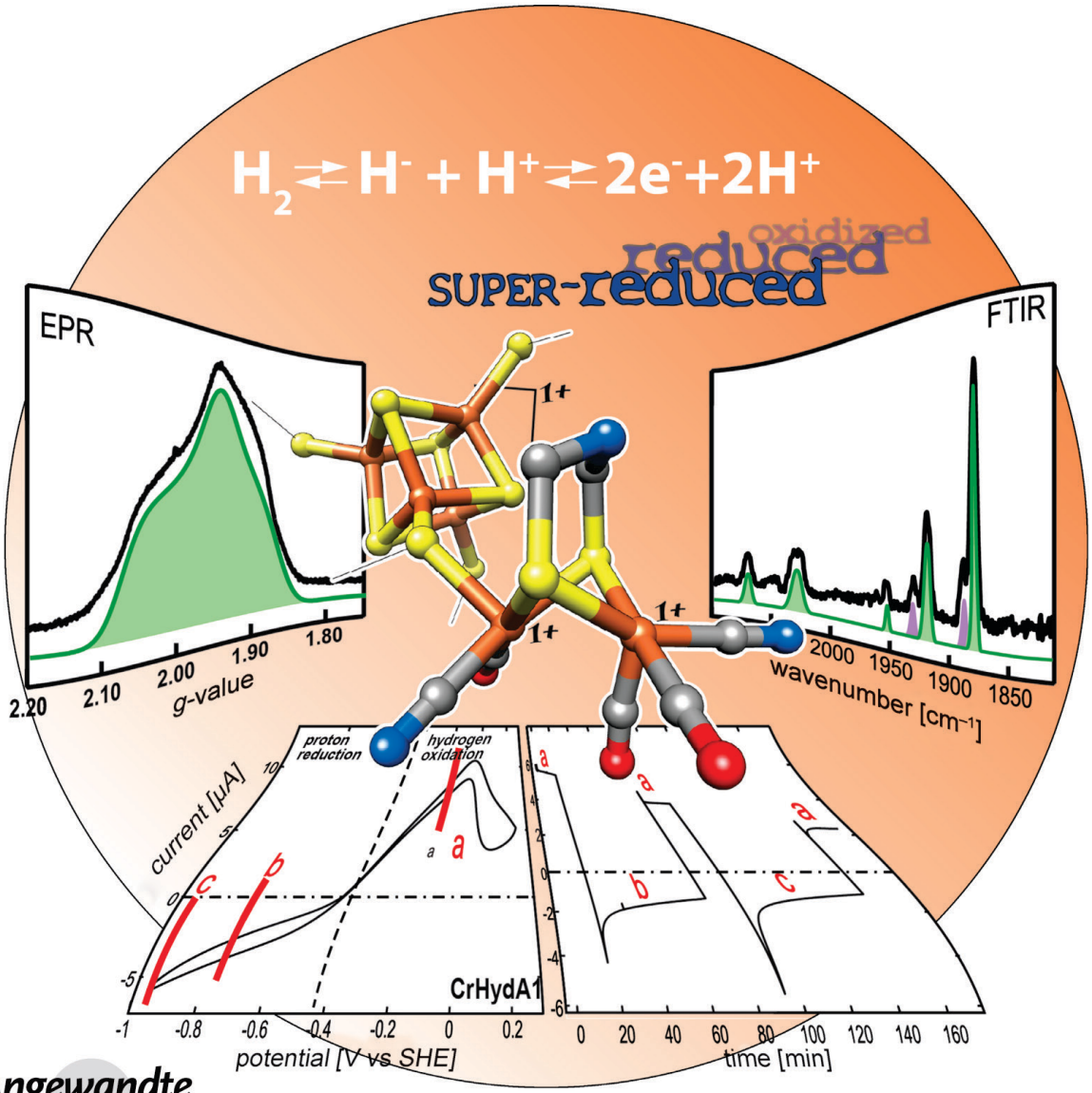


Angewandte Chemie

 

Hydrogenases catalyze the reversible heterolytic formation of $H_2$ from protons and electrons. According to the type of metals in the active site, these enzymes are classified into three groups: [NiFe], [FeFe], and [Fe] hydrogenases.[1,2] All of these enzymes are of high interest in biotechnology, aiming at the generation and conversion of $H_2$ as renewable energy carrier.[1,3] Since [FeFe] hydrogenases are highly efficient in hydrogen production in vivo, elucidation of their catalytic mechanism is of particular relevance for developing artificial hydrogen production systems.[4,5]

The active site of [FeFe] hydrogenase contains the so-called H-cluster (Figure 1) consisting of a di-iron center [2Fe], which is covalently attached via a cysteine thiol bridge to

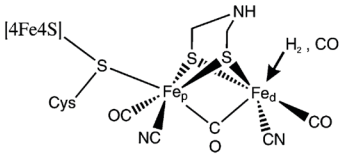


***Figure 1.*** Structure of the active site (H-cluster) in [FeFe] hydrogenases. The arrow points to the open coordination site on the distal iron atom ($Fe_d$).

a cubane-like [4Fe-4S] subcluster.[1,6–8] In the [2Fe] subcluster, both Fe ions are coordinated by CO and CN ligands, keeping the iron centers in low oxidation and spin states.[8–11] The iron atoms in the [2Fe] subcluster are bridged by an azadithiolate group (adt, $(SCH_2)_2NH$).[8,12] The iron distal to the [4Fe4S] subcluster ($Fe_d$) has an open coordination site, which is most likely the $H_2$ binding site (Figure 1).[1,13] It has been proposed that the adt-amine group, which is in a perfect position with respect to the open coordination site, is involved in the proton transfer to and from the catalytic site.[8,12]

Until now, two redox states of the H-cluster were identified that are believed to take part in the catalytic cycle: that is, the active "oxidized" state $H_{ox}$ which is paramagnetic and characterized by a mixed-valence ($Fe^IFe^{II}$) binuclear part, and the active "reduced" state $H_{red}$, which adopts the ($Fe^IFe^I$) configuration.[1]

These active forms can be inhibited by CO, resulting in a single oxidized state, $H_{ox}$-CO.[1,6,9] The [4Fe4S]$_H$ subcluster in these states is oxidized (+2) and formally diamagnetic ($S_{4Fe4S}=0$).[14,15] The redox transition $H_{ox}$ to $H_{red}$ has its midpoint potential around −400 mV (pH 8.0) and has been studied in the [FeFe] hydrogenase from *Desulfovibrio desulfuricans* (*Dd*H) using FTIR spectroelectrochemistry.[11] The same study also identified a subsequent irreversible reduction step at $E_m=-540$ mV to the so-called "super-reduced state" $H_{sred}$. An analogous study of the [FeFe] hydrogenase of *Chlamydomonas reinhardtii* (*Cr*HydA1) showed the same redox transitions.[16] However, in *Cr*HydA1 the super-reduced species $H_{sred}$ occurs at a much higher potential $E_m=-460$ mV (pH 8.0) and the $H_{red}$ to $H_{sred}$ transition is fully reversible.[16] The redox potentials of both $H_{red}$ and $H_{sred}$ in *Cr*HydA1 are close to that of its (isolated) natural redox partner PetF (that is, −400 mV at pH 7.0).[17] Moreover, it has been shown that the PetF redox potential can be reduced substantially upon interaction with its redox partners, such as ferredoxin-$NADP^+$ reductase (FNR).[18] Therefore, in *Cr*HydA1, $H_{sred}$ seems to be a resting state of the enzyme, similar to $H_{ox}$ and $H_{red}$. There are two possibilities for the electronic structure of the H-cluster in the $H_{sred}$ state: either the binuclear part is further reduced to [$Fe^0$-$Fe^I$] or the [4Fe-4S]$^{2+}$ subcluster is reduced to [4Fe-4S]$^+$. Similar to $H_{ox}$, $H_{sred}$ is expected to be paramagnetic, exhibiting an $S=1/2$ ground state.

In this work, we aim to identify and characterize the $H_{sred}$ state from *Cr*HydA1 in detail using EPR and FTIR spectroscopy. To verify the possible catalytic role of the $H_{sred}$ state, we performed protein film electrochemistry (PFE) on *Cr*HydA1 as well as *Dd*H, and the [FeFe] hydrogenase from *Clostridium acetobutylicum* (*Ca*HydA).

*Cr*HydA1 overexpressed in *C. acetobutylicum* was subjected to different reductive and oxidative treatments. Figure 2 presents a selection of the corresponding FTIR- and FID-detected (Q-band) EPR spectra for each sample going from oxidative (A) to reductive conditions (D). The characteristic IR bands and $g$ values for each H-cluster species are indicated at the top of the spectra. The FTIR frequencies were taken from the literature[16] and presented in more detail in the Supporting Information, Figure S1. It is clear that the as isolated samples with sodium dithionite (NaDT) in the buffer show a mixture of $H_{ox}$, $H_{red}$, and $H_{sred}$. Treatment with $H_2$ or with additional equivalents of NaDT shifts the equilibrium towards the reduced species, while thionine treatment induces the formation of oxidized species.[19]

The EPR spectra in Figure 2 clearly show the appearance of a broad contribution with low $g$ values ($2.076\pm0.002$, $1.943\pm0.003$, $1.868\pm0.001$) in the reduced samples. The spectral parameters of this species resemble typical reduced [4Fe-4S] cluster signals.[20] The contribution of $H_{ox}$ and $H_{ox}$-CO to each EPR spectrum was also evaluated using spectral simulations as indicated in Figure 2. As it is evident from the comparison of the EPR and FTIR data, the increase of the [4Fe4S]-like EPR signal coincides with the appearance of the $H_{sred}$ signal in the FTIR measurements. We therefore assign this EPR signal to the $H_{sred}$ state. This shows that $H_{sred}$ is characterized by a [$Fe^IFe^I$][4Fe4S]$^+$ configuration rather than for example, [$Fe^IFe^0$][4Fe4S]$^{2+}$. According to the FTIR and EPR spectra, most preparations contain a mixture of the

[*] A. Adamska, Dr. A. Silakov, Dr. O. Rüdiger, Dr. E. Reijerse, Prof. W. Lubitz
Max-Planck-Institut für Chemische Energiekonversion
Stiftstrasse 34–36, 45470 Mülheim an der Ruhr (Germany)
E-mail: aus40@psu.edu
edward.reijerse@cec.mpg.de
wolfgang.lubitz@cec.mpg.de
Dr. C. Lambertz, Prof. T. Happe
Lehrstuhl Biochemie der Pflanzen, AG Photobiotechnologie, Ruhr Universität Bochum,
Universitätsstrasse 150, 44801 Bochum (Germany)

[**] Gudrun Klihm and Leslie Currell are gratefully acknowledged for their technical support in the EPR and FTIR experiments. Financial Support from the Max Planck Society and the EU (FP7 Energy 212508 "SOLAR H2") is gratefully acknowledged.

Supporting information for this article is available on the WWW under http://dx.doi.org/10.1002/anie.201204800.

  

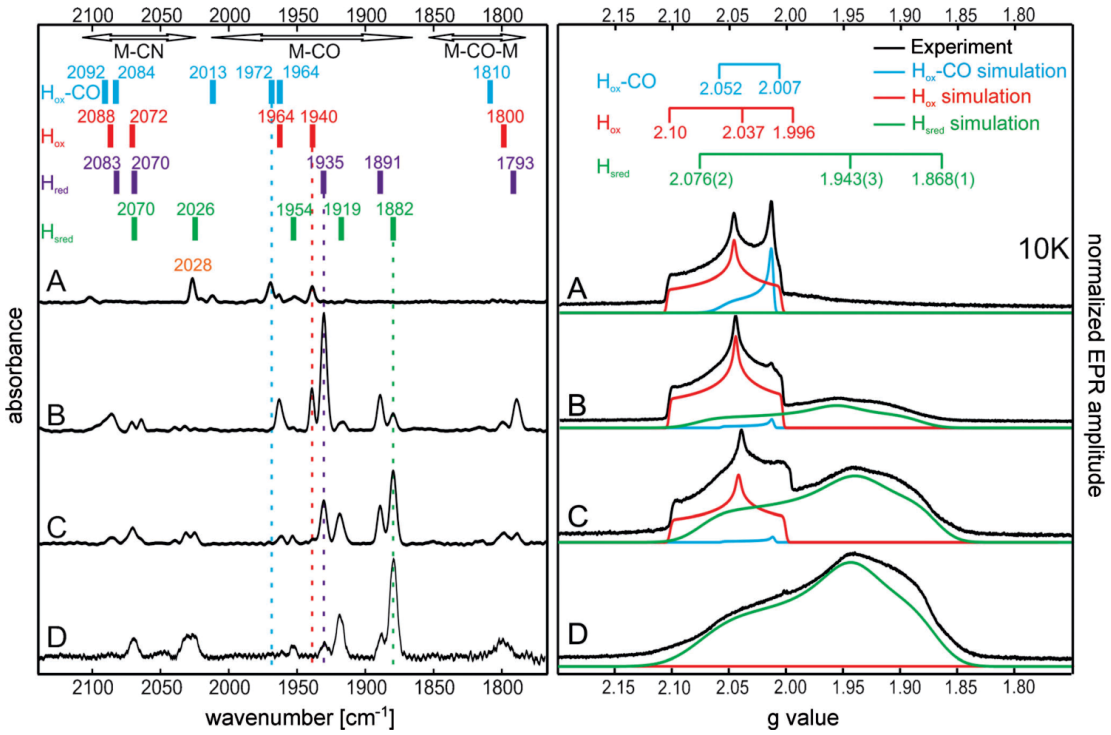


***Figure 2.*** Left: FTIR spectra normalized to 500 μM enzyme concentration and recorded at 100 K. Right: Normalized Q-band FID-detected EPR spectra measured at 10 K. Sample compositions: A) 700 μM *Cr*HydA1 and 1.5 mM thionine; B) 700 μM *Cr*HydA1; C) 700 μM *Cr*HydA1, 12 mM Na-dithionite; D) 280 μM *Cr*HydA1, flushed with 1 bar $H_2$. All samples initially contained 2 mM NaDT to avoid oxygen damage to the protein. Information about FTIR and EPR signal positions for each redox state is presented at the top of the figure. Further details of sample preparation are collected in the Supporting Information.

three states, $H_{ox}$, $H_{red}$, and in particular $H_{sred}$. Our experiments show that even samples that are predominantly in the $H_{sred}$ state could be completely oxidized with thionine. This shows that all redox states are in equilibrium with each other. Importantly, all samples, including those with high concentrations of $H_{sred}$, show a high hydrogenase activity (typically 560 nmol $H_2$ per minute and μg protein), suggesting that $H_{sred}$ is an active state.

To confirm the catalytic activity of the enzyme at the low potentials at which $H_{sred}$ is formed, protein film electrochemistry (PFE) was performed on *Cr*HydA1, which was adsorbed on a carbon rotating-disk electrode.[21] For comparison, the same electrochemical experiments were performed for *Dd*H and *Ca*HydA, which were covalently attached to the rotating-disk electrode (see the Experimental Section and the Supporting Information). The cyclic voltammograms of the three studied enzymes (Figure 3, top) show that $H^+$ reduction activity increases with negative potential. No inactivation processes are observed at very low potentials during the experiments. The persistence and stability of the observed catalytic currents was verified using chronoamperometry (Figure 3, lower part). In these experiments, the potential is kept constant initially at the reference potential of −209 mV at which anaerobic oxidation is not dominant and a steady $H_2$ oxidation current is observed. Subsequently, two negative potentials (−960 and −760 mV) were applied for one hour each. While the experiments on *Dd*H and *Ca*HydA showed persistent negative $H^+$ reduction catalytic currents at each potential step, the experiment on *Cr*HydA1 showed some current loss, which we assign to film loss owing to the noncovalent immobilization of the enzyme. As shown above, reductive treatment favors formation of the $H_{sred}$ state. If this would be a dead-end state, these conditions would allow accumulation of this state and we should see a substantial reduction of the catalytic current when applying more negative potentials. As this is clearly not the case, these experiments indicate that $H_{sred}$ is a part of the catalytic cycle.

$H_{sred}$ seems to be better stabilized in algal [FeFe] hydrogenases than for example in *Dd*H. It is tempting to infer that this must be related to the lack of accessory [4Fe-4S] clusters in these enzymes (the so-called "F-clusters"). It seems likely that the redox potential of the $H_{sred}/H_{red}$ transition is changing depending on the presence of the F-clusters owing to the so-called redox cooperativity effect commonly observed in systems with multiple redox centers.[22] In prokaryotic [FeFe] hydrogenases, $H_{sred}$ may only occur as transient species, as the cubane part is quickly reoxidized during the reaction cycle by the F-clusters, thus generating the $H_{red}$ state. Therefore, in these enzymes under turnover conditions the

  

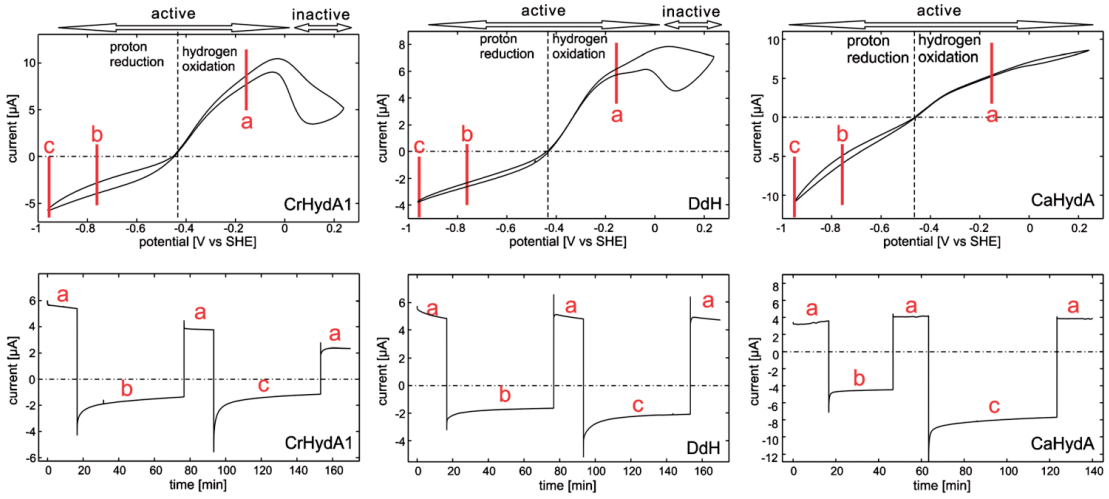


***Figure 3.*** From left to right: cyclic voltammetry (upper part) and chronoamperometric experiments (lower part) on *Cr*HydA1 adsorbed on and *Dd*H and *Ca*HydA covalently attached to a pyrolytic graphite edge (PGE) electrode. Perpendicular markings and letters on the cyclic voltammograms indicate the potentials used in the chronoamperometric measurements ($a = -209$ mV, $b = -759$ mV, $c = -959$ mV). The experiments were carried out at pH 7.0, 10°C, 1 bar $H_2$ and 2500 rpm electrode rotation rate.

low potential resting state is $H_{red}$, while in eukaryotic enzymes (lacking the F-clusters), $H_{sred}$ accumulates as the resting state.

We will now consider the possible role of the $H_{sred}$ state in the catalytic cycle. The H-cluster in *Cr*HydA1 has to perform a turnover involving two protons and two electrons in the absence of accessory [4Fe4S] clusters. The hydrogen oxidation cycle, which presumably starts with $H_{ox}$ (as "ready state") will result in an exit state where two electrons (reduction equivalents) are left on the H-cluster. As a stable $Fe^0Fe^I$ configuration has never been observed for the H-cluster, the most likely candidate for such "exit" state is $H_{sred}$. It is therefore not surprising that particularly large amounts of $H_{sred}$ are formed in HydA1 under $H_2$ without a redox partner (electron acceptor) being present in the buffer. $H_{sred}$ is, however, also formed under reductive conditions without $H_2$. Under these conditions, high turnover activities ($H_2$ production) are measured in vitro. Our PFE experiments also show high catalytic activity at negative potentials at which $H_{sred}$ is shown to be present. Thus, it seems very likely that the $H_{sred}$ state is a part of the catalytic cycle. Moreover, as the structure of the H-cluster is highly conserved in all [FeFe] hydrogenases and the same behavior at negative potentials was found for *Cr*HydA1, *Dd*H, and *Ca*HydA hydrogenases in our PFE experiments, it can be assumed that its catalytic mechanism also is conserved. We therefore propose that $H_{sred}$ is the starting point for proton reduction in the reaction cycle of all [FeFe] hydrogenases.

The implication of these considerations is reflected in Figure 4, which shows our proposed reaction cycle for *Cr*HydA1, including $H_{sred}$. Although certainly some speculation is involved, most of these intermediates were postulated earlier; in particular, the hydride form of $H_{sred}$ has already been discussed.[10] It is clear that a few questions are still left to be answered: We propose $H_{sred}$ to be the active species reacting with the bound proton to form the (terminal) hydride, which in turn reacts with the proton available at the ADT amine, ultimately producing molecular hydrogen. It is not clear at which stage this "hydride-to-be" proton is bound to the H-cluster. Interestingly, all DFT-calculated protonated or unprotonated variants of the $H_{sred}$ species are characterized by a reduced [4Fe4S] cluster.[23] According to these DFT calculations, only the second protonation (in the ADT bridge) triggers the electron transfer from the $[4Fe4S]_H$ cluster to the 2Fe subcluster and the formation of the hydride bound to the mixed-valence 2Fe core.[24,25] How the first proton is stabilized at the reduced states of the H-cluster ($H_{red}$ and/or $H_{sred}$) is still not clear. Experimental evidence for the existence of hydrides in $H_{sred}$ and/or $H_{red}$ as well as detailed QM calculations of the reaction mechanism including the role of the cubane subcluster might help to solve these open questions.

In conclusion, our combined electrochemical, FTIR, and EPR investigations on HydA1 identified the superreduced state $H_{sred}$ as paramagnetic and catalytically active. We therefore propose that $H_{sred}$ is involved in the reaction cycle of all [FeFe] hydrogenases, but it is stabilized as resting state only in algal enzymes owing to the lack of F-clusters, which immediately reoxidize $H_{sred}$ to $H_{red}$ in bacterial enzymes. The reaction cycles of prokaryotic and eukaryotic enzymes are identical but because of the presence or absence of F-clusters in the protein, different resting states of the active site are stabilized at low potential.

The involvement of $H_{sred}$ in the catalytic cycle is mechanistically attractive because it enables heterolytic splitting of $H_2$ bound to $H_{ox}$ without the need for any intermediate electron-transfer step.[10] Also it would explain why the cubane sub-cluster is an essential part of the active site of [FeFe] hydrogenases in contrast to [NiFe] hydrogenase, where such a redox-active "ligand" to the binuclear site is not required.

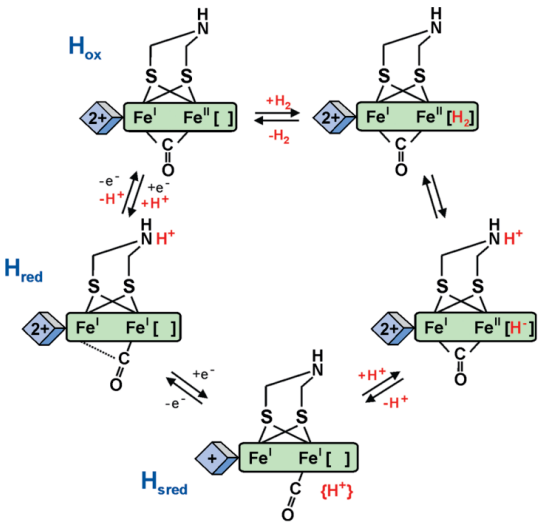


***Figure 4.*** Proposed catalytic cycle for [FeFe] hydrogenase including the $H_{sred}$ state. $\{H^+\}$ in $H_{sred}$ indicates that the proton is believed to be associated with the H-cluster and possibly bound to a nearby amino acid residue.

## *Experimental Section*

*Cr*HydA1 was obtained from *Clostridium acetobutylicum* (overexpressed) as reported previously.[26,27] All sample preparation steps, including treatment with thionine and exposure to $H_2$, were performed under strictly anaerobic conditions in a glovebox under a nitrogen atmosphere with 1.5–2% $H_2$. FTIR measurements were performed on a BRUKER IFS 66 v/s FTIR spectrometer equipped with a Bruker MCT (mercury cadmium telluride) detector. Q-band EPR spectra were recorded using free induction decay (FID)-detected EPR with a 1 μs microwave pulse. All pulse experiments were performed on a Bruker ELEXYS E580 Q-band spectrometer with a SuperQ-FT microwave bridge and home-built resonator described earlier.[28] Protein-film electrochemistry experiments were carried out inside an anaerobic glovebox (MBraun) using a gas-tight three-electrode setup connected to an electrode rotator (Princeton Applied Research model 636A). Electrochemical experiments were controlled by a VersaStat 4 potentiostat (Princeton Applied Research). Detailed experimental procedures are described in the Supporting Information.

Received: June 19, 2012
Revised: August 6, 2012
Published online: October 26, 2012

**Keywords:** biohydrogen · electron spin resonance · FTIR spectroscopy · hydrogenase · protein film electrochemistry

[1] W. Lubitz, E. Reijerse, M. van Gastel, *Chem. Rev.* **2007**, *107*, 4331–4365.
[2] P. M. Vignais, B. Billoud, *Chem. Rev.* **2007**, *107*, 4206–4272.
[3] R. Cammack, *Hydrogen as a Fuel* (Eds.: R. Cammack, M. Frey, R. Robson), Taylor & Francis, London, **2001**.
[4] S. T. Stripp, T. Happe, *Dalton Trans.* **2009**, 9960–9969.
[5] E. C. Hatchikian, N. Forget, V. M. Fernandez, R. Williams, R. Cammack, *Eur. J. Biochem.* **1992**, *209*, 357–365.
[6] B. J. Lemon, J. W. Peters, *Biochemistry* **1999**, *38*, 12969–12973.
[7] A. S. Pandey, T. V. Harris, L. J. Giles, J. W. Peters, R. K. Szilagyi, *J. Am. Chem. Soc.* **2008**, *130*, 4533–4540.
[8] Y. Nicolet, A. L. De Lacey, X. Vernede, V. M. Fernandez, E. C. Hatchikian, J. C. Fontecilla-Camps, *J. Am. Chem. Soc.* **2001**, *123*, 1596–1601.
[9] A. J. Pierik, M. Hulstein, W. R. Hagen, S. P. J. Albracht, *Eur. J. Biochem.* **1998**, *258*, 572–578.
[10] J. C. Fontecilla-Camps, A. Volbeda, C. Cavazza, Y. Nicolet, *Chem. Rev.* **2007**, *107*, 4273–4303.
[11] W. Roseboom, A. L. De Lacey, V. M. Fernandez, E. C. Hatchikian, S. P. J. Albracht, *J. Biol. Inorg. Chem.* **2006**, *11*, 102–118.
[12] A. Silakov, B. Wenk, E. Reijerse, W. Lubitz, *Phys. Chem. Chem. Phys.* **2009**, *11*, 6592–6599.
[13] P. E. Siegbahn, J. W. Tye, M. B. Hall, *Chem. Rev.* **2007**, *107*, 4414–4435.
[14] A. S. Pereira, P. Tavares, I. Moura, J. J. G. Moura, B. H. Huynh, *J. Am. Chem. Soc.* **2001**, *123*, 2771–2782.
[15] C. V. Popescu, E. Münck, *J. Am. Chem. Soc.* **1999**, *121*, 7877–7884.
[16] A. Silakov, C. Kamp, E. Reijerse, T. Happe, W. Lubitz, *Biochemistry* **2009**, *48*, 7780–7786.
[17] A. M. Terauchi, S. F. Lu, M. Zaffagnini, S. Tappa, M. Hirasawa, J. N. Tripathy, D. B. Knaff, P. J. Farmer, S. D. Lemaire, T. Hase, S. S. Merchant, *J. Biol. Chem.* **2009**, *284*, 25867–25878.
[18] C. J. Batie, H. Kamin, *J. Biol. Chem.* **1981**, *256*, 7756–7763.
[19] It should be noted that, in oxidized preparations additionally, an FTIR band at 2028 $cm^{-1}$ appears that cannot be assigned to any known state of the H-cluster. Assuming that this band originates from a CO stretch, its blue-shifted character would suggest that the corresponding ligand is associated with highly oxidized iron species. It could be a breakdown product of the H-cluster or, alternatively, an inactive form of the H-cluster as was observed in protein film electrochemistry at very high potentials.[17] Furthermore, it should be noted that owing to the sapphire inner windows of the Helium cryostat, the spectral response below 1850 $cm^{-1}$ is strongly attenuated and affected by instrumental artifacts. The position and intensity of the bridging CO signals (around 1800 $cm^{-1}$) is therefore less reliable than that of the other FTIR signals. In particular, the occurrence of a bridging CO signal in the strongly reduced samples and lack thereof in the strongly oxidized samples is attributed to these instrumental problems.
[20] B. Guigliarelli, P. Bertrand, *Adv. Inorg. Chem.* **1999**, *47*, 421–497.
[21] Covalent attachment of HydA1 did not lead to electrical contact between the electrode and the H-cluster.
[22] I. A. C. Pereira, A. V. Xavier in *Encyclopedia of Inorganic Chemistry* (Ed.: R. B. King), Wiley, New York, **2005**, pp. 3360–3376.
[23] L. Yu, C. Greco, M. Bruschi, U. Ryde, L. De Gioia, M. Reiheet, *Inorg. Chem.* **2011**, *50*, 3888–3900.
[24] M. Bruschi, C. Greco, M. Kaukonen, P. Fantucci, U. Ryde, L. De Gioia, *Angew. Chem.* **2009**, *121*, 3555–3558; *Angew. Chem. Int. Ed.* **2009**, *48*, 3503–3506.
[25] C. Greco, L. De Gioia, *Inorg. Chem.* **2011**, *50*, 6987–6995.
[26] S. Stripp, O. Sanganas, T. Happe, M. Haumann, *Biochemistry* **2009**, *48*, 5042–5049.
[27] G. von Abendroth, S. Stripp, A. Silakov, C. Croux, P. Soucaille, L. Girbal, T. Happe, *Int. J. Hydrogen Energy* **2008**, *33*, 6076–6081.
[28] E. Reijerse, F. Lendzian, R. Isaacson, W. Lubitz, *J. Magn. Reson.* **2012**, *214*, 237–243.

  

Angewandte Chemie
Eine Zeitschrift der Gesellschaft Deutscher Chemiker

Supporting Information



69451 Weinheim, Germany

# Identification and Characterization of the "Super-Reduced" State of the H-Cluster in [FeFe] Hydrogenase: A New Building Block for the Catalytic Cycle?**

*Agnieszka Adamska, Alexey Silakov,* Camilla Lambertz, Olaf Rüdiger, Thomas Happe, Edward Reijerse,* and Wolfgang Lubitz**

anie_201204800_sm_miscellaneous_information.pdf

**List of abbreviations:**

IR (InfraRed spectroscopy)

FTIR (Fourier Transform IR)

CW (Continues Wave)

FID (Free Induced Decay)

EPR (Electron Paramagnetic Resonance)

PCET (Proton-Coupled Electron Transfer)

PFE (Protein Film Electrochemistry)

*Cr*HydA1 ([FeFe] hydrogenase from *Clamydomonas reinhardtii*)

*Ca*HydA ([FeFe] hydrogenase from *Clostridium acetobutylicum*)

*Dd*H ([FeFe] hydrogenase from *Desulfovibrio desulfuricans*)

*Cp*I ([FeFe] hydrogenase from *Clostridium pasteurianum*)

Tris (tris(hydroxymethyl)aminomethane)

MES (2-(*N*-morpholino)ethanesulfonic acid)

HEPES (4-(2-hydroxyethyl)-1-piperazineethanesulfonic acid)

TAPS (3-[[1,3-dihydroxy-2-(hydroxymethyl)propan-2-yl]amino]propane-1-sulfonic acid)

CHES (*N*-Cyclohexyl-2-aminoethanesulfonic acid)

DETAILED EXPERIMENTAL PROCEDURES

**Enzyme preparations:**

*Cr*HydA1 was obtained from *Clostridium (C.) acetobutylicum* (overexpressed) as reported previously.[1,2] All sample preparation steps were performed under strictly anaerobic conditions in a glovebox under a nitrogen atmosphere with 1.5-2% $H_2$. HydA1, overexpressed in *C. acetobutylicum*, was isolated in a 100 mM TRIS buffer (pH 8.0) with additional 2mM Na-dithionite (to avoid oxygen damage to the protein) and concentrated (Amicon Ultracel 10 kDa, Millipore) to approximately 700µM or 280 µM (experiments were performed on two sets of samples).[3] Wild type *Cr*HydA1 was isolated in 50 mM MES buffer (pH 6.0) with additional 2mM Na-dithionite. For all samples a high specific activity (approx. 560 nmol $H_2$ per minute and µg protein) was determined by gas chromatography.[2]

For thionine treatment the protein solution was loaded on a dry layer of thionine. The ratio thionin:enzyme was ≈ 2:1. One sample was reduced by additional Na-dithionite (final concentration 12mM). Treatment with $H_2$ was performed in a glovebox by using a home built gas line and gas controller. Samples were flushed for 15 minutes under 1 bar of $H_2$. Each preparation was split into an FTIR and EPR sample that were immediately frozen in liquid nitrogen.

**FTIR and EPR spectroscopy.**

FTIR measurements were performed on a BRUKER IFS 66 v/s FTIR spectrometer equipped with a Bruker MCT (mercury cadmium telluride) detector. The spectrometer was controlled by Bruker Opus software on a Windows PC. FTIR measurements were performed at 100K using an Oxford OptistatCF continuous helium flow cryostat. The spectra were accumulated in the double-sided, forward-backward mode with 2000 or more scans and obtained with a resolution of 2 $cm^{-1}$. Data processing was facilitated by home-written routines in MATLAB programming environment.

Q-band EPR spectra were recorded using free induction decay (FID) detected EPR with a 1µs microwave pulse. All pulse experiments were performed on a Bruker ELEXYS E580 Q-band spectrometer with a SuperQ-FT microwave bridge and home build resonator described earlier.[4] Cryogenic temperatures (10-20K) were achieved using an Oxford CF935 Helium flow cryostat. For the interpretation of all EPR experimental data, a home written simulation program (based on the EasySpin package [5]) in MATLAB was used. Experiments were performed under non-saturating conditions with a shot repetition time of 1 ms.

**Protein Film Electrochemistry.**

Protein film electrochemistry experiments were carried out inside an anaerobic glovebox (MBraun) using a gas tight three electrode setup connected to an electrode rotator (Princeton Applied Research model 636A). Electrochemical experiments were controlled by a VersaStat 4 potentiostat (Princeton Applied Research). The cell was water jacketed to provide temperature control during the experiment. A saturated calomel electrode (SCE) was used as reference electrode, placed on a side-arm to keep it at room temperature, connected to the main cell compartment by a Luggin capillary. A Pt wire was used as counter electrode. A pyrolytic graphite edge disk electrode with the "edge plane" facing the solution (0.03 $cm^2$ area) was used as working electrode. Potentials in this paper are converted to standard hydrogen electrode (SHE) using the correction $E_{SHE} = E_{SCE} + 241$ mV at 298 K. The electrochemical cell contained a buffer mixture of MES, HEPES, TAPS, CHES and sodium acetate (15 mM each) and NaCl (0.1 M).

*Dd* (purified as reported previously [6]) and *C. acetobutylicum* (purified as reported previously[2]) hydrogenases were covalently attached to the electrode following previously described strategies [7,8] (see below).

It was not possible to measure a catalytic current for *Cr*HydA covalently attached to the PGE electrode using any of the described strategies. We suggest that since the *Cr*HydA1 hydrogenase has the active site close to the surface of the protein, the linkage with the electrode could compromise the integrity of the protein. Therefore, the results shown here are for adsorbed *Cr*HydA1 following the same protocol reported by Armstrong and co-workers.[9]

Hydrogenase modified electrodes were rinsed with buffer and placed in an enzyme-free buffer solution in the electrochemical cell. Experiments were carried out at 2500 rpm rotation rate to avoid mass transport limitations to the electrode.

**Protein covalent immobilization.**

Figure S1 shows the strategy followed to obtain direct electron transfer between the PGE electrode and *C. acetobutylicum* and *Dd* hydrogenases. A 4-aminophenyl monolayer was chosen for *Dd* hydrogenase immobilization, after observing negative charges on the surface of the protein surrounding the most exposed [4Fe-4S] cluster. Based on the results recently reported for the immobilization of *C. acetobutylicum* hydrogenase on self assembled monoyalers on gold [8] a 4-carboxyphenyl monolayer was used for *Ca*HydA hydrogenase immobilization on PGE electrodes.[10]

***Dd* hydrogenase covalent immobilization.** A PGE electrode was polished with abrasive paper and 1 μm α-alumina (Buehler), and then immersed in a 10 mM solution of 4-nitrobenzene diazonium tetrafluoroborate salt 96% (ABCR) in acetonitrile (Merck) for 5 minutes. Once rinsed with EtOH and $H_2O$, immobilized 4-nitrobenzene molecules were electrochemically reduced to 4-aminobenzene in $H_2SO_4$ 0.1 M by doing a cyclic voltammetry from 0.9 V to -0.75 V (vs SHE) at 0.2 V/s. Afterwards 4 μL of 50 μM DdH hydrogenase in 10 mM MES buffer (pH 6.52) were left on top of the electrode for 20 minutes to orientate the protein electrostatically. Then 2.3 μL N-hydroxysuccinimide (Sigma) and 2.5 μL N-(3-dimethylaminopropyl)-N'-ethylcarbodiimide hydrochloride (Sigma) 60 mM each were added and left to react and form the covalent bonds between enzyme and electrode, at 10°C for 1 hour 45 minutes.

***C. acetobutylicum* hydrogenase covalent immobilization.** 4-carboxyphenyl diazonium tetrafluoroborate salt was synthesised in the laboratory following a previously described protocol [111]. PGE electrodes were electrochemically modified by applying two cyclic voltametric runs at 0.2 V/s from 0.941 V to -359 V (vs SHE) on a 1 mM 4-carboxyphenyl diazonium tetrafluoroborate salt solution in acetonitrile with 0.2 M tetrabutylammonium tetrafluoroborate (Aldrich) as supporting electrolyte. Afterwards the electrode was modified inside the anaerobic glovebox with *C. acetobutylicum* hydrogenase as described before for *Dd.*

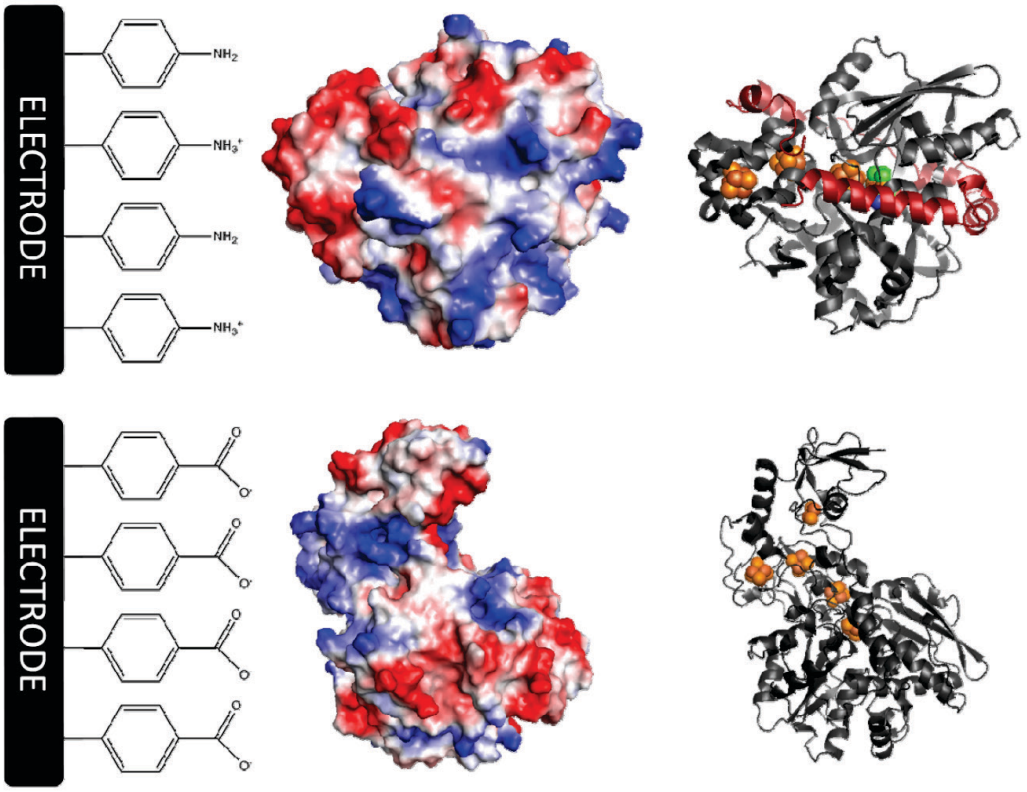


**Figure S1 Schematic representation of the *D. desulfuricans* (top, PDB code 1HFE) and *C. acetobutylicum* (bottom) hydrogenases orientation on a graphite electrode modified with 4-nitrobenzendiazonium salt and 4-carboxyphenyl diazonium salt respectively. In red negatively charged areas, in blue positively charged areas are shown The surface vacuum electrostatic charges map was generated using Pymol v 0.98. At the moment there is no crystal structure from CaHydA, the crystal structure from *Cp*I (PDB code 1FEH) was used as a model based on the sequence similarity between both proteins.[12]**

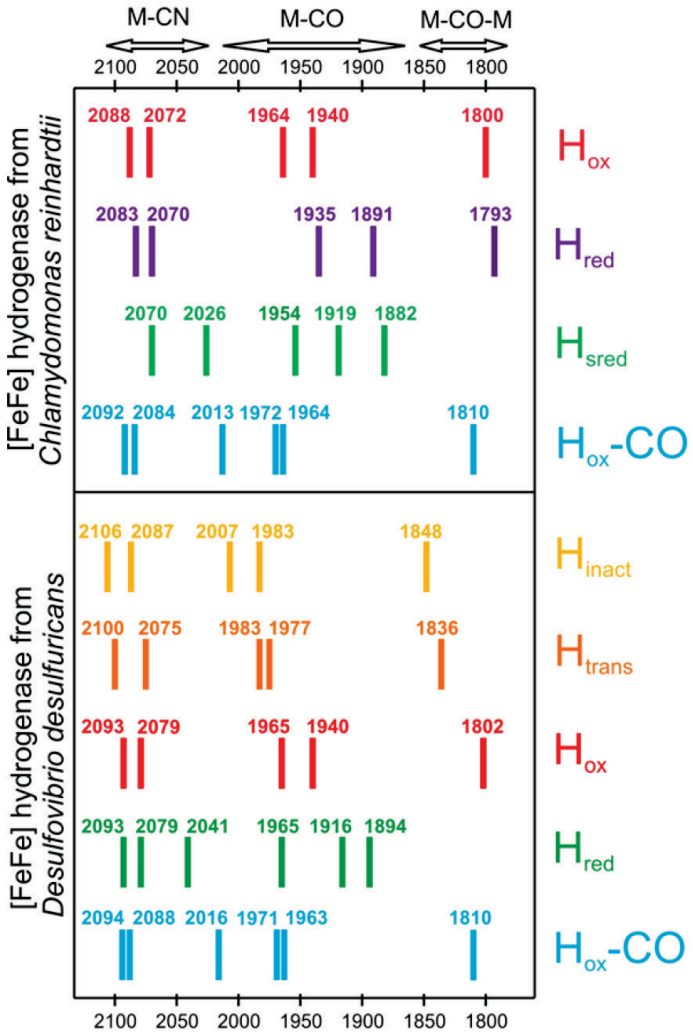


**Figure S2 Stretching vibrations [$cm^{-1}$] of the CO and CN ligands of the H-cluster for all known redox states of *Cr*HydA1 and DdH based on spectroelectrochemical measurements.**[13,14]

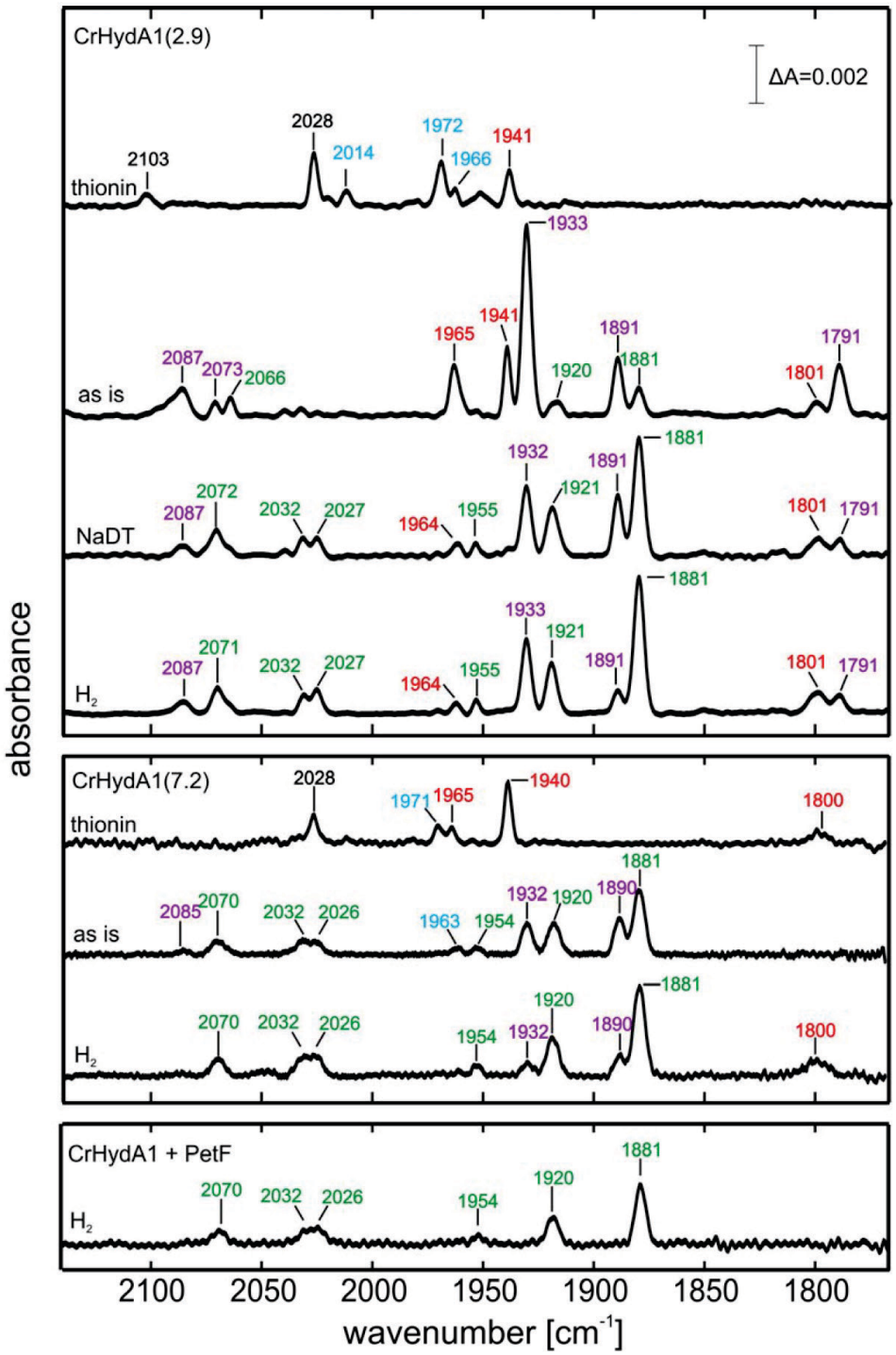


**Figure S3 Collected FTIR spectra for all samples with marked peak positions. HydA1(2.9) represents 700µM *Cr*HydA1 and 2mM Na-dithionite, i.e. a Na-dithionite/protein ratio of 2.9; HydA1(7.2) represents 280µM *Cr*HydA1 and 2mM Na-dithionite, i.e. a Na-dithionite/protein ratio of 7.2. CrHydA1 + PetF represents a sample containing 200µM CrHydA1, 200µM PetF and 2mM sodium dithionite. The additional thionine, Na-dithionite and $H_2$ sample treatments are described in detail in the enzyme preparation section. The colors of the numbers indicate the redox states from which each peak originates and correspond to the color code in figure S2. It should be noted that due to the sapphire inner windows of the cryostat the spectral range below 1850 $cm^{-1}$ is strongly attenuated and affected by instrumental artifacts. The position and intensity of the bridging CO band is therefore less reliable than the other FTIR signals.**

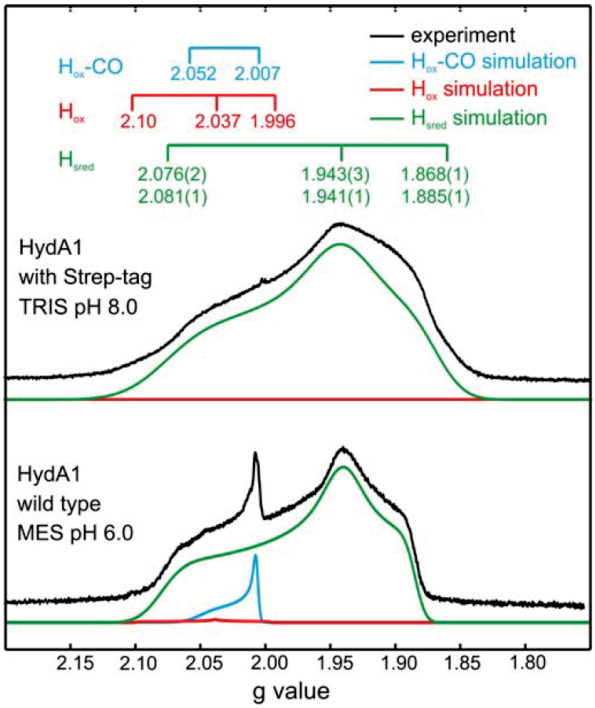


**Figure S4 Comparison of the super reduced state obtained for *Cr*HydA1 overexpressed in *C. acetobutylicum* and in wild type. Both samples were flushed with $H_2$ .**

Table S1: Collection of the obtained g values for $H_{sred}$ in *Cr*HydA1 compared to g parameters for related $[4Fe\text{-}4S]^+$ clusters: i.e. unmaturated *Cr*HydA1(ΔEFG) and $H_{trans}$* in *Dd*H and the C169S mutant of *Cr*HydA1.[15-17]

| hydrogenase preparation | Redox state | Measurement temperature | $g_1$ | $g_2$ | $g_3$ |
|---|---|---|---|---|---|
| CrHydA1 | $H_{sred}$ | 10K | 2.076 ±0.002 | 1.943 ±0.003 | 1.868 ±0.001 |
| Wild type CrHydA1 (figure S4) | $H_{sred}$ | 10K | 2.081 ±0.001 | 1.941 ±0.001 | 1.885 ±0.001 |
| CrHydA1(ΔEFG) [15] | $[4Fe\text{-}4S]^+$ | 10K | 2.050 | 1.915 | 1.852 |
| DdH [16] | $H_{trans}$ | 35K CW EPR | 2.06 | 1.96 | 1.89 |
| C169S mutant of CrHydA1 [17] | $H_{trans}$ | 10K | 2.067 | 1.941 | 1.880 |

* It is assumed that $H_{trans}$ has a $[4Fe\text{-}4S]^+$-[Fe(II)Fe(II)] configuration whereas the $H_{sred}$ state is assigned to $[4Fe\text{-}4S]^+$-[Fe(I)Fe(I)].

Reference List


[1] S. Stripp, O. Sanganas, T. Happe, M. Haumann, *Biochemistry* **2009,** *48* 5042-5049.

[2] G. von Abendroth, S. Stripp, A. Silakov, C. Croux, P. Soucaille, L. Girbal, T. Happe, *Intern. J. Hydrogen Energy* **2008,** *33* 6076-6081.

[3] M. M. Bradford, *Anal. Biochem.* **1976,** *72* 248-254.

[4] E. Reijerse, F. Lendzian, R. Isaacson, W. Lubitz, *J. Magn. Reson.* **2012,** *214* 237-243.

[5] S. Stoll, A. Schweiger, *J. Magn. Reson.* **2006,** *178* 42-55.

[6] A. Silakov, B. Wenk, E. Reijerse, S. P. Albracht, W. Lubitz, *J. Biol. Inorg. Chem.* **2009,** *14* 301-313.

[7] O. Rüdiger, J. M. Abad, E. C. Hatchikian, V. M. Fernandez, A. L. De Lacey, *J. Am. Chem. Soc.* **2005,** *127* 16008-16009.

[8] C. Madden, M. D. Vaughn, I. Diez-Perez, K. A. Brown, P. W. King, D. Gust, A. L. Moore, T. A. Moore, *J. Am. Chem. Soc.* **2012,** *134* 1577-1582.

[9] G. Goldet, C. Brandmayr, S. T. Stripp, T. Happe, C. Cavazza, J. C. Fontecilla-Camps, F. A. Armstrong, *J. Am. Chem. Soc.* **2009,** *131* 14979-14989.

[10] A. Adenier, E. Cabet-Deliry, A. Chausse, S. Griveau, F. Mercier, J. Pinson, C. Vautrin-Ul, *Chem. Mater.* **2005,** *17* 491-501.

[11] S. Baranton, D. Belanger, *J. Phys. Chem. B* **2005,** *109* 24401-24410.

[12] M. F. Gorwa, C. Croux, P. Soucaille, *J. Bacteriol.* **1996,** *178* 2668-2675.

[13] W. Roseboom, A. L. De Lacey, V. M. Fernandez, E. C. Hatchikian, S. P. J. Albracht, *J. Biol. Inorg. Chem.* **2006,** *11* 102-118.

[14] A. Silakov, C. Kamp, E. Reijerse, T. Happe, W. Lubitz, *Biochemistry* **2009,** *48* 7780-7786.

[15] I. Czech, A. Silakov, W. Lubitz, T. Happe, *Febs Lett.* **2010,** *584* 638-642.

[16] S. P. J. Albracht, W. Roseboom, E. C. Hatchikian, *J. Biol. Inorg. Chem.* **2006,** *11* 88-101.

[17] P. Knoerzer, A. Silakov, C. E. Foster, F. A. Armstrong, W. Lubitz, T. Happe, *J. Biol. Chem.* **2012,** *287* 1489-1499.

LETTER

doi:10.1038/nature12239

# Biomimetic assembly and activation of [FeFe]-hydrogenases

G. Berggren[1,2]†, A. Adamska[3]*, C. Lambertz[4]*, T. R. Simmons[1]*, J. Esselborn[4], M. Atta[1], S. Gambarelli[5], J.-M. Mouesca[5], E. Reijerse[3], W. Lubitz[3], T. Happe[4], V. Artero[1] & M. Fontecave[1,2]

**Hydrogenases are the most active molecular catalysts for hydrogen production and uptake[1,2], and could therefore facilitate the development of new types of fuel cell[3–5]. In [FeFe]-hydrogenases, catalysis takes place at a unique di-iron centre (the [2Fe] subsite), which contains a bridging dithiolate ligand, three CO ligands and two $CN^-$ ligands[6,7]. Through a complex multienzymatic biosynthetic process, this [2Fe] subsite is first assembled on a maturation enzyme, HydF, and then delivered to the apo-hydrogenase for activation[8]. Synthetic chemistry has been used to prepare remarkably similar mimics of that subsite[1], but it has failed to reproduce the natural enzymatic activities thus far. Here we show that three synthetic mimics (containing different bridging dithiolate ligands) can be loaded onto bacterial *Thermotoga maritima* HydF and then transferred to apo-HydA1, one of the hydrogenases of *Chlamydomonas reinhardtii* algae. Full activation of HydA1 was achieved only when using the HydF hybrid protein containing the mimic with an azadithiolate bridge, confirming the presence of this ligand in the active site of native [FeFe]-hydrogenases[9,10]. This is an example of controlled metalloenzyme activation using the combination of a specific protein scaffold and active-site synthetic analogues. This simple methodology provides both new mechanistic and structural insight into hydrogenase maturation and a unique tool for producing recombinant wild-type and variant [FeFe]-hydrogenases, with no requirement for the complete maturation machinery.**

Complexes **1**[11–13], **2**[14] and **3**[15] (Fig. 1a) represent the closest synthetic mimics of the [2Fe] subsite in HydA1. They all share the same primary coordination sphere with four CO, two $CN^-$ and a bridging dithiolate ligand. They do however differ in the nature of the central bridgehead atom of the dithiolate: carbon in **1**, nitrogen in **2** and oxygen in **3**. The nature of this atom in the enzyme [2Fe] subsite has been a matter of controversy[7,9,10,16]. Anaerobic reaction of HydF from *T. maritima* (expressed in *Escherichia coli*), containing a [4Fe-4S] cluster[17] and named 'HydF' in the following, with a tenfold molar excess of complex **1**, **2** or **3**, led to new hybrid species, **x**–HydF (**x** = **1**, **2** or **3** respectively), that could be isolated in pure form and characterized. Indeed, in all cases, iron quantification showed an increase from $3.9 \pm 0.4$ to $5.6 \pm 0.4$ iron atoms per protein, and the ultraviolet–visible spectrum of these hybrids displayed features consistent with a ~1:1 ratio of the synthetic complexes and the HydF protein (Supplementary Fig. 1a–c).

Fourier transform infrared (FTIR) spectroscopy is a convenient method for characterizing metalloproteins such as hydrogenases containing CO and $CN^-$ ligands[18]. Thus, further evidence for the incorporation of synthetic complexes in HydF was obtained from their FTIR spectra, which contained $CN^-$-stretching bands between 2,000 and 2,100 $cm^{-1}$ and four partly overlapping CO-stretching bands in the 1,800–2,000 $cm^{-1}$ range (Fig. 2b and Supplementary Table 1). The high-energy bands underwent a 40 $cm^{-1}$ shift on $^{13}C$-labelling of the $CN^-$ ligands (Supplementary Fig. 2). Interestingly, the width of the FTIR bands is still identical to those of the unbound complexes (Fig. 2a) but their positions show strong similarities to those of *Clostridium acetobutylicum* HydF (Fig. 2b and Supplementary Table 1), a HydF preparation isolated from a strain of *C. acetobutylicum* expressing the complete maturase machinery (including HydE and HydG)[19]. *Clostridium acetobutylicum* HydF contains, in addition to a [4Fe-4S] cluster, a still-undefined [2Fe] centre and is capable of activating the apo form of HydA1[19]. Although the width of the FTIR bands of the hybrids would suggest a ligand conformational freedom similar to that of the unbound complexes, the position of the FTIR bands is a clear indication that the synthetic complexes closely mimic the natural [2Fe] subsite in HydF.

The arrangements in which the synthetic complexes are bound to HydF and its [4Fe-4S] cluster are not evident from the FTIR spectra. In particular, FTIR spectroscopy does not allow terminal and bridging cyanide ligands to be definitively distinguished (see below and

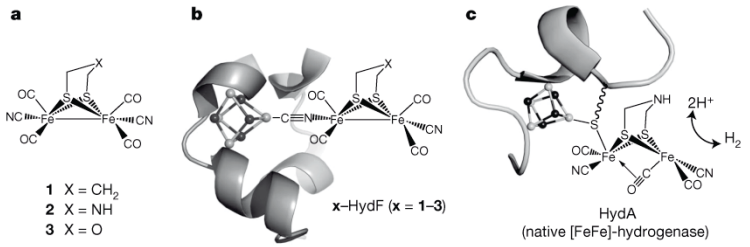


**Figure 1 | Structures of the di-iron clusters discussed in the study.** **a**, The synthetic mimics **1**[11–13], **2**[14] and **3**[15]. **b**, Proposed structure for the **x**–HydF (**x** = **1**–**3**) hybrid proteins. **c**, The H-cluster (active site) of [FeFe]-hydrogenase. The protein ribbon and the [4Fe-4S] clusters (shown as balls and sticks with Fe shown as white spheres) are shown only schematically.

[1]Laboratoire de Chimie et Biologie des Métaux (CEA/Université Grenoble 1/CNRS), 17 rue des Martyrs, F-38054 Grenoble Cedex 9, France. [2]Collège de France, 11 place Marcelin-Berthelot, F-75231 Paris Cedex 5, France. [3]Max-Planck-Institut für Chemische Energiekonversion, Stiftstrasse 34–36, 45470 Mülheim an der Ruhr, Germany. [4]Lehrstuhl Biochemie der Pflanzen, AG Photobiotechnologie, Ruhr Universität Bochum, Universitätsstrasse 150, 44801 Bochum, Germany. [5]Laboratoire de Chimie Inorganique et Biologique (CEA-INAC, Université Grenoble 1, UMR-E 3), 17 rue des Martyrs, F-38054 Grenoble Cedex 9, France. †Present address: Department of Biochemistry and Biophysics, Stockholm University, Svante Arrhenius väg 16, 106 91 Stockholm, Sweden.
*These authors contributed equally to this work.

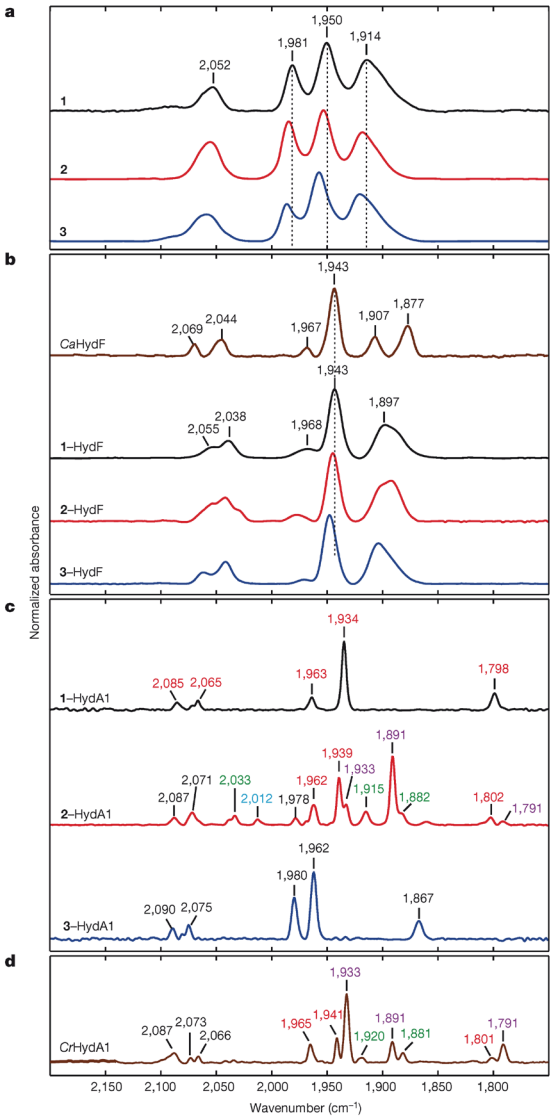


**Figure 2 | Normalized FTIR spectra recorded in liquid solution at 15 °C.** **a**, Complexes **1**–**3**. **b**, *Clostridium acetobutylicum* (*Ca*)HydF (from ref. 19) and **x**–HydF (**x** = **1**–**3**) hybrid species. **c**, HydA1 after treatment of apo-HydA1 with **1**–HydF (**1**–HydA1), **2**–HydF (**2**–HydA1) and **3**–HydF (**3**–HydA1). Peak positions in the spectrum of **2**–HydA1 are colour coded to indicate the contributions from $H_{ox}$ (red), $H_{red}$ (violet), $H_{sred}$ (green) and $H_{ox}$-CO (blue) (see Supplementary Fig. 6 for a complete data set). **d**, HydA1 from *C. reinhardtii* expressed in *C. acetobutylicum* (*Cr*HydA1) (ref. 18). Colour code as in **c**. Samples of complexes **1**–**3** and **x**–HydF (**x** = **1**–**3**) were prepared in HEPES buffer (20 mM, 100 mM KCl) pH 7.5. Samples of **x**–HydA1 were prepared in 10 mM Tris-HCl buffer pH 8 containing sodium dithionite (2 mM).

Supplementary Discussion)[20]. Electron paramagnetic resonance (EPR) and two-dimensional hyperfine sub-level correlation (HYSCORE) spectroscopies are more powerful in this respect. They demonstrate a close interaction between the cluster and the synthetic complex, as revealed for the case of **1**–HydF. First, the EPR spectrum of the spin-half ($S = 1/2$) $[4Fe\text{-}4S]^{1+}$ cluster in dithionite-reduced **1**–HydF was markedly different from that of the reduced cluster in unloaded HydF, with the high-field feature at $g = 1.90$ ($g$ is the Landé factor) in HydF shifted to $g = 1.93$ in **1**–HydF (Fig. 3a). A comparable shift was observed in the case of hybrids **2**–HydF and **3**–HydF (Supplementary Fig. 3). The absence of additional signals indicated that, in all cases, the synthetic complex remained in the EPR-silent Fe(I)Fe(I) state (both iron centres are in a low-spin $S = 1/2$ configuration but are antiferromagnetically coupled, leading to a diamagnetic $S = 0$ ground state).

Second, pulsed EPR spectroscopy unambiguously demonstrated that the [4Fe-4S] cluster and the [2Fe] subsite analogue shared a $CN^-$ ligand in **1**–HydF. For this purpose we used a nuclear coherence-transfer experiment, CF-NF[21], correlating the combination frequencies (CF) with the nuclear frequencies (NF), which is more sensitive than HYSCORE spectroscopy for disordered systems and best adapted for the observation of $^{13}C$ signals in the presence of weakly coupled $^{14}N$ atoms. This is the first time to our knowledge that a metalloprotein has been characterized in such an experiment. The CF-NF spectrum of **1**–HydF (Fig. 3b, right) displayed peaks from distant $^{13}C$ carbon atoms present in natural abundance. When **1** was prepared with $^{13}C$-labelled $CN^-$, the spectrum of **1**–HydF displayed a new feature reflecting coupling of the unpaired electron in the [4Fe-4S] cluster with the $^{13}C$ nucleus, characterized by a hyperfine coupling constant of $4.0 \pm 0.2$ MHz (Fig. 3b, left). As shown in Supplementary Fig. 4, the HYSCORE spectrum of reduced **1**–HydF displayed an additional feature consistent with the presence of a nitrogen atom weakly coupled to the [4Fe-4S] cluster in **1**–HydF. The hyperfine coupling constant ($a_N \leq 1$ MHz) is significantly smaller than those generally obtained when a N atom is directly coordinated to an Fe-S cluster[17,22,23] ($a_N$ in the range of 4–7 MHz).

These coupling constants are consistent with a $CN^-$ ligand bridging one iron of the [4Fe-4S] cluster and one iron of **1**, as established by density functional theory (DFT) calculations (a detailed description of the DFT calculations is provided as Supplementary Discussion and in Supplementary Tables 2–5). More precisely, computed hyperfine coupling constants indicate that the cyanide C atom is bound to one iron atom belonging to a mixed-valence ($Fe^{2.5+}$) iron of the [4Fe-4S] cluster and that the N atom is bound to the di-iron complex, implying cyanide linkage isomerism on formation of **1**–HydF, as found in the synthesis of Prussian blue analogues[24] and other molecular metal clusters[20,25]. Furthermore, DFT calculated values of CO and CN stretching frequencies (2,010 and 2,060 $cm^{-1}$) of a **1**–HydF model, containing a CN ligand bridging the [4Fe-4S] cluster and complex **1**, are well in the range of the experimental values (2,038 and 2,055 $cm^{-1}$; see Supplementary Discussion and Supplementary Table 6).

The hybrid **x**–HydF proteins were studied for their potential to activate apo-HydA1 from *C. reinhardtii* containing a single [4Fe-4S] cluster and no [2Fe] subsite[26]. A pure preparation of apo-HydA1 was incubated anaerobically with 10 equiv. of the hybrid protein, the optimal excess ratio (Supplementary Fig. 5), in phosphate buffer pH 6.8 at 37 °C for 30 min, and hydrogen evolution was monitored under standard conditions (Methods)[26]. No $H_2$ evolution could be detected using HydF, **1**–HydF or **3**–HydF (Fig. 4). In contrast, vigorous $H_2$ evolution was observed using **2**–HydF, corresponding to a specific activity of 700–800 μmol $H_2$ per min per mg HydA1, comparable to the activity values reported for wild-type HydA1[27], thus indicating complete maturation/activation of HydA1 by **2**–HydF[28] (Fig. 4 and Supplementary Fig. 5). Furthermore, activation by **2**–HydF was more efficient than by *C. acetobutylicum* HydF (specific activity, 350–400), assayed under the same conditions (Fig. 4). Indeed, *C. acetobutylicum* HydF provided full activation only when present in larger excess[19]. **2**–HydF by itself did not show any hydrogenase activity. Finally, apo-HydA1 was treated with a fourfold excess of **x**–HydF (**x** = **1**, **2** or **3**), under reducing conditions, then separated from HydF by affinity chromatography and analysed by FTIR spectroscopy. In all cases, the

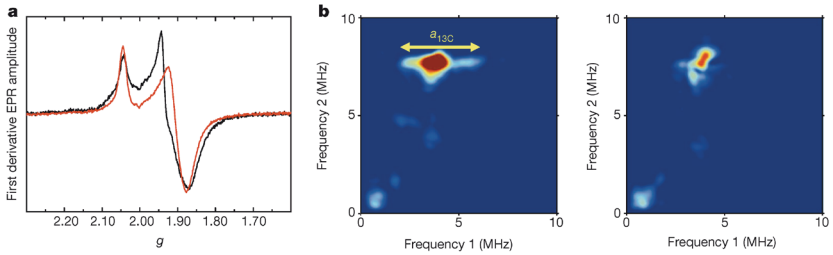


**Figure 3 | Continuous wave and pulsed EPR spectra of 1–HydF. a**, X-band EPR spectra recorded at 10 K for dithionite-reduced **1**–HydF (red line) and HydF (black line) in 50 mM Tris-HCl buffer, 150 mM NaCl, 5 mM sodium dithionite, pH 8. Microwave power, 100 μW; modulation amplitude, 1 mT; microwave frequency, 9.39 GHz. The shoulder observed at $g = 1.90$ in the **1**–HydF spectrum, corresponding to a few per cent of the total signal intensity, is assigned to a small fraction of HydF lacking **1**. **b**, X-band two-dimensional pulsed electron spin echo envelope modulation (ESEEM) spectroscopy (CF-NF) of **1**–HydF labelled with $^{13}CN^-$ (left) and unlabelled **1**–HydF (right). The horizontal ridge seen at a frequency $\nu_2$ of 7.7 MHz along the frequency 2 axis ($\nu_2$ being equal to $2\nu_{13C}$ with $\nu_{13C}$ the Zeeman frequency of a $^{13}C$ nuclear spin) is attributed to a hyperfine interaction ($a_{13C}$) between a $^{13}C$ nucleus and the paramagnetic [4Fe-4S] cluster. Its extension ($\Delta\nu_1$) along the frequency 1 axis yields the magnitude of the coupling ($\Delta\nu_1 = 4.0$ MHz $= a_{13C}$). This feature is absent from the unlabelled **1**–HydF spectrum.

presence of characteristic narrow Fe–CO and Fe–CN bands demonstrated that the synthetic complex had been transferred from HydF to HydA1 (Fig. 2c and Supplementary Fig. 6). The FTIR spectrum of HydA1 after treatment with **2**–HydF shows a strong correspondence to that of fully active wild-type HydA1 (Fig. 2d)[18]. Specifically, both species exist as a mixture of oxidized ($H_{ox}$), reduced ($H_{red}$) and super-reduced ($H_{sred}$) redox states of the H-cluster (the H-cluster is the complete active site of HydA shown in Fig. 1c) that all participate in the catalytic cycle[18]. Furthermore, after flushing with CO, a complete conversion to $H_{ox}$–CO occurred (Supplementary Fig. 7).

These data demonstrate that **2** is efficiently transferred from HydF to apo-HydA1, where it acquires the structure of the natural active [2Fe] subsite. This implies isomerization of one $CN^-$ ligand, replacement of one CO by a cysteinate ligand of the proximal [4Fe-4S] cluster in HydA1 and conformational rearrangement to adopt the inverted square pyramid structure required for opening a substrate binding site on the distal iron atom of the [2Fe] subsite (Fig. 1)[29]. We note that **1**–HydA1 and **3**–HydA1 both show 'H-cluster-like' FTIR signatures. In fact, the FTIR spectrum of **1**–HydA1 has strong similarities with the $H_{ox}$-state (Fig. 2c and Supplementary Fig. 6) whereas the FTIR spectrum of **3**–HydA1 does not resemble that of any known H-cluster redox state, but seems to indicate a pure redox state and even shows a band assigned to a bridging CO.

Besides unequivocally demonstrating that nitrogen is the bridgehead atom in the dithiolate ligand of the H-cluster, these results shed light on a number of important questions regarding hydrogenase maturation. They strongly support the hypothesis that HydF transiently binds a di-iron precursor of the active [2Fe] subsite of HydA1 and suggest stabilization through interactions with the [4Fe-4S] cluster. The structure of this natural precursor is likely to be very close to that of **2**. Further investigation of HydA1 maturation by the hybrid system, combining site-directed mutagenesis experiments and synthetic manipulation of the [2Fe] subsite (for example, isotopic labelling as shown here with $^{13}CN$), will probably provide additional insight into the transfer mechanism and the structure of both HydF and HydA1 binding sites. These data also demonstrate the unique properties of the HydA1 protein binding pocket in converting the otherwise inactive complex **2** into an active catalyst. More importantly, this novel artificial hybrid maturase system provides a unique, simple and straightforward biotechnological tool for producing active recombinant hydrogenases, with no requirement for coexpression with the still incompletely characterized complex biosynthetic machinery.

Because this procedure has been shown to work with proteins (HydF from *T. maritima* and HydA1 from *C. reinhardtii*) from two completely different organisms, it is very likely that [FeFe]-hydrogenases from other microorganisms, overexpressed in their apo form in *E. coli* (which lacks the maturation machinery), could also be activated through simple reaction with **2**–HydF. This reaction could thus be used for exploring a large variety of [FeFe]-hydrogenases—for example, from different species or derived from directed mutagenesis—with the aim of finding the most active and stable enzymes for exploitation in biotechnological processes of $H_2$ production[30] as well as in bioelectrodes in (photo)electrolysers or fuel cells[3–5].

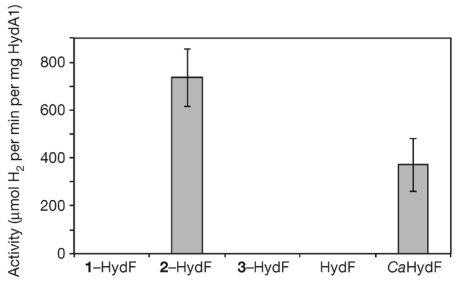


**Figure 4 | Specific hydrogenase activity of reconstituted HydA1.** Activity of HydA1 (μmol $H_2$ per min per mg HydA1) was measured in the presence of methyl viologen (10 mM) and sodium dithionite (100 mM) after *in vitro* maturation of apo-HydA1 for 30 min at 37 °C with 10 equiv. of **x**–HydF (**x** = **1**–**3**), HydF or *C. acetobutylicum* (*Ca*)HydF. The value for the last was obtained after a 60-min reaction and was taken from ref. 23. Data show mean ± s.d.

## METHODS SUMMARY

Recombinant *T. maritima* HydF protein was isolated, and its [4Fe-4S] cluster introduced using enzymatic reconstitution, as previously described[17]. The synthetic complexes **1**[11–13], **2**[14] and **3**[15] were prepared as previously described with slight modifications of the purification procedures described in the Supplementary Information. Hybrid proteins (**1**–HydF, **2**–HydF and **3**–HydF) were prepared under strictly anaerobic conditions in a glove-box. In a standard experiment, 150 μM HydF in 50 mM Tris-HCl, 150 mM NaCl, buffer pH 8 was incubated with a tenfold molar excess of the complex (**1**, **2** or **3**) for 30 min. The protein was then desalted on a NAP-25 cartridge (GE Healthcare) and concentrated with Amicon Ultra centrifugal filters 10K (Millipore). The protein was stored in liquid nitrogen.

*In vitro* maturation of apo-HydA1 from *C. reinhardtii* overexpressed in *E. coli* by the HydF hybrids was assayed as previously described[19]. Apo-HydA1 was incubated in 0.1 M potassium phosphate buffer pH 6.8, 2 mM sodium dithionite with an excess of the respective **x**–HydF hybrid protein for 30 min at 37 °C in a total volume of 400 μl. The specific hydrogenase activity was determined as described[19] by transferring the maturation solution to a 1.6 ml reaction mixture containing 100 mM sodium dithionite and 10 mM methyl viologen in the same buffer. For

FTIR measurements, apo-HydA1 and 4 equiv. **x**–HydF were incubated in 10 mM Tris-HCl pH 8.0, 2 mM sodium dithionite for 1 h at 37 °C and HydA1 was purified through a strep tag affinity column.

**Full Methods** and any associated references are available in the online version of the paper.

**Received 20 January; accepted 29 April 2013.**
**Published online 26 June 2013.**

1. Tard, C. & Pickett, C. J. Structural and functional analogues of the active sites of the [Fe]-, [NiFe]-, and [FeFe]-hydrogenases. *Chem. Rev.* **109,** 2245–2274 (2009).
2. Cracknell, J. A., Vincent, K. A. & Armstrong, F. A. Enzymes as working or inspirational electrocatalysts for fuel cells and electrolysis. *Chem. Rev.* **108,** 2439–2461 (2008).
3. Hambourger, M. *et al.* [FeFe]-hydrogenase-catalyzed $H_2$ production in a photoelectrochemical biofuel cell. *J. Am. Chem. Soc.* **130,** 2015–2022 (2008).
4. Krishnan, S. & Armstrong, F. A. Order-of-magnitude enhancement of an enzymatic hydrogen-air fuel cell based on pyrenyl carbon nanostructures. *Chem. Sci.* **3,** 1015–1023 (2012).
5. Ciaccafava, A. *et al.* An innovative powerful and mediatorless $H_2/O_2$ biofuel cell based on an outstanding bioanode. *Electrochem. Commun.* **23,** 25–28 (2012).
6. Peters, J. W., Lanzilotta, W. N., Lemon, B. J. & Seefeldt, L. C. X-ray crystal structure of the Fe-only hydrogenase (CpI) from *Clostridium pasteurianum* to 1.8 angstrom resolution. *Science* **282,** 1853–1858 (1998).
7. Nicolet, Y., Piras, C., Legrand, P., Hatchikian, C. E. & Fontecilla-Camps, J. C. *Desulfovibrio desulfuricans* iron hydrogenase: the structure shows unusual coordination to an active site Fe binuclear center. *Structure* **7,** 13–23 (1999).
8. Mulder, D. W. *et al.* Stepwise [FeFe]-hydrogenase H-cluster assembly revealed in the structure of $HydA^{\Delta EFG}$. *Nature* **465,** 248–251 (2010).
9. Nicolet, Y. *et al.* Crystallographic and FTIR spectroscopic evidence of changes in Fe coordination upon reduction of the active site of the Fe-only hydrogenase from *Desulfovibrio desulfuricans*. *J. Am. Chem. Soc.* **123,** 1596–1601 (2001).
10. Silakov, A., Wenk, B., Reijerse, E. & Lubitz, W. $^{14}N$ HYSCORE investigation of the H-cluster of [FeFe] hydrogenase: evidence for a nitrogen in the dithiol bridge. *Phys. Chem. Chem. Phys.* **11,** 6592–6599 (2009).
11. Le Cloirec, A. *et al.* A di-iron dithiolate possessing structural elements of the carbonyl/cyanide sub-site of the H-centre of Fe-only hydrogenase. *Chem. Commun.* 2285–2286 (1999).
12. Lyon, E. J., Georgakaki, I. P., Reibenspies, J. H. & Darensbourg, M. Y. Carbon monoxide and cyanide ligands in a classical organometallic complex model for Fe-only hydrogenase. *Angew. Chem. Int. Edn Engl.* **38,** 3178–3180 (1999).
13. Schmidt, M., Contakes, S. M. & Rauchfuss, T. B. First generation analogues of the binuclear site in the Fe-only hydrogenases: $[Fe_2(\mu\text{-}SR)_2(CO)_4(CN)_2]^{2-}$. *J. Am. Chem. Soc.* **121,** 9736–9737 (1999).
14. Li, H. X. & Rauchfuss, T. B. Iron carbonyl sulfides, formaldehyde, and amines condense to give the proposed azadithiolate cofactor of the Fe-only hydrogenases. *J. Am. Chem. Soc.* **124,** 726–727 (2002).
15. Song, L. C., Yang, Z. Y., Bian, H. Z. & Hu, Q. M. Novel single and double diiron oxadithiolates as models for the active site of [Fe]-only hydrogenases. *Organometallics* **23,** 3082–3084 (2004).
16. Pandey, A. S., Harris, T. V., Giles, L. J., Peters, J. W. & Szilagyi, R. K. Dithiomethylether as a ligand in the hydrogenase H-cluster. *J. Am. Chem. Soc.* **130,** 4533–4540 (2008).
17. Brazzolotto, X. *et al.* The [Fe-Fe]-hydrogenase maturation protein HydF from *Thermotoga maritima* is a GTPase with an iron-sulfur cluster. *J. Biol. Chem.* **281,** 769–774 (2006).
18. Adamska, A. *et al.* Identification and characterization of the "super-reduced" state of the H-cluster in [FeFe] hydrogenase: a new building block for the catalytic cycle? *Angew. Chem. Int. Ed.* **51,** 11458–11462 (2012).
19. Czech, I., Silakov, A., Lubitz, W. & Happe, T. The [FeFe]-hydrogenase maturase HydF from *Clostridium acetobutylicum* contains a CO and $CN^-$ ligated iron cofactor. *FEBS Lett.* **584,** 638–642 (2010).
20. Geiss, A. & Vahrenkamp, H. M. (μ-CN)Fe(μ-CN)M′ chains with phthalocyanine iron centers: preparation, structures, and isomerization. *Inorg. Chem.* **39,** 4029–4036 (2000).
21. Hubrich, M., Jeschke, G. & Schweiger, A. The generalized hyperfine sublevel coherence transfer experiment in one and two dimensions. *J. Chem. Phys.* **104,** 2172–2184 (1996).
22. Gambarelli, S., Luttringer, F., Padovani, D., Mulliez, E. & Fontecave, M. Activation of the anaerobic ribonucleotide reductase by S-adenosylmethionine. *ChemBioChem* **6,** 1960–1962 (2005).
23. Chen, D. W., Walsby, C., Hoffman, B. M. & Frey, P. A. Coordination and mechanism of reversible cleavage of S-adenosylmethionine by the [4Fe-4S] center in lysine 2,3-aminomutase. *J. Am. Chem. Soc.* **125,** 11788–11789 (2003).
24. Coronado, E. *et al.* Pressure-tuning of magnetism and linkage isomerism in iron(II) hexacyanochromate. *J. Am. Chem. Soc.* **127,** 4580–4581 (2005).
25. Shatruk, M. *et al.* Properties of Prussian blue materials manifested in molecular complexes: observation of cyanide linkage isomerism and spin-crossover behavior in pentanuclear cyanide clusters. *J. Am. Chem. Soc.* **129,** 6104–6116 (2007).
26. Happe, T. & Naber, J. D. Isolation, characterization and N-terminal amino-acid-sequence of hydrogenase from the green-alga *Chlamydomonas reinhardtii*. *Eur. J. Biochem.* **214,** 475–481 (1993).
27. Kamp, C. *et al.* Isolation and first EPR characterization of the [FeFe]-hydrogenases from green algae. *Biochim. Biophys. Acta Bioenerg.* **1777,** 410–416 (2008).
28. Sybirna, K. *et al. Shewanella oneidensis*: a new and efficient system for expression and maturation of heterologous [Fe-Fe] hydrogenase from *Chlamydomonas reinhardtii*. *BMC Biotechnol.* **8,** 73–81 (2008).
29. Darensbourg, M. Y., Lyon, E. J., Zhao, X. & Georgakaki, I. P. The organometallic active site of [Fe] hydrogenase: models and entatic states. *Proc. Natl Acad. Sci. USA* **100,** 3683–3688 (2003).
30. Mertens, R. & Liese, A. Biotechnological applications of hydrogenases. *Curr. Opin. Biotechnol.* **15,** 343–348 (2004).

**Supplementary Information** is available in the online version of the paper.

**Acknowledgements** G.B. acknowledges support from the Bengt Lundqvist Minnesfond, FORMAS (contract number 213-2010-563) and the Swedish Royal Academy of Sciences. This work was supported by the French National Research Agency (ANR) through grant 07-BLAN-0298-01 and the Labex programme (ARCANE, 11-LABX-003). V.A. acknowledges support from the European Research Council under the European Union's Seventh Framework Programme (FP/2007-2013/ERC Grant Agreement no. 306398). T.H. was supported by the Deutsche Forschungsgemeinschaft (HA 255/2-1), the BMBF (Bio-H2) and the Volkswagen foundation (LigH2t). A.A., E.R. and W.L. thank the Max Planck Society for financial support, and A. Silakov for providing the FTIR processing software.

**Author Contributions** G.B., V.A., M.A., W.L., T.H. and M.F. designed the research; G.B. and T.R.S. prepared and characterized synthetic complexes and hybrid species; C.L., J.E. and G.B. contributed to maturation experiments and $H_2$ evolution measurements; A.A. and C.L. performed FTIR measurements; G.B. and S.G. performed EPR measurements; J.-M.M. did DFT calculations; and M.F., G.B, E.R. and V.A. wrote the paper.

**Author Information** Reprints and permissions information is available at www.nature.com/reprints. The authors declare no competing financial interests. Readers are welcome to comment on the online version of the paper. Correspondence and requests for materials should be addressed to M.F. (marc.fontecave@cea.fr).

## METHODS

All chemicals were purchased from Sigma-Aldrich and used as received unless otherwise stated. NMR was recorded on a Bruker AC300 using the residual solvent peak as internal standard. Complex $(Et_4N)_2[Fe_2(adt)(CO)_4(CN)_2]$ (**2**, $adt^{2-}$ = 2-azapropanedithiolate)[14] was synthesized following literature procedure, and $(Et_4N)_2[Fe_2(pdt)(CO)_4(CN)_2]$ (**1**, $pdt^{2-}$ = propanedithiolate)[11], $(Et_4N)_2[Fe_2(pdt)(CO)_4(^{13}CN)_2]$[31] and $(Et_4N)_2[Fe_2(odt)(CO)_4(CN)_2]$ (**3**, $odt^{2-}$ = 2-oxopropanedithiolate)[15] were prepared by modified literature procedures (see Supplementary Information) and their thin-film solution FTIR spectra were recorded on a Perkin Elmer Spectrum-100 spectrometer. *Tm*HydF (referred to as HydF throughout the text) was overexpressed, purified and its [4Fe-4S] cluster reconstituted as previously described[17]. Apo-*Cr*HydA1 (referred to as apo-HydA1 throughout the text) was overexpressed in *E. coli* BL21 DE3 ΔiscR using growth conditions and a pET plasmid as previously published for the production of active HydA1 in *E. coli*[32].

Protein purity was assessed by gel electrophoresis by loading samples on Any kD Mini-Protean TGX precast gels (Biorad) alongside Precision Plus Protein standards (Biorad). Migration was achieved on a Mini-Protean apparatus (Biorad) at 200 V for 30 min. Protein concentrations were determined with the Biorad Protein Assay, using bovine serum albumin as a standard as well as by optical absorption measurements. Aerobic ultraviolet–visible absorption spectra were recorded on a Cary 1Bio spectrophotometer (Varian) and anaerobic measurements were made with a fibre-optic-fitted UvikonXL spectrophotometer (BioTek Instruments). Iron and sulphur quantification were performed following the methods of refs 33 and 34, respectively. The specific hydrogenase activity was determined as described previously[35].

**Spectroscopic characterization.** FTIR spectra of protein samples were recorded on a Bruker IFS 66 v/s FTIR spectrometer equipped with a Bruker MCT (mercury cadmium telluride) detector. The spectrometer was controlled by Bruker Opus software. All measurements were performed at 15 °C with a resolution of 2 $cm^{-1}$. The spectra were accumulated in the double-sided, forward-backward mode with 1,000 scans. Data were processed using custom-written routines in the MATLAB programming environment. FTIR samples of complexes **1**–**3** and **x**–HydF (**x** = **1**–**3**) were prepared in HEPES buffer (20 mM, 100 mM KCl) pH 7.5. FTIR samples of **x**–HydA1 were prepared in 10 mM Tris-HCl buffer pH 8.0 containing sodium dithionite (10 mM). For the FTIR measurement of maturated HydA1, apo-HydA1 was washed twice with 10 mM Tris-HCl pH 8.0, 2 mM sodium dithionite (a buffer referred to below as TPW2) by concentration and dilution to remove any trace of desthiobiotin originating from the prior purification of apo-HydA1 by strep-tag affinity chromatography. 100 µl of TPW2 buffer containing 100 µM apo-HydA1 and a fourfold molar excess of the hybrid protein (**1**–HydF, **2**–HydF or **3**–HydF, respectively) was incubated for 60 min at 37 °C. Afterwards, 500 µl of TPW2 buffer was added, and the solution was loaded on a 750 µl Strep-Tactin Superflow (IBA) column. The HydA1 protein was separated from **1**–HydF (**1**–HydA1), **2**–HydF (**2**-HydA1) or **3**–HydF (**3**-HydA1) by affinity chromatography using 10 mM Tris-HCl pH 8.0, 2 mM sodium dithionite, 200 mM NaCl as washing buffer and TPW2 buffer, 2.5 mM desthiobiotin for elution. The isolated protein was concentrated using Amicon Ultra centrifugal filters 10K (Millipore) and stored as described previously[36]. For the FTIR spectra shown in Supplementary Fig. 7, the preparation was done as described above with **2**–HydF but without the final purification step.

X-band EPR spectra were recorded on a Bruker ESP 300D spectrometer equipped with an Oxford Instruments ESR 900 flow cryostat. Protein samples were anaerobically reduced with 10 molar equivalents of sodium dithionite before freezing. Hyperfine sublevel correlation (HYSCORE) spectra and their Combination Frequency (CF) – Nuclear Frequency (NF) variants were recorded on a Bruker Elexsys E-580 X band (frequency, 9.71 GHz) pulsed spectrometer with a Bruker ER4118X dielectric resonator and continuous-flow He cryostat (Oxford Instruments CF935) controlled by an Oxford Instruments temperature controller ITC 503. Experiments (128 × 128 data set) were performed at 8 K using the standard four-pulse sequence ($\pi/2-\tau-\pi/2-t_1-\pi-t_2-\pi/2$–echo) with a nominal pulse width of 16 ns for $\pi/2$ pulses, a $\tau$ value of 132 ns and a pulse repetition rate of 1 kHz. In the HYSCORE experiment, the delays before ($t_1$) and after ($t_2$) the mixing $\pi$ pulse were incremented in 20-ns steps from an initial value ($t_{ini}$ = 200 ns) according to the following formula: $t_1 = t_{ini} + d_1$ and $t_2 = t_{ini} + d_2$. In the CF-NF experiment, $t_1$ and $t_2$ were incremented in 20-ns steps according to the following formula: $t_1 = t_{ini} + d_1$ and $t_2 = t_{ini} + d_1 + d_2$. The value of $t_{ini}$ was chosen to be as long as 1,000 ns to remove as much as possible the broad features arising from $^{14}N$ quadrupole coupling. Unwanted echoes were removed by four-step phase cycling. The background decay in both dimensions was subtracted using a linear fit followed by apodization with a Hamming window and zero-filling to 2,048 points in each dimension. The 2D Fourier transform magnitude spectrum was then calculated. The static magnetic field was set at 3,600 G ($g_\perp$).

**DFT calculations.** These were performed using the ADF2012 quantum chemistry code (see Supplementary Discussion). Hyperfine coupling constants were computed using the parameter-free PBE0 exchange-correlation potential with triple-zeta basis sets (+ two polarization functions) and unfrozen cores.


31. Fiedler, A. T. & Brunold, T. C. Combined spectroscopic/computational study of binuclear Fe(I)-Fe(I) complexes: implications for the fully-reduced active-site cluster of Fe-only hydrogenases. *Inorg. Chem.* **44,** 1794–1809 (2005).
32. Kuchenreuther, J. M. *et al.* High-yield expression of heterologous [FeFe] hydrogenases in *Escherichia coli*. *PLoS ONE* **5,** e15491 (2010).
33. Fish, W. W. Rapid colorimetric micromethod for the quantitation of complexed iron in biological samples. *Methods Enzymol.* **158,** 357–364 (1988).
34. Beinert, H. Semi-micro methods for analysis of labile sulfide and of labile sulfide plus sulfane sulfur in unusually stable iron sulfur proteins. *Anal. Biochem.* **131,** 373–378 (1983).
35. Hemschemeier, A., Melis, A. & Happe, T. Analytical approaches to photobiological hydrogen production in unicellular green algae. *Photosynth. Res.* **102,** 523–540 (2009).
36. Stripp, S. T. *et al.* How oxygen attacks [FeFe] hydrogenases from photosynthetic organisms. *Proc. Natl Acad. Sci. USA* **106,** 17331–17336 (2009).

doi:10.1038/nature12239

## Synthesis

**$(Et_4N)_2[Fe_2(pdt)(CO)_4(CN)_2]$ (1):** $(Et_4N)CN$ (0.16 g, 1.00 mmol) was dissolved in MeCN (5 mL) and added *via* cannula to a solution of $[Fe_2(pdt)(CO)_6]$ [1] (0.15 g, 0.40 mmol) in MeCN (5 mL) under argon. The reaction mixture was stirred for 2 hours at room temperature to give a dark red solution. The solvent was removed under reduced pressure to give a dark red oily residue. This was dissolved in acetone (10 mL) and filtered *via* cannula to give a dark red filtrate. The solution was mixed with EtOAc (10 mL) and cooled to –26 ºC to give $(Et_4N)_2$**1** as a deep red crystalline solid (0.22 g, 85%) $\nu_{max}/cm^{-1}$ (acetonitrile) 2076, 1964, 1922, 1884, 1873 (sh) (CO).

**$(Et_4N)_2[Fe_2(pdt)(CO)_4(^{13}CN)_2]$:** K ($^{13}CN$) (0.05 g, 0.80 mmol) was dissolved in MeOH (5 mL) and added *via* cannula to a solution of $[Fe_2(pdt)(CO)_6]$ [1] (0.15 g, 0.40 mmol) in MeCN (5 mL) under Argon. The reaction mixture was stirred for 2 hours at room temperature to give a dark red solution. $(Et_4N)Br$ (0.20 g, 0.95 mmol) was dissolved in MeCN (10 mL) and added to the reaction mixture, which was stirred for a further 30 minutes. The solvent was removed under reduced pressure to give a dark red oily residue. This was dissolved in acetone (10 mL) and filtered *via* cannula to give a dark red filtrate. The solution was mixed with EtOAc (20 ml) and cooled to –26 ° to give $(Et_4N)_2[Fe_2(pdt)(CO)_4(^{13}CN)_2]$ as a deep red solid (0.18 g, 72%) $\nu_{max}/cm^{-1}$ (acetonitrile) 2032 ($^{13}CN$), 1963, 1922, 1885, 1871(sh) (CO).

**$(Et_4N)_2[Fe_2(odt)(CO)_4(CN)_2]$ (3)** $(Et_4N)CN$ (0.08 g, 0.50 mmol) was dissolved in MeCN (5 ml) and added *via* cannula to a solution of $[Fe_2(odt)(CO)_6]$ [2] (0.10 g, 0.25 mmol) in MeCN (10 ml) under argon. The reaction mixture was stirred for 2 hours at room temperature to give a dark red solution. The solvent was removed under reduced pressure to give a dark red oily residue. This was dissolved in acetone (10 ml) and filtered *via* cannula to give a dark red filtrate. The solution was mixed with EtOAc (10 ml) and cooled to -26 ºC to give $(Et_4N)_2$**3** as a deep red crystalline solid (0.14 g, 88%) $\nu_{max}/cm^{-1}$ (acetonitrile) 2077, 1968, 1929, 1891, 1878 (sh) (CO).

## Supplementary discussion

### DFT calculations.

*Molecular models of the hybrid.* We modelled the three cysteine ligands of the [4Fe-4S] cluster of the hybrid as $EtS^-$ thiolate ligands, as is common practice. Consequently, the reduced cluster stands as a $[Fe_4\text{-}(\mu_3\text{-}S)_4(SEt)_3]^{2-}$ molecular anion (one iron ligand is yet vacant).

In all our DFT calculations, we kept the molecular integrity of the $[Fe_2]$ complex, $[Fe_2(pdt)(CO)_4(CN)_2]^{2-}$, constructed from $[Fe_2(pdt)(CO)_6]$ (CSD file md239) in which two of the neutral carbonyl ligands (one on each iron site) have been appropriately replaced by isoelectronic $CN^-$ ligands. The diiron $[Fe_2(pdt)(CO)_4(CN)_2]^{2-}$ complex is diamagnetic. Each iron site is low-spin S=0 (we verified computationally that this is indeed the case).

The full hybrid model thus assumes the following chemical formula: ($[Fe_4(\mu_3\text{-}S)_4(SEt)_3].[Fe_2(pdt)(CO)_4(CN)_2]$) of total charge –4. We will consider in the following two bridging modes for the -C≡N- ligand: [4Fe-4S]-N≡C-$[Fe_2]$ (**model 1**) and [4Fe-4S]-C≡N-$[Fe_2]$ (**model 2**).

*Electronic/magnetic states of the [4Fe-4S] cluster***.** In its reduced state (S=1/2), the [4Fe-4S] cluster is made of a mixed-valence pair (of spin +9/2) antiferromagnetically coupled to a ferrous pair of spin -8/2 resulting into the S=1/2 ground state. There are therefore six possible spin alignments among the four iron atoms. As the spin-coupled S=1/2 state is not directly accessible through DFT mono-determinantal codes, one relies on the computation of spin-uncoupled broken symmetry (BS) states for which the magnetic quantum number $m_s$=1/2 is constrained while preserving local iron high spins[3]. We called them $BS_{ij}$ = $BS_{12}$, $BS_{13}$, $BS_{14}$, $BS_{23}$, $BS_{24}$ and $BS_{34}$, respectively, where 'ij' refers to the ferrous pair (Table S2). Note that $Fe_4$ will always be the one linked to the diiron complex via the -C≡N- bridging ligand.

*Spin coupling procedure***.** For both $^{13}C$ and $^{14}N$ nuclei, DFT isotropic hyperfine coupling constants {A} are first computed for each *spin uncoupled* ($m_s$=1/2) BS states. These DFT quantities have to be *spin-coupled* in order to provide hyperfine couplings {a} for comparison with the experimental values. The correction for $^{13}C$ and $^{14}N$ coupling is the same because both nuclei belong to the same $CN^-$ ligand bound to the same cluster. Both DFT-computed {A} and predicted {a} quantities are related by $a = K(Fe)\,[A/(2S_{Fe})]$ where $2S_{Fe}$ is twice the

local spin of $Fe_4$ (ferrous : $2S_{Fe} = 4$ and mixed-valence : $2S_{Fe} = 4.5$). K(Fe) is a spin-coupling coefficient linking the local spins [$S_{Fe}$] to the total spin S=1/2. For symmetric reduced S=1/2 [4Fe-4S](Cys)$_4$ clusters, experimentally-derived values would be the following[4]: $K(Fe^{2.5+}) \approx +1.5$ and $K(Fe^{2+}) \approx -1.0$ (with $\Sigma_{Fe}$ K(Fe) = 1).

In practice, these {K(Fe)} values would result in a $\approx A/3$ if $Fe_4$ belongs to the mixed-valence pair, and a $\approx A/4$ if $Fe_4$ belongs to the ferrous pair. In the present case however, $Fe_4$ is bound to a cyanide bridging ligand, and the exact {K(Fe)} values in such an asymmetric case are unknown. The above corrections leading from {A} to {a} are thus tentative. In Tables S3 and S4, we also compute the ratio $A_{^{13}C}/A_{^{14}N}$, which simply turns out to be equal to $a_{^{13}C}/a_{^{14}N}$ as both nuclei are borne by the same iron atom. This ratio is moreover independent from the spin-coupling procedure and will therefore serve as a more reliable guide. Let us recall here that, experimentally: $|a_{^{13}C}| \approx 4$ MHz, $|a_{^{14}N}| < \approx 1$ MHz. We therefore expect: $a_{^{13}C}/a_{^{14}N} > \approx 4$.

*DFT calculations of hyperfine coupling constants*. We relied on the electronic structures and the subsequent hyperfine coupling constants computed by the ADF2012 density functional code[5]. Both hybrid **models 1** and **2**, each in the six possible broken symmetry states, have been fully geometry-optimized *in vacuo* using the standard VBP potential, i.e. Wilk, Vosko and Nusair functional[6], completed by Becke correction for the exchange[7] and Perdew correction for the correlation[8].

All hyperfine couplings' calculations were performed using the PBE0 exchange-correlation potential[9], a parameter-free density functional model whose results regarding spectroscopic properties are close to those computed by heavily parameterized functionals. For the second hybrid **model 2** [4Fe-4S cluster]-C≡N-[$Fe_2$] and for the first $BS_{12}$ broken symmetry state we have compared the carbon and nitrogen PBE0 hyperfine values (Table S3) to those computed first with the *local* VBP potential and for two *non-local* potentials. One is the standard B3LYP potential[10] (mixing in 20% of the pure Hartree-Fock (HF) exchange) and the other is a variant thereof mixing in only 5% of HF exchange, presented[11] as being suitable to describe metal-ligand (i.e. iron-sulfur) covalency within iron-sulfur clusters (data presented in Table S4).

Finally, triple-zeta + two polarization functions have been used for all atoms (TZ2P basis set in SCM-ADF nomenclature). Moreover, when estimating hyperfine coupling constants, no frozen core approximation has been set allowing all s atomic functions to be fully polarized as is required.

The computed isotropic hyperfine coupling values for both **models 1** and **2**, each in the six possible BS states, are presented in Tables S3 and S4, respectively. For **model 1**, when $Fe_4$ belongs to the delocalized mixed-valence pair (as for the first three BS states of Table S2, for $BS_{12}$, $BS_{13}$ and $BS_{23}$), we found on the average that $A_{^{13}C} \approx 20.5$ MHz and $A_{^{14}N} \approx 15.6$ MHz, that is $a_{^{13}C} \approx 6.8$ MHz and $a_{^{14}N} \approx 5.2$ MHz, with $a_{^{13}C}/a_{^{14}N} \approx 1.31$. The nitrogen hyperfine coupling is much too large, and the ratio $a_{^{13}C}/a_{^{14}N}$ too small to be compatible with the experiment.

For **model 1**, when $Fe_4$ now belongs to the ferrous pair (as for the last three BS states of Table S2, for $BS_{14}$, $BS_{24}$ and $BS_{34}$), we found on the average $A_{^{13}C} \approx -20.9$ MHz and $A_{^{14}N} \approx -9.9$ MHz, that is $a_{^{13}C} \approx 5.3$ MHz and $a_{^{14}N} \approx 2.5$ MHz, with $a_{^{13}C}/a_{^{14}N} \approx 2.11$. The nitrogen hyperfine coupling is still large, and the ratio $a_{^{13}C}/a_{^{14}N}$ still too small to be fully compatible with experiment.

The gyromagnetic ratios of $^{13}C$ and $^{14}N$ nuclei are in the 3.5 ratio (1.4/0.4). All other things being equal, we would therefore expect the computed hyperfine coupling constants $A_{^{13}C}$ and $A_{^{14}N}$ to be in that ratio. This is not the case, even though both nuclei are linked via a triple bond. In other words, the spin density of the nucleus closest to the iron ion (here, the nitrogen) is more affected than that of the other (carbon) nucleus. It can be seen in Table S2 that, indeed, the magnitude of $A_{^{13}C}$ does not vary much as a function of the formal iron valence (2.5+ or 2+). That of $A_{^{14}N}$ is reduced from 16 MHz to 9.8 MHz, thus by 6.2 MHz. We will come back to that last value below.

For **model 2**, with $Fe_4$ belonging to the ferrous pair (as for the last three BS states of Table S3, for $BS_{14}$, $BS_{24}$ and $BS_{34}$), we found on average that $A_{^{13}C} \approx -2.4$ MHz and $A_{^{14}N} \approx -8.0$ MHz, that is $a_{^{13}C} \approx -0.4$ MHz and $a_{^{14}N} \approx 2.0$ MHz, with $a_{^{13}C}/a_{^{14}N} \approx 0.30$. The carbon hyperfine coupling is now too small, which excludes this possibility.

Finally, for **model 2**, when $Fe_4$ now belongs to the delocalized mixed-valence pair (as for the first three BS states of Table S3, for $BS_{12}$, $BS_{13}$ and $BS_{23}$), we found on average that $A_{^{13}C} \approx 25.8$ MHz and $A_{^{14}N} \approx 7.7$ MHz, that is $a_{^{13}C} \approx 8.6$ MHz and $a_{^{14}N} \approx 2.6$ MHz, with $a_{^{13}C}/a_{^{14}N} \approx 3.4$ (even 3.85 in the case of $BS_{13}$). Although the PBE0 potential exaggerates the magnitudes of the couplings, the computed values (and their ratio) are satisfyingly compatible with the experiment. The dependence of the computed hyperfine coupling constants on the choice of the exchange-correlation potential is illustrated in Table S5.

As for **model 1**, the magnitudes of the hyperfine coupling constants computed for the nucleus further away from the iron ion (here, the nitrogen) cluster around a value of 8 MHz. In contrast, those corresponding to the closest nucleus (here, the carbon) are drastically reduced from 25.8 MHz (mixed-valence $Fe_4$) down to 2.4 MHz (ferrous $Fe_4$). This represents an average reduction by 23.4 MHz. In the same position (closest to the iron) we had 6.2 MHz for the nitrogen nucleus. These two values (23.4 and 6.2) are indeed proportional to the nuclear gyromagnetic ratios 1.4 and 0.4, respectively. Both carbon and nitrogen nuclei, when directly linked to $Fe_4$, are therefore equally affected by the nearby change from mixed-valence to ferrous.

We conclude this theoretical section by stating that the experimental data are compatible with the presence of a cyanide ion bridging both the [4Fe-4S] cluster and the [$Fe_2$] complex according to **model 2**: [4Fe-4S cluster]-C≡N-[$Fe_2$], more specifically with $Fe_4$ belonging to the mixed-valence (i.e. being formally $Fe^{2.5+}$).

*Simulation of IR spectra.* Within the IR module of the ADF2012-DFT code, there are two ways to compute IR transitions, one (analytical) being 3 to 5 times faster than the other one (numerical). The choice of the analytical procedure restricts that of the exchange-correlation potentials compatible with that module. We therefore proceeded to various tests in order to calibrate our method : (i) for CO and $CN^-$ in solution (target experimental values: 2143 $cm^{-1}$ and 2080 $cm^{-1}$, respectively, in water[12]); (ii) for complex **1** in solution (target experimental values : 1914 $cm^{-1}$, 1950 $cm^{-1}$ and 1981 $cm^{-1}$ for the CO ligands, and a massif centred around 2052 $cm^{-1}$ for the $CN^-$ ligands; see Figure 2A of main text). The exchange-correlation potential of choice turned out to be the one modelling the Stoll treatment of correlation[13]. The IR simulation required full geometry-reoptimization of the systems for that potential, in solution (dielectric constant $\varepsilon = 78$ for the whole calibration procedure), followed by the IR module at the optimized geometry. The results of the calibration are presented in Table S6. As can be seen there, the experimental values are quite well reproduced by the proposed DFT procedure.

For hybrids, and because of the computation time necessary for precise calculations, we chose a test case, that of one of our three candidates for **1**-HydF, that is the [4Fe-4S]-C≡N-[$Fe_2$] hybrid called $BS_{12}$ in Table S4 (experimental values reported in Figure 2B for **1**-HydF). Its geometry has been fully-reoptimized with the Stoll potential within a continuum dielectric constant of $\varepsilon = 4$ (mimicking the average polarizing effect of the protein matrix) and its IR

stretching frequencies calculated as above. It has to be noticed that the calculated frequencies for the charged $CN^-$ ion are more sensitive to solvation/protein environment than those for the neutral CO molecule. Plotting the vibration frequency as a function of (1-1/ε) yields a slope of 6 $cm^{-1}$ for CO against 37 $cm^{-1}$ for $CN^-$.

## Supplementary tables

**Table S1**. FTIR data recorded for the hybrid protein **1**-HydF and complex **1**. Values reported for as-isolated samples of CaHydF containing the natural co-factor are shown for comparison.

| **Sample** | **Frequencies ($cm^{-1}$)** |
|---|---|
| CaHydF isolated from *C. acetobutylicum*[14] | 2069(w), 2044(m), 1967(w), 1943(s), 1907(m), 1877(m) |
| CaHydF isolated from *E. coli* expressing the maturation system[15] | 2046(m), 2027(m), 1940 (s), 1881(m) |
| **1**-HydF | 2055(w), 2038(m), 1968(w), 1943(s), 1987 (bs) |
| **1** | 2052, 1981, 1950, 1914 |

**Table S2.** Formal iron valences and spin alignment in the various Electronic/magnetic states of the [4Fe-4S] cluster

| **BS states**[a] | **Formal iron valences & spin alignment**[b] |
|---|---|
| $BS_{12}$ | $Fe^{2+}(\downarrow)$- $Fe^{2+}(\downarrow)$- $Fe^{2.5+}(\uparrow)$- $Fe^{2.5+}(\uparrow)$ |
| $BS_{13}$ | $Fe^{2+}(\downarrow)$- $Fe^{2.5+}(\uparrow)$- $Fe^{2+}(\downarrow)$- $Fe^{2.5+}(\uparrow)$ |
| $BS_{23}$ | $Fe^{2.5+}(\uparrow)$- $Fe^{2+}(\downarrow)$- $Fe^{2+}(\downarrow)$- $Fe^{2.5+}(\uparrow)$ |
| $BS_{14}$ | $Fe^{2+}(\downarrow)$- $Fe^{2.5+}(\uparrow)$- $Fe^{2.5+}(\uparrow)$- $Fe^{2+}(\downarrow)$ |
| $BS_{24}$ | $Fe^{2.5+}(\uparrow)$- $Fe^{2+}(\downarrow)$- $Fe^{2.5+}(\uparrow)$- $Fe^{2+}(\downarrow)$ |
| $BS_{34}$ | $Fe^{2.5+}(\uparrow)$- $Fe^{2.5+}(\uparrow)$- $Fe^{2+}(\downarrow)$- $Fe^{2+}(\downarrow)$ |

(a) Each Broken Symmetry (BS) state is described by a label ('12', '13', etc.) indicating which iron pair is ferrous. (b) In the order $Fe_1$-$Fe_2$-$Fe_3$-$Fe_4$.

**Table S3.** DFT computed $^{13}C$ and $^{14}N$ {A} hyperfine coupling constants

| **[4Fe-4S]-N≡C-[Fe$_2$]** | | | | |
|---|---|---|---|---|
| BS states[a] | E(eV)[b] | $A_{14_N}$ (MHz) | $A_{13_C}$ (MHz) | $A_{13_C}/A_{14_N}$[c] |
| $BS_{12}$ | -450.079 | +15.1 | +20.4 | 1.35 |
| $BS_{13}$ | -449.913 | +17.0 | +20.3 | 1.19 |
| $BS_{23}$ | -450.032 | +14.8 | +20.8 | 1.41 |
| *average* | | ***+15.6*** | ***+20.5*** | ***1.31*** |
| $BS_{14}$ | -450.127 | -9.9 | -21.0 | 2.12 |
| $BS_{24}$ | -450.103 | -10.1 | -20.8 | 2.06 |
| $BS_{34}$ | -450.112 | -9.7 | -20.9 | 2.15 |
| *average* | | ***-9.9*** | ***-20.9*** | ***2.11*** |

(a) Each Broken Symmetry (BS) state is described by a label ('12', '13', etc.) indicating which iron pair is ferrous. $Fe_4$ is the one bearing the cyanide bridging ligand. (b) Bonding energies (eV) computed for the optimized geometries. (c) This ratio is independent from the spin-coupling procedure (i.e. $A_{13_C}/A_{14_N} = a_{13_C}/a_{14_N}$).

**Table S4** DFT computed $^{13}C$ and $^{14}N$ {A} hyperfine coupling constants

| **[4Fe-4S]-C≡N-[Fe$_2$]** | | | | |
|---|---|---|---|---|
| BS states[a] | E(eV)[b] | $A_{14_N}$ (MHz) | $A_{13_C}$ (MHz) | $A_{13_C}/A_{14_N}$[c] |
| $BS_{12}$ | -449.555 | +7.5 | +23.3 | 3.11 |
| $BS_{13}$ | -449.489 | +7.8 | +30.0 | 3.85 |
| $BS_{23}$ | -449.523 | +7.8 | +24.0 | 3.08 |
| *average* | | ***+7.7*** | ***+25.8*** | ***3.35*** |
| $BS_{14}$ | -449.642 | -7.9 | -2.6 | 0.33 |
| $BS_{24}$ | -449.658 | -8.1 | -2.0 | 0.25 |
| $BS_{34}$ | -449.642 | -8.0 | -2.7 | 0.34 |
| *average* | | ***-8.0*** | ***-2.4*** | ***0.30*** |

(a) Each Broken Symmetry (BS) state is described by a label ('12', '13', etc.) indicating which iron pair is ferrous. $Fe_4$ is the one bearing the cyanide bridging ligand. (b) Bonding energies (eV) computed for the optimized geometries. (c) This ratio is independent from the spin-coupling procedure (i.e. $A_{13_C}/A_{14_N} = a_{13_C}/a_{14_N}$).

**Table S5** DFT computed $^{13}C$ and $^{14}N$ {A} hyperfine coupling constants

| **[4Fe-4S]-C≡N-[Fe$_2$]** | | | |
|---|---|---|---|
| XC potential[a] | $A^{14}_{N}$ (MHz) | $A^{13}_{C}$ (MHz) | $A^{13}_{C}/A^{14}_{N}$[b] |
| VBP | +6.9 | +10.6 | **1.53** |
| PBE0 | +7.5 | +23.3 | **3.11** |
| B3LYP (5% HF) | +9.2 | +27.5 | **2.99** |
| B3LYP (20% HF) | +9.3 | +35.3 | **3.80** |

These calculations are performed for the $BS_{12}$ state. (a) Exchange-correlation (XC) potential (see main text of the methods summary). (b) This ratio is independent from the spin-coupling procedure (i.e. $A^{13}_{C}/A^{14}_{N} = a^{13}_{C}/a^{14}_{N}$).

**Table S6**. DFT-computed versus experimental CO and $CN^-$ IR stretching frequencies ($cm^{-1}$).

| Systems | Method | CO | $CN^-$ |
|---|---|---|---|
| Isolated[a] | Exp[c]. | **2143** | **2080** |
| | DFT | *2148* | *2078* |
| [Fe$_2$] Complex[a] | Exp[d]. | **1914**<br>**1950**<br>**1981** | **2052** |
| | DFT | *1904, 1910*<br>*1946*<br>*1961* | *2066*<br>*2071* |
| [4Fe-4S]-C≡N-[Fe$_2$] Hybrid[b] | Exp[e]. | **1897**<br>**1943**<br>**1968** | **2038**<br>**2055** |
| | DFT | 1886, 1894<br>1944<br>1958 | 2010[f]<br>2060[g] |

(a) ε = 78; (b) ε = 4; (c) ref 23; (d) From Figure 2A for complex **1**; (e) From Figure 2B for **1**-HydF; (f) bridging $CN^-$; (g) terminal $CN^-$.

## Supplementary figures

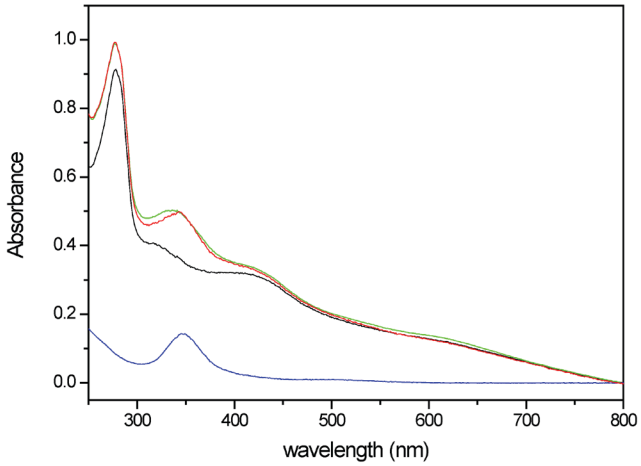


**Figure S1a. UV/Vis spectra of 1-HydF in Tris-HCl buffer (50 mM, 150 mM NaCl, pH 8).** **1**-HydF (20 μM, red line); the HydF protein (20 μM, black line); complex **1** (20 μM, blue line); Calculated spectrum obtained through mathematical addition of **1** and HydF spectra in a 1:1 ratio (20 μM, green line)

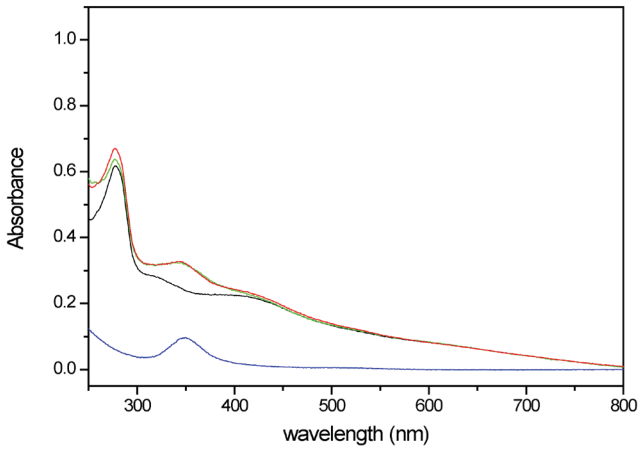


**Figure S1b. UV/Vis spectra of 2-HydF in Tris buffer (50 mM, 150 mM NaCl, pH 8).** **2**-HydF (14 μM, red line); the HydF protein (14 μM, black line); complex **2** (14 μM, blue line); Calculated spectrum obtained through mathematical addition of **2** and HydF spectra in a 0.95:1 ratio (14 μM, green line)

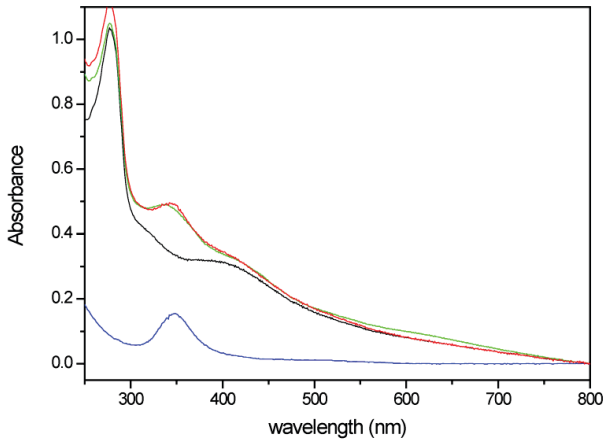


**Figure S1c. UV/Vis spectra of 3-HydF in Tris buffer (50 mM, 150 mM NaCl, pH 8).** 3-HydF (20 μM, red line); the HydF protein (20 μM, black line); complex **3** (20 μM, blue line); Calculated spectrum obtained through mathematical addition of **3** and HydF spectra in a 1:1 ratio (20 μM, green line)

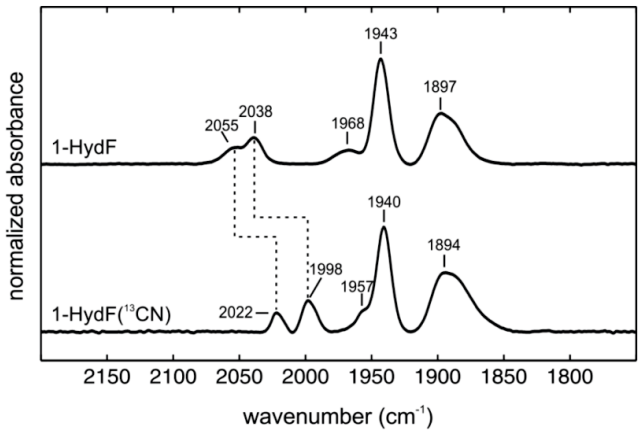


**Figure S2.** Solution Fourier-transform infrared spectra of **1**-HydF in solution with $^{12}CN$ and $^{13}CN$ ($^{13}C$ labelled cyanide ligands in **1**) recorded in HEPES buffer (20 mM, 100 mM KCl, pH 7.5).

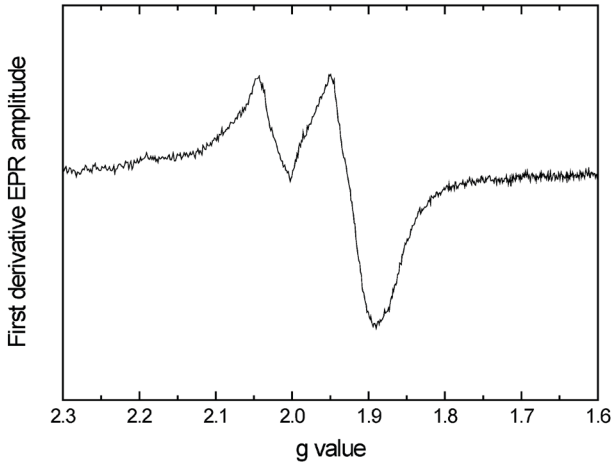


**Figure S3a: Continuous wave EPR spectrum of 2-HydF.** X-band EPR spectrum recorded at 10K for dithionite-reduced **2**-HydF in Tris-HCl buffer (50 mM, 150 mM NaCl, $Na_2S_2O_4$ 5 mM, pH 8). Microwave power = 100 µW, mod. amp. = 1 mT, mwfreq. = 9.65 GHz..

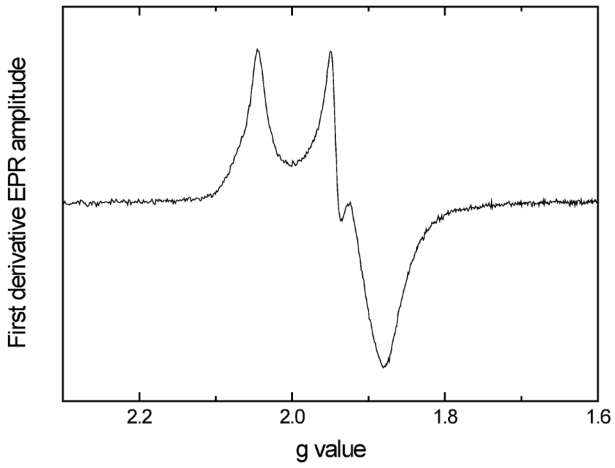


**Figure S3b: Continuous wave EPR spectrum of 3-HydF.** X-band EPR spectrum recorded at 10K for dithionite-reduced **3**-HydF in Tris-HCl buffer (50 mM, 150 mM NaCl, $Na_2S_2O_4$ 5 mM, pH 8). Microwave power = 100 µW, mod. amp. = 1 mT, mwfreq. = 9.65 GHz. On the basis of its power saturation behaviour at 10K, the contribution observed at g = 1.90 and corresponding to only a few percent of the total signal intensity is assigned to a small fraction of residual HydF lacking the synthetic co-factor.

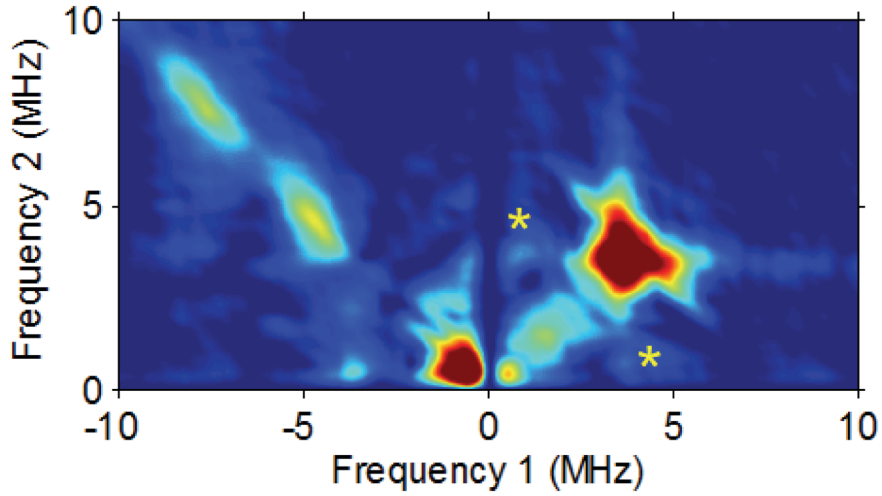


**Figure S4:** X-band HYSCORE spectrum of $^{13}CN^-$-labelled **1**-HydF recorded at B=360 mT (corresponding to $g_\perp$) and T=8K (see above for more details). The antidiagonal ridge centered around 3.6 MHz in the (+,+) quadrant is attributed to $^{13}C$ hyperfine coupling. It is much more visible on the CF-NF experiment displayed in Figure 3. The other features noted by asterisks (*) in this quadrant can be attributed to a weakly coupled $^{14}N$ nucleus. While CF-NF (Figure 3) and HYSCORE (this figure) provide essentially the same information, the former is more sensitive for disordered system[16]. It correlates the combination frequencies ($\nu_\alpha+\nu_\beta$) in one direction with the nuclear frequencies ($\nu_\alpha$ and $\nu_\beta$ ) in the other direction. This means that, to first order, a small hyperfine tensor for an I=1/2 spin is detected as a straight horizontal line in the (+,+) quadrant. HYSCORE correlates nuclear frequencies in the two directions and so displays a small hyperfine tensor for an I=1/2 spin as an antidiagonal ridge in the (+,+) quadrant.

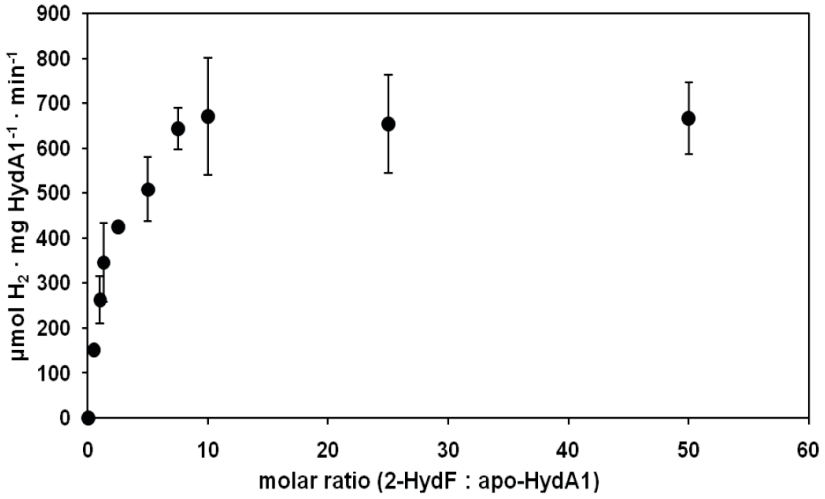


**Figure S5:** Dependence of the specific activity of HydA1 on the number of equivalents of **2**-HydF used during a 30 min transfer reaction, as described in the experimental section. Errors bars correspond to standard deviations.

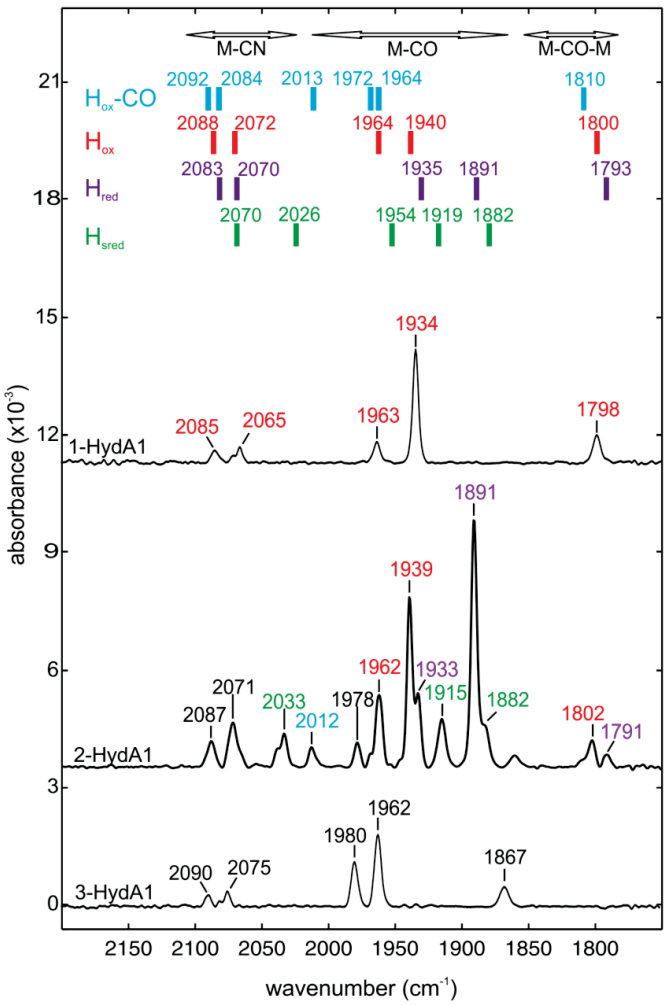


**Figure S6:** FTIR spectra recorded for HydA1 after treatment of apo-HydA1 with **1**-HydF (**1**-HydA1), **2**-HydF (**2**-HydA1) and **3**-HydF (**3**-HydA1) together with complete information on the FTIR signal positions for each redox state of native HydA1. The colour code indicates the contributions from $H_{ox}$, $H_{red}$, $H_{sred}$ and $H_{ox}$-CO ( the $H_{ox}$ state is marked in red, the $H_{red}$ state in violet, the $H_{sred}$ state in green and the $H_{ox}$-CO state in light blue).

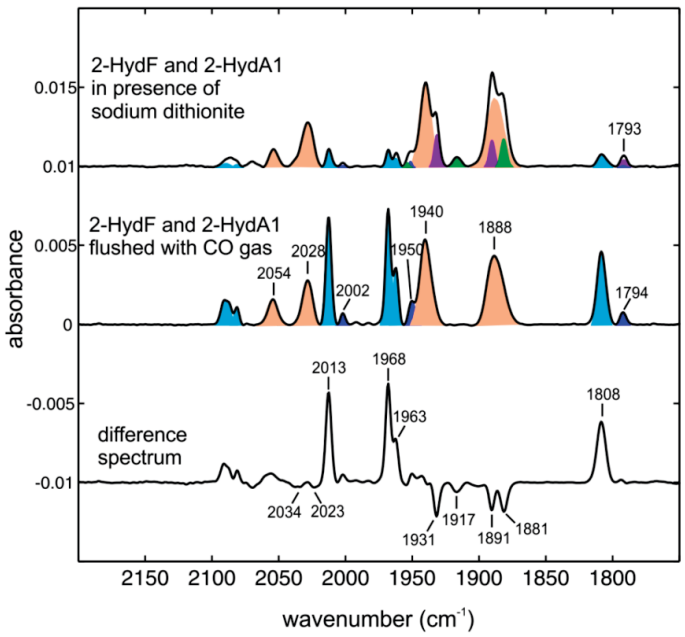


**Figure S7**. FTIR spectra of a mixture of apo-HydA1 and **2**-HydF (2-4 molar equivalents) after 60 min (top) and after additional exposure to CO gas (middle). The difference spectrum is shown at the bottom. Bands shaded in orange originate from **2**-HydF, light blue from **2**-HydA1 in the $H_{ox}$-CO state, violet from **2**-HydA1 in the $H_{red}$ state, green from **2**-HydA1 in the $H_{sred}$ state. Interestingly, additional low intensity $H_{ox}$-CO "ghost" peaks (indicated in dark blue) previously observed in heterologously expressed HydA1[5] are also visible in our preparation. The positive peaks in the difference trace represent the $H_{ox}$-CO state while the negative peaks show the positions of the $H_{red}$ and $H_{sred}$ bands.

## References

1. Seyferth, D. et al. Novel Anionic Rearrangements in Hexacarbonyldiiron Complexes of Chelating Organosulfur Ligands. *Organometallics* **6**, 283-294 (1987).
2. Song, L.C., Yang, Z.Y., Bian, H.Z. & Hu, Q.M. Novel single and double diiron oxadithiolates as models for the active site of [Fe]-Only hydrogenases. *Organometallics* **23**, 3082-3084 (2004).
3. Noodleman, L., Peng, C.Y., Case, D.A. & Mouesca, J.M. Orbital Interactions, Electron Delocalization and Spin Coupling in Iron-Sulfur Clusters. *Coordination Chemistry Reviews* **144**, 199-244 (1995).
4. Moriaud, F., Gambarelli, S., Lamotte, B. & Mouesca, J.M. Detailed proton Q-band ENDOR study of the electron spin population distribution in the reduced [4Fe-4S]$^{1+}$ state. *Journal of Physical Chemistry B* **105**, 9631-9642 (2001).
5. Velde, G.T. & Baerends, E.J. Numerical-Integration for Polyatomic Systems. *Journal of Computational Physics* **99**, 84-98 (1992).
6. Vosko, S.H., Wilk, L. & Nusair, M. Accurate Spin-Dependent Electron Liquid Correlation Energies for Local Spin-Density Calculations - a Critical Analysis. *Canadian Journal of Physics* **58**, 1200-1211 (1980).
7. Becke, A.D. Density-Functional Exchange-Energy Approximation with Correct Asymptotic-Behavior. *Physical Review A* **38**, 3098-3100 (1988).
8. Perdew, J.P. Density-Functional Approximation for the Correlation-Energy of the Inhomogeneous Electron-Gas. *Physical Review B* **33**, 8822-8824 (1986).
9. Adamo, C. & Barone, V. Toward reliable density functional methods without adjustable parameters: The PBE0 model. *Journal of Chemical Physics* **110**, 6158-6170 (1999).
10. Stephens, P.J., Devlin, F.J., Chabalowski, C.F. & Frisch, M.J. Ab-Initio Calculation of Vibrational Absorption and Circular-Dichroism Spectra Using Density-Functional Force-Fields. *Journal of Physical Chemistry* **98**, 11623-11627 (1994).
11. Szilagyi, R.K. & Winslow, M.A. On the accuracy of density functional theory for iron - Sulfur clusters. *Journal of Computational Chemistry* **27**, 1385-1397 (2006).
12. Nakamoto, K. (ed.) *Infrared spectra of inorganic and coordination compounds*, (Wiley-Interscience, 1970).
13. Stoll, H., Pavlidou, C.M.E. & Preuss, H. Calculation of Correlation Energies in Spin-Density Functional Formalism. *Theoretica Chimica Acta* **49**, 143-149 (1978).
14. Czech, I., Silakov, A., Lubitz, W. & Happe, T. The [FeFe]-hydrogenase maturase HydF from Clostridium acetobutylicum contains a CO and CN- ligated iron cofactor. *FEBS Letters* **584**, 638-642 (2010).
15. Shepard, E.M. et al. Synthesis of the 2Fe subcluster of the [FeFe]-hydrogenase H cluster on the HydF scaffold. *Proceedings of the National Academy of Sciences of the United States of America* **107**, 10448-10453 (2010).
16. Hubrich, M., Jeschke, G. & Schweiger, A. The generalized hyperfine sublevel coherence transfer experiment in one and two dimensions. *Journal of Chemical Physics* **104**, 2172-2184 (1996).

nature chemical biology

BRIEF COMMUNICATION

PUBLISHED ONLINE: 11 AUGUST 2013 | DOI: 10.1038/NCHEMBIO.1311

# Spontaneous activation of [FeFe]-hydrogenases by an inorganic [2Fe] active site mimic

Julian Esselborn[1], Camilla Lambertz[1,6], Agnieszka Adamska-Venkatesh[2,6], Trevor Simmons[3,6], Gustav Berggren[3,5], Jens Noth[1], Judith Siebel[2], Anja Hemschemeier[1], Vincent Artero[3], Edward Reijerse[2], Marc Fontecave[3,4], Wolfgang Lubitz[2] & Thomas Happe[1]*

**Hydrogenases catalyze the formation of hydrogen. The cofactor ('H-cluster') of [FeFe]-hydrogenases consists of a [4Fe-4S] cluster bridged to a unique [2Fe] subcluster whose biosynthesis *in vivo* requires hydrogenase-specific maturases. Here we show that a chemical mimic of the [2Fe] subcluster can reconstitute apo-hydrogenase to full activity, independent of helper proteins. The assembled H-cluster is virtually indistinguishable from the native cofactor. This procedure will be a powerful tool for developing new artificial $H_2$-producing catalysts.**



Research on hydrogenase enzymes has gained considerable interest as these biocatalysts efficiently produce molecular hydrogen ($H_2$). To develop inexpensive but highly active chemical mimics, detailed knowledge about the structure, reaction mechanism and assembly of the active site in these enzymes is required. Hydrogenases of the [FeFe] type (HYDA) are the most active $H_2$ producers[1]. They contain a complex cofactor, the H-cluster, consisting of a simple cubane [4Fe-4S] cluster bound via cysteine to a unique [2Fe] subcluster in which two Fe atoms are coordinated by CO, $CN^-$ and a dithiolate[2,3] (**Fig. 1**). In the living cell, biosynthesis of the [2Fe] subcluster requires three hydrogenase-specific maturases, HYDE, HYDF and HYDG[4]. HYDF is the scaffold for [2Fe] subcluster assembly and transfers the cluster to the HYDA protein containing a preassembled [4Fe-4S] cluster (apo-HYDA)[2,5,6]. Numerous model compounds have been synthesized to investigate different features of the [2Fe] subcluster[7]. All of the mimics tested so far, including the most structurally relevant ones[8,9], have only low $H_2$ evolving efficiencies *in vitro*. A major challenge is therefore to understand the role of the protein environment in allowing the inorganic clusters to come to full activity[10]. Notably, a synthetic mimic of the [2Fe] subcluster can be loaded onto HYDF from *Thermotoga maritima in vitro*[11]. This artificially loaded HYDF is able to transfer the di-iron analogs to the apo form of [FeFe]-hydrogenase HYDA1 from *Chlamydomonas reinhardtii* (apo-HYDA1), resulting in a fully active hydrogenase[11].

Little is known about the mechanistic details of the transfer of the [2Fe] subcluster from HYDF to apo-HYDA. At present, it is not clear whether HYDF, apart from serving as a scaffold for the [2Fe] precursor, has an additional function in inserting the [2Fe] subcluster. Therefore we tested whether a [2Fe] subsite mimic containing an azadithiolate bridge ($[2Fe]^{MIM}$; **Fig. 1**)[9,11] would be able to integrate into the HYDA1 apo-protein in the absence of HYDF. We combined inactive apo-HYDA1 heterologously produced in *Escherichia coli* with pure $[2Fe]^{MIM}$ solutions. Remarkably, this procedure resulted in high specific hydrogenase activities (**Fig. 2a**), despite the absence of helper proteins such as HYDF. The resulting activities were similar to those obtained using $[2Fe]^{MIM}$-loaded HYDF ($HYDF^{(MIM)}$)[11] and could be reached at a lower molar excess of $[2Fe]^{MIM}$ (**Fig. 2a**). A 2.5-fold excess of $[2Fe]^{MIM}$ over apo-HYDA1 sufficed to yield a specific activity as high as that of native HYDA1 maturated in *Clostridium acetobutylicum*, an established host for heterologous production of active [FeFe]-hydrogenases[10] (**Fig. 2b**). This indicates that the $[2Fe]^{MIM}$ compound was able to autonomously integrate into apo-HYDA1 very efficiently.

In contrast to *C. reinhardtii* HYDA1, which consists only of the H-cluster–containing H-domain, most bacterial HYDA proteins have further domains holding additional [FeS] clusters[3,12]. The spontaneous integration of $[2Fe]^{MIM}$ into algal apo-HYDA1 might therefore be restricted to these single-domain proteins and not suited for broad applications. The crystal structure of *C. reinhardtii* apo-HYDA1 revealed a positively charged channel connecting the protein surface to the active site niche[5]. As this channel is not observed in holo-HYDA enzymes[3,13], it might serve as the entry pathway for the [2Fe] subcluster, closing upon its attachment

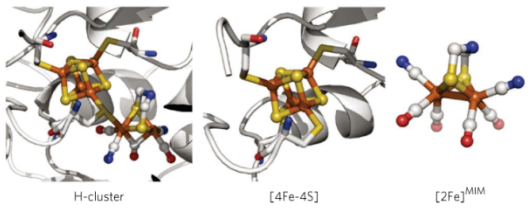


**Figure 1 | The H-cluster is assembled from a regular [4Fe-4S] cluster and a unique [2Fe] subcluster.** The synthetic [2Fe] subcluster ($[2Fe]^{MIM}$) differs from the binuclear subsite of the H-cluster by an additional CO group. Models of the H-cluster and the [4Fe-4S] cluster were generated in PyMOL on the basis of Protein Data Bank structures 3C8Y and 3LX4, respectively. Some amino acids were deleted to provide an unobstructed view of the clusters. $[2Fe]^{MIM}$ was also modeled in PyMOL according to information given in ref. 11. The metal clusters are in ball-and-stick representation, and the coordinating cysteines are shown as sticks. Color coding is as follows: orange, iron; yellow, sulfur; gray, carbon; blue, nitrogen; red, oxygen.

[1]Ruhr-Universität Bochum, Fakultät für Biologie und Biotechnologie, AG Photobiotechnologie, Bochum, Germany. [2]Max-Planck-Institut für Chemische Energiekonversion, Mülheim an der Ruhr, Germany. [3]Laboratoire de Chimie et Biologie des Métaux (Commissariat à l'énergie atomique et aux énergies alternatives–Université Grenoble 1–Centre national de la recherche scientifique), Grenoble, France. [4]Collège de France, Paris, France. [5]Present address: Department of Biochemistry and Biophysics, Stockholm University, Stockholm, Sweden. [6]These authors contributed equally to this work. *e-mail: thomas.happe@rub.de

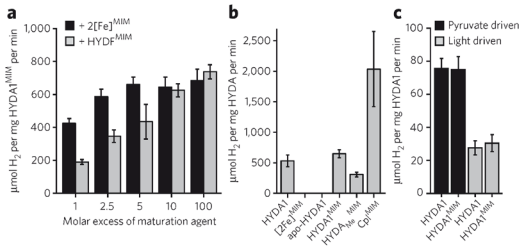


**Figure 2 | Various types of HYDA enzymes can be spontaneously activated by [2Fe]$^{MIM}$ and behave like the natural enzymes.** (**a**) Specific $H_2$ evolution activities of *C. reinhardtii* HYDA1 after combination of apo-HYDA1 with [2Fe]$^{MIM}$ alone or [2Fe]$^{MIM}$-loaded HYDF. Molar ratios are indicated on the *x* axis. (**b**) HYDA1$^{MIM}$ reached the same specific activity as HYDA1 heterologously produced in *C. acetobutylicum*[10], whereas neither [2Fe]$^{MIM}$ nor apo-HYDA1 showed any activities. [2Fe]$^{MIM}$ also activated apo-HYDA enzymes of *M. elsdenii* (HYDA$_{Me}^{MIM}$) and *C. pasteurianum* (CpI$^{MIM}$). We measured $H_2$ evolution using reduced methyl viologen as electron donor. (**c**) $H_2$ production was also achieved in reconstitution assays including pyruvate, acetyl-CoA, pyruvate:ferredoxin oxidoreductase PFR1 and ferredoxin PETF in the dark[17] (pyruvate-driven) or with photosystem 1 (PS1), PETF and the necessary PS1-reducing agents[16] in the light (light-driven). In **a**–**c**, all of the values shown are mean values ± s.d. from at least four independent experiments.

to the [4Fe-4S] site. In multidomain HYDA enzymes, the entry site of the [2Fe] compound might be obstructed, making a chaperone or maturase indispensable for integrating the [2Fe] subcluster. Therefore we examined the activity of enzymes from *Megasphaera elsdenii* (HYDA$_{Me}$) and *Clostridium pasteurianum* (CpI) after treatment with [2Fe]$^{MIM}$. These have two and four additional [FeS] clusters, respectively, and accordingly longer N termini[3,14]. In both cases, the apo-enzymes produced in *E. coli* did not show any $H_2$ evolution activity. However, after *in vitro* maturation with [2Fe]$^{MIM}$, specific activities of 308 ± 40 µmol $H_2$ per mg HYDA$^{MIM}$ per min and 2,037 ± 616 µmol $H_2$ per mg HYDA$^{MIM}$ per min were achieved by HYDA$_{Me}^{MIM}$ and CpI$^{MIM}$, respectively (**Fig. 2b**). These activities were in a similar range as those of native *M. elsdenii* HYDA[15] and heterologously produced CpI[10].

We also tested whether HYDA1$^{MIM}$ would be able to interact with its natural electron delivery systems. The cellular electron donor of HYDA1 is the ferredoxin PETF, and in illuminated algae, the major electron source for $H_2$ production is photosystem 1 (PS1)[16]. In the dark, pyruvate oxidation and subsequent PETF reduction by pyruvate:ferredoxin oxidoreductase (PFR1) are responsible for $H_2$ generation in *Chlamydomonas*[17]. In *in vitro* assays in which either PS1 or PFR1 were used as PETF-reducing components, the $H_2$ evolution activities of HYDA1$^{MIM}$ and HYDA1 were the same (**Fig. 2c**). The comparable rate of electron transfer between PETF and HYDA1 or HYDA1$^{MIM}$ suggests very similar structural properties and indicates that the *in vivo* functionality of HYDA1$^{MIM}$ is identical to that of native HYDA1.

Electron paramagnetic resonance (EPR) spectroscopy gives detailed information about the electronic structure of the H-cluster, whereas the CO and $CN^-$ vibrations, as observed in Fourier transform infrared (FTIR) spectroscopy, can be used as a reporter on the valence state of the di-iron core[18]. Therefore, we examined the reconstituted and subsequently purified HYDA1$^{MIM}$ protein using both methods (**Fig. 3**). To obtain well-defined EPR and FTIR spectra of the H-cluster, we treated HYDA1$^{MIM}$ with CO to generate the characteristic $H_{ox}$-CO state. Indeed, the EPR spectrum of this preparation (**Fig. 3a**) unequivocally identified it as the native $H_{ox}$-CO state[19]. Also, its FTIR spectrum (**Fig. 3b**) showed the CO and $CN^-$ bands at the positions previously observed for the native $H_{ox}$-CO state[20]. For comparison, **Figure 3** also shows the EPR and FTIR spectra of the starting materials, that is, apo-HYDA1 (**Fig. 3a**) and [2Fe]$^{MIM}$ (**Fig. 3b**). EPR spectra of apo-HYDA1 indicated typical *g* values for [4Fe-4S] clusters and were very similar to the values previously observed for apo-HYDA1 (ref. 6) (**Fig. 3a**). The shift of the FTIR bands when going from free [2Fe]$^{MIM}$ to HYDA1$^{MIM}$-CO (**Fig. 3b**) is consistent with the change of the ligand geometry occurring upon integration of [2Fe]$^{MIM}$ into the polypeptide, which involves its attachment to the [4Fe-4S] cluster and rearrangement of one CO ligand into a bridging Fe-CO-Fe position (**Fig. 1**). In the as-isolated form, [FeFe]-hydrogenases usually show a mixture of redox states, which represent the different electronic configurations of individual steps of the catalytic cycle[19]. In EPR (**Fig. 3a**) and FTIR (**Fig. 3b**) spectra of untreated HYDA1$^{MIM}$, these signals were also observed. Again, peak shapes and *g*-tensor values corresponded well to previously published data[19–21]. The spectroscopic data therefore show that the spontaneous integration of [2Fe]$^{MIM}$ into the apo-HYDA1 protein results in an H-cluster virtually identical to the native one.

One of the four CO ligands of [2Fe]$^{MIM}$ must dissociate to yield active HYDA1$^{MIM}$ (**Fig. 1**). We verified the release of CO spectroscopically by monitoring the binding of free CO to deoxyhemoglobin over time. This hemoglobin-based assay can sensitively detect dissolved CO[22]. Indeed, the typical CO-induced shift of the hemoglobin Soret band occurred when apo-HYDA1 and [2Fe]$^{MIM}$ were mixed (**Supplementary Results**, **Supplementary Fig. 1a**), and the reaction was complete after 2–3 min. The release of CO depended linearly on the apo-HYDA1 concentration (**Supplementary Fig. 1b**).

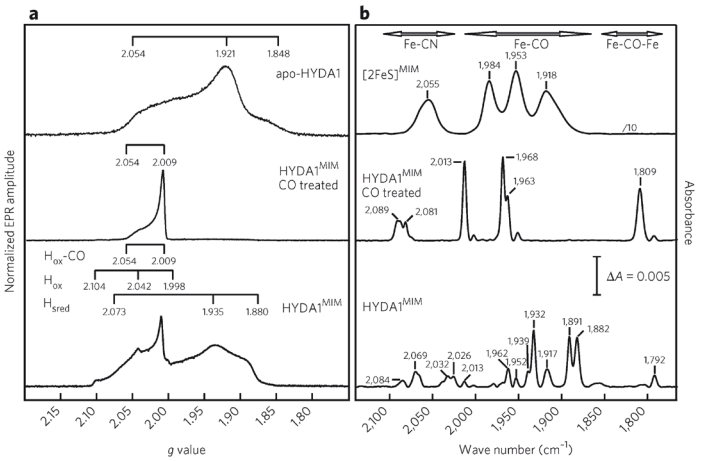


**Figure 3 | The chemically reconstituted H-cluster is virtually indistinguishable from the native form.** (**a**) EPR-spectra of apo-HYDA1, HYDA1$^{MIM}$ in the CO-inhibited $H_{ox}$-CO state and as isolated HYDA1$^{MIM}$ comprising all of the EPR active states. (**b**) FTIR spectra of [2Fe]$^{MIM}$ in solution, CO-treated HYDA1$^{MIM}$ and as isolated HYDA1$^{MIM}$. EPR simulations for each state[19,21] are shown in **Supplementary Figure 2a**. The *g* values are indicated above the spectra. The assignments of the FTIR signals to the different redox states are collected in **Supplementary Figure 2b**. All of the spectra were recorded on two independently prepared samples. One representative result is shown.

We estimated that approximately 0.6 mol of CO were detected per mol apo-HYDA1.

To test whether the spontaneous integration of the [2Fe] subcluster reported here was strictly specific for the native cofactor $[2Fe]^{MIM}$, carrying a secondary amine as the dithiolate bridgehead, we attempted to integrate a similar mimic into apo-HYDA1. $[2Fe]^{pdt}$ features a 1,3-propanedithiolate and thus differs from $[2Fe]^{MIM}$ only by the head atom of the bridging dithiolate, which in this case is a carbon instead of a nitrogen. $[2Fe]^{pdt}$, transferred to apo-HYDA1 by HYDF, does not form an active H-cluster[11]. After treating apo-HYDA1 with $[2Fe]^{pdt}$ in the absence of HYDF, we measured no hydrogenase activity. Nevertheless, the FTIR spectrum of $HYDA1^{pdt}$ proved the presence of $[2Fe]^{pdt}$ within the protein (**Supplementary Fig. 3**). In contrast to $HYDA1^{MIM}$, which shows a mixture of states (**Fig. 3b**), $HYDA1^{pdt}$ is stabilized as a single species resembling the native $H_{ox}$ state (**Supplementary Figs. 2b** and **3**)[11]. The unassisted integration of $[2Fe]^{pdt}$ shows that the [2Fe] subcluster integration is not strictly selective. This property could open new avenues to investigate other synthetic cluster derivatives in a protein environment.

In conclusion, the results presented here show that, under *in vitro* conditions, no [2Fe] subcluster transferase is needed for HYDA activation and, therefore, offer new insights into the *in vivo* maturation process of [FeFe]-hydrogenases. They indicate that, after synthesis of the [2Fe]-subsite precursor and its transfer to apo-HYDA, the last three steps of HYDA activation might also naturally occur without further assistance of maturases. First, the [2Fe] subcluster must find its way from the protein surface to the preassembled [4Fe-4S] cluster. It was suggested that the water-filled channel reaching from the protein surface to the [4Fe-4S] cluster in apo-HYDA1 (ref. 5) might allow an entropically driven insertion of the [2Fe] subcluster[23]. Charged residues lining the channel surface are suitable candidates for interacting with the [2Fe] subsite and directing its steric orientation by providing the correct electrostatic attracting and repelling forces[23]. Once the [2Fe] subcluster is positioned at the end of the channel, coordination via a bridging residue to the [4Fe-4S] cluster is required. The coordination of a thioether ligand onto [2Fe] mimics can be oxidatively induced, yielding an intermediate species with a structure closely related to the $H_{ox}$-CO state[24]. Finally, the fourth CO ligand present in $[2Fe]^{MIM}$, and probably also in the naturally synthesized [2Fe] subcluster present on HYDF[6], dissociates. At which step of H-cluster assembly this happens remains to be elucidated. A transient formation of the $H_{ox}$-CO state followed by the release of the excess CO ligand should be considered.

Biochemists have long been fascinated by the structure of the [2Fe] subcluster, which, apart from the cysteinyl bridge, has only noncovalent interactions with the protein. One cannot resist the idea that the [2Fe] subsite may originate from an inorganic complex that spontaneously formed in the prebiotic world, as suggested earlier[12]. Both HYDF-assisted[11] and the unassisted integration of $[2Fe]^{MIM}$ and $[2Fe]^{pdt}$ into apo-HYDA1 reported herein are powerful demonstrations of the synergy between chemistry and biology. Given the enormous efforts made over the years in both biomimetic chemistry of the [2Fe] subcluster[7] and the elucidation of the functional aspects of the HYDA protein matrix[25], bridging the gap between the two fields promises new insights into the chemistry of [FeFe] hydrogenases. Moreover, the HYDF-independent procedure described here opens up new areas for hydrogenase research. To date, only a subset of HYDA enzymes has been analyzed in biochemical and biophysical detail owing to the difficulty of generating large amounts of fully active enzymes. The ability to reconstitute apo-hydrogenases even in the absence of maturation factors now permits the analysis of the whole spectrum of HYDA sequences.

In particular, the chaperone-independent assembly of (synthetic) clusters will allow us to unravel protein-based structure-function relationships from an entirely new perspective. To date, these are investigated by site-directed mutagenesis of the protein. But with a system of spontaneous cluster assembly at hand, attempts can be made to engineer and test artificial protein environments. This might result in entirely artificial hydrogenases with applications in biohydrogen production and biofuel cell technology.

Received 22 May 2013; accepted 1 July 2013;
published online 11 August 2013

## METHODS

Methods and any associated references are available in the online version of the paper.

## References

1. Frey, M. *ChemBioChem* **3**, 153–160 (2002).
2. Peters, J.W. & Broderick, J.B. *Annu. Rev. Biochem.* **81**, 429–450 (2012).
3. Peters, J.W., Lanzilotta, W.N., Lemon, B.J. & Seefeldt, L.C. *Science* **282**, 1853–1858 (1998).
4. Posewitz, M.C. *et al. J. Biol. Chem.* **279**, 25711–25720 (2004).
5. Mulder, D.W. *et al. Nature* **465**, 248–251 (2010).
6. Czech, I., Silakov, A., Lubitz, W. & Happe, T. *FEBS Lett.* **584**, 638–642 (2010).
7. Tard, C. & Pickett, C.J. *Chem. Rev.* **109**, 2245–2274 (2009).
8. Tard, C. *et al. Nature* **433**, 610–613 (2005).
9. Li, H. & Rauchfuss, T.B. *J. Am. Chem. Soc.* **124**, 726–727 (2002).
10. Knörzer, P. *et al. J. Biol. Chem.* **287**, 1489–1499 (2012).
11. Berggren, G. *et al. Nature* **499**, 66–69 (2013).
12. Meyer, J. *Cell Mol. Life Sci.* **64**, 1063–1084 (2007).
13. Nicolet, Y., Piras, C., Legrand, P., Hatchikian, C.E. & Fontecilla-Camps, J.C. *Structure* **7**, 13–23 (1999).
14. Atta, M. & Meyer, J. *Biochim. Biophys. Acta* **1476**, 368–371 (2000).
15. van Dijk, C. & Veeger, C. *Eur. J. Biochem.* **114**, 209–219 (1981).
16. Winkler, M., Kuhlgert, S., Hippler, M. & Happe, T. *J. Biol. Chem.* **284**, 36620–36627 (2009).
17. Noth, J., Krawietz, D., Hemschemeier, A. & Happe, T. *J. Biol. Chem.* **288**, 4368–4377 (2013).
18. Lubitz, W., Reijerse, E. & van Gastel, M. *Chem. Rev.* **107**, 4331–4365 (2007).
19. Kamp, C. *et al. Biochim. Biophys. Acta* **1777**, 410–416 (2008).
20. Silakov, A., Kamp, C., Reijerse, E., Happe, T. & Lubitz, W. *Biochemistry* **48**, 7780–7786 (2009).
21. Adamska, A. *et al. Angew. Chem. Int. Ed. Engl.* **51**, 11458–11462 (2012).
22. Shepard, E.M. *et al. J. Am. Chem. Soc.* **132**, 9247–9249 (2010).
23. Mulder, D.W. *et al. Structure* **19**, 1038–1052 (2011).
24. Razavet, M. *et al. Chem. Commun. (Camb.)* **7**, 700–701 (2002).
25. Winkler, M., Esselborn, J. & Happe, T. *Biochim. Biophys. Acta* **1827**, 974–985 (2013).

## Acknowledgments

This work was supported by the Bundesministerium für Bildung und Forschung Bio-H2 project (to T.H. and W.L.), the Max Planck Society, the French National Research Agency (NiFe–Cat ANR–10–BLAN–711 and Labex Program ARCANE 11–LABX–003 to T.S.,V.A. and M.F.) and the European Research Council under the European Union's Seventh Framework Programme (FP/2007-2013/ERC grant agreement no. 306398 to V.A.). G.B. gratefully acknowledges the Bengt Lundqvist Minnesfond, The Swedish Research Council for Environment, Agricultural Sciences and Spatial Planning (contract no. 213-2010-563) and the Swedish Royal Academy of Sciences. T.H. gratefully acknowledges support from the Deutsche Forschungsgemeinschaft (HA 255/2-1) and the Volkswagen foundation (LigH2t). J.E. is financed by the Studienstiftung des deutschen Volkes.

## Author contributions

C.L., J.E., J.N., A.H., M.F., W.L. and T.H. conceived and designed experiments. C.L., J.S., J.E., J.N. and A.A. performed the experiments. C.L., J.E., J.N., A.H., A.A. and T.H. analyzed the data. G.B., T.S., V.A. and M.F. provided the $[2Fe]^{MIM}$ and $[2Fe]^{pdt}$ complexes. A.A., E.R. and W.L. performed and analyzed the EPR and FTIR experiments. All of the authors discussed the results. A.H., J.E. and T.H. wrote the manuscript.

## Competing financial interests

The authors declare no competing financial interests.

## Additional information

Supplementary information is available in the online version of the paper. Reprints and permissions information is available online at http://www.nature.com/reprints/index.html. Correspondence and requests for materials should be addressed to T.H.

## ONLINE METHODS

**Heterologous expression and purification of proteins.** Apo-HYDA1 and apo-CpI were produced anaerobically in *E. coli* BL21(DE3) Δ*iscR*[26], making use of optimized sequences and the pET expression system as described earlier[27] but without co-expression of maturase genes. *M. elsdenii hydA* was expressed accordingly after cloning of $hydA_{Me}$ from pT7HME[14] into pTSH_hydA1Cr_STII[28]. Purification of hydrogenases was carried out under strictly anaerobic conditions using a one-step strep-tactin affinity chromatography protocol, as described earlier, with minor modifications[28]. Heterologous synthesis of active HYDA1 in *Clostridium acetobutylicum* ATCC82414 (ref. 28), isolation of PSI[29] and plastocyanin from *C. reinhardtii*[30] as well as heterologous expression of PETF[16] and PFR1 (ref. 17) in *E. coli* were described earlier.

**Preparation of [2Fe]$^{MIM}$ and [2Fe]$^{pdt}$.** Synthesis of [2Fe]$^{MIM}$ and [2Fe]$^{pdt}$ (refs. 31,32) followed the previously published protocol[9], and, in the case of [2Fe]$^{pdt}$, with modifications as described earlier[11]. Crystalline compounds were dissolved in 20 mM HEPES, pH 7.5, 100 mM KCl; handled strictly anaerobically; and stored at −80 °C.

***In vitro* maturation of [FeFe]-hydrogenases.** *In vitro* maturation of hydrogenases was achieved by incubating 800 ng apo-protein (0.04 µM HYDA1) under strictly anaerobic conditions in 400 µl of 0.1 M potassium phosphate buffer, pH 6.8, with 2 mM sodium dithionite (NaDT) at 25 °C for 30 min with a tenfold molar excess of [2Fe]$^{MIM}$, unless stated otherwise. Subsequent *in vitro* activity measurements using NaDT-reduced methyl viologen as artificial electron donor were done as previously described[33]. Maturation of HYDA1$^{MIM}$ for EPR and FTIR measurements was carried out with 150 µM apo-HYDA1. The protein was subsequently purified and rebuffered to 0.01 M Tris-HCl, pH 8.0, 2 mM NaDT, by size-exclusion chromatography using a NAP-5 column (GE Healthcare) and concentrated to 500 µM for EPR and FTIR measurements using Amicon Ultra centrifugal filters 10K (Millipore). Spectra of 12 mM [2Fe]$^{MIM}$ were recorded in 20 mM HEPES buffer, pH 7.5, 100 mM KCl.

**Pyruvate-driven and light-driven hydrogen evolution assays.** Each pyruvate-driven reaction contained PFR1, PETF and *C. reinhardtii* HYDA1 or HYDA1$^{MIM}$ and pyruvate and acetyl-CoA in potassium phosphate buffer, pH 6.8, as described earlier[17]. The reaction mixtures were incubated for 30 min at 37 °C before analyzing the amount of $H_2$ in the gas phase. For light-driven measurements, PSI and plastocyanin from *C. reinhardtii*, ascorbate and dichlorophenolindophenol were combined with HYDA1 or HYDA1$^{MIM}$ and PETF as previously published[16]. These reaction mixtures were illuminated for 30 min at 30 °C using monochromatic white and red light (250 µE).

**Detection of CO by a hemoglobin-based assay.** Bovine hemoglobin (Sigma-Aldrich) was reduced to deoxyhemoglobin (Hb) under strictly anaerobic conditions with NaDT and was brought to ~4.5 µM hemoglobin in 100 mM potassium phosphate buffer, pH 6.8, with 2 mM NaDT. Spectra and single-wavelength kinetics were taken with a UV-2450 spectrophotometer (Shimadzu) at room temperature in sealed 1-ml micro UV-cuvettes to keep anaerobic conditions. [2Fe]$^{MIM}$ and apo-HYDA1 were injected with gastight syringes (Hamilton) from sealed, anaerobic vials. [2Fe]$^{MIM}$ was added to 10× the intended concentration of apo-HYDA1 (2 µM unless otherwise stated). After each injection, thorough mixing was ensured by inverting the cuvette several times. During the whole process, the absorbance at 419 nm characteristic for the maximum of the Soret peak of carbon monoxyhemoglobin (HbCO) was recorded. Concentrations of HbCO were calculated using the difference of the molar absorption coefficients of Hb and HbCO at 419 nm, which can be calculated from spectra of known concentrations of fully reduced Hb and fully saturated HbCO, respectively. The heme concentration could accurately be measured using published molar absorption coefficients of characteristic bands in the visible range[34].

**EPR and FTIR analyses.** FTIR spectra were obtained with a Bruker IFS 66v/s FTIR spectrometer equipped with a Bruker MCT (mercury cadmium telluride) detector. The spectra were accumulated in the double-sided, forward-backward mode with 1,000 scans and a resolution of 2 $cm^{-1}$ at 15 °C. Data processing was facilitated by home-written routines in the MATLAB program environment.

Q-band EPR spectra were measured using the two-pulse echo-detected EPR technique. The length of the π/2 and π MW pulses were set to 16 ns and 32 ns, respectively, separated with τ = 500 ns. The shot repetition time was set to 1 ms. All of the measurements were performed on a home-built Q-band pulse spectrometer. The temperature was controlled in a custom-built cryogen-free cryostat from Advanced Research Systems (base temperature 8 K). The sample was accommodated in a homebuilt Q-band ENDOR resonator insert[35].

**Statistical analyses.** All hydrogenase activity tests were done at least four times. Values shown are averages, and error bars show the s.d. EPR and FTIR analyses were done on two independently prepared samples.


26. Akhtar, M.K. & Jones, P.R. *Appl. Microbiol. Biotechnol.* **78**, 853–862 (2008).
27. Kuchenreuther, J.M. *et al. PLoS ONE* **5**, e15491 (2010).
28. von Abendroth, G. *et al. Int. J. Hydrogen Energy* **33**, 6076–6081 (2008).
29. Gulis, G., Narasimhulu, K.V., Fox, L.N. & Redding, K.E. *Photosynth. Res.* **96**, 51–60 (2008).
30. Kuhlgert, S., Drepper, F., Fufezan, C., Sommer, F. & Hippler, M. *Biochemistry* **51**, 7297–7303 (2012).
31. Schmidt, M., Contakes, S.M. & Rauchfuss, T.B. *J. Am. Chem. Soc.* **121**, 9736–9737 (1999).
32. Razavet, M. *et al. Dalton Trans.* **2003**, 586–595 (2003).
33. Hemschemeier, A., Melis, A. & Happe, T. *Photosynth. Res.* **102**, 523–540 (2009).
34. Zijlstra, W.G. & Buursma, A. *Comp. Biochem. Physiol. B* **118**, 743–749 (1997).
35. Reijerse, E., Lendzian, F., Isaacson, R. & Lubitz, W. *J. Magn. Reson.* **214**, 237–243 (2012).






doi:10.1038/nchembio.1311

**Spontaneous activation of [FeFe]-hydrogenases by an inorganic [2Fe] active site mimic**

Julian Esselborn[1], Camilla Lambertz[1,6], Agnieszka Adamska-Venkatesh[2,6], Trevor Simmons[3,6], Gustav Berggren[3,5], Jens Noth[1], Judith Siebel[2], Anja Hemschemeier[1], Vincent Artero[3], Edward Reijerse[2], Marc Fontecave[3,4], Wolfgang Lubitz[2] & Thomas Happe[1*]

## Supplementary Results

### Supplementary Figure 1

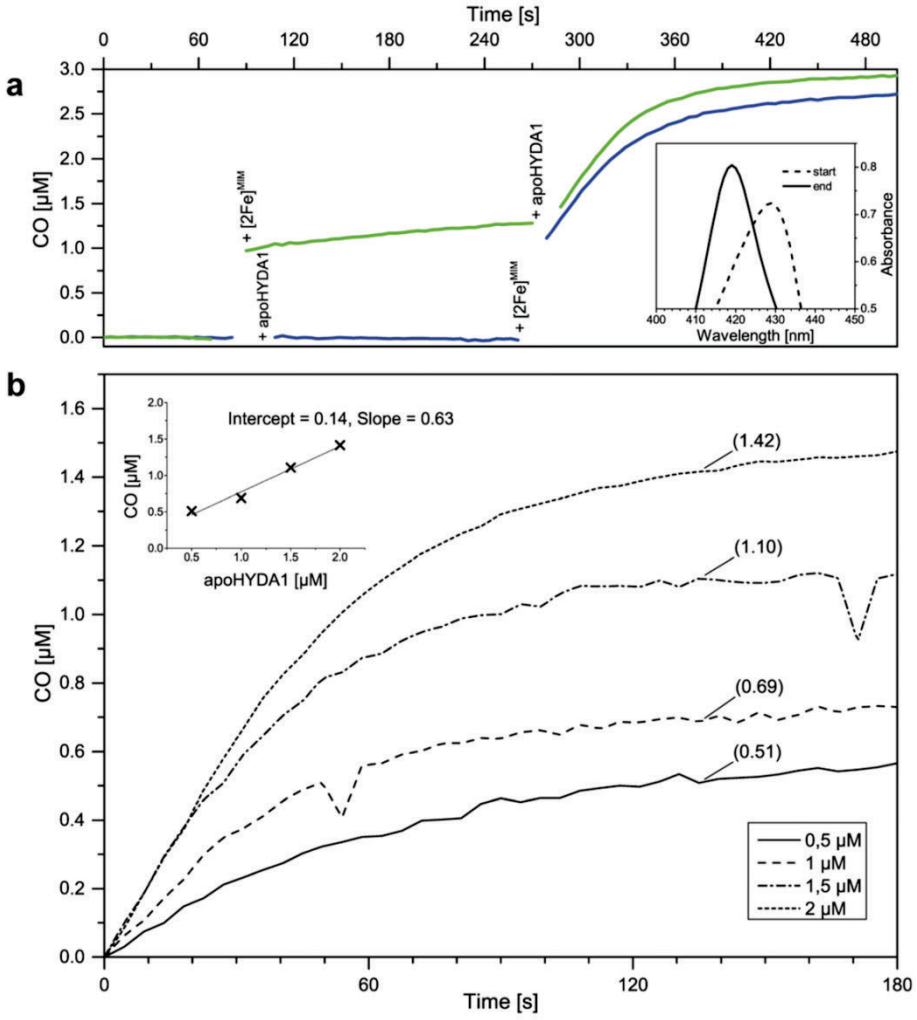




Nature Chemical Biology: doi:10.1038/nchembio.1311

**Supplementary Figure 1 | CO is released during the activation of apoHYDA1 by $[2Fe]^{MIM}$.** **(a)**, Time dependent evolution of CO monitored by the absorption of carbonmonoxyhemoglobin (HbCO) at 419 nm. $[2Fe]^{MIM}$ and apoHYDA1 were added to a final concentration of 20 µM and 2 µM, respectively, to a solution of ~ 4.5 µM deoxyhemoglobin (Hb) in potassium phosphate buffer pH 6.8 with 2 mM sodium dithionite at the indicated time points. Addition of $[2Fe]^{MIM}$ before application of apoHYDA1 (green line) resulted in an immediate increase of HbCO concentration probably due to accumulated CO in the $[2Fe]^{MIM}$ solution. Subsequently, a constant increase of $A_{419}$, interpreted as instability of $[2Fe]^{MIM}$ in solution at room temperature, was observed. Addition of apoHYDA1 first (blue line) did not result in formation of HbCO. In both cases the combination of apoHYDA1 and $[2Fe]^{MIM}$ led to a time dependent accumulation of HbCO. Typical spectra taken at the start and at the end of the assay show characteristic maxima at 430 nm (Hb) and 419 nm (HbCO) respectively (insert of **a**). **(b)**, Time dependent evolution of CO for different concentrations of apoHYDA1. CO evolution was analyzed like in **a** except that apoHYDA1 was added to different final concentrations to a solution of Hb (~ 4.5 µM) and $[2Fe]^{MIM}$ (20 µM). Calculated concentrations of CO in µM at 135 s after the mixing are given in parenthesis for each experiment. Plotting of these values against the respective final concentrations of apoHYDA1 results in a good linear fit indicating evolution of 0.63 mol CO per mol of apoHYDA1 (insert of **b**). The intercept value of 0.14 µM CO corresponds to evolution of CO due to spontaneous break-down of $[2Fe]^{MIM}$ over the course of 135 s as observed in **b**.

**Supplementary Figure 2**

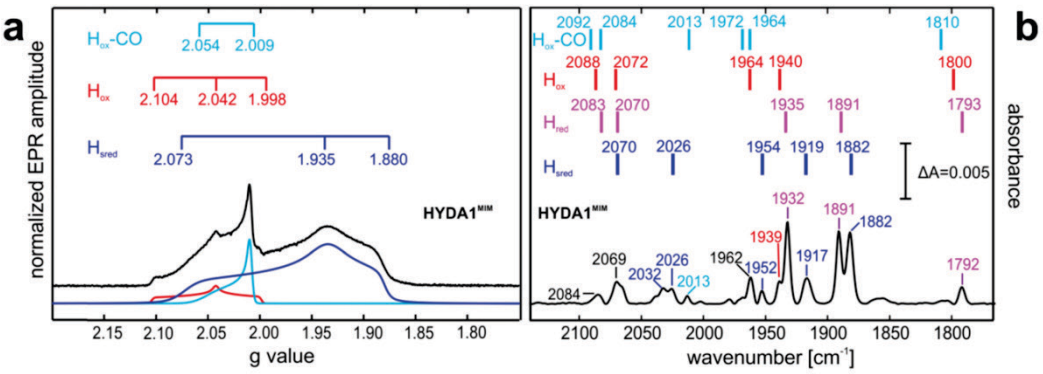


**Supplementary Figure 2 | EPR and FTIR spectra of chemically activated HYDA1 correspond well to simulations and previously reported peaks. (a)**, EPR spectrum of HYDA1$^{MIM}$ samples comprising all EPR active states as in Fig. 2a. Simulations of the signals for each state[19,21] are presented in color. The *g* values used for these simulations are displayed above the spectrum. **(b)**, FTIR spectrum of HYDA1$^{MIM}$ samples from Fig. 2b. Previously reported peak positions of as isolated *in vivo* matured HYDA1[20] are indicated above the spectrum. The colors correspond to the respective state.



Nature Chemical Biology: doi:10.1038/nchembio.1311

**Supplementary Figure 3**

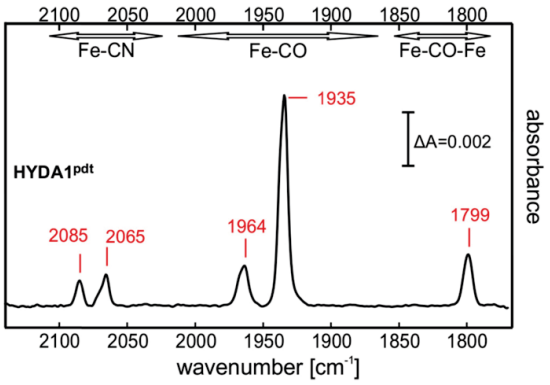


**Supplementary Figure 3 | Although catalytically inactive, the metallocluster which results from reconstitution of apoHYDA1 with [2Fe]$^{pdt}$ resembles the $H_{ox}$ state of the native H-cluster.** HYDA1$^{pdt}$ was generated and analyzed by FTIR spectroscopy as described in the materials and methods section. Unlike active HYDA1 or HYDA1$^{MIM}$, which show a mixture of states, HYDA1$^{pdt}$ features a signal representing only one defined state. This state is identical to the one observed in HYDA1$^{pdt}$ maturated by HYDF$^{pdt}$ as we have reported before[11].



Nature Chemical Biology: doi:10.1038/nchembio.1311

JACS
JOURNAL OF THE AMERICAN CHEMICAL SOCIETY
Article
pubs.acs.org/JACS

# New Redox States Observed in [FeFe] Hydrogenases Reveal Redox Coupling Within the H-Cluster

Agnieszka Adamska-Venkatesh,[†] Danuta Krawietz,[‡] Judith Siebel,[†] Katharina Weber,[†] Thomas Happe,[‡] Edward Reijerse,*[,†] and Wolfgang Lubitz*[,†]

[†]Max-Planck-Institut für Chemische Energiekonversion, Stiftstrasse 34-36, 45470 Mülheim an der Ruhr, Germany

[‡]Fakultät für Biologie und Biotechnologie, Lehrstuhl für Biochemie der Pflanzen, AG Photobiotechnologie, Ruhr Universität Bochum, Universitätsstraße 150, 44801 Bochum, Germany

Supporting Information

**ABSTRACT:** Active [FeFe] hydrogenases can be obtained by expressing the unmaturated enzyme in *Escherichia coli* followed by incubation with a synthetic precursor of the binuclear [2Fe] subcluster, namely: $[NEt_4]_2[Fe_2(adt)(CO)_4(CN)_2]$ (adt = $[S\text{-}CH_2\text{-}NH\text{-}CH_2\text{-}S]^{2-}$). The binuclear subsite $Fe_2(adt)(CO)_3(CN)_2$ is attached through a bridging cysteine side chain to a [4Fe-4S] subcluster already present in the unmaturated enzyme thus yielding the intact native "H-cluster". We present FTIR electrochemical studies of the [FeFe] hydrogenase from *Chlamydomonas reinhardtii*, CrHydA1, maturated with the precursor of the native cofactor $[Fe_2(adt)(CO)_4(CN)_2]^{2-}$ as well as a non-natural variant $[Fe_2(pdt)(CO)_4(CN)_2]^{2-}$ in which the bridging amine functionality is replaced by $CH_2$. The obtained active enzyme CrHydA1(adt) shows the same redox states in the respective potential range as observed for the native system ($E_{(ox/red)}$ = −400 mV, $E_{(red/sred)}$ = −470 mV). For the $H_{ox} \rightarrow H_{red}$ transition the reducing equivalent is stored on the binuclear part, ($[4Fe\text{-}4S]^{2+}Fe^{II}Fe^{I} \rightarrow [4Fe\text{-}4S]^{2+}Fe^{I}Fe^{I}$), while the $H_{red} \rightarrow H_{sred}$ transition is characterized by a reduction of the [4Fe-4S] part of the H-cluster ($[4Fe\text{-}4S]^{2+}Fe^{I}Fe^{I} \rightarrow [4Fe\text{-}4S]^{+}Fe^{I}Fe^{I}$). A similar transition is reported here for the CO inhibited state of the H-cluster: ($[4Fe\text{-}4S]^{2+}Fe^{I}Fe^{II}CO \rightarrow [4Fe\text{-}4S]^{+}Fe^{I}Fe^{II}CO$). An FTIR electrochemical study of the inactive variant with the pdt ligand, CrHydA1(pdt), identified two redox states $H^{pdt}$-ox and $H^{pdt}$-"red". Both EPR and FTIR spectra of $H^{pdt}$-ox are virtually identical to those of the $H^{adt}$-ox and the native $H_{ox}$ state. The $H^{pdt}$-"red" state is also characterized by a reduced [4Fe-4S] subcluster. In contrast to CrHydA1(adt), the $H^{pdt}$-ox state of CrHydA1(pdt) is stable up to rather high potentials (+200 mV). This study demonstrates the distinct redox coupling between the two parts of the H-cluster and confirms that the $[4Fe\text{-}4S]_H$ subsite is also redox active and as such an integral part of the H-cluster taking part in the catalytic cycle.

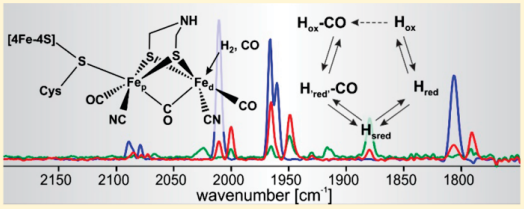


## 1. INTRODUCTION

Hydrogenases are metalloenzymes which catalyze both the production and oxidation of $H_2$ and are therefore of high interest for a future biohydrogen technology.[1−11] Since [FeFe] hydrogenases are the most active enzymes in hydrogen production *in vivo*, a detailed understanding of their catalytic mechanism is of great interest for developing artificial hydrogen production systems.[12,13] The active site of this enzyme is highly conserved and is referred to as the "H-cluster".[7,14−17] It contains a "classical" $[4Fe\text{-}4S]_H$ cluster coupled via one of its coordinating cysteine side groups to a unique binuclear subcluster $[2Fe]_H$, which is coordinated by $CN^-$ and CO ligands as well as a dithiolate bridging ligand.[16−23] Recent studies showed that various biomimetic complexes modeling the binuclear subcluster can be inserted directly or with the help of the maturation factor HydF into unmaturated [FeFe] hydrogenases that only contain the $[4Fe\text{-}4S]_H$ part of the H-cluster.[24,25] However, only the insertion of the binuclear cofactor containing the amine group in the dithiolate bridging ligand (adt) leads to the assembly of the native H-cluster (see Figure 1) and affords fully active enzyme.[24,25]

During the catalytic process of hydrogen conversion the iron centers in the H-cluster change their oxidation states.[7] In the most oxidized active redox state called $H_{ox}$ the binuclear subcluster is in the mixed valence $Fe^{I}Fe^{II}$ state while the [4Fe-4S] cluster is oxidized (2+).[7,26,27] This state is paramagnetic and shows a characteristic EPR signal with $g$ = [2.10, 2.037, 1.996].[27] Upon a fully reversible one-electron reduction (−400 mV for the native [FeFe] hydrogenase from *Chlamydomonas reinhardtii*: CrHydA1) $H_{ox}$ is converted into the active reduced state $H_{red}$ which has the binuclear site presumably in an $Fe^{I}Fe^{I}$ ($S$ = 0) configuration.[7,28] A subsequent fully reversible one-electron reduction (−460 mV for native CrHydA1) causes conversion of $H_{red}$ to the "super reduced" active state $H_{sred}$.[28] EPR studies showed that $H_{sred}$ is paramagnetic and gives a signal characteristic for a reduced $[4Fe\text{-}4S]^+$ cluster.[26] According to our previously

**Received:** April 4, 2014
**Published:** July 15, 2014

  

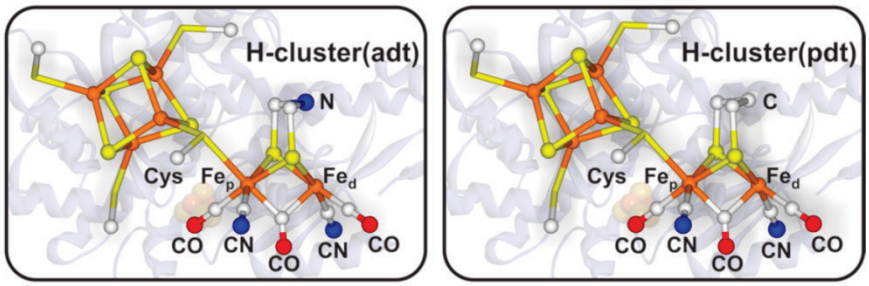


**Figure 1.** Structure of the active site (H-cluster) of artificially maturated [FeFe] hydrogenase with natural ($H^{adt}$) and non-natural ($H^{pdt}$) binuclear subsite.

proposed mechanism all these states are involved in the catalytic cycle.[26] In protein film electrochemistry (PFE) it was observed that CrHydA1 is very active over a large potential range and especially at low potentials shows high turnover rates in hydrogen production.[29]

The H-cluster of the active protein can be inhibited by CO generating the $H_{ox}$-CO state.[7,15,30] The electronic structure of $H_{ox}$-CO is similar to that of $H_{ox}$ and is characterized by a mixed valence ($Fe^{I}Fe^{II}$) subsite in combination with an oxidized $[4Fe\text{-}4S]_H^{2+}$ subcluster.[7] The characteristic EPR and FTIR spectra of $H_{ox}$-CO are often observed in [FeFe] hydrogenase preparations that are exposed to light and/or oxygen. In this case the CO inhibited state is generated by the so-called "cannibalization process" in which the CO ligands released from destroyed H-clusters are captured by H-clusters that are still intact.[31,32] Up to now, no redox activity of the $H_{ox}$-CO state has been reported. In fact, a recent protein film electrochemical study in combination with DFT calculations indicated that reduction of $H_{ox}$-CO leads to damage or even dissociation of the H-cluster.[33]

In the current study we present FTIR spectroelectrochemical investigations of artificially maturated CrHydA1 using both the precursor of the native [2Fe] cofactor $[Fe_2(adt)(CO)_4(CN)_2]^{2-}$ and the non-natural variant $[Fe_2(pdt)(CO)_4(CN)_2]^{2-}$ in which the central bridging amine (NH) function is substituted by $CH_2$ (see Figure 1). For the native "hybrid protein" CrHydA1(adt) also the CO-inhibited state was investigated. We show that both CrHydA1(adt) under CO and CrHydA1(pdt) exhibit a redox transition which most likely involves the $[4Fe\text{-}4S]_H$ subsite.

## 2. EXPERIMENTAL SECTION

The synthesis of the $[Fe_2(adt)(CO)_4(CN)_2]^{2-}$ and $[Fe_2(pdt)(CO)_4(CN)_2]^{2-}$ biomimetic complexes followed previously published protocols.[34−36] Crystalline compounds were dissolved in DMSO and then diluted in Tris/HCl pH 8.0 buffer or directly dissolved in the buffer and handled strictly anaerobically.

$CrHydA1^{\Delta EFG}$ (hydrogenase expressed without maturases) was produced in *Escherichia coli* as described earlier.[25,37] The *in vitro* maturation of the [FeFe] hydrogenase was also described previously.[25] All steps were carried out under strict anaerobic conditions. CrHydA1 was prepared in 100 mM Tris/HCl pH 8.0, 2 mM sodium dithionate buffer with addition of 100 mM KCl to samples on which electrochemical experiments were performed. Oxidized samples were prepared by FTIR monitored stepwise titration with thionine.

Fourier transform infrared (FTIR) measurements were carried out using a Bruker IFS 66v/s FTIR spectrometer equipped with a nitrogen cooled Bruker mercury cadmium telluride (MCT) detector. The spectra were accumulated in the double-sided, forward−backward mode with 1000 scans (14 min) and a resolution of 2 $cm^{-1}$ at 15 °C. Data processing was facilitated by home written routines in the MATLAB programming environment.

All spectroelectrochemical experiments were performed using a home-built electrochemical IR cell, constructed according to an original design by Moss et al.[7,38] Samples were loaded in between two $CaF_2$ windows on an electrochemically reduced gold mesh (approximately 50 $\mu$m thick) in electrical contact with the platinum counter electrode. An Ag/AgCl (1 M KCl) electrode was used as reference and was calibrated before and after each measurement by reduction/oxidation of methyl viologen. All potentials are listed versus the normal hydrogen electrode (NHE), and the uncertainty of the midpoint potentials was estimated to be ±20 mV. In the titrations the potential was controlled by an Autolab PGSTAT101 potentiostat using the Nova software. Since no mediators were used an extended equilibration time period of 30 min was applied at each potential. The temperature was controlled by a Huber Minichiller, and all experiments were performed at 15 °C.

Q-band EPR spectra were recorded using free induction decay (FID) detected EPR with a microwave pulse length of 1 $\mu$s. All pulse experiments were performed on a Bruker ELEXYS E580 Q-band spectrometer with a SuperQ-FT microwave bridge and a home-built resonator described earlier.[39] The magnetic field was calibrated using a Bruker ER035D NMR gaussmeter. X-band continuous wave (CW) EPR measurements were performed on a Bruker ELEXYS E-580 X-band spectrometer with a SuperX-FT microwave bridge and Bruker ER EN4118X-MD5 dielectric resonator. Cryogenic temperatures (10−20 K) were obtained by an Oxford CF935 flow cryostat. For the interpretation of all EPR experimental data, a home written simulation program (based on the EasySpin package)[40] in MATLAB was used.

## 3. RESULTS AND DISCUSSION

**3.1. FTIR Electrochemistry for CrHydA1(adt) (Active Hybrid Enzyme).** Figure 2A shows selected FTIR spectra of CrHydA1(adt) recorded during electrochemical oxidation. The potentials were chosen such that in each spectrum one of the well-known redox states $H_{ox}$, $H_{red}$, and $H_{sred}$ has its maximum contribution.[28] In Figure 2B the intensities of one representative CO band for each of the states $H_{ox}$, $H_{red}$, and $H_{sred}$ is plotted against the redox potential in the FTIR cell. Two fully reversible one-electron transitions with midpoint potentials in agreement (within experimental uncertainty) with the previously reported values for the native CrHydA1 hydrogenase were observed.[28] No signal loss occurred upon reduction from $H_{red}$ to $H_{sred}$ and reoxidation back to $H_{red}$ (see Supporting Information). This suggests that no irreversible damage takes place at low potentials. A different situation is observed at high potentials. Above −300 mV the intensity of the oxidized state rapidly decreases (see Figure 2B), which can be attributed to irreversible damage of the H-cluster and release of the CO ligands. At the same time, an increase of the signal originating from the CO inhibited state ($H_{ox}$-CO) is observed corresponding to the "cannibalization

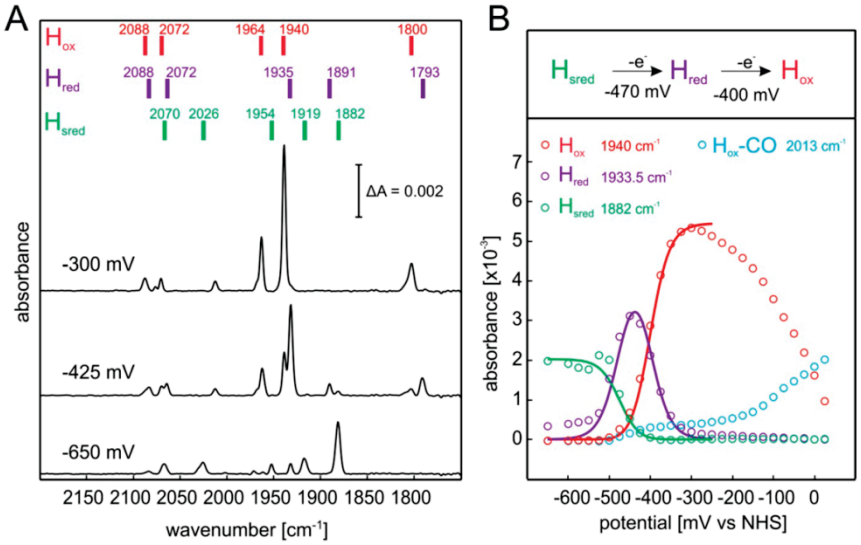


**Figure 2.** (A) Selected IR spectra of 1 mM CrHydA1(adt) in 100 mM Tris/HCl buffer pH 8.0, 100 mM KCl, 2 mM sodium dithionate at different redox potentials measured at 15 °C. At the top of the figure the band positions of the active states are indicated.[28] In the spectra taken at −300 and −425 mV also a fraction of $H_{ox}$-CO (signal position: 2092, 2084, 2013, 1970, 1964, and 1810 $cm^{-1}$) is present. (B) Oxidative titration of the active enzyme. The red circles correspond to the intensity of the most prominent CO band of the $H_{ox}$ state at 1940 $cm^{-1}$, violet circles represent the signal at 1933.5 $cm^{-1}$ characteristic for $H_{red}$, green circles indicate the signal at 1882 $cm^{-1}$ of $H_{sred}$, while the light-blue circles indicate the band amplitude at 2013 $cm^{-1}$ of the $H_{ox}$-CO state. The solid lines correspond to $n$ = 1 Nerstian curves, $E_{ox/red}$ = −400 mV ± 20 mV and $E_{red/sred}$ = −470 mV ± 20 mV.

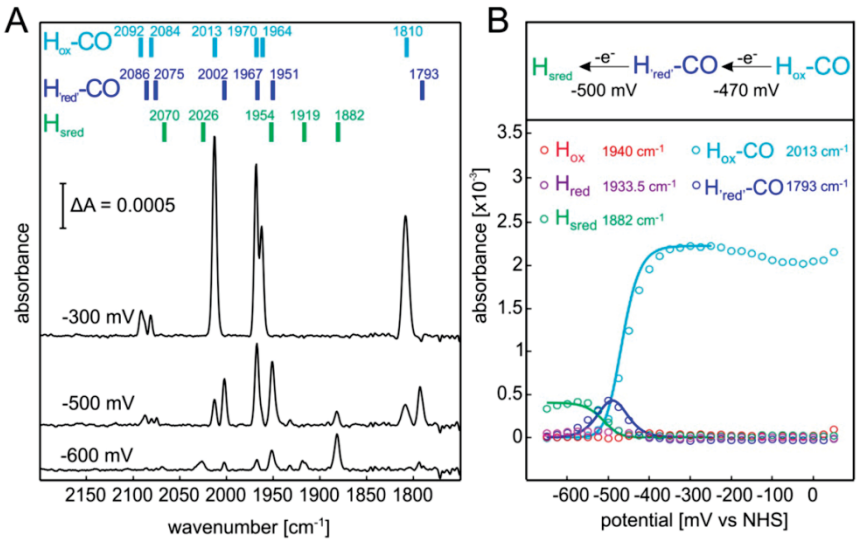


**Figure 3.** (A) Selected IR spectra of CrHydA1(adt) under CO gas at different redox potentials measured at 15 °C. The top of the figure shows the signal positions of the observed redox states.[28] (B) Reductive titration of the CO inhibited enzyme. The red circles correspond to intensity of the most prominent CO band of the $H_{ox}$ state at 1940 $cm^{-1}$, violet circles to the signal at 1933.5 $cm^{-1}$ characteristic for $H_{red}$, the green ones to 1882 $cm^{-1}$ of $H_{sred}$, the light blue ones to 2013 $cm^{-1}$ from the $H_{ox}$-CO state, and the blue ones to 1793 $cm^{-1}$ of the $H_{red}$-CO state. The solid lines correspond to $n$ = 1 Nerstian curves, $E_{ox\text{-}CO/red\text{-}CO}$ = −470 mV ± 20 mV and $E_{red\text{-}CO/sred}$ = −500 mV ± 20 mV.

effect".[31,32] It is interesting to note that in this type of experiment no reversible transition to a "super oxidized" state is observed.[32] This is in contrast to the situation in PFE experiments where for many [FeFe] hydrogenases the cyclic voltammogram shows a reversible oxidative inhibition at high potentials.[12,41] However, this discrepancy could be related to the different experimental


dx.doi.org/10.1021/ja503390c | J. Am. Chem. Soc. 2014, 136, 11339−11346

conditions in the respective electrochemical cells. For example, a recent study by Leger et al. showed that reversible oxidative inactivation at high potentials is facilitated by the presence of $H_2$ which, apparently, stabilizes high potential inactive states of the H-cluster.[42]

**3.2. FTIR Electrochemistry on CrHydA1(adt) in the Presence of CO (Reductive Titration).** By keeping the sample at high potential (+50 mV) the H-clusters are progressively disintegrated leading to a decreasing intensity of the $H_{ox}$ signal and a steady increase of the $H_{ox}$-CO signal until eventually only this species remains in FTIR. It is estimated that this harsh procedure leaves approximately 20−25% (see Supporting Information) of the H-clusters as $H_{ox}$-CO, while the rest is disintegrated and the released CO and CN ligands are no longer iron bound and therefore do not show up in the FTIR range of the H-cluster. The sample can now be considered as CO inhibited [FeFe] hydrogenase. Upon reducing the redox potential from 50 to −300 mV the signal intensity from $H_{ox}$-CO does not change suggesting that no further damage occurs (see Figure 3B).

Lowering the potential further results in a decrease of the signal from $H_{ox}$-CO and the appearance of new signals at 2086 and 2075 $cm^{-1}$ assigned to the $CN^-$ ligands as well as signals at 2002, 1967, and 1951 $cm^{-1}$ which are assigned to coupled vibrations of terminal CO ligands and finally a signal at 1793 $cm^{-1}$ which is typical for a bridging CO ligand. The maximum of this new signal is reached at −500 mV (see Figure 3A). The FTIR peak positions of this signal were previously observed in FTIR spectra obtained for heterologously expressed CrHydA1 flushed with CO gas.[25,37] However, at that time these signals could not be assigned to a particular H-cluster state. From the current experiment we must conclude that this new signal is associated with a one-electron reduced CO inhibited state. The small shifts of the CO bands (in the range 3−17 $cm^{-1}$) with respect to the $H_{ox}$-CO spectrum as well as the midpoint potential of −470 mV, which is the same as $E_{red/sred}$, would suggest that reduction takes place on the $[4Fe\text{-}4S]_H$ cluster generating a $[4Fe\text{-}4S]^+$ configuration. To further support this hypotheses experiments involving light induced $^{13}CO$ scrambling were carried out and presented in Supporting Information (Figure S9).[32] Figure 4 presents the shift of the IR bands originating from the CO ligands of CrHydA1(adt) in the CO inhibited states after stepwise replacement of $^{12}CO$ by $^{13}CO$: (i) exposure to $^{13}CO$ in the dark; and (ii) CO scrambling by illumination. It was confirmed that the 2002 $cm^{-1}$ band from $H_{red}$-CO corresponds to the band at 2013 $cm^{-1}$ from $H_{ox}$-CO and the 1967 $cm^{-1}$ band corresponds to that at 1970 $cm^{-1}$. These two bands were previously assigned to $\nu_{sym}$ and $\nu_{asym}$ of the two vibrationally coupled terminally CO ligands bound to the distal iron.[32] Thus, the largest shift is observed for the band assigned to the CO ligand bound to the proximal iron from 1964 $cm^{-1}$ ($H_{ox}$-CO) to 1951 $cm^{-1}$ ($H_{red}$-CO). Although FTIR does not provide *direct* information on the oxidation state of the H-cluster, given the very small difference in the band positions of both states a change of the oxidation state of $Fe_d$ seems very unlikely. The maximum intensity of the so-called $H_{red}$-CO signal is observed around −500 mV. Already at this potential the signal originating from the $H_{sred}$ state appears. Further lowering of the potential leads to complete conversion into the super reduced state ($H_{sred}$) (with CO release) leaving the binuclear center in the $Fe^IFe^I$ form. No signals characteristic for oxidized ($H_{ox}$) and reduced states ($H_{red}$) were observed during this titration.

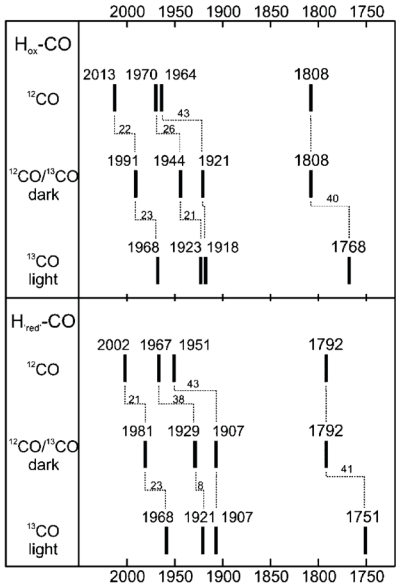


**Figure 4.** Overview of shifts of IR bands originating from the CO ligands of CrHydA1(adt) in the CO inhibited states upon replacing $^{12}CO$ by $^{13}CO$. The first rows in both panels display the band positions for the samples prepared under $^{12}CO$. The middle rows show the shifted band positions resulting from $^{13}CO$ treatment in the dark. For these samples only one distal CO and (surprisingly) the proximal CO is exchanged to $^{13}CO$. In the last rows the band positions upon complete $^{13}CO$ exchange (scrambling by illumination) are presented.

The CO inhibition of various [FeFe] hydrogenases was studied extensively by PFE experiments as well as through DFT calculations.[33,41,43] It was observed that at high potentials CO inhibition is complete and fully reversible, while at low potentials it is not. From these observations it was concluded that CO strongly binds to the $H_{ox}$ state and less tightly to $H_{red}$ leading to partial but irreversible damage of the H-cluster.[33,41] It should be noted, however, that the individual redox states cannot be observed in these experiments since the protein is under turnover. Therefore, all redox states involved in the active cycle will occur. DFT studies predict that binding of CO to the $H_{red}$ state, where the H-cluster is in the $[4Fe\text{-}4S]^{2+}$ $Fe^IFe^I$ configuration, causes elongation of the Fe-$S_{cys}$ distance and subsequent cleavage of this bond.[33] However, our experiments show that the oxidized CO inhibited state is present in a potential range where both uninhibited oxidized and reduced states can also occur. Also no signal originating from a released binuclear site was observed (see original spectra in Supporting Information) suggesting no dissociation of the binuclear site. DFT calculations also show that $H_{sred}$ has a very low affinity for CO and that the structural integrity of the H-cluster would be maintained in this state.[33] This would explain why after the second reduction the extrinsic CO ligand is released and the super reduced state is formed. The reduced CO inhibited configuration observed in our experiments $[4Fe\text{-}4S]^+Fe^IFe^{II}$ was however not considered in these DFT studies and turns out to be perfectly stable.

Protein film electrochemistry studies by Armstrong and co-workers of three [FeFe] hydrogenases, including CrHydA1,

under addition of CO have revealed that the relative inhibition of the enzyme as a function of the applied electrochemical potential can be divided into three ranges, each separated by a one-electron redox transition.[43] In the high potential range, where $H_{ox}$ should be present, the active site is strongly inhibited by CO (90%) while in the lowest potential range, where $H_{sred}$ should be accumulated, activity is hardly affected (10%).[43] The middle range (presumably $H_{red}$) shows around 75% inhibition. These data would suggest that under turnover conditions at the electrode $H_{red}$ can be inhibited to a certain extent, thus implicating a CO binding event. Our data are in agreement with these observations and allow us to postulate that also in other [FeFe] hydrogenases a "reduced" CO inhibited state may exist. However, in these multidomain [FeFe] hydrogenases, $H_{red}$-CO similar to $H_{sred}$, does not occur as a resting state because the reduced $[4Fe\text{-}4S]_H$ subcluster is quickly reoxidized through the redox coupling with the accessory [4Fe-4S] clusters.[7,26]

**3.3. FTIR Electrochemistry for CrHydA1(adt) in the $H_{sred}$ State in the Presence of CO.** In Figure 5 the oxidative titration of the $H_{sred}$ sample under CO obtained at the end of the previous run (section 3.2) is presented. Figures 3B and 5 show that also under CO, the intensity of the signal originating from the super

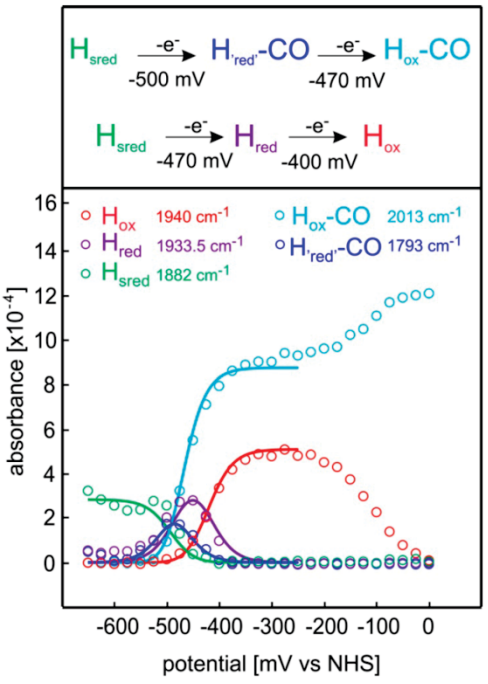


**Figure 5.** Oxidative titration of CrHydA1(adt) in the presence of CO gas. The red circles correspond to the intensity of the most prominent CO band of the $H_{ox}$ state at 1940 $cm^{-1}$, violet circles to the signal at 1933.5 $cm^{-1}$ characteristic for $H_{red}$, the green ones belong to 1882 $cm^{-1}$ from $H_{sred}$, the light blue ones to 2013 $cm^{-1}$ from the $H_{ox}$-CO state and the blue ones to 1793 $cm^{-1}$ from the $H_{red'}$-CO state. The solid lines correspond to $n = 1$ Nerstian curves, $E_{ox/red} = -400$ mV ± 20 mV, $E_{red/sred} = -470$ mV ± 20 mV, $E_{ox\text{-}CO/red'\text{-}CO} = -470$ mV ± 20 mV and $E_{red'\text{-}CO/sred} = -500$ mV ± 20 mV.

reduced state does not change which indicates that no H-cluster destruction occurs. Figure 5 shows that during $H_{sred}$ oxidation in the presence of CO, two processes take place: The reduced CO inhibited state ($H_{red'}$-CO) reappears and further converts into the $H_{ox}$-CO state. Simultaneously, as was previously observed during the titration without CO, conversion from $H_{sred}$ to $H_{red}$ and subsequently to $H_{ox}$ occurs. This indicates that reactivation of the CO inhibited sample proceeds through the $H_{sred}$ state. The fact that upon oxidation of $H_{sred}$ not all H-clusters are converted back into the $H_{red'}$-CO state may be related to CO gas diffusing out of the electrochemically active volume of the FTIR cell thereby reducing effective CO partial pressure in the cell.

The observations described above allow us to construct the scheme shown in Figure 6 presenting two fully reversible

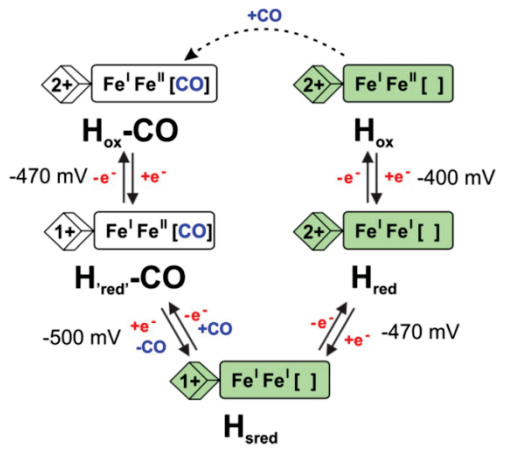


**Figure 6.** Schematic representation of the redox state conversion with and without CO gas. Under CO the oxidation of $H_{sred}$ to $H_{ox}$-CO proceeds through $H_{red'}$-CO as an intermediate state, while without CO the "active" oxidation path is chosen along the catalytic states $H_{red}$ and $H_{ox}$. Redox states involved in the catalytic cycle are marked in green.[26] The scheme representing the catalytically active cycle is presented in the Supporting Information.

"pathways": one CO inhibited path and a second active path, joined through the super reduced state. It is shown that artificially maturated [FeFe] hydrogenase behaves exactly the same way as the native enzyme; when no external CO is present the active oxidative path is chosen. With increasing CO partial pressure, the CO-path will become more dominant. It is interesting that even though the active sites of [FeFe] and [NiFe] hydrogenases are structurally very different they show a parallel behavior of their redox processes in the presence of extrinsic CO. Also in [NiFe] hydrogenase the most reduced state cannot be inhibited by CO gas and during its oxidation two CO inhibited states separated by one-electron transition are appearing.[7,44]

**3.4. FTIR Electrochemistry and EPR Studies on CrHydA1(pdt).** In recent studies it was demonstrated that the non-natural cofactor $[Fe_2(pdt)(CO)_4(CN)_2]^{2-}$, in which the bridging amine group is changed from NH to $CH_2$, can be incorporated into the unmaturated [FeFe] hydrogenase (containing only the [4Fe-4S] cluster).[24,25] It was also shown that this hybrid does not have any significant hydrogenase activity. At the same time it was noted that its FTIR spectrum (with band positions 2084 and 2065 $cm^{-1}$ for the $CN^-$ ligands,

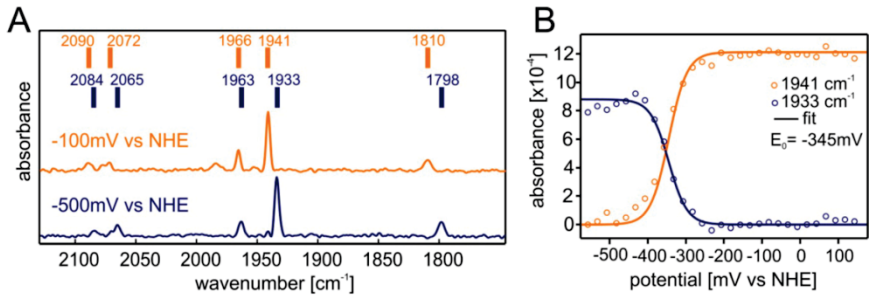


**Figure 7.** (A) Selected IR spectra of CrHydA1(pdt) at different redox potentials measured at 15 °C. On top the signal positions of the observed redox states are indicated. (B) Oxidative titration of the enzyme. The orange circles correspond to the intensity of the most prominent CO band of the oxidized state at 1941 $cm^{-1}$ and the dark-blue circles to the signal at 1933 $cm^{-1}$ characteristic for the reduced form. The solid lines correspond to $n = 1$ Nerstian curves, $E_{oxidized/reduced} = -345$ mV ± 20 mV.

1963 and 1933 $cm^{-1}$ for the terminal CO ligands and 1798 $cm^{-1}$ for the bridging CO ligand) strongly resembles that of the $H_{ox}$ state of the native hydrogenase (see Figure 7A).

Figure 7B shows the FTIR monitored electrochemical titration of the CrHydA1(pdt) hybrid. Although inactive, the enzyme still shows one fully reversible one-electron redox transition. The originally reported signal[24,25] belongs to the reduced form, whereas the oxidized state is characterized by a very similar signal with slightly shifted band positions at 2090 and 2072 $cm^{-1}$ for the $CN^-$ ligands, 1966 and 1941 $cm^{-1}$ for the terminal CO ligands and 1810 $cm^{-1}$ for the bridging CO as depicted in Figure 7A. In both oxidation states the bridging CO is present as well as two bands from terminal CO ligands indicating that the additional CO ligand from the biomimetic complex was released upon insertion and that the open coordination site at the distal iron still should be present. Short exposure of the sample to low amounts of oxygen leads to complete loss of the H-cluster FTIR signature. However, despite the high oxygen sensitivity of this CrHydA1-(pdt) hybrid no CO inhibited form could be identified. The nonaccessibility of the open coordination site might be related to the distortion of the bridging headgroup which is not able to create hydrogen bonds with the surrounding protein environment thereby blocking access for CO. The phenomenon will be investigated in more detail in a future study.

It is demonstrated in Figure 7B that in contrast to CrHydA1(adt) destruction of the active site occurs neither at low (−550 mV) nor at high potentials (+150 mV). This would suggest that turnover of the native enzyme and the active CrHydA1(adt) hybrid at high potentials leads to damage of the H-cluster. Presumably, the redox transition to the overoxidized state ($[4Fe\text{-}4S]^{2+}Fe^{II}Fe^{II}$) which is unstable in CrHydA1, occurs at much higher potential for CrHydA1(pdt).

The EPR spectrum recorded for the oxidized form of CrHydA1(pdt) shown in Figure 8 resembles the $H_{ox}$ state of the native system with $g$ values [2.094, 2.039, 1.998] which suggests that this form can be described by an oxidized $[4Fe\text{-}4S]^{2+}$ cluster and binuclear center in the mixed valence state $Fe^{I}Fe^{II}$. One-electron reduction can take place either on the cubane subsite leading to $[4Fe\text{-}4S]^{+}Fe^{I}Fe^{II}$ or on the binuclear subsite yielding $[4Fe\text{-}4S]^{2+}Fe^{I}Fe^{I}$ analogous to the "native" $H_{red}$-state. Both configurations are expected to be EPR silent due to the strong exchange couplings in the H-cluster. Spin counting (see Supporting Information) confirmed that the reduced CrHydA1(pdt) hybrid is indeed EPR silent.

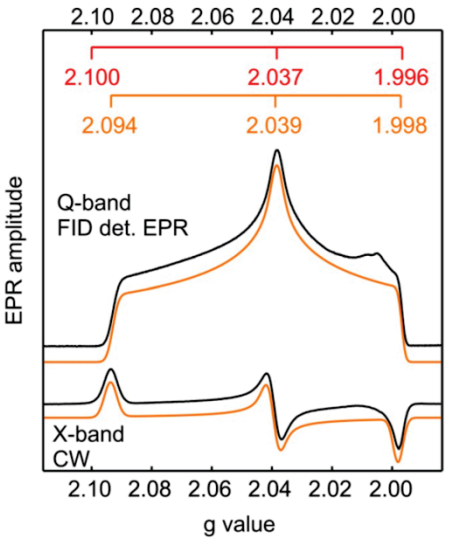


**Figure 8.** X-band continuous wave and Q-band FID detected EPR spectra (black) and simulations (orange) obtained for the oxidized form of CrHydA1(pdt) measured at 20 K. For comparison the corresponding $g$ values of the $H_{ox}$ state of the native enzyme are presented in red at the top of the figure.[26]

The shift of the FTIR band positions between reduced and oxidized forms is very small; for the CO ligands it lies in the range between 3 and 12 $cm^{-1}$. The same small shift is observed for the two CO inhibited states in the native system (*vide supra*). Following the same arguments this would suggest that the reduction occurs on the $[4Fe\text{-}4S]_H$ subcluster.

In principle it can be rationalized that the lack of a protonatable headgroup on the binuclear subsite in CrHydA1(pdt) would lead to a decrease of its redox potential since proton coupled electron transfer (PCET) would be inhibited.[45] This would then favor a reduction of the cubane part of the H-cluster. This argument, however, does not explain why the resulting redox potential of the cubane subcluster is even higher (−345 mV) than that of the $H_{ox}$-$H_{red}$ transition in the native system (−400 mV). A similar argument can be invoked for the redox behavior of CrHydA1-(adt) in the $H_{ox}$-CO state. The extrinsic donor ligand (CO) will

shift the electron density in the binuclear subsite toward the proximal iron: While the binuclear subsite in $H_{ox}$ is valence delocalized, $H_{ox}$-CO shows a $Fe(I)_pFe(II)_d$ configuration.[27,46] A similar trend is observed in model systems but there the transition is from $Fe(II)_pFe(I)_d$ in $H_{ox}$ models to $Fe(1.5)_pFe(1.5)_d$ in $H_{ox}$-CO models.[47,48] These complexes are shown to become oxidized easier.[49] In analogy, a similar effect could be expected for the H-cluster. Indeed, in this case the resulting midpoint potential (−470 mV) is lower than that of the regular CrHydA1(adt) $H_{ox} \rightarrow H_{red}$ transition (−400 mV).

## 4. CONCLUSIONS

We identified two new redox states in [FeFe] hydrogenases in which the $[4Fe\text{-}4S]_H$ subsite is reduced while the binuclear part remains mixed valence ($Fe^IFe^{II}$). For both species: $H^{adt}_{red}$-CO and $H^{pdt}_{red}$ it can be argued that the redox potential of the binuclear part is lowered by changes of the catalytic site of the H-cluster, i.e., modification of the aza-dithiol bridge to propanedithiol or blocking the open coordination site in the native H-cluster by CO. This leads to a redirection of the electron flow from the binuclear part toward the $[4Fe\text{-}4S]_H$ subsite. Therefore, it can be concluded that the electronic structure of the H-cluster is governed by a strong redox coupling between the two subsites which also must be relevant for its catalytic properties.

We also demonstrated that extrinsic CO binds both in the $H_{ox}$ and $H_{red'}$ state of the native H-cluster. The binding of CO to $H_{red'}$, however, causes a change of the redox equilibrium between the two subsites and induces a transfer of the redox equivalent from the $Fe^IFe^I$ binuclear subcluster to the $[4Fe\text{-}4S]_H$ unit leaving the binuclear part in the $Fe^IFe^{II}$ state. It can therefore be concluded that CO exclusively binds to the divalent distal iron.

Intriguingly, the (effective) redox potential of the $[4Fe\text{-}4S]_H$ subcluster amounts to −470 mV for both the $H_{ox}$-CO to $H_{red'}$-CO transition and the $H_{red}$ to $H_{sred}$ transition. Apparently, the redox properties of the $[4Fe\text{-}4S]_H$ subcluster do not change when the binuclear subcluster is in the $Fe^IFe^{II}CO_{ext}$ or $Fe^IFe^I$ configuration.

Although the CrHydA1(pdt) is oxygen sensitive like CrHydA1(adt), CO does not seem to bind to CrHydA1(pdt). In native CrHydA1 the adt bridge is conformationally controlled by weak hydrogen bridges to the surrounding amino acid site chains. These interactions are absent in CrHydA1(pdt).We must therefore conclude that the conformation of the dithiol bridge plays an important role in controlling access to the exchangeable site at the distal iron.

## ■ ASSOCIATED CONTENT

### Supporting Information

FTIR electrochemical data processing, determination of the redox midpoint potentials, $^{13}CO$ exchange experiments, spin counting, and associated figures. This material is available free of charge via the Internet at http://pubs.acs.org.

## ■ AUTHOR INFORMATION

### Corresponding Authors

edward.reijerse@cec.mpg.de
wolfgang.lubitz@cec.mpg.de

### Notes

The authors declare no competing financial interest.

## ■ ACKNOWLEDGMENTS

This work builds on our collaborative project with Marc Fontecave and Vincent Artero (Paris/Grenoble) who laid the foundation for the technique of artificial maturation. We gratefully acknowledge their contribution. We would like to thank Gudrun Klihm for her excellent technical support in the EPR experiments. Furthermore, the Max Planck Society is gratefully acknowledged for its generous financial support. Also support from DFG (HA255/2-1) and Volkswagen Foundation (Project ref. 90352) is gratefully acknowledged.

## ■ REFERENCES

(1) Miyake, J.; Igarashi, Y.; Rögner, M. *Biohydrogen III*; Elsevier: Amsterdam, 2004.
(2) Rand, D. A. J.; Dell, R. M. *Hydrogen Energy Challenges and Prospects*; RSC Publishing: Cambridge, 2008.
(3) Mertens, R.; Liese, A. *Curr. Opin. Biotechnol.* **2004**, *15*, 343.
(4) Kim, J. Y. H.; Cha, H. J. *Korean J. Chem. Eng.* **2013**, *30*, 1.
(5) Jugder, B.-E.; Welch, J.; Aguey-Zinsou, K.-F.; Marquis, C. P. *RSC Adv.* **2013**, *3*, 8142.
(6) Bockris, J. O. M. *Int. J. Hydrogen Energy* **2013**, *38*, 2579.
(7) Lubitz, W.; Ogata, H.; Rüdiger, O.; Reijerse, E. *Chem. Rev.* **2014**, *114*, 4081.
(8) Vignais, P. M.; Billoud, B. *Chem. Rev.* **2007**, *107*, 4206.
(9) *Hydrogen as a Fuel: Learning from Nature*, Cammack, R. F. M.; Robson, R., Eds.; Taylor & Francis: London, 2001.
(10) *Chemical Energy Storage*; Schlögl, R., Ed.; De Gruyter: Berlin, 2013.
(11) *Molecular Solar Fuels*; Wydrzynski, T. J., Hillier, W., Eds. Royal Society of Chemistry: Cambridge, 2012.
(12) Stripp, S. T.; Happe, T. *Dalton Trans.* **2009**, 9960.
(13) Hatchikian, E. C.; Forget, N.; Fernández, V. M.; Williams, R.; Cammack, R. *Eur. J. Biochem.* **1992**, *209*, 357.
(14) Nicolet, Y.; de Lacey, A. L.; Vernède, X.; Fernández, V. M.; Hatchikian, E. C.; Fontecilla-Camps, J. C. *J. Am. Chem. Soc.* **2001**, *123*, 1596.
(15) Lemon, B. J.; Peters, J. W. *Biochemistry* **1999**, *38*, 12969.
(16) Peters, J. W.; Lanzilotta, W. N.; Lemon, B. J.; Seefeldt, L. C. *Science* **1998**, *282*, 1853.
(17) Nicolet, Y.; Piras, C.; Legrand, P.; Hatchikian, C. E.; Fontecilla-Camps, J. C. *Structure* **1999**, *7*, 13.
(18) Fontecilla-Camps, J. C.; Volbeda, A.; Cavazza, C.; Nicolet, Y. *Chemi. Rev.* **2007**, *107*, 4273.
(19) Silakov, A.; Wenk, B.; Reijerse, E.; Lubitz, W. *Phys. Chem. Chem. Phys.* **2009**, *11*, 6592.
(20) Siegbahn, P. E. M.; Tye, J. W.; Hall, M. B. *Chem. Rev.* **2007**, *107*, 4414.
(21) Nicolet, Y.; Cavazza, C.; Fontecilla-Camps, J. C. *J. Inorg. Biochem.* **2002**, *91*, 1.
(22) Pandey, A. S.; Harris, T. V.; Giles, L. J.; Peters, J. W.; Szilagyi, R. K. *J. Am. Chem. Soc.* **2008**, *130*, 4533.
(23) Schilter, D.; Rauchfuss, T. B. *Angew. Chem., Int. Ed.* **2013**, *52*, 13518.
(24) Berggren, G.; Adamska, A.; Lambertz, C.; Simmons, T.; Esselborn, J.; Atta, M.; Gambarelli, S.; Mouesca, J.; Reijerse, E.; Lubitz, W.; Happe, T.; Artero, V.; Fontecave, M. *Nature* **2013**, *499*, 66.
(25) Esselborn, J.; Lambertz, C.; Adamska-Venkatesh, A.; Simmons, T.; Berggren, G.; Noth, J.; Siebel, J.; Hemschemeier, A.; Artero, V.; Reijerse, E.; Fontecave, M.; Lubitz, W.; Happe, T. *Nat. Chem. Biol.* **2013**, *9*, 607.
(26) Adamska, A.; Silakov, A.; Lambertz, C.; Rüdiger, O.; Happe, T.; Reijerse, E.; Lubitz, W. *Angew. Chem., Int. Ed.* **2012**, *51*, 11458.
(27) Silakov, A.; Reijerse, E. J.; Albracht, S. P. J.; Hatchikian, E. C.; Lubitz, W. *J. Am. Chem. Soc.* **2007**, *129*, 11447.
(28) Silakov, A.; Kamp, C.; Reijerse, E.; Happe, T.; Lubitz, W. *Biochemistry* **2009**, *48*, 7780.
(29) Armstrong, F. A. *Photosynth. Res.* **2009**, *102*, 541.

(30) Pierik, A. J.; Hulstein, M.; Hagen, W. R.; Albracht, S. P. J. *Eur. J. Biochem.* **1998**, *258*, 572.
(31) Albracht, S. P. J.; Roseboom, W.; Hatchikian, E. C. *J. Biol. Inorg. Chem.* **2006**, *11*, 88.
(32) Roseboom, W.; de Lacey, A. L.; Fernández, V. M.; Hatchikian, E. C.; Albracht, S. P. J. *J. Biol. Inor. Chem.* **2006**, *11*, 102.
(33) Baffert, C.; Bertini, L.; Lautier, T.; Greco, C.; Sybirna, K.; Ezanno, P.; Etienne, E.; Soucaille, P.; Bertrand, P.; Bottin, H.; Meynial-Salles, I.; De Gioia, L.; Léger, C. *J. Am. Chem. Soc.* **2011**, *133*, 2096.
(34) Le Cloirec, A.; Best, S. P.; Borg, S.; Davies, S. C.; Evans, D. J.; Hughes, D. L.; Pickett, C. J. *Chem. Commun.* **1999**, 2285.
(35) Li, H. X.; Rauchfuss, T. B. *J. Am. Chem. Soc.* **2002**, *124*, 726.
(36) Schmidt, M.; Contakes, S. M.; Rauchfuss, T. B. *J. Am. Chem. Soc.* **1999**, *121*, 9736.
(37) Kuchenreuther, J. M.; Grady-Smith, C. S.; Bingham, A. S.; George, S. J.; Cramer, S. P.; Swartz, J. R. *PLoS One* **2010**, *5*, e15491.
(38) Moss, D.; Nabedryk, E.; Breton, J.; Mäntele, W. *Eur. J. Biochem.* **1990**, *187*, 565.
(39) Reijerse, E.; Lendzian, F.; Isaacson, R.; Lubitz, W. *J. Magn. Reson.* **2012**, *214*, 237.
(40) Stoll, S.; Schweiger, A. *J. Magn. Reson.* **2006**, *178*, 42.
(41) Goldet, G.; Brandmayr, C.; Stripp, S. T.; Happe, T.; Cavazza, C.; Fontecilla-Camps, J. C.; Armstrong, F. A. *J. Am. Chem. Soc.* **2009**, *131*, 14979.
(42) Fourmond, V.; Greco, C.; Sybirna, K.; Baffert, C.; Wang, P. H.; Ezanno, P.; Montefiori, M.; Bruschi, M.; Meynial-Salles, I.; Soucaille, P.; Blumberger, J.; Bottin, H.; De Gioia, L.; Léger, C. *Nat. Chem.* **2014**, *6*, 336.
(43) Foster, C. E.; Kraemer, T.; Wait, A. F.; Parkin, A.; Jennings, D. P.; Happe, T.; McGrady, J. E.; Armstrong, F. A. *J. Am. Chem. Soc.* **2012**, *134*, 7553.
(44) De Lacey, A. L.; Stadler, C.; Fernández, V. M.; Hatchikian, E. C.; Fan, H. J.; Li, S. H.; Hall, M. B. *J. Biol. Inorg. Chem.* **2002**, *7*, 318.
(45) Camara, J. M.; Rauchfuss, T. B. *Nat. Chem.* **2012**, *4*, 26.
(46) Silakov, A.; Reijerse, E. J.; Lubitz, W. *Eur. J. Inorg. Chem.* **2011**, 1056.
(47) Silakov, A.; Shaw, J. L.; Reijerse, E. J.; Lubitz, W. *J. Am. Chem. Soc.* **2010**, *132*, 17578.
(48) Silakov, A.; Olsen, M. T.; Sproules, S.; Reijerse, E. J.; Rauchfuss, T. B.; Lubitz, W. *Inorg. Chem.* **2012**, *51*, 8617.
(49) Gloaguen, F.; Rauchfuss, T. B. *Chem. Soc. Rev.* **2009**, *38*, 100.

**SUPPORTING INFORMATION**

for

# New redox states observed in [FeFe] hydrogenases reveal redox coupling within the H-cluster.

Agnieszka Adamska-Venkatesh[1], Danuta Krawietz[7], Judith Siebel[1], Katharina Weber[1], Thomas Happe[2], Edward Reijerse[1]*, Wolfgang Lubitz[1]*

[1] Max-Planck-Institut für Chemische Energiekonversion, Stiftstrasse 34-36, 45470 Mülheim an der Ruhr, Germany

[2] Ruhr Universität Bochum, Fakultät für Biologie und Biotechnologie, Lehrstuhl für Biochemie der Pflanzen, AG Photobiotechnologie, 44801 Bochum, Germany

*corresponding authors: edward.reijerse@cec.mpg.de, wolfgang.lubitz@cec.mpg.de

## FTIR ELECTROCHEMICAL DATA PROCESSING

FTIR baseline corrections were performed in two steps: First the spectra measured during each titration experiment were joined into a 2D dataset. Representative baseline points were manually selected and a cubic spline baseline correction was applied to the whole 2D dataset. Subsequently, individual FTIR spectra were analyzed and regions with strongly overlapping signals were separately baseline corrected. The resulting 2D FTIR datasets are presented as 3D plots (see figures S1 to S6). For the determination of the redox potentials one representative band (showing minimal overlap with other signals) was chosen for each redox state.

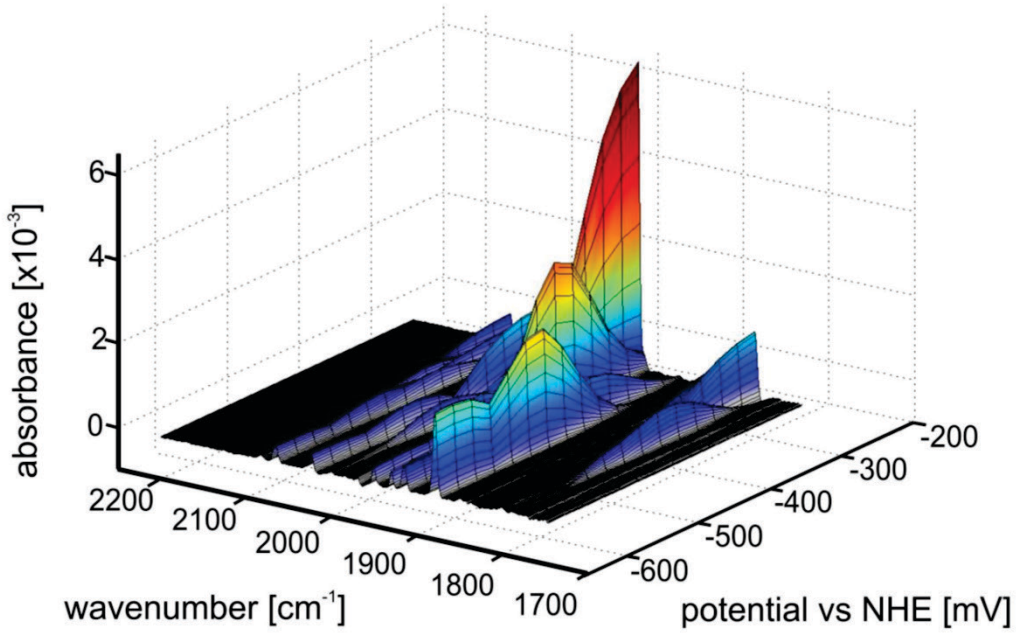


**Figure S1. FTIR spectra of CrHydA1(adt) measured during the spectroelectrochemical reduction of as isolated HydA1(adt) starting from the open circuit potential. The spectra were accumulated in the double-sided, forward-backward mode with 1000 scans (14 minutes) and a resolution of 2 cm$^{-1}$ at T = 15 °C. Since no mediators were used an extended equilibration time period of 30 minutes was applied at each potential.**

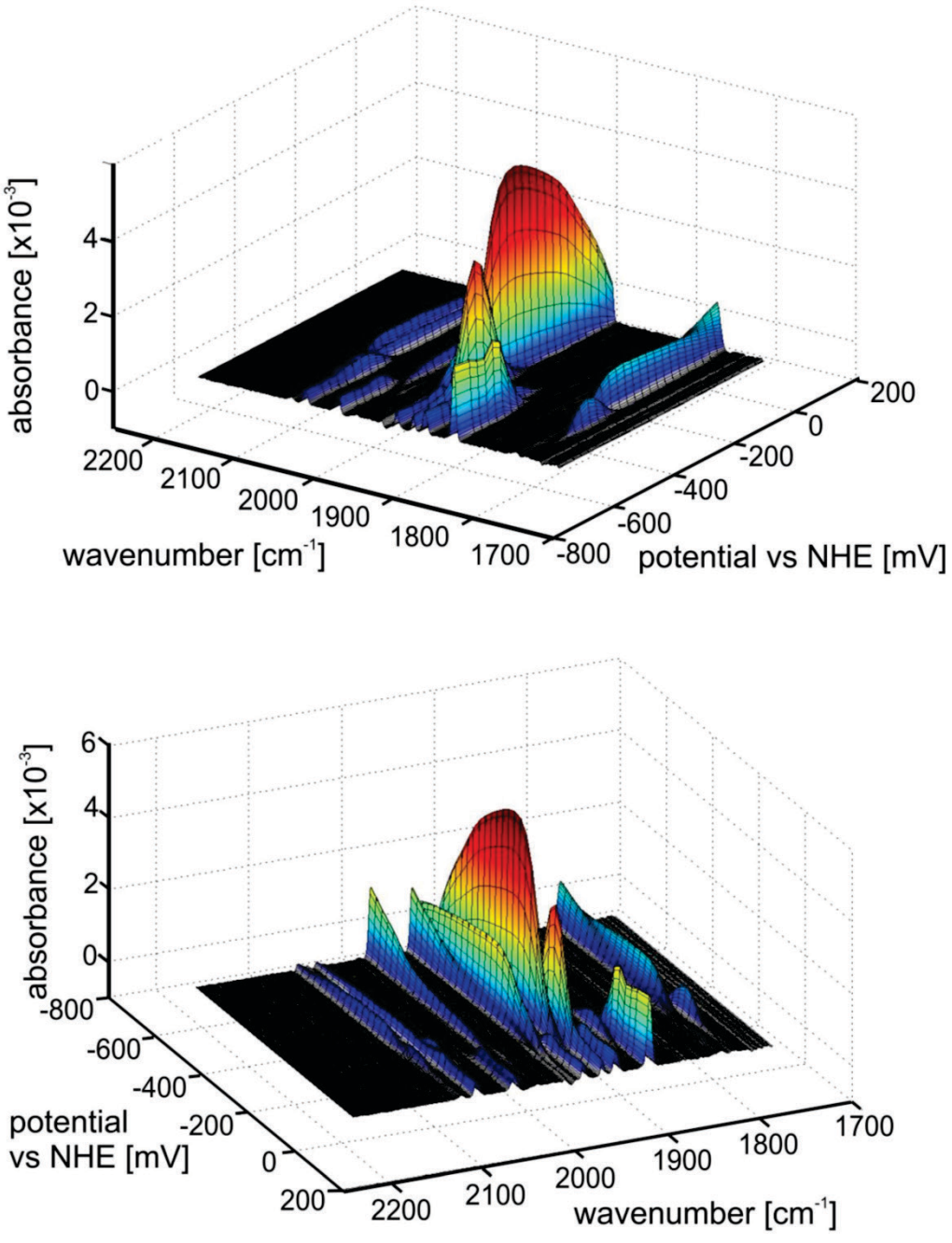


**Figure S2. FTIR spectra of CrHydA1(adt) measured during the spectroelectrochemical oxidation of the enzyme in the $H_{sred}$ state. Both panels show the same spectra but from a different perspective. The spectra were accumulated in the double-sided, forward-backward mode with 1000 scans (14 minutes) and a resolution of 2 $cm^{-1}$ at T = 15 °C. Since no mediators were used an extended equilibration time period of 30 minutes was applied at each potential.**

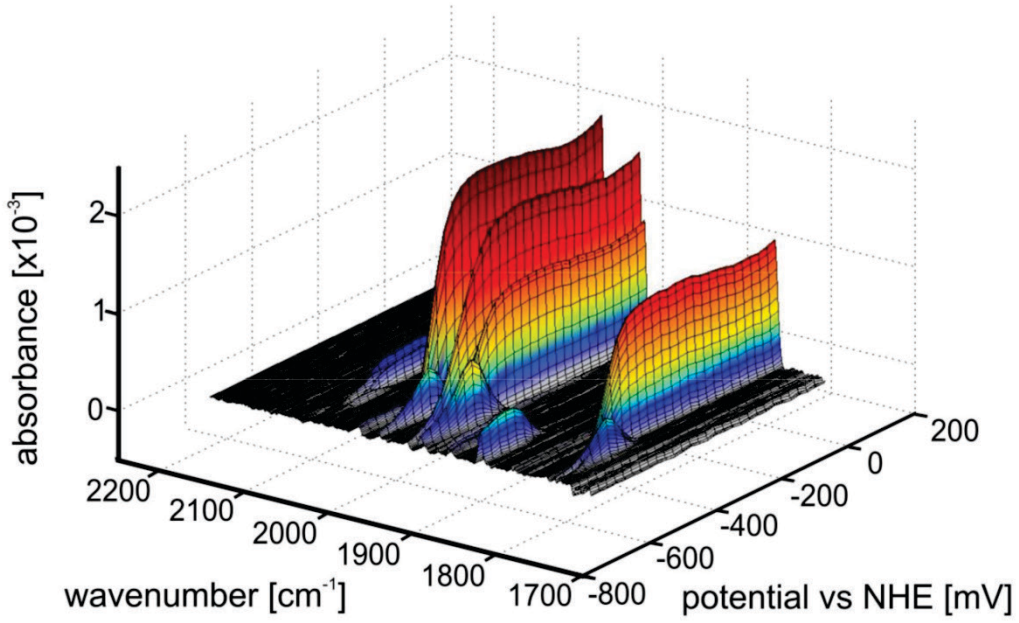


**Figure S3. FTIR spectra of CrHydA1(adt) in the $H_{ox}$-CO state measured during the spectroelectrochemical reduction in the presence of CO gas in the cell. The spectra were accumulated in the double-sided, forward-backward mode with 1000 scans (14 minutes) and a resolution of 2 cm$^{-1}$ at T = 15 °C. Since no mediators were used an extended equilibration time period of 30 minutes was applied at each potential.**

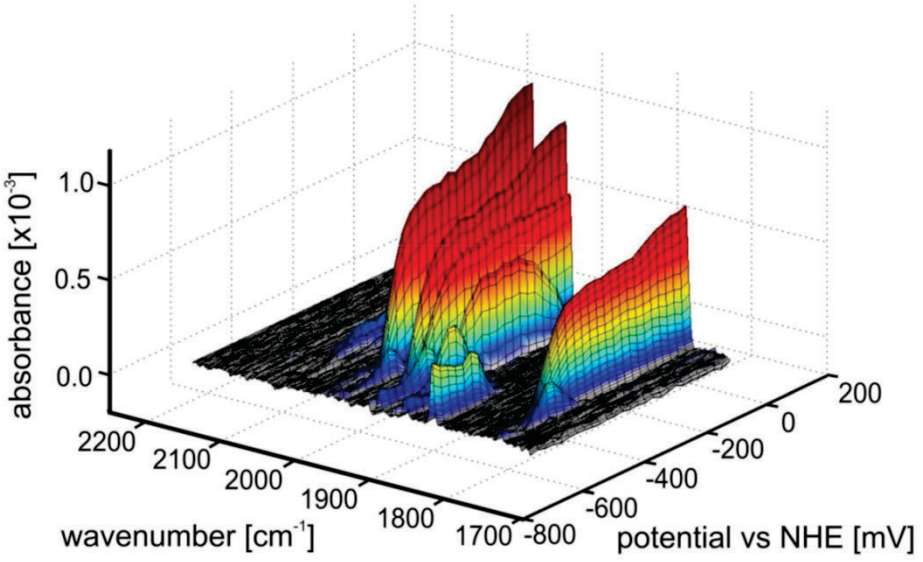


**Figure S4. FTIR spectra of CrHydA1(adt) in the $H_{sred}$ state measured during the spectroelectrochemical oxidation in the presence of CO gas in the cell. The spectra were accumulated in the double-sided, forward-backward mode with 1000 scans (14 minutes) and a resolution of 2 cm$^{-1}$ at T = 15 °C. Since no mediators were used an extended equilibration time period of 30 minutes was applied at each potential.**

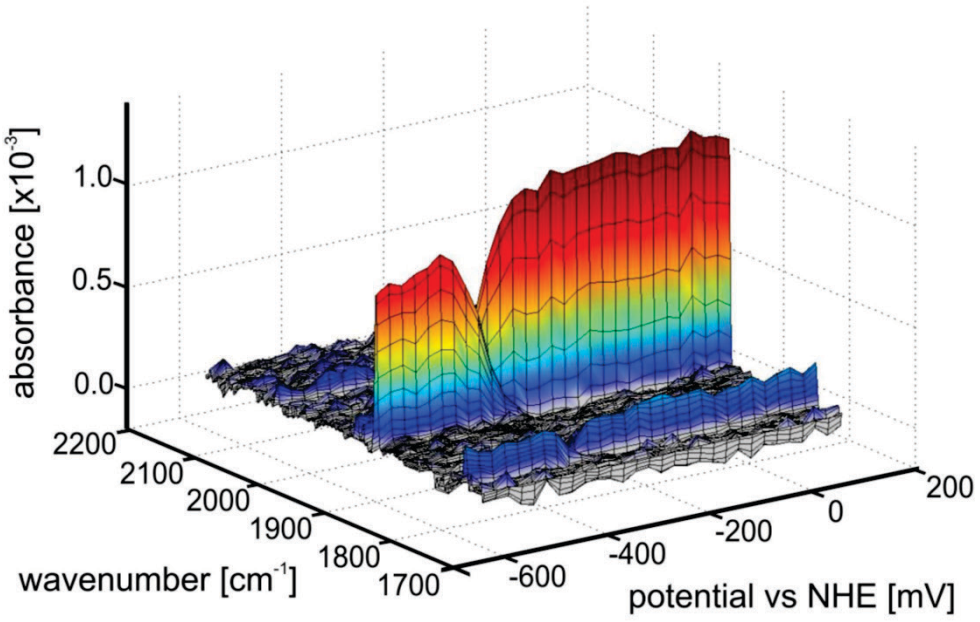


**Figure S5. FTIR spectra of CrHydA1(pdt) measured during the spectroelectrochemical oxidation starting at the open circuit potential. The spectra were accumulated in the double-sided, forward-backward mode with 1000 scans (14 minutes) and a resolution of 2 cm$^{-1}$ at T = 15 °C. Since no mediators were used an extended equilibration time period of 30 minutes was applied at each potential.**

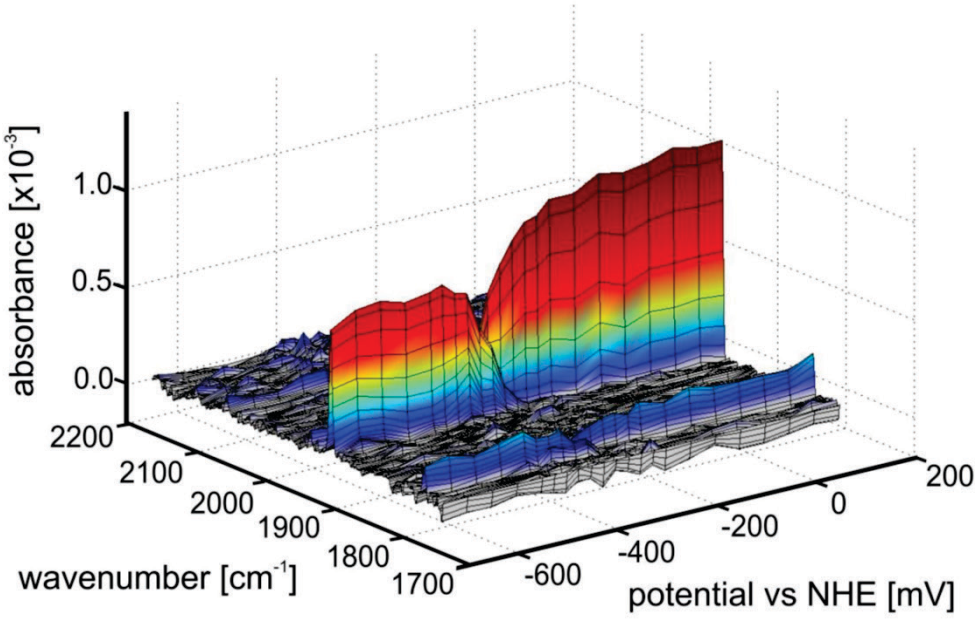


**Figure S6. FTIR spectra of CrHydA1(pdt) measured during the spectroelectrochemical reduction of the oxidized enzyme. The spectra were accumulated in the double-sided, forward-backward mode with 1000 scans (14 minutes) and a resolution of 2 cm$^{-1}$ at T = 15 °C. Since no mediators were used an extended equilibration time period of 30 minutes was applied at each potential.**

DETERMINATION OF THE REDOX MIDPOINT POTENTIALS

The obtained experimental data was fitted with a Nerstian curve using the following assumptions (example for oxidative titration of CrHydA1(adt)):

$$E = E_{ox/red} + \frac{RT}{zF} \ln \frac{[ox]}{[red]}$$

$$E = E_{red/sred} + \frac{RT}{zF} \ln \frac{[red]}{[sred]}$$

$$[ox] + [red] + [sred] = 1$$

where:

$E$ is the electrochemical potential,

$E_{ox/red}$ and $E_{red/sred}$ are respective midpoint potentials,

$R = 8.314 \frac{J}{K*mol}$ is the universal gas constant,

$T = 278.15\ K$ is the temperature,

$n = 1$ is the number of transferred electrons,

$F = 96485 \frac{C}{mol}$ is Faraday's constant,

$[ox]$, $[red]$ and $[sred]$ are the fractional concentrations of the enzyme in the respective redox states.

This procedure of data analysis was applied to all data with proper adjustment.

FOLLOWING BANDS ORGINATING FROM $H_{'red'}$-CO

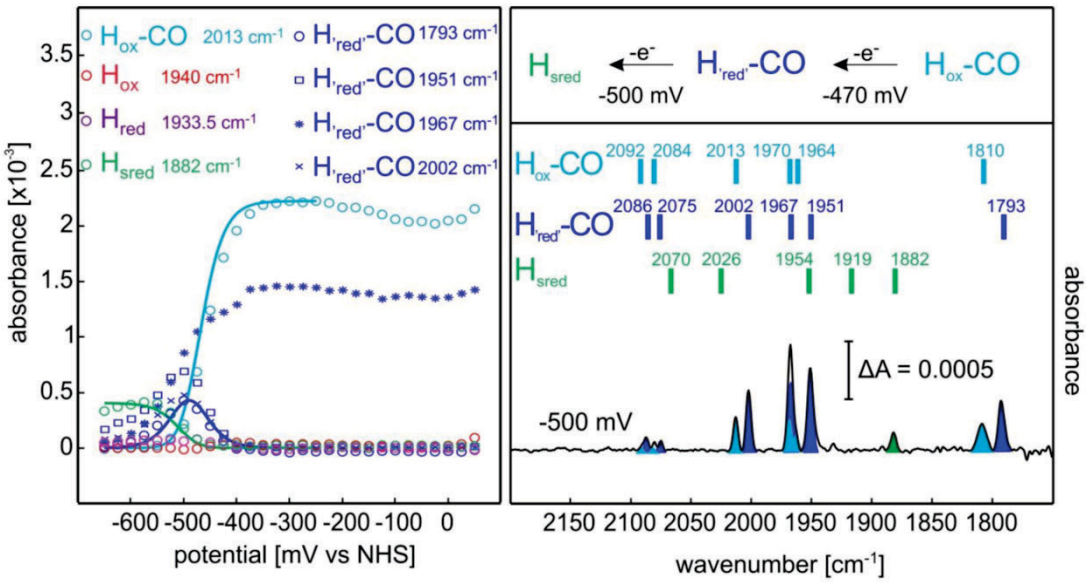


**Figure S7. Left: Reductive titration of the CO inhibited enzyme. The red circles correspond to the intensity of the most prominent CO band of the $H_{ox}$ state at 1940 $cm^{-1}$, violet circles to the signal at 1933.5 $cm^{-1}$ characteristic for $H_{red}$ , green circles to the 1882 $cm^{-1}$ band of $H_{sred}$ and light blue circles to the 2013 $cm^{-1}$ band from the $H_{ox}$-CO state. In blue color the intensities of all signals assigned to the CO ligands of CrHydA1(adt) in the $H_{'red'}$-CO state are presented. The solid lines correspond to n =1 Nerstian curves, $E_{ox\text{-}CO/'red'\text{-}CO}$= -470 mV ±20 mV and $E_{'red'\text{-}CO/sred}$ = -500 mV±20 mV. Right: IR spectrum measured at -500 mV under CO gas at T = 15°C. Bands shaded in blue originate from $H_{'red'}$-CO, light blue from $H_{ox}$-CO and green from the $H_{sred}$ state. The top of the figure shows the signal positions of the observed redox species.**

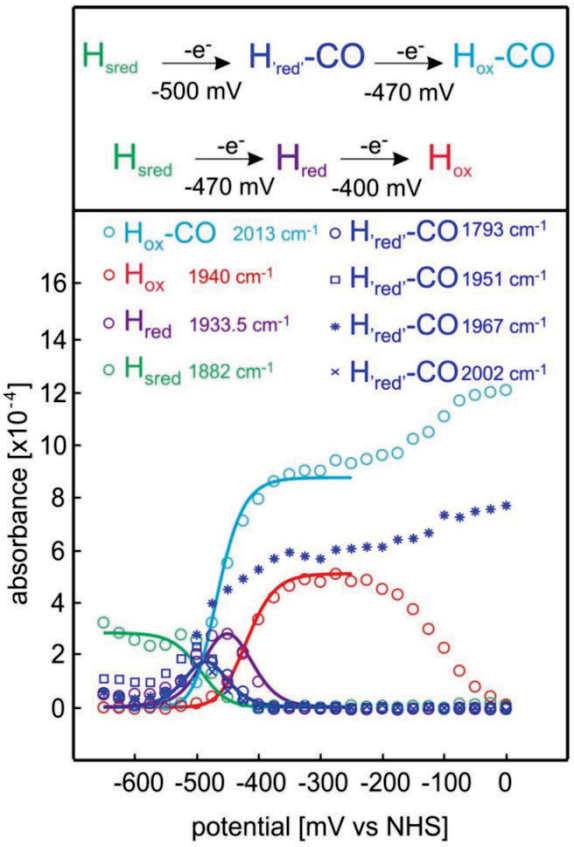


**Figure S8. Oxidative titration of CrHydA1(adt) in the presence of CO gas. The red circles correspond to the intensity of the most prominent CO band of the $H_{ox}$ state at 1940 $cm^{-1}$, violet circles to the band at 1933.5 $cm^{-1}$ characteristic for $H_{red}$, green circles to the 1882 $cm^{-1}$ band of $H_{sred}$ and light blue circles to the 2013 $cm^{-1}$ band of $H_{ox}$-CO. In blue color the intensities of all signals assigned to the CO ligands of CrHydA1(adt) in the $H_{'red'}$-CO state are presented. The solid lines correspond to n =1 Nerstian curves, $E_{ox\text{-}CO/'red'\text{-}CO}$= -470 mV ±20 mV and $E_{'red'\text{-}CO/sred}$ = -500 mV±20 mV.**

Figures S7 and S8 present the reductive and oxidative titration of CrHydA1(adt) in the presence of CO gas, as described in the main text and presented in figures 3B and 4 of the manuscript. It is obvious that the signal at 1967 $cm^{-1}$ (marked with ∗) cannot be used to follow the appearance and disappearance of the $H_{'red'}$-CO due to its overlap with two bands (at 1970 $cm^{-1}$ and 1964 $cm^{-1}$) from the $H_{ox}$-CO state. Similarly, the signal at 1951 $cm^{-1}$ (marked with □) is obscured by its overlap at low potentials with the signal from the $H_{sred}$ state (at 1954 $cm^{-1}$). The intensity changes of the signals at 2002 $cm^{-1}$ and 1793 $cm^{-1}$ are in good agreement for both cases. In principle, the signal at 1793 $cm^{-1}$ should overlap with the signal originating from the bridging CO ligand from $H_{red}$, however, in the reductive titration $H_{red}$ does not appear and in the oxidative titration its intensity is too low to affect the presented data.

## $^{13}$CO EXCHANGE EXPERIMENTS

To facilitate the assignment of the bands in the $H_{'red'}$-CO state experiments with $^{13}$CO have been performed. Several samples were prepared with different concentrations of reductant (2 and 7 mM of sodium dithionate) and with different light exposure times, which initiates the scrambling process. Figure S9 (top) displays the FTIR spectrum of the 7 mM sodium dithionite sample after inhibition with $^{12}$CO. The subsequent spectra show the effect of $^{13}$CO exposure in the dark, after 2.5 hours of illumination, and after 4.5 hours illumination with a halogen lamp (50 Watts). In all spectra a mixture of signals originating from $H_{ox}$-CO and $H_{'red'}$-CO is present. Based on difference spectra, extraction and assignment of the signals to the different redox states and the number of exchanged ligands could be determined and is shown in Figure 4 of the main text. The observed isotope shifts are in the range 40-47 cm$^{-1}$ which is in agreement with the expected theoretical shift (44.3 cm$^{-1}$) upon exchange of $^{12}$C with $^{13}$C.

The two high frequency CO bands in both the $H_{ox}$-CO and $H_{'red'}$-CO species shift in two steps, suggesting that they originate from coupled vibrations and that only one of the contributing CO ligands gets exchanged in the dark. It can therefore be concluded that the 2002 cm$^{1}$ band from $H_{'red'}$-CO corresponds to the 2013 cm$^{-1}$ band from $H_{ox}$-CO whereas the 1967 cm$^{-1}$ band corresponds to the 1970 cm$^{-1}$ band from $H_{ox}$-CO. These bands in $H_{ox}$-CO were previously assigned to the $\nu_{sym}$ and $\nu_{asym}$ bands of the two vibrationally coupled terminal CO ligands of the distal Fe ($Fe_d$). This indicates that the electronic structure of the binuclear subsite in $H_{ox}$-CO and $H_{'red'}$-CO is very similar and that a change of the oxidation state of $Fe_d$ is very unlikely due to the very small difference in the band position of both states.

The one step shift of both the 1964 cm$^{1}$ band ($H_{ox}$-CO) and the corresponding 1951 cm$^{1}$ band ($H_{'red'}$-CO) (see figure 4 in the main text) was very surprising. This would indicate that the proximal CO ligand is "scrambled" already in the dark whereas Roseboom et al. and Silakov et al. reported that for DdH no scrambling of the proximal CO occurs at all[1,2]! On the other hand, the shift of the signal originating from the bridging CO is in perfect agreement with the previously obtained data from DdH and occurs only upon light induced scrambling.

Overall, these observations strongly support our proposal that reduction of the CO inhibited state does not take place on the diiron sub-cluster but rather on the [4Fe-4S] sub-cluster. The strong coupling between both parts of the H-cluster, which in $H_{ox}$-CO is around five times stronger than in $H_{ox}$, causes a change in the spin distribution also over the diiron sub-cluster and this is why we observe subtle changes in the FTIR spectra.

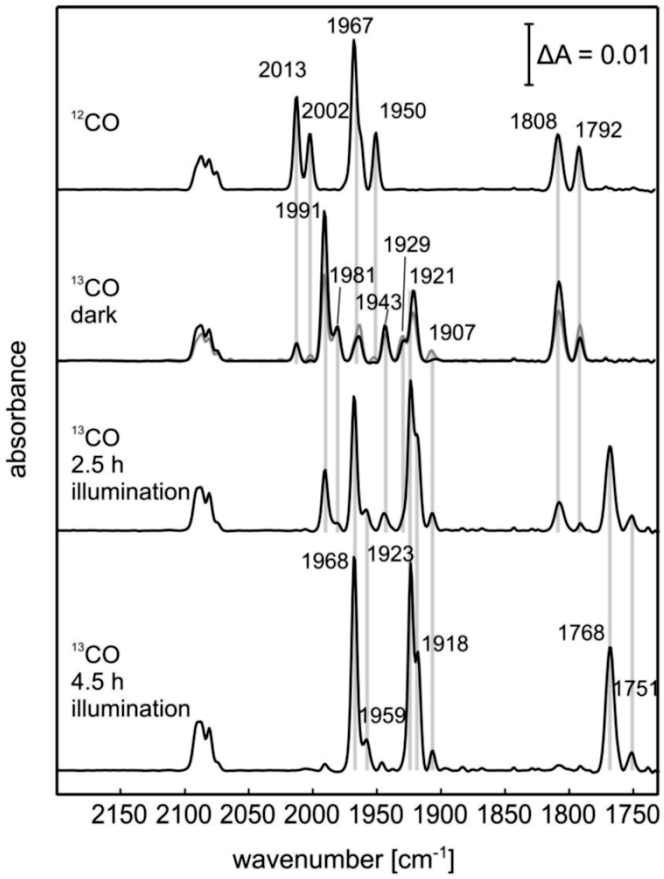


**Figure S9. Selected FTIR spectra of CrHydA1(adt) exposed to $^{12}CO$, or exposed to $^{13}CO$ in the dark, and with $^{13}CO$ followed by illumination for 2.5 and 4.5 hours. The grey lines mark band positions that do not change during the treatment. All samples were prepared under reductive conditions using 2 mM ($^{13}CO$ spectra) or 7 mM ($^{12}CO$ spectrum and $^{13}CO$ spectrum prepared in dark) sodium dithionite.**

SPIN COUNTING

To follow the conversion of unmaturated CrHydA1 to CrHydA1(pdt) the EPR spectra of three preparations were compared (see Figure S10): unmaturated CrHydA1 reduced with 10 mM sodium dithionite showing the reduced $[4Fe\text{-}4S]^{+}$ cluster, CrHydA1(pdt) reduced with 10 mM sodium dithionite which also showed a reduced $[4Fe\text{-}4S]^{+}$ cluster, and CrHydA1(pdt) oxidized with thionine giving rise to an $H_{ox}$-like EPR signal. These samples were also analyzed by FTIR to verify the redox state of the H-cluster. The EPR spectra originating from $CrHydA1^{\Delta EFG}$ and reduced CrHydA1(pdt) show identical signals characteristic for the reduced $[4Fe\text{-}4S]^{+}$ cluster of the unmaturated enzyme. Comparing the double integral of these signals against a Cu(II) standard revealed that around 20% of $CrHydA1^{\Delta EFG}$ contained a $[4Fe\text{-}4S]^{+}$ cluster and 40% of that fraction was converted into reduced CrHydA1(pdt) which is EPR silent. The double integral of the oxidized CrHydA1(pdt) EPR spectrum confirmed that all CrHydA1(pdt) can be oxidized (see table S1).

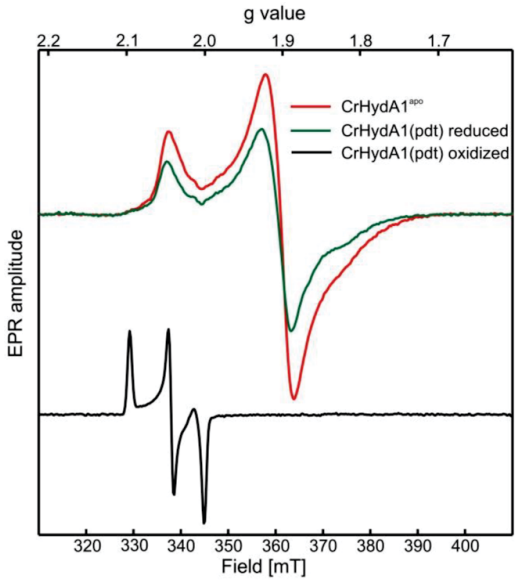


**Figure S10. X-band cw EPR spectra of 450 µM CrHydA1 containing only the [4Fe-4S] cluster (red) and with inserted pdt complex in the reduced (415 µM) (blue) and oxidized (340 µM) (black) form. Spectra were measured at T = 10 K with 0.75 mT modulation amplitude, 100 kHz modulation frequency, 40.96 ms time constant and 200 µW (30 dB) or 12.6 µW (42 dB) microwave power for samples characterized by signals from the $[4Fe\text{-}4S]^{+}$ cluster (top) and the binuclear site (bottom), respectively.**

| Sample | Number of spins per protein | Fraction of the protein containing: | | |
|---|---|---|---|---|
| | | no cluster | [4Fe-4S] cluster | [4Fe-4S]FeFe hybrid |
| $CrHydA1^{apo}$ | 0.19 ± 0.02 | 81% ± 2% | 19% ± 2% | - |
| reduced CrHydA1(pdt) | 0.12 ± 0.02 | 81% ± 2% | 12% ± 2% | 7% ± 2% |
| oxidized CrHydA1(pdt) | 0.08 ± 0.02 | 81% ± 2% | 11% ± 2% | 8% ± 2% |

**Table S1. Spin counting results compared with Cu(II) standard and assigned fractional composition of the samples.**

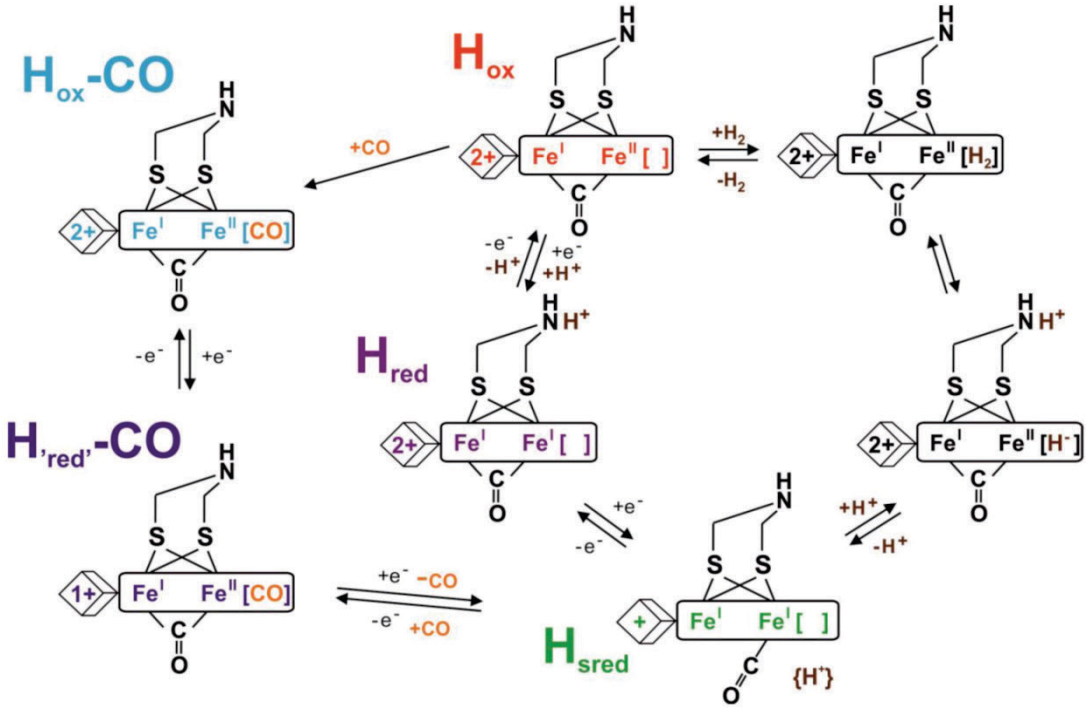


**Figure S11. Schematic representation of the proposed catalytic cycle and the formation of the CO inhibited states.**

Reference List

(1) Roseboom, W.; de Lacey, A. L.; Fernández, V. M.; Hatchikian, E. C.; Albracht, S. P. J. *J. Biol. Inorg. Chem.* **2006**, *11*, 102.

(2) Silakov, A.; Wenk, B.; Reijerse, E.; Albracht, S. P. J.; Lubitz, W. *J. Biol. Inorg. Chem.* **2009**, *14*, 301.

A. Adamska-Venkatesh, T. Simmons, J. Siebel, V. Artero, M. Fontecave, E. Reijerse, W. Lubitz, *Phys. Chem. Chem. Phys.* 2015, 17 (7), 5421-5430.

http://pubs.rsc.org/en/Content/ArticleLanding/2015/CP/C4CP05426A#!divAbstract

# Artificially Maturated [FeFe] Hydrogenase from C*hlamydomonas reinhardtii*: A HYSCORE and ENDOR Study of a Non-Natural H-cluster

Agnieszka Adamska-Venkatesh[1], Trevor R. Simmons[2], Judith F. Siebel[1], Vincent Artero[2], Marc Fontecave[2,3], Edward Reijerse[1], Wolfgang Lubitz[1]

[1] Max Planck Institut für Chemische Energiekonversion, Stiftstrasse 34-36, 45470 Mülheim an der Ruhr, Germany

[2] Laboratoire de Chimie et Biologie des Métaux; Université Grenoble Alpes , CEA, CNRS, 17 rue des martyrs, 38000 Grenoble, France

[3] Laboratoire de Chimie des Processus Biologiques, Collège de France, Université Pierre et Marie Curie, CNRS UMR 8229, 11 place Marcelin Berthelot, 75005 Paris, France

## I. Abstract

Hydrogenases are enzymes which catalyze the oxidation of $H_2$ as well as the reduction of protons to form $H_2$. The active site of [FeFe] hydrogenase is referred to as the "H-cluster" and consists of a "classical" [4Fe-4S] cluster connected *via* a bridging cysteine thiol group to a unique $[2Fe]_H$ sub-cluster, containing $CN^-$ and CO ligands as well as a bidentate azadithiolate ligand. It has been recently shown that the biomimetic $[Fe_2(adt)(CO)_4(CN)_2]^{2-}$ ($adt^{2-}$ = azadithiolate) complex resembling the diiron sub-cluster can be inserted *in vitro* into the apo-protein of [FeFe] hydrogenase, which contains only the [4Fe-4S] part of the H-cluster, resulting in a fully active enzyme. This synthetic tool allows convenient incorporation of a variety of diiron mimics thus generating hydrogenases with artificial active sites. [FeFe] hydrogenase from *Chlamydomonas reinhardtii* maturated with the biomimetic complex $[Fe_2(pdt)(CO)_4(CN)_2]^{2-}$ ($pdt^{2-}$ = propanedithiolate), in which the bridging $adt^{2-}$ ligand is replaced by $pdt^{2-}$ can be stabilized in a state strongly resembling the active oxidized ($H_{ox}$) state of the native protein. This state is EPR active and the signal originates from the mixed valence $Fe^IFe^{II}$ state of the diiron sub-cluster. Taking advantage of

the variant with $^{15}N$ and $^{13}C$ isotope labeled $CN^-$ ligands we performed HYSCORE and ENDOR studies on this hybrid protein. The $^{13}C$ hyperfine couplings originating from both $CN^-$ ligands were determined and assigned. Only the $^{15}N$ coupling from the $CN^-$ ligand bound to the terminal iron was observed. Detailed orientation selective ENDOR and HYSCORE experiments at multiple field positions enabled the extraction of accurate data for the relative orientations of the nitrogen and carbon hyperfine tensors. These data are consistent with the crystal structure assuming a g-tensor orientation following the local symmetry of the binuclear sub-cluster.

## II. Introduction

Over the last few decades, the growing interest in renewable energy technologies has stimulated research on biotechnological hydrogen production using microorganisms[1-9]. A wide range of microorganisms from archaea, bacteria to some eukaryotes use metalloenzymes called hydrogenases as a part of their energy metabolism[1,10]. Hydrogenases catalyze the reversible conversion of molecular hydrogen into two protons and two electrons. The hydrogenases can be classified into three groups, according to the metal composition of their active site: [NiFe] hydrogenases with the subgroup of [NiFeSe] hydrogenases, [FeFe] hydrogenases and [Fe] hydrogenases[9,10]. The [FeFe] hydrogenases were found to be the most active for hydrogen production *in vivo*[11,12]. The quite unique active site of these enzymes is highly conserved, and referred to as the "H-cluster"[9,13-16]. It contains a typical $[4Fe\text{-}4S]_H$ cluster which is coupled by one of its coordinating cysteine side groups to a unique binuclear sub-cluster $[2Fe]_H$ shown in figure 1[9,13-16]. The low oxidation state of the iron atoms in the binuclear sub-cluster are stabilized by $CN^-$ and CO ligands[13,17]. In addition, a bidentate dithiol ligand bridges the two iron centers. For many years the nature of the central atom of this ligand was strongly debated, since it could not be uniquely identified in the crystal structure[13,14,16,18]. Soon, however, based on structural and mechanistic arguments an amine function was proposed[13]. This proposal was later experimentally supported by pulsed EPR data[19,20]. In recent studies it was shown that it is possible to insert various biomimetic complexes into unmaturated [FeFe] hydrogenase that contains only the $[4Fe\text{-}4S]_H$ part of the H-cluster[21,22]. It was shown that the enzyme was fully activated only when the biomimic complex $[Fe_2(adt)(CO)_4(CN)_2]^{2-}$ ($adt^{2-}$ = azadithiolate)

containing the amine group in the dithiolate bridging ligand ($adt^{2-}$) was inserted, whereas those activated with complexes containing other dithiolate ligands showed very little or no activity[21-23]. Spectroscopic characterization of this "hybrid" enzyme showed it to be indistinguishable from the native one[24].

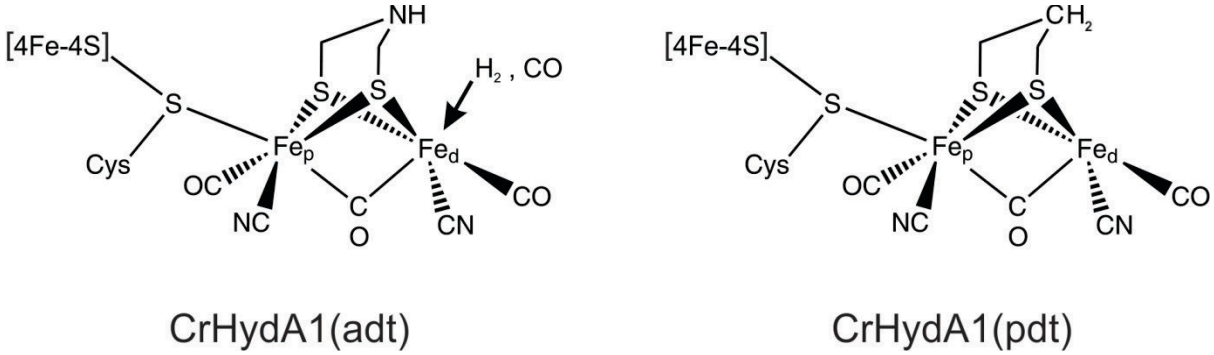


**Figure 1. Schematic representation of the structure of the H-cluster of artificially maturated [FeFe] hydrogenase from *C. reinhardtii* with natural CrHydA1(adt) and the non-natural CrHydA1(pdt) binuclear sub-site.**

The H-cluster of the isolated native enzyme usually exists as a mixture of redox states that have been identified and spectroscopically characterized[9]. The oxidized active state $H_{ox}$ is characterized by a mixed valence configuration of the $[2Fe]_H$ sub-cluster ($Fe^{I}Fe^{II}$), while the $[4Fe\text{-}4S]_H$ sub-cluster is in the oxidized 2+ state ($2Fe^{II}2Fe^{III}$)[9,17,25]. The iron atoms in the $[2Fe]_H$ sub-cluster are in a low spin state and exhibit a characteristic rhombic S=1/2 EPR signal[9,25]. This state can be inhibited by external CO, generating the $H_{ox}$-CO state, which is electronically very similar to $H_{ox}$ but shows an axial EPR signal[9]. This signal is often present in [FeFe] hydrogenase preparations due to the so-called "cannibalization process" in which the CO ligands from light or oxygen damaged H-clusters are released and captured by H-clusters that are still intact[24,26-28].

In the algal [FeFe] hydrogenase from *Chlamydomonas reinhardtii* (CrHydA1), upon two fully reversible one electron reductions $H_{ox}$ is converted first to the active reduced state $H_{red}$ and then to the "super reduced" active state $H_{sred}$[28]. It was recently shown that the $H_{ox}$-CO state can also be reversibly reduced to the CO inhibited reduced state $H_{'red'}$-CO which upon subsequent reversible one electron reduction (accompanied with CO dissociation) yields the $H_{sred}$ state[24]. This state is paramagnetic and gives a signal characteristic for a reduced $[4Fe\text{-}4S]^{+}$ cluster while both iron atoms in the $[2Fe]_H$ sub-cluster are antiferromagnetically coupled in an $Fe^{I}Fe^{I}$ (S = 0) configuration[29].

The electronic structure of $H_{ox}$ and $H_{ox}$-CO have previously been the subject of intensive investigation[9,19,25-28,30-35]. The $^{57}Fe$ hyperfine interactions indicate that the spin

density distribution over the H-cluster drastically changes upon conversion from $H_{ox}$ to $H_{ox}$-CO[25]. In the $H_{ox}$ state, the unpaired spin density is more or less equally distributed over both iron atoms in the $[2Fe]_H$ sub-cluster, while in the $H_{ox}$-CO state most of spin density is shifted towards the proximal iron. The formally diamagnetic $[4Fe\text{-}4S]_H^{2+}$ sub-cluster has a strong influence on the electronic structure of the binuclear sub-cluster because in model complexes in which the cubane sub-cluster is lacking, the spin distribution clearly deviates from what is found in the native system[25,32,36-38]. By studying $^{13}C$ labeled CO ligands and signals from $^{14}N$ in the $CN^-$ ligands it was found that in the $H_{ox}$-CO state the spin density is largely distributed over the CO ligands while almost no spin density was detected on the $CN^-$ ligands[33]. A different situation was observed in the $H_{ox}$ state. $^{14}N$ ESEEM studies showed a very rich pattern of hyperfine couplings that was assigned to the nitrogen from the $CN^-$ ligand bound to the distal iron, the nitrogen in the dithiolate bridge and the nitrogen of the side chain of the lysine hydrogen bonded to the distal $CN^-$ ligand[39,19]. No spin density was found for the $CN^-$ ligand bound to the proximal iron.

In a recent study it was shown that CrHydA1 maturated with the biomimic complex $[Fe_2(pdt)(CO)_4(CN)_2]^{2-}$ ($pdt^{2-}$ = propanedithiolate) (referred as pdt complex) containing a $CH_2$ group in the dithiolate bridge affords an almost inactive hybrid enzyme CrHydA1(pdt) that can be stabilized in two redox states (oxidized and reduced)[23,24]. FTIR and EPR studies showed that the oxidized form of CrHydA1(pdt) is almost identical to the native $H_{ox}$ state. It is therefore concluded that the $[2Fe]_H$ sub-cluster ($Fe^{I}Fe^{II}$) is in the mixed valence configuration, while the $[4Fe\text{-}4S]_H$ sub-cluster is oxidized (2+). It was suggested that reduction takes place in the $[4Fe\text{-}4S]_H$ sub-cluster and due to strong exchange coupling within the H-cluster this state is EPR silent. No other states (including $H_{ox}$-CO) were observed for this hybrid.

In the present study, we confirm through detailed EPR studies that oxidized CrHydA1(pdt) can be used as a good structural and electronic model system for the native $H_{ox}$ state. As discussed below the pdt analog offers multiple advantages: (i) straightforward synthesis and stability of the pdt complex; (ii) the possibility to obtain a pure redox state for the reconstituted enzyme, thus facilitating spectroscopic characterization. To obtain additional information about the spin density distribution over the $CN^-$ ligands we synthesized $^{13}C$ and $^{15}N$ labeled pdt complex and performed HYSCORE and ENDOR experiments on the labeled H-cluster of the reconstituted hydrogenase.

## III. Materials and methods

### Sample preparation

All chemicals used were purchased from Sigma-Aldrich and used as received unless otherwise stated. Solvents were freshly distilled under an inert atmosphere of argon from an appropriate drying agent. FTIR spectra of synthetic complexes were recorded on a Perkin Elmer Spectrum-100 spectrometer *via* a thin film solution. $Fe_2(pdt)(CO)_6$ and $[Et_4N]_2[Fe_2(pdt)(CO)_4(CN)_2]$ were prepared according to literature procedures[40,41] while $[Et_4N]_2[Fe_2(pdt)(CO)_4(^{13}CN)_2]$ and $[Et_4N]_2[Fe_2(pdt)(CO)_4(C^{15}N)_2]$ were prepared by modified literature procedures as described below.

**$[Et_4N]_2[Fe_2(pdt)(CO)_4(^{13}CN)_2]$**

$Fe_2(pdt)(CO)_6$ (0.15 g, 0.40 mmol) was dissolved in MeCN (10 ml) and added *via* cannula to a solution of $[K][^{13}CN]$ (0.05 g, 0.80 mmol) in MeOH (5 ml) under argon. The reaction mixture was stirred for 2 hours at room temperature to give a dark red solution. $[Et_4N][Br]$ (0.20 g, 0.95 mmol) dissolved in MeCN (10 ml) was added to the reaction mixture, which was allowed to stir for an additional hour. The solvent was removed under reduced pressure to give a dark red solid. This was dissolved in acetone (10 ml) and filtered *via* cannula to give a dark red filtrate. The solution was mixed with EtOAc (20 ml) and cooled to -26 °C to give $[Et_4N]_2[Fe_2(pdt)(CO)_4(^{13}CN)_2]$ as a deep red crystalline solid (0.18 g, 72%) $\nu_{max}/cm^{-1}$ (acetonitrile) 2032 ($^{13}CN$), 1963, 1922, 1885, 1871 (sh) (CO).

**$[Et_4N]_2[Fe_2(pdt)(CO)_4(C^{15}N)_2]$**

$Fe_2(pdt)(CO)_6$ (0.07 g, 0.20 mmol) was dissolved in MeCN (5 ml) and added *via* cannula to a solution of $[K][C^{15}N]$ (0.03 g, 0.40 mmol) in MeOH (2 ml) under argon. The reaction mixture was stirred for 2 hours at room temperature to give a dark red solution. $[Et_4N][Br]$ (0.10 g, 0.50 mmol) dissolved in MeCN (5 ml) was added to the reaction mixture, which was allowed to stir for an additional hour. The solvent was removed under reduced pressure to give a dark red solid. This was dissolved in acetone (5 ml) and filtered *via* cannula to give a dark red filtrate. The solution was mixed with EtOAc (10 ml) and cooled to -26 °C to give $[Et_4N]_2[Fe_2(pdt)(CO)_4(C^{15}N)_2]$ as a deep red crystalline solid (0.08 g, 65%) $\nu_{max}/cm^{-1}$ (acetonitrile) 2046 ($C^{15}N$), 1963, 1922, 1884, 1871 (sh) (CO).

**Enzyme maturation**

Unmaturated CrHydA1 containing only the [4Fe-4S] cluster was expressed and isolated from *Escherichia coli* as described earlier[22,42]. Active [FeFe] hydrogenase was obtained through direct insertion of the binuclear sub-site complex as described previously[22,23]. CrHydA1(pdt) was prepared in 25 mM Tris/HCl, pH 8.0, 25 mM KCl. Samples were oxidized by stepwise titration with thionine monitored by FTIR. All manipulations and treatments were done under strict anaerobic conditions.

**FTIR measurements**

Fourier transform infrared (FTIR) measurements were carried out using a Bruker IFS 66v/s FTIR spectrometer equipped with a nitrogen cooled Bruker mercury cadmium telluride (MCT) detector. The spectra were accumulated in the double-sided, forward-backward mode with 1000 scans (14 minutes) and a resolution of 2 $cm^{-1}$ at 15 °C. Data processing was facilitated by home written routines in the MATLAB™ programming environment.

**EPR measurements**

Field swept X- and Q-band EPR spectra were recorded in the pulsed mode using FID detection after a 1μs π/2 excitation pulse. After a pseudomodulation transformation, the spectra obtained in this way are comparable to those using CW EPR[43].

Electron nuclear double resonance (ENDOR) was used to study the $^{13}C$ hyperfine interactions. In this investigation the Davies ENDOR sequence was used: $[\pi]\text{-}t_{d1}\text{-}[RF]\text{-}t_{d2}\text{-}[\pi/2]\text{-}\tau\text{-}[\pi]\text{-}\tau\text{-}(ESE)$[44,45]. The excitation of nuclear spin transitions is detectable through an increase in the inverted ESE intensity. The microwave preparation pulse was set to 140 ns whereas the length of the radiofrequency (RF) pulse was adjusted through an RF nutation experiment in order to maximize the ENDOR effect.

Hyperfine sublevel correlation spectroscopy (HYSCORE) experiments were performed, to extract the $^{15}N$ and $^{14}N$ hyperfine interactions, using the standard HYSCORE pulse sequence: $[\pi/2]\text{-}\tau\text{-}[\pi/2]\text{-}t_1\text{-}[\pi]\text{-}t_2\text{-}[\pi/2]\text{-}\tau\text{-}(ESE)$[45-47]. The length of the microwave [π/2] and [π] pulses was adjusted to the maximum available microwave power (1kW). The delay between the first two pulses (τ) was adjusted in order to avoid “blind spots” in the

important spectral regions using a series of three pulse ESEEM experiments as a function of τ. The starting $t_1$ and $t_2$ delays in all measurements were 100 ns. To suppress the effect of unwanted echoes, a four step phase cycling of the microwave pulses was used.

X-band measurements were performed on a Bruker ELEXYS E-580 X-band spectrometer with a SuperX-FT microwave bridge and a Bruker ER EN4118X-MD4 ENDOR dielectric resonator. Cryogenic temperatures (10-20 K) were obtained by an Oxford CF935 flow cryostat. ENDOR experiments were performed using random (stochastic) acquisition technique and making use of a 500W ENI 5100 L RF amplifier.

Q-band experiments were performed on a Bruker ELEXYS E580 spectrometer with a SuperQ-FT microwave bridge and a home built resonator described earlier[48]. Cryogenic temperatures (10-20 K) were obtained by an Oxford CF935 flow cryostat. ENDOR experiments were performed using random (stochastic) acquisition technique making use of a 300W ENI 300 L RF amplifier. A Trilithic™ H4LE35-3-AA-R high-power low pass filter (cut off frequency around 35 MHz) was used to suppress the "harmonics" of the $^1$H ENDOR signals.

**Data analysis and simulation**

The simulations of the EPR, ENDOR and HYSCORE spectra were based on the spin Hamiltonian approach

$$H_0 = \beta_e \vec{\boldsymbol{B}}_{\boldsymbol{0}} \cdot \boldsymbol{g} \cdot \vec{\boldsymbol{S}} - \sum_i g_n^i \beta_n \vec{\boldsymbol{B}}_{\boldsymbol{0}} \cdot \vec{\boldsymbol{I}}_{\boldsymbol{i}} + \sum_{\boldsymbol{i}} \vec{\boldsymbol{S}} \cdot \boldsymbol{A}_{\boldsymbol{i}} \cdot \vec{\boldsymbol{I}}_{\boldsymbol{i}} + \sum_{\boldsymbol{i}} \vec{\boldsymbol{I}}_{\boldsymbol{i}} \cdot \boldsymbol{P}_{\boldsymbol{i}} \cdot \vec{\boldsymbol{I}}_{\boldsymbol{i}}$$

where $\beta_e$ is the Bohr magneton, $\beta_n$ the nuclear magneton, $g_n^i$ the g-factor of the ith nucleus and $\boldsymbol{g}$ represents the electronic g-tensor, $\vec{\boldsymbol{B}}_{\boldsymbol{0}}$ the magnetic field vector, $\vec{\boldsymbol{S}}$ the effective spin vector, $\vec{\boldsymbol{I}}_{\boldsymbol{i}}$ nuclear spin vector, $\boldsymbol{A}_{\boldsymbol{i}}$ the hyperfine tensor, $\boldsymbol{P}_{\boldsymbol{i}}$ the nuclear quadrupole tensor and the sum runs over all nuclei (i) interacting with the unpaired electron spin. The first and the second terms represent the electron and nuclear Zeeman effects. The third term represents the hyperfine interaction of the unpaired electron with the nuclear spins and the last term represents the quadrupole coupling. The last term was used in the simulations only for $^{14}$N nuclei where I=1. The quadrupole tensor $\boldsymbol{P}_{\boldsymbol{i}}$ is traceless and its principal values can be rewritten in the following way:

$$\left[P_x, P_y, P_z\right] = \frac{e^2 qQ}{4I(2I-1)h}\left[-(1-\eta), -(1+\eta), 2\right] \ .$$

In this work we will use the two parameters: $K = \frac{e^2qQ}{4I(2I-1)h}$ and $\eta = \frac{P_x - P_y}{P_z}$ with $|P_z| \geq |P_y| \geq |P_x|$ and $0 \leq \eta \leq 1$ to characterize the quadrupole coupling.

All the simulations were performed in the EasySpin based program written in MATLAB™ environment[49]. ENDOR spectra were simulated using the "salt" routine and the frequency domain calculations of HYSCORE spectra were simulated using the "saffron" routine. Signals corresponding to the different nuclei were simulated separately in order to reduce computing time.

The orientations of the hyperfine and quadrupole tensors are presented with respect to the principal axes of the electronic g-tensor using Euler angels. In the convention used in EasySpin the first rotation is by angle $\alpha$ along the z axis, the second by angle $\beta$ around the new y' axis and the third by angle $\gamma$ around the new z'' axis[45]. The geometric details e.g. distances and angles for the [2Fe] sub-cluster used for the g-tensor orientation within the H-cluster molecular structure were extracted from the X-ray crystal data using the Pymol software[50].

## IV. Results

### FTIR of reduced and oxidized CrHydA1(pdt)

Figure 2 shows the FTIR spectra obtained for CrHydA1 with inserted labeled and non-labeled $[Fe_2(pdt)(CO)_4(CN)_2]^{2-}$ complexes in the reduced ("as obtained") and thionine oxidized states. Each spectrum contains only one component indicating that the preparations represent pure states and do not contain residual unbound $[Fe_2(pdt)(CO)_4(CN)_2]^{2-}$ complexes in solution. The IR band positions in the spectra obtained for non-labeled CrHydA1(pdt) are in agreement with previously reported data[21,22,24]. Upon labeling the $CN^-$ ligands of the pdt complexes the IR bands originating from the CO ligands are not affected while the ones originating from $CN^-$ vibrations are shifted by 29-31 $cm^{-1}$ upon $^{15}N$ exchange and 43-46 $cm^{-1}$ upon $^{13}C$ exchange.

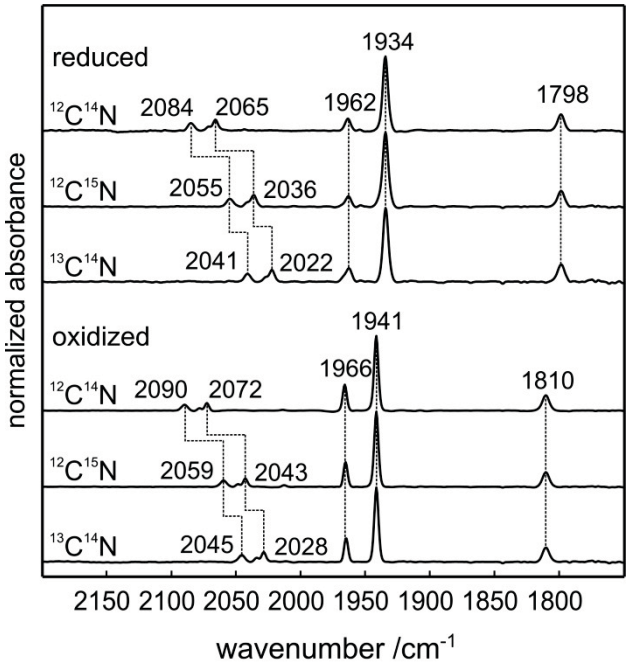


**Figure 2. Normalized FTIR spectra recorded for CrHydA1(pdt) containing non-labeled and two labeled pdt complexes in the reduced and oxidized states measured in 15°C. In the labeled complexes either N or C was labeled. All samples were prepared in 25 mM Tris/HCl, pH 8.0, 25 mM KCl. Oxidized samples also contained thionine.**

The EPR spectrum obtained for oxidized non-labeled CrHydA1(pdt) shows a pure state characterized by a rhombic signal virtually identical to the one obtained for native $H_{ox}$ (see supplementary information). The obtained g-values 2.093, 2.038 and 1.996, are in agreement with previously reported data on CrHydA1(pdt)[24].

It has been shown previously using $^{57}$Fe ENDOR that for the native H-cluster in the $H_{ox}$ state the spin density is delocalized over both iron atoms in the binuclear sub-cluster[25]. Additional information about the electronic structure can be obtained by investigating the distribution of the unpaired spin density over the ligands of the binuclear sub-cluster. In particular, the $CN^-$ ligands are of great interest and previously controlled isotope labeling of these ligands was not easily obtained[51,52].

## $^{13}$C interaction of the $CN^-$ ligands

The effect of $^{13}$C labeling of the $CN^-$ ligands is readily evident in the X-band EPR spectra where a splitting of all three g-components is easily observed (see figure 3A). In the Q-band EPR spectra this $^{13}$C hyperfine splitting is, however, washed out due to the increased line broadening. The X-band EPR spectra already allow an estimation of the $^{13}$C hyperfine coupling with principal values in the range of 21-29 MHz (depending on the g position) suggesting one strongly coupled $^{13}$C. More accurate values of this coupling can be

obtained using ENDOR spectroscopy. Moreover, this technique also allows for the identification of much weaker couplings that are not resolved in the EPR of $^{13}$CN labeled CrHydA1(pdt).

The most prominent signal in the X-band Davies ENDOR spectra (see figure 3B) recorded at the three canonical positions is centered at 14.5 MHz and is also present in the non-enriched sample (see supplementary information). This $^{1}$H ENDOR signal with maximum splitting of 3.5 MHz is very similar to the one obtained for native $H_{ox}$ and was assigned to the β-protons of the cysteine ligands coordinating the $[4Fe\text{-}4S]_H$ sub-cluster[37]. At this point, a full analysis of this signal is not possible due to the overlap of contributions from at least eight different protons. The observation of this $^{1}$H signal, however, confirms that the electronic structure of $H_{ox}$ in CrHydA1(pdt) is virtually identical to that of native $H_{ox}$ in which part of the spin density is delocalized on the $[4Fe\text{-}4S]_H$ sub-cluster.

In the X-band Davies ENDOR spectra (see figure 3B) two additional signals around and partially overlapping with the $^{1}$H ENDOR signal are observed, which are split by twice the Larmor frequency of $^{13}$C. The position of these signals at half the hyperfine interaction of the strongly coupled carbon nucleus is consistent with the splitting observed in the X-band pseudomodulated FID detected EPR spectrum (see figure 3A). However, it is not possible to simulate the spectra with high accuracy due to the large linewidth of these signals and their partial overlap with the $^{1}$H ENDOR signals. At low frequency the ENDOR spectra in figure 3B show another very sharp line around 6 MHz. This signal can be assigned to the weakly coupled $^{13}$C of the second $CN^-$ ligand. The low frequency line belonging to this doublet will fall below 1.5 MHz and cannot be detected due to the low sensitivity of the Davies ENDOR method in this frequency range.

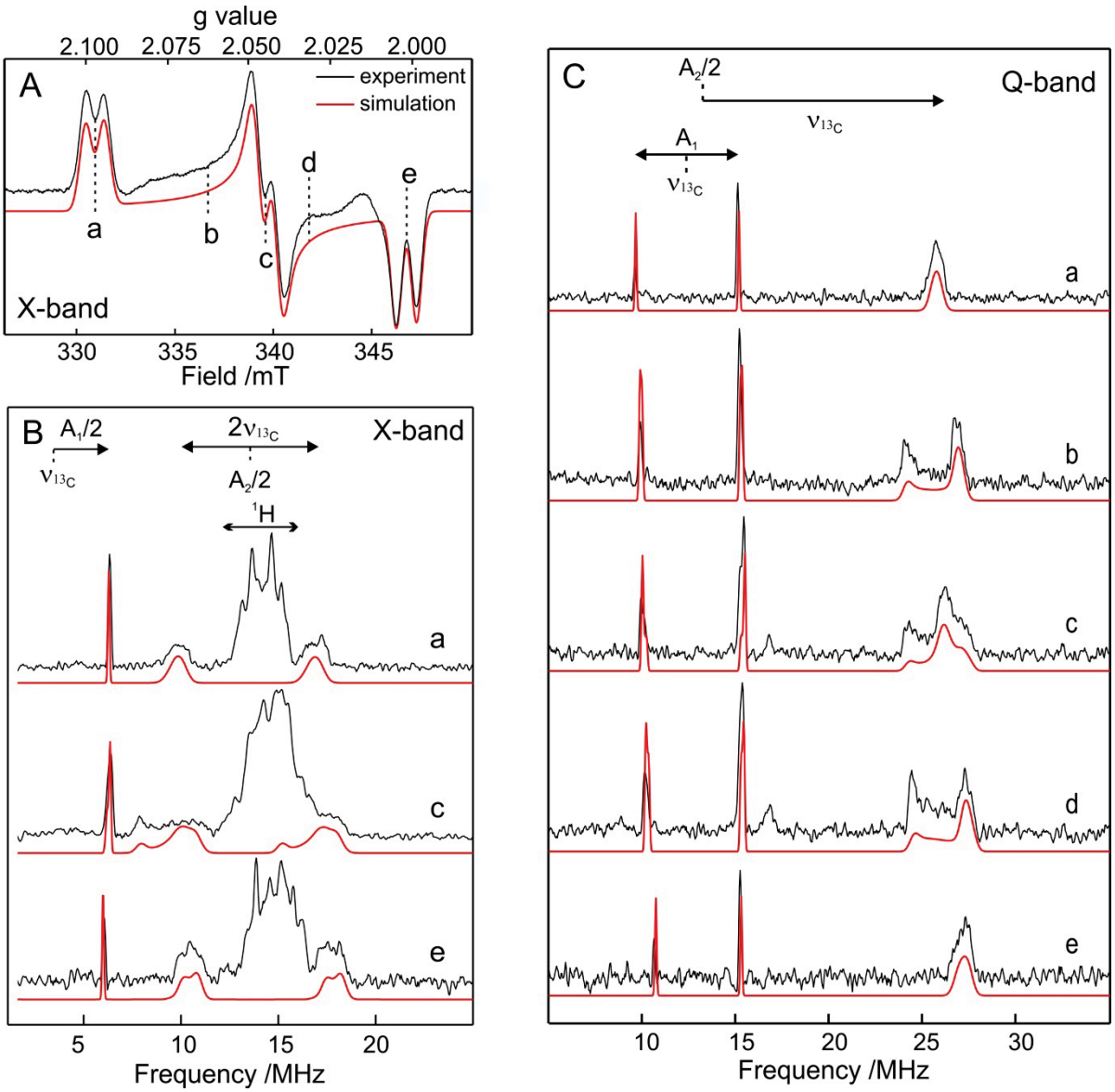


**Figure 3. EPR and ENDOR spectra recorded for oxidized CrHydA1(pdt) with $^{13}C$ labeled $CN^-$ ligands at 15 K including simulations. A) First derivative of X-band FID detected EPR spectra, microwave pulse length 1 µs, shot repetition time 2 ns, microwave frequency 9.715 GHz. The field positions at which the ENDOR spectra were recorded are marked a) to e). B) X-band Davies ENDOR spectra recorded with an RF pulse of 20 µs, shot repetition time 2 µs, microwave frequency 9.716 GHz, field positions: a) 330.9 mT ($g_1$), c) 339.7 mT ($g_2$), e) 346.8 mT ($g_3$). C) Q-band Davies ENDOR spectra recorded with an RF pulse of 20 µs, shot repetition time 2 µs, microwave frequency 33.921 GHz, field positions: a) 1158.2 mT ($g_1$), b) 1176.65 mT c) 1189.3 mT ($g_2$), d) 1195.1 mT e) 1213.6 mT ($g_3$). The black line represents experimental data and the red line the sum of the simulations. The assignment of the hyperfine splittings is indicated above the figure. The X-band FID detected EPR and Davies ENDOR spectra were simulated using the hyperfine values determined from the Q-band Davies ENDOR spectra.**

Complementary information can be obtained from the Q-band Davies ENDOR spectra, which were measured at five field positions and are presented in figure 3C. Here, only the high frequency transition of the $^{13}C$ doublet assigned to the strongly coupled cyanide ligand is visible and now appears around 27 MHz. Due to the better orientation selection and higher sensitivity at Q-band, the spectral resolution is enhanced as compared to the X-band ENDOR spectra. Both ENDOR signals assigned to the weakly coupled $^{13}C$ are

observable and can be simulated very accurately. Table 1 shows all obtained parameters, which were also used to simulate the spectra presented in figure 3.

**Table 1. Principal values of the $^{13}C$ hyperfine tensor of the $CN^-$ ligands of the oxidized CrHydA1(pdt).**

| | $A_1$ (MHz) | $A_2$ (MHz) | $A_3$ (MHz) | $A_{iso}$ (MHz) | α (°) | β (°) | γ (°) |
|---|---|---|---|---|---|---|---|
| $A_{1C}$ | 5.52 (0.05) | 5.52 (0.05) | 4.55 (0.05) | 5.2 | 0 (10) | 0 (10) | 0 (10) |
| $A_{2C}$ | 30 (0.5) | 28.5 (0.5) | 22.7 (0.5) | 27.1 | 0 (10) | 119 (10) | 46 (10) |

The signs of the hyperfine couplings cannot be determined. Numbers in parenthesis are uncertainties.

Both hyperfine tensors have an axial or nearly axial character but $A_{2C}$(iso) is around five times larger than $A_{1C}$(iso), which indicates a substantial difference in the spin density distribution over the two $CN^-$ ligands. By virtue of the well resolved $^{13}C$-ENDOR lineshapes for the strongly coupled $A_{2C}$, (see figure 3C), the relative orientation of $A_{2C}$ with respect to the g-tensor could be determined with high precision (table 1). The Euler angles of the hyperfine interaction tensor $A_{2C}$ in the g-tensor axis frame are remarkably similar to the orientation of the Fe-CN bond relative to the Fe-Fe vector extracted from the X-ray crystal structures of CpI and DdH (see figure 4). As discussed below, assuming $A_{2C}$ is oriented along the Fe-CN bond, this information can be used to make proposals concerning the g-tensor orientation within the H-cluster.

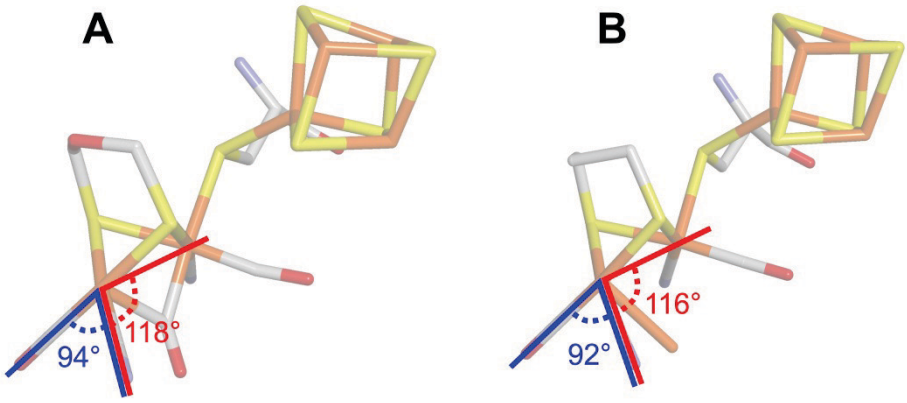


**Figure 4. The H-cluster according to the X-ray structures obtained for CpI (A) and DdH (B) with marked angles between the Fe-Fe vector and the Fe-C(N) bond (red) and between the Fe-C(N) and Fe-C(O) bonds (blue)[14,18].**

## $^{15}N$ interaction of the $CN^-$ ligands

The $^{14}N$ hyperfine couplings were previously obtained for DdH in the $H_{ox}$ state and can be used to compare the oxidized CrHydA1(pdt) system to the native one[19]. The

obtained HYSCORE spectra of DdH in the $H_{ox}$ state were very crowded due to the contributions of three $^{14}N$ nuclei with different quadrupole interactions. In the DdH study these three $^{14}N$ signals were assigned to the distal $CN^-$, the adt amine group and the coordinating Lys amine[19]. The $^{15}N$ labeled CrHydA1(pdt) hybrid protein offers a substantial simplification with respect to the CrHydA1(adt). Since the bridging amine is lacking and both $CN^-$ ligands are enriched with $^{15}N$, HYSCORE spectra are much easier to interpret.

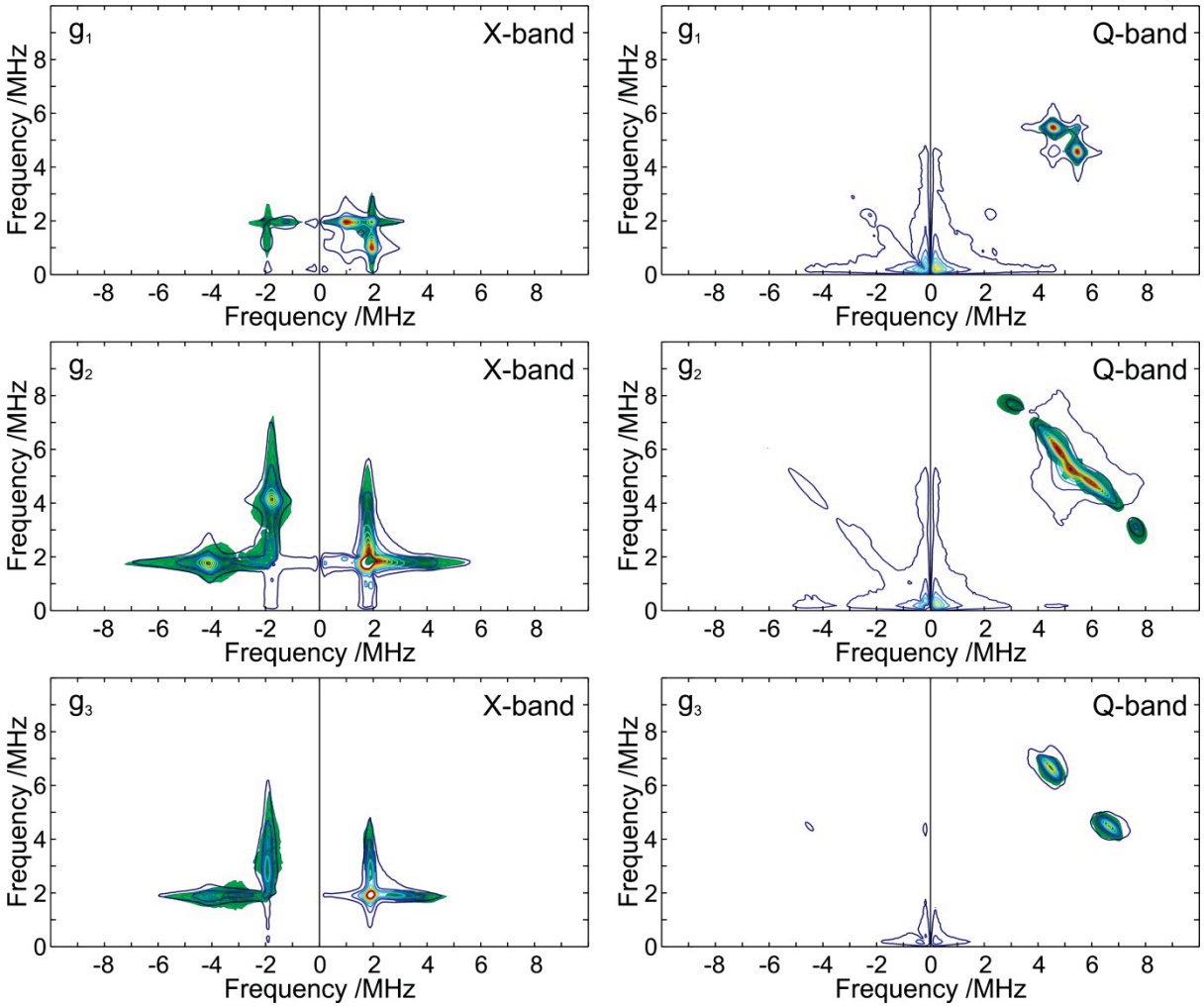


**Figure 5. X-band and Q-band HYSCORE spectra recorded for oxidized CrHydA1(pdt) with $^{15}N$ labeled $CN^-$ ligands at 20 K. Simulations are indicated in color (green). Left: X-band HYSCORE spectra recorded with $t_1$ and $t_2$ step 16 ns, shot repetition time 500 μs, microwave frequency 9.709 GHz, delay between two first microwave pulses (τ) 180 ns, length of microwave pulses (π/2) 8 ns and field positions (from the top) ($g_1$) 330.6 mT, ($g_2$) 339.5 mT, ($g_3$) 346.5 mT. Right: Q-band HYSCORE spectra recorded with $t_1$ and $t_2$ step 16 ns, shot repetition time 500 μs, microwave frequency 33.879 GHz, delay between two first microwave pulses (τ) 268 ns, length of microwave pulses (π/2) 16 ns and field positions (from the top) ($g_1$) 1156.9 mT, ($g_2$) 1187.7 mT, ($g_3$) 1212.5 mT. All the spectra were simulated using parameters from table 2 and are presented in green overlaid to experimental results.**

Figure 5 shows the CrHydA1(pdt)-$C^{15}N$ orientation selective HYSCORE spectra at X and Q-band overlaid with their simulations. The hyperfine simulation parameters are presented in table 2. In general, in the HYSCORE spectra crosspeaks originating from nuclei with weak hyperfine couplings ($|\nu_n|>|A/2|$) appear in the (++) quadrant, and spectral features

associated with strong hyperfine couplings ($|\nu_n|<|A/2|$) show up in the (-+) quadrant. While X-band HYSCORE signals occur in both (++) and (-+) quadrants of the 2D pattern, the Q-band HYSCORE spectra show only contributions in the (++) quadrant. This already allows the conclusion that the $^{15}N$ hyperfine principal values are in the range of twice the Larmor frequency at X-band (i.e. around 1.5 MHz)[45].

**Table 2. Principal values of the $^{15}N$ hyperfine tensor of the $CN^-$ ligands of the oxidized CrHydA1(pdt).**

| $A_1$ (MHz) | $A_2$ (MHz) | $A_3$ (MHz) | $A_{iso}$ (MHz) | $\alpha$ (°) | $\beta$ (°) | $\gamma$ (°) |
|---|---|---|---|---|---|---|
| -1.3 (0.2) | -1.1 (0.2) | 6.2 (0.2) | 1.3 | 0 (10) | 50 (10) | 90 (10) |

The signs of the hyperfine couplings cannot be determined. Numbers in parenthesis are uncertainties.

Although both $CN^-$ ligands are labeled with $^{15}N$ only one $^{15}N$ contribution is observed in the HYSCORE spectra. It is reasonable to assign this nitrogen to the $CN^-$ ligand in which we observed the strongly coupled $^{13}C$. Assuming that the isotropic hyperfine interaction of $^{13}C$ in a $CN^-$ ligand is a reflection of the spin density at that ligand, the spin density ratio between the two $CN^-$ ligands is larger by a factor of 5. If the same ratio would apply to the nitrogen nuclei of the $CN^-$ ligands the corresponding $^{15}N$ coupling of the "weakly coupled" ligand is expected to be ≈0.25 MHz and this would be too small to be detectable.

The hyperfine tensor obtained for $^{15}N$ also has a nearly axial character. Interestingly, the orientation of the hyperfine tensor obtained for $^{15}N$ is different from the one obtained for the strongly coupled $^{13}C$. The X-ray crystal structure indicates that both nitrogen atoms create hydrogen bonds with surrounding amino acids. The nitrogen in the $CN^-$ ligand bound to the distal iron atom can create three hydrogen bonds. It is shown in figure 6 that the distances and angles between this $CN^-$ ligand and the hydrogen bonds formed with Lys, Pro, Gln or Ile (for CpI and DdH, respectively) are very similar in both structures. The related angles are in the range from 99° to 139°. Evaluation of the relative angles between the $^{15}N$ and $^{13}C$ hyperfine tensors (see supplementary information) would suggest that the z axis of the $^{15}N$ hyperfine tensor should be aligned along one of the hydrogen bonds, or at least is strongly affected by the presence of multiple hydrogen bonds in which the $CN^-$ nitrogen takes part.

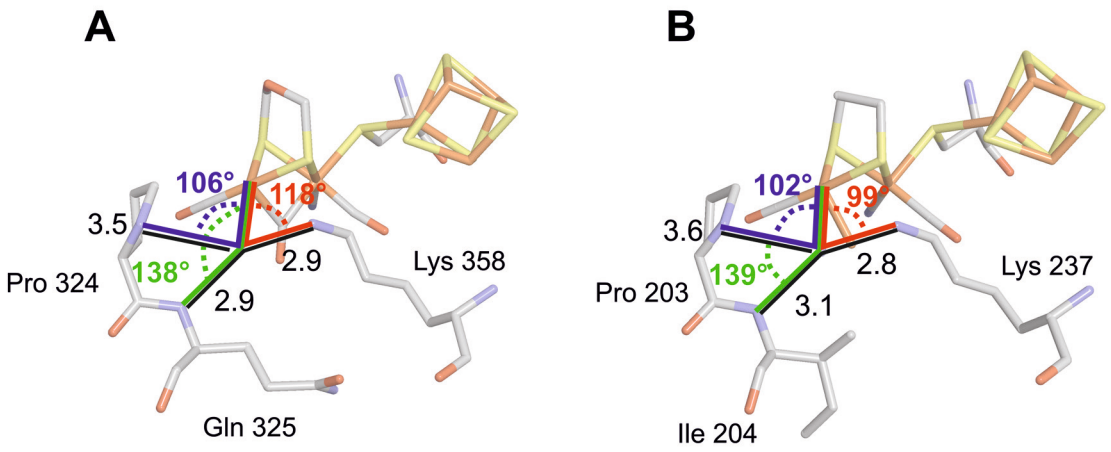


**Figure 6. The H-cluster from the X-ray structures obtained for CpI (A) and DdH (B) with marked angles between $CN^-$ ligand and the H-bond donor in lysine (red), proline (violet) and glutamine or isoleucine (green), respectively[14,18]. In black are marked distances in Å between nitrogen atoms.**

## $^{14}N$ Hyperfine and quadrupole coupling of the $CN^-$ ligand

The $^{15}N$ hyperfine interactions of the distal $CN^-$ ligand determined in the previous section can now be used to assess the signals from the naturally abundant $^{14}N$ $CN^-$ signals of CrHydA1(pdt). X- and Q-band field dependent HYSCORE spectra measured at $g_1$ and $g_2$ for DdH [FeFe] hydrogenase in the $H_{ox}$ state have been previously reported[19], therefore to allow for the direct comparison of the results for oxidized CrHydA1(pdt) with native $H_{ox}$ DdH studies with identical experimental settings were used. The obtained spectra are hardly distinguishable from the previously published data (see supplementary information). This demonstrates that after incorporation into the apo-protein of [FeFe] hydrogenase the modified pdt complex is “assembled” in the same way as the native H-cluster. Moreover the active site in [FeFe] hydrogenases from algae and bacteria are virtually identical.

For the sample containing native [FeFe] hydrogenases prepared in the $H_{ox}$ state it is very common that EPR spectra contain an additional component originating from the $H_{ox}$-CO state. The additional signal rather strongly overlaps with the high field part of the $H_{ox}$ spectrum, especially with the $g_3$ position, and significantly hinders or precludes assignment of the signal components in the HYSCORE spectra measured at this field. For oxidized CrHydA1(pdt) we can take advantage of the fact that no additional, overlapping signals are present. The $^{14}N$ HYSCORE spectrum measured at the field position corresponding to $g_3$ shows a very rich, informative pattern. The obtained X-band and Q-band HYSCORE spectra together with their simulation are presented in figure 7.

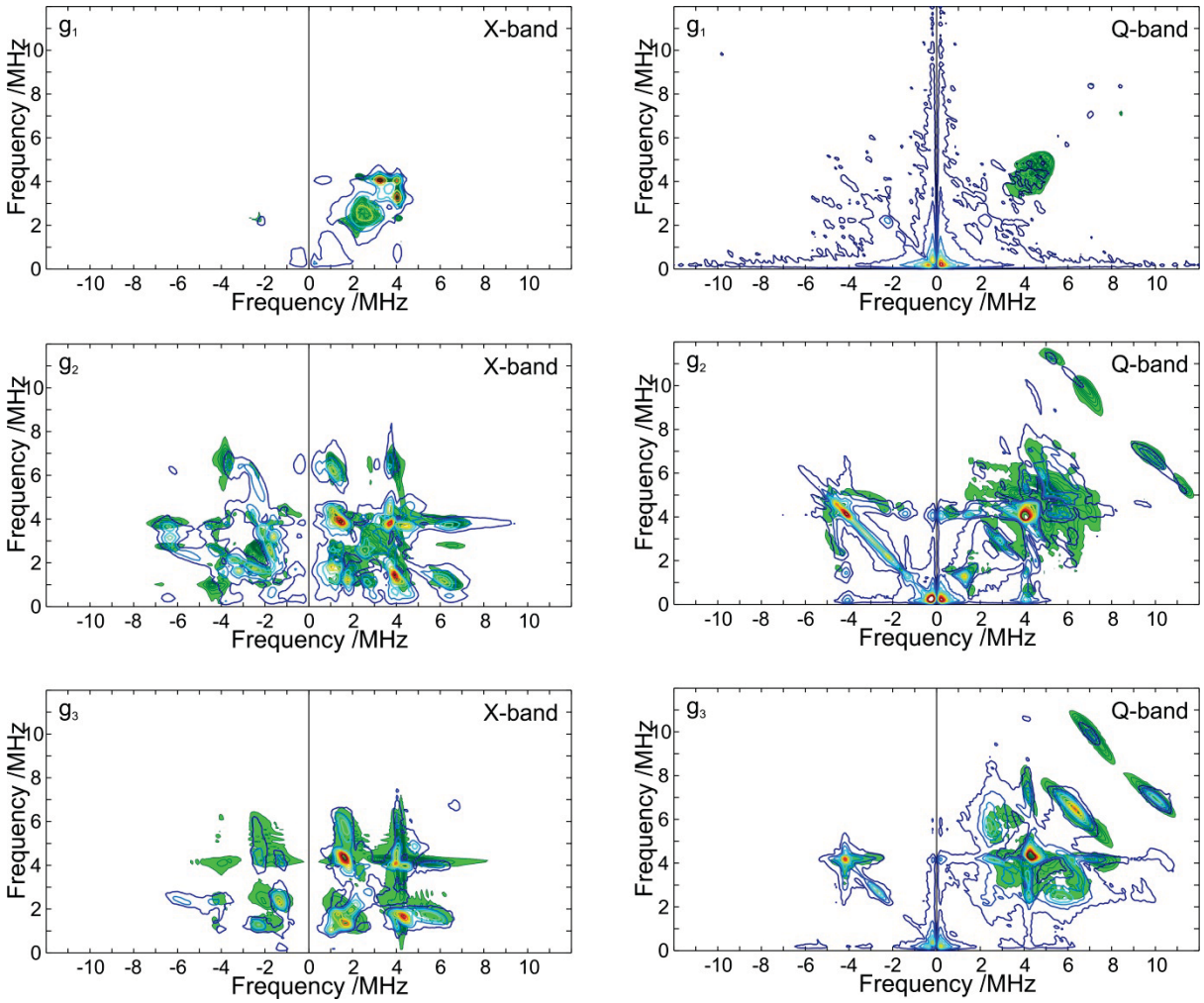


**Figure 7. X-band and Q-band HYSCORE spectra measured for oxidized CrHydA1(pdt) at 20 K. Simulations are indicated in color (green). Left: X-band HYSCORE spectra recorded with $t_1$ and $t_2$ step 16 ns, shot repetition time 500 µs, microwave frequency 9.717 GHz, delay between two first microwave pulses (τ) 180 ns, length of microwave pulses (π/2) 8 ns and field positions (from the top) ($g_1$) 330.8 mT, ($g_2$) 339.9 mT, ($g_3$) 346.9 mT. Right: Q-band HYSCORE spectra recorded with $t_1$ and $t_2$ step 16 ns, shot repetition time 500 µs, microwave frequency 33.867 GHz, delay between two first microwave pulses (τ) 268 ns, length of microwave pulses (π/2) 16 ns and field positions (from the top) ($g_2$) 1187.4 mT, ($g_3$) 1212.1 mT. All the spectra were simulated using parameters from table 3 and are presented in green and overlaid to the experimental results.**

The $^{14}$N HYSCORE features are dominated by the nuclear quadrupole interaction, which strongly depends on the ligand surrounding. For the $^{14}$N from $CN^-$ the quadrupole parameter K lies in the range between 0.7 and 1.0 MHz. The $^{14}$N hyperfine parameters are much more difficult to extract from the HYSCORE spectra. Therefore, we used the scaled hyperfine values obtained from the $^{15}$N HYSCORE experiments (table 2) and included previously reported quadrupole parameters as starting values in our simulations, only changing the orientation of the quadrupole tensor. The resulting simulation parameters are presented in table 3 and the corresponding spectra are overlaid on the experimental data as shown in figure 7. Both single and double quantum HYSCORE features are represented very

well by the simulations. The obtained quadrupole parameters K and η are in agreement with previously obtained values for the $CN^-$ ligands in DdH hydrogenase as well as an inorganic $[2Fe]_H$ model complex[19,53]. The $^{14}N$ nuclear quadrupole interaction Euler angles, however, deviate from the previously estimated value for DdH in $H_{ox}$. This could be due to inaccuracies in the determination of the Euler angles for DdH which had to be extracted from three overlapping $^{14}N$ HYSCORE patterns[19]. Interestingly, the $CN^-$ $^{14}N$ quadrupole tensor seems to be aligned with the $^{13}C$ hyperfine tensor (table 1 and 3). This would support the assumption that the z-axes of both the $^{14}N$ quadrupole and $^{13}C$ hyperfine tensors are aligned along the Fe-$CN_d$ bond (see below).

**Table 3. Principal values of the $^{14}N$ hyperfine and quadrupole tensors of the oxidized CrHydA1(pdt) and previously assigned to $CN_d$ in $H_{ox}$ DdH and in a model complex[19,53].**

| Hyperfine coupling | | | | | | | |
|---|---|---|---|---|---|---|---|
| $A_1$ (MHz) | $A_2$ (MHz) | $A_3$ (MHz) | $A_{iso}$ (MHz) | α (°) | β (°) | γ (°) | |
| -0.9 (0.2) | -0.8 (0.2) | 4.4 (0.2) | 0.9 | 0 (10) | 50 (10) | 90 (10) | pdt |
| 1.5 (0.4) | 3.8 (0.2) | -0.4 (0.2) | 1.5 | 41 (10) | 24 (10) | 0 (10) | $H_{ox}$ DdH[19] |
| 0.86 | 3.00 | 1.04 | 1.63 | - | - | - | model[53] |
| Quadrupole coupling | | | | | | | |
| K (MHz) | | η | | α (°) | β (°) | γ (°) | |
| 0.9 (0.03) | | 0.34 (0.02) | | 0 (10) | 119 (10) | 46 (10) | pdt |
| 0.95 (0.03) | | 0.34 (0.02) | | -26 (10) | 24 (10) | 0 (10) | $H_{ox}$ DdH[19] |
| 0.91 | | 0.00 | | - | - | - | model[53] |

The signs of the hyperfine couplings have not been determined. Numbers in parenthesis are uncertainties.

## V. Discussion

### Spin density distribution

It was found previously that in the native $H_{ox}$ state of the H-cluster the spin density is distributed over both iron atoms in the $[2Fe]_H$ sub-cluster[25]. Our current results on oxidized CrHydA1(pdt) show that the modified active site in this hybrid protein basically shows the same electronic structure. The ENDOR signal from the weakly coupled β-protons of the cysteines that coordinate the $[4Fe\text{-}4S]_H$ sub-cluster is identical for CrHydA1(pdt) and DdH (wild type) (figure S5 in supplementary information) suggesting that the same intercluster exchange interaction occurs in both proteins.

In recent work by Myers et al.[52], the [FeFe] hydrogenase from CpI was generated *in vitro* using the maturases HydE, HydF and HydG in combination with $^{13}C$ and $^{15}N$ labeled tyrosine as substrate for HydG. Analogous to our current work, the $CN^-$ ligands of the H-cluster were isotopically labeled with $^{13}C$ and $^{15}N$, and the signals from two $CN^-$ $^{13}C$ nuclei and one from $^{15}N$ were observed. The same large difference in the spin density distribution over both carbons was found (≈5:1) and the signal from the nitrogen was assigned to the $CN^-$ ligand in which we observed the strongly coupled $^{13}C$[52]. The $^{14}N$ HYSCORE spectra obtained for oxidized CrHydA1(pdt) strongly resembles previously reported spectra for native $H_{ox}$ in DdH[19]. In this work, supported by DFT calculations, the $^{14}N$ signal was assigned to the $CN^-$ ligand bound to the distal iron atom[19]. Although the $^{57}Fe$ hyperfine couplings indicate an almost equal spin distribution between the two irons in the bi-nuclear sub-cluster, apparently, the electronic structure is strongly affected by the protein environment and the inter-cluster exchange interaction between the $[2Fe]_H$ and $[4Fe\text{-}4S]_H$ cluster which causes the spin density distribution between the two $CN^-$ ligands to be shifted towards the distal $CN^-$ [25].

Due to the absence of the $adt^{2-}$ bridging amine in oxidized CrHydA1(pdt), the $^{14}N$ HYSCORE spectra are substantially simplified as compared to the situation for the native $H_{ox}$ state in DdH where three $^{14}N$ signals are observed ($CN^-$, adt, and Lys)[19]. Since the surrounding of the H-cluster is highly conserved one would expect to observe the same Lys $^{14}N$ contributions as in the native DdH $H_{ox}$ state. However, in the spectra obtained for the protein labeled with $[Fe_2(pdt)(CO)_4(C^{15}N)_2]^{2-}$ no signals originating from natural abundance $^{14}N$(Lys) were present. The HYSCORE spectra obtained for non-labeled oxidized CrHydA1(pdt) could be simulated with parameters describing only one component. The reported hyperfine coupling for the lysine in DdH is very small ($A_{iso}$ = 0.57 MHz)[19]. It is possible that this signal is overlapping with signals originating from the $CN^-$ ligand, but this is rather unlikely. Since there may be small differences in structure between the algal hydrogenase used in this study and the bacterial DdH enzyme used in the work of Silakov et al.[19], one can also speculate that less spin density is delocalized towards the Lys in CrHydA1 and the $^{14}N$(Lys) hyperfine coupling can no longer be observed.

**Orientation of the g tensor within the H-cluster**

Unfortunately, up to now, the DFT studies on the H-cluster were not successful in predicting the magnetic resonance properties of the iron core (g-tensor and $^{57}$Fe hyperfine interaction) with any confidence[54,55]. Although the effect of CO binding to the exchangeable site (i.e. a spin density shift towards the $[4Fe\text{-}4S]_H$ sub-cluster) is correctly predicted, the influence of the [4Fe-4S] cluster is not represented very well. In fact, the DFT predicted spin density distributions rather reflect the situation occurring in binuclear model complexes without the $[4Fe\text{-}4S]_H$ unit[32,37,38,55]. In $H_{ox}$-CO a strong intercluster exchange (95 $cm^{-1}$) interaction is apparent based on the $^{57}$Fe hyperfine interaction data which led us to speculate that the $g_z$-component could be oriented along the intercluster axis[25]. Since in $H_{ox}$ and oxidized CrHydA1(pdt) the intercluster exchange interaction is much smaller (25 $cm^{-1}$) and the spin density seems to be equally distributed over both iron atoms in $[2Fe]_H$, it is reasonable to assume that the vector connecting $Fe_p$ and $Fe_d$ represents a local symmetry axis and defines the orientation of the g tensor[25]. The other g-axis would be defined by the local symmetry plane through both irons and the bridging CO ligand (bisecting the dithiol ligand). Figure 8 shows the proposed g-tensor axis orientation and the angles of the $Fe_d$-CN bond in this axis system. The Euler angles of both the $CN^-$ carbon hyperfine $A_{2C}$ and nitrogen quadrupole $Q_N$ tensors (0,119,46) degrees correspond to a rotation matrix which defines the orientation of the tensor z-components with respect to the g-tensor axes as (127, 51, 119) degrees. These values fit perfectly to the orientation of the Fe-CN bond with respect to the g-tensor orientation as proposed in figure 8.

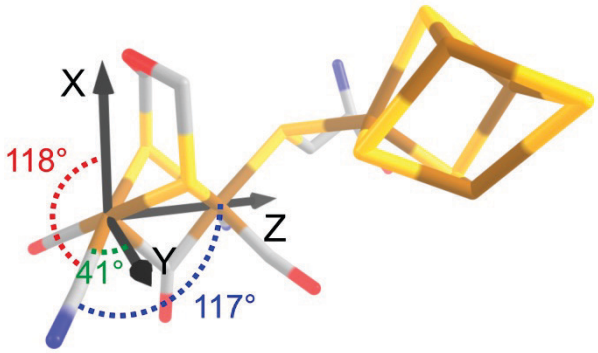


**Figure 8. The coordinate system describing the position of the g-tensor overlaid onto the H-cluster from the X-ray structure obtained for CpI[18].**

## VI. Conclusions

The oxidized state of the artificially maturated CrHydA1(pdt) hybrid is shown to be a very accurate and useful structural mimic of the native active oxidized state of CrHydA1. The $^{1}$H ENDOR and $^{14}$N HYSCORE spectra of oxidized CrHydA1(pdt) are virtually indistinguishable from those of native $H_{ox}$ (apart from the lacking $^{14}$N $adt^{2-}$ contribution). The high resolution $^{15}$N and $^{13}$C hyperfine interaction data of the $CN^-$ ligands confirmed the previously proposed model of the electronic structure of the H-cluster in which the spin density is delocalized over the two iron atoms of the bi-nuclear sub-cluster. In addition, the accurate data on the relative orientation of the distal $CN^-$ ligand in the g-axis frame, allowed to suggest an orientation of the g-tensor adapted to the local symmetry of the complete binuclear sub-cluster in which the Fe-Fe bond represents one of the g- principal axes. The accurate data obtained on the $^{14}$N/$^{15}$N coupling of the distal $CN^-$ ligand will facilitate the assignment and analysis of the nitrogen couplings of the adt bridge in the CrHydA1($^{15}$N adt) hybrid which is currently under investigation in our group. Although oxidized CrHydA1(pdt) is shown to be a perfect structural and electronic mimic for native $H_{ox,}$ even showing residual hydrogenase activity, the other resting states of the native enzyme ($H_{red}$, $H_{sred}$ and $H_{ox}$-CO) are lacking[23,24]. At this point it is not clear how this intriguing behavior can be related to the presence or absence of the bridging amine (adt) function. Detailed comparative spectroscopic and quantum chemical investigations may reveal the subtle structural dependencies triggering the conversion between the diverging resting (and intermediate) states of CrHydA1(pdt) and CrHydA1(adt). The current study is one of the first steps in this endeavor.

## VII. Acknowledgements

We would like to thank Gudrun Klihm for her excellent technical support in the EPR experiments. Furthermore, the Max Planck Society, the Deutsche Forschungsgemeinschaft (DIP project), the Life Science Division of CEA (Bio-energy program), the French National Research Agency (NiFe–Cat project, ANR–10–BLAN–711, Labex program ARCANE, ANR-11-LABX-0003-01 and DYNAMO, ANR-11-LABX-0011) and from Fondation de l'Orangerie for individual Philanthropy and its donors are gratefully acknowledged for their financial support.

Reference List


(1) *Hydrogen as a Fuel: Learning from Nature*, Cammack, R.; Frey, M.; Robson, R., eds.; Talor & Francis: London **2001**.

(2) Nath, K.; Das, D. *Appl. Microbiol. Biotechnol.* **2004**, *65*, 520.

(3) Kotay, S. M.; Das, D. *Int. J.Hydrogen Energy* **2008**, *33*, 258.

(4) Miyake, J.; Igarashi, Y.; Rögner, M. *Biohydrogen III*, **2004**.

(5) Rand, D. A. J.; Dell, R. M. *Hydrogen Energy Challenges and Prospects*, RSC Publishing: Cambridge, **2008**.

(6) Mertens, R.; Liese, A. *Curr. Opin. Biotechnol.* **2004**, *15*, 343.

(7) Kim, J. Y. H.; Cha, H. J. *Korean J. Chem. Eng.* **2013**, *30*, 1.

(8) Bockris, J. O. M. *Int. J.Hydrogen Energy* **2013**, *38*, 2579.

(9) Lubitz, W.; Ogata, H.; Rüdiger, O.; Reijerse, E. *Chem. Rev.* **2014**, *114*, 4081.

(10) Vignais, P. M.; Billoud, B. *Chem. Rev.* **2007**, *107*, 4206.

(11) Stripp, S. T.; Happe, T. *Dalton Trans.* **2009**, *45*, 9960.

(12) Hatchikian, E. C.; Forget, N.; Fernandez, V. M.; Williams, R.; Cammack, R. *Eur. J. Biochem.* **1992**, *209*, 357.

(13) Nicolet, Y.; de Lacey, A. L.; Vernede, X.; Fernandez, V. M.; Hatchikian, E. C.; Fontecilla-Camps, J. C. *J. Am. Chem. Soc.* **2001**, *123*, 1596.

(14) Nicolet, Y.; Piras, C.; Legrand, P.; Hatchikian, C. E.; Fontecilla-Camps, J. C. *Struct. Fold. Des.* **1999**, *7*, 13.

(15) Lemon, B. J.; Peters, J. W. *Biochemistry* **1999**, *38*, 12969.

(16) Peters, J. W.; Lanzilotta, W. N.; Lemon, B. J.; Seefeldt, L. C. *Science* **1998**, *282*, 1853.

(17) Pierik, A. J.; Hulstein, M.; Hagen, W. R.; Albracht, S. P. J. *Eur. J.Biochem.* **1998**, *258*, 572.

(18) Pandey, A. S.; Harris, T. V.; Giles, L. J.; Peters, J. W.; Szilagyi, R. K. *J. Am. Chem. Soc.* **2008**, *130*, 4533.

(19) Silakov, A.; Wenk, B.; Reijerse, E.; Lubitz, W. *Phys.Chem.Chem. Phys.***2009**, *11*, 6592.

(20) Erdem, Ö. F.; Schwartz, L.; Stein, M.; Silakov, A.; Kaur-Ghumaan, S.; Huang, P.; Ott, S.; Reijerse, E. J.; Lubitz, W. *Angew.Chem., Int.Ed.* **2011**, *50*, 1439.

(21) Berggren, G.; Adamska, A.; Lambertz, C.; Simmons, T.; Esselborn, J.; Atta, M.; Gambarelli, S.; Mouesca, J.; Reijerse, E.; Lubitz, W.; Happe, T.; Artero, V.; Fontecave, M. *Nature* **2013**, *499*, 66.

(22) Esselborn, J.; Lambertz, C.; Adamska-Venkatesh, A.; Simmons, T.; Berggren, G.; Noth, J.; Siebel, J.; Hemschemeier, A.; Artero, V.; Reijerse, E.; Fontecave, M.; Lubitz, W.; Happe, T. *Nat. Chem. Biol.* **2013**, *9*, 607.

(23) Siebel, J.F.; Adamska-Venkatesh, A.; Weber, K.; Rumpel, S.; Reijerse, E.; Lubitz, W. *Biochemistry* **submitted for publication**.

(24) Adamska-Venkatesh, A.; Krawietz, D.; Siebel, J.; Weber, K.; Happe, T.; Reijerse, E.; Lubitz, W. *J. Am. Chem. Soc.* **2014**, *136*, 11339.

(25) Silakov, A.; Reijerse, E. J.; Albracht, S. P. J.; Hatchikian, E. C.; Lubitz, W. *J. Am. Chem. Soc.* **2007**, *129*, 11447.

(26) Albracht, S. P. J.; Roseboom, W.; Hatchikian, E. C. *J. Biol. Inorg. Chem.***2006**, *11*, 88.

(27) Roseboom, W.; de Lacey, A. L.; Fernandez, V. M.; Hatchikian, E. C.; Albracht, S. P. J. *J. Biol. Inorg. Chem.* **2006**, *11*, 102.

(28) Silakov, A.; Kamp, C.; Reijerse, E.; Happe, T.; Lubitz, W. *Biochemistry* **2009**, *48*, 7780.

(29) Adamska, A.; Silakov, A.; Lambertz, C.; Rüdiger, O.; Happe, T.; Reijerse, E.; Lubitz, W. *Angew.Chem., Int.Ed.* **2012**, *51*, 11458.

(30) Lubitz, W.; Reijerse, E.; van Gastel, M. *Chem. Rev.* **2007**, *107*, 4331.

(31) Chen, Z. J.; Lemon, B. J.; Huang, S.; Swartz, D. J.; Peters, J. W.; Bagley, K. A. *Biochemistry* **2002**, *41*, 2036.

(32) Silakov, A.; Olsen, M. T.; Sproules, S.; Reijerse, E. J.; Rauchfuss, T. B.; Lubitz, W. *Inorg.Chem.***2012**, *51*, 8617.

(33) Silakov, A.; Wenk, B.; Reijerse, E.; Albracht, S. P. J.; Lubitz, W. *J. Biol. Inorg. Chem.* **2009**, *14*, 301.

(34) Pereira, A. S.; Tavares, P.; Moura, I.; Moura, J. J. G.; Huynh, B. H. *J. Am. Chem. Soc.* **2001**, *123*, 2771.

(35) Pierik, A. J.; Hagen, W. R.; Redeker, J. S.; Wolbert, R. B. G.; Boersma, M.; Verhagen, M.; Grande, H. J.; Veeger, C.; Mutsaers, P. H. A.; Sands, R. H.; Dunham, W. R. *Eur. J. Biochem.* **1992**, *209*, 63.

(36) Popescu, C. V.; Münck, E. *J. Am. Chem. Soc.* **1999**, *121*, 7877.

(37) Silakov, A.; Reijerse, E. J.; Lubitz, W. *Eur. J. Inorg. Chem.* **2011**, *7*, 1056.

(38) Silakov, A.; Shaw, J. L.; Reijerse, E. J.; Lubitz, W. *J. Am. Chem. Soc.* **2010**, *132*, 17578.

(39) Van Dam, P. J.; Reijerse, E. J.; Hagen, W. R. *Eur. J. Biochem.***1997**, *248*, 355.

(40) Seyferth, D.; Womack, G. B.; Gallagher, M. K.; Cowie, M.; Hames, B. W.; Fackler, J. P.; Mazany, A. M. *Organometallics* **1987**, *6*, 283.

(41) Le Cloirec, A.; Best, S. P.; Borg, S.; Davies, S. C.; Evans, D. J.; Hughes, D. L.; Pickett, C. J. *Chem. Commun.* **1999**, 2285.

(42) Kuchenreuther, J. M.; Grady-Smith, C. S.; Bingham, A. S.; George, S. J.; Cramer, S. P.; Swartz, J. R. *PLoS One* **2010**, *5*, e15491.

(43) Hyde, J. S.; Pasenkiewicz-Gierula, M.; Lesmanowicz, A.; Antholine, W. E. *Appl. Magn. Reson.* **1990**, *1*, 483.

(44) Davies, E. R. *Phys. Lett. A* **1974**, *A 47*, 1.

(45) Schweiger, A.; Jeschke, G. *Principles of Pulse Electron Paramagnetic Resonance*; Oxford University Press : Oxford, **2001**.

(46) Höfer, P.; Grupp, A.; Nebenführ, H.; Mehring, M. *Chem. Phys. Lett.* **1986**, *132*, 279.

(47) Shane, J. J.; Hofer, P.; Reijerse, E. J.; Deboer, E. *J. Magn. Reson.* **1992**, *99*, 596.

(48) Reijerse, E.; Lendzian, F.; Isaacson, R.; Lubitz, W. *J. Magn. Reson.* **2012**, *214*, 237.

(49) Stoll, S.; Schweiger, A. *J. Magn. Reson.* **2006**, *178*, 42.

(50) The PyMOL Molecular Graphics System. Version 1.5.0.4 Schrödinger, LLC.

(51) Kuchenreuther, J. M.; George, S. J.; Grady-Smith, C. S.; Cramer, S. P.; Swartz, J. R. *PLoS One* **2011**, *6*, e20346.

(52) Myers, W. K.; Stich, T. A.; Suess, D. L. M.; Kuchenreuther, J. M.; Swartz, J. R.; Britt, R. D. *J. Am. Chem. Soc.* **2014**, *136*, 12237.

(53) Erdem, Ö. F.; Stein, M.; Kaur-Ghumaan, S.; Reijerse, E. J.; Ott, S.; Lubitz, W. *Chem.Eur. J.* **2013**, *19*, 14566.

(54) Fiedler, A. T.; Brunold, T. C. *Inorg.Chem.* **2005**, *44*, 9322.

(55) Greco, C.; Silakov, A.; Bruschi, M.; Ryde, U.; De Gioia, L.; Lubitz, W. *Eur. J. Inorg. Chem.* **2011**, *7*, 1043.

# SUPPORTING INFORMATION

for

# Artificially Maturated [FeFe] Hydrogenase from *Chlamydomonas reinhardtii*: A HYSCORE and ENDOR Study of a Non-Natural H-cluster

Agnieszka Adamska-Venkatesh[1], Trevor R. Simmons[2], Judith F. Siebel[1], Vincent Artero[2], Marc Fontecave[2,3], Edward Reijerse[1], Wolfgang Lubitz[1]

[1] Max Planck Institut für Chemische Energiekonversion, Stiftstrasse 34-36, 45470 Mülheim an der Ruhr, Germany

[2] Laboratoire de Chimie et Biologie des Métaux; Université Grenoble Alpes , CEA, CNRS, 17 rue des martyrs, 38000 Grenoble, France

[3] Laboratoire de Chimie des Processus Biologiques, Collège de France, Université Pierre et Marie Curie, CNRS UMR 8229, 11 place Marcelin Berthelot, 75005 Paris, France

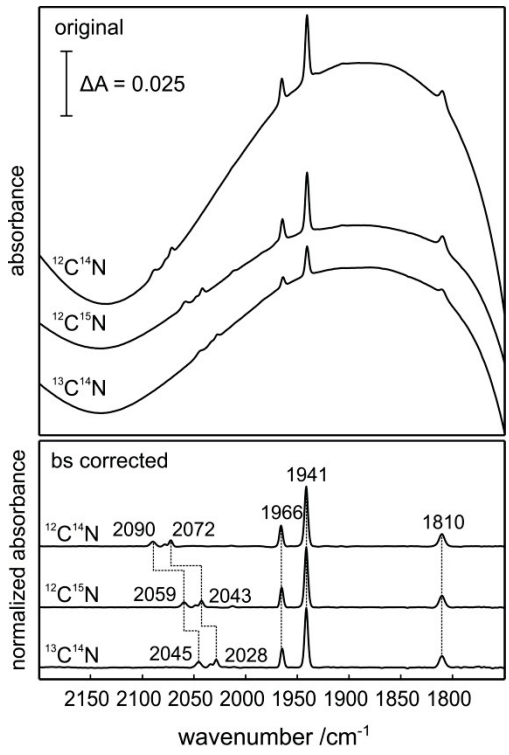


**Figure S1. FTIR absorbance spectra and the baseline corrected spectra recorded for oxidized CrHydA1(pdt) containing non-labeled and two labeled pdt complexes.**

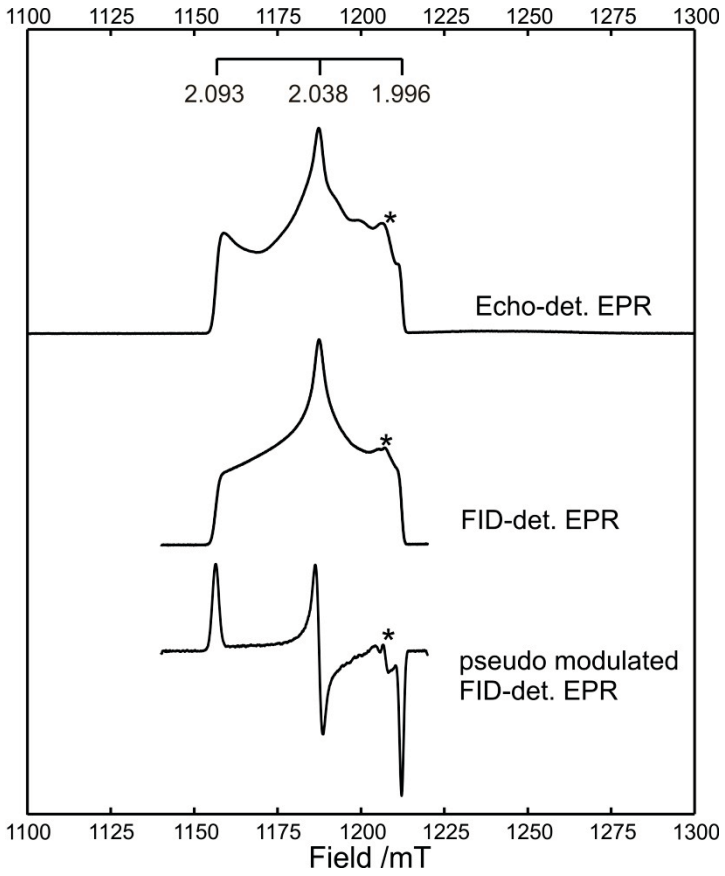


**Figure S2. Q-band 2-pulse detected EPR (top), FID detected EPR (middle) and first derivative of FID-detected EPR (bottom) spectra of oxidized CrHydA1(pdt) measured at 20 K. The 2-pulse detected EPR spectrum was measured with microwave pulse lengths $\pi/2$ = 16 ns and $\pi$ = 32 ns and the, separation between the two pulses was $\tau$ = 500 ns. The shot repetition time was 1 ms and the microwave frequency 33.868 GHz. The FID detected EPR spectrum was measured with a microwave pulse length of 1 μs, shot repetition time 1 ms, microwave frequency 33.868 GHz. Above the spectra g-values obtained from simulation are presented. The asterisk indicates an overlapping signal originating from a small amount of [3Fe-4S] cluster.**

The 2-pulse echo detected EPR spectrum is affected by the field dependent phase memory time and nuclear spin modulations originating from interactions with $^{14}$N nuclei. To avoid such distortion FID-detected EPR spectra were recorded for each sample.

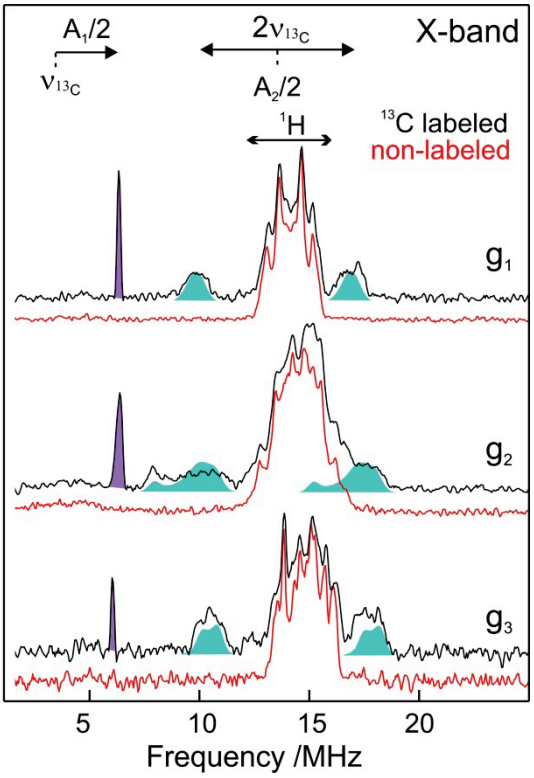


**Figure S3. X-band Davies ENDOR spectra measured for non-labeled (red) and $^{13}C$ labeled $CN^-$ ligands (black) of oxidized CrHydA1(pdt) at 15 K at the field positions corresponding to $g_1$, $g_2$ and $g_3$. All spectra were recorded using an RF pulse of 20 µs and a shot repetition time of 2 ms. The microwave frequency for measurement on the labeled sample was 9.716 GHz and the field positions: 330.9 mT ($g_1$), 339.7 mT ($g_2$), 346.8 mT ($g_3$). For the non-labeled sample a microwave frequency of 9.716 GHz was used at field positions: 331 mT ($g_1$), 339.8 mT ($g_2$), 346.9 mT ($g_3$). The assignments of the hyperfine couplings are indicated at the top of the figure.**

The most prominent signal in the X-band Davies ENDOR spectra (see figure S3) is centered at 14.5 MHz and is also present in the non-enriched sample. This $^1H$ ENDOR signal with maximum splitting of 3.5 MHz is very similar to the one obtained for native $H_{ox}$ and was assigned to the β-protons of the cysteine ligands coordinating the $[4Fe\text{-}4S]_H$ sub-cluster.

**Calculation of the angle between $^{13}C$ and $^{15}N$ hyperfine tensors**

To obtained angles between two hyperfine tensors first the rotation matrixes were calculated (using EasySpin in Matlab). EasySpin is using the following convention for the definition of Euler angles:

$$R = R_{z''}(\gamma) \cdot R_{y'}(\beta) \cdot R_z(\alpha)$$

$$= \begin{pmatrix} cos\gamma & sin\gamma & 0 \\ -sin\gamma & cos\gamma & 0 \\ 0 & 0 & 1 \end{pmatrix} \cdot \begin{pmatrix} cos\beta & 0 & -sin\beta \\ 0 & 1 & 0 \\ sin\beta & 0 & cos\beta \end{pmatrix} \cdot \begin{pmatrix} cos\alpha & sin\alpha & 0 \\ -sin\alpha & cos\alpha & 0 \\ 0 & 0 & 1 \end{pmatrix}$$

$$= \begin{pmatrix} cos\gamma cos\beta cos\alpha - sin\gamma sin\alpha & cos\gamma cos\beta sin\alpha + sin\gamma cos\alpha & -cos\gamma sin\beta \\ -sin\gamma cos\beta cos\alpha - cos\gamma sin\alpha & -sin\gamma cos\beta sin\alpha + cos\gamma cos\alpha & sin\gamma sin\beta \\ sin\beta cos\alpha & sin\beta sin\alpha & cos\beta \end{pmatrix}$$

Subsequently, the relative angles between the two tensor axis frames can be calculated by evaluating the inproduct matrix of the two rotation matrices as shown below:

The rotation matrix for the $^{13}C$ hyperfine tensor rotated around $\alpha$ = 0, $\beta$ = 119 and $\gamma$ = 46 is calculated as:

$$R_{13C} = \begin{pmatrix} -0.3368 & 0.7193 & -0.6076 \\ 0.3487 & 0.6947 & 0.6291 \\ 0.8746 & 0 & -0.4848 \end{pmatrix}$$

For the rotation matrix for the $^{15}N$ hyperfine tensor rotated around $\alpha$ = 0, $\beta$ = 50 and $\gamma$ = 90 we obtain:

$$R_{15N} = \begin{pmatrix} 0 & 1 & 0 \\ -0.6428 & 0 & 0.7660 \\ 0.7660 & 0 & 0.6428 \end{pmatrix}$$

The matrix representing the relative angles in degree between the axes of these two tensors equals to:

$$angles = \begin{pmatrix} 63.5 & 116.5 & 140.9 \\ 109.7 & 44 & 127.4 \\ 33.9 & 57.8 & 80.2 \end{pmatrix}$$

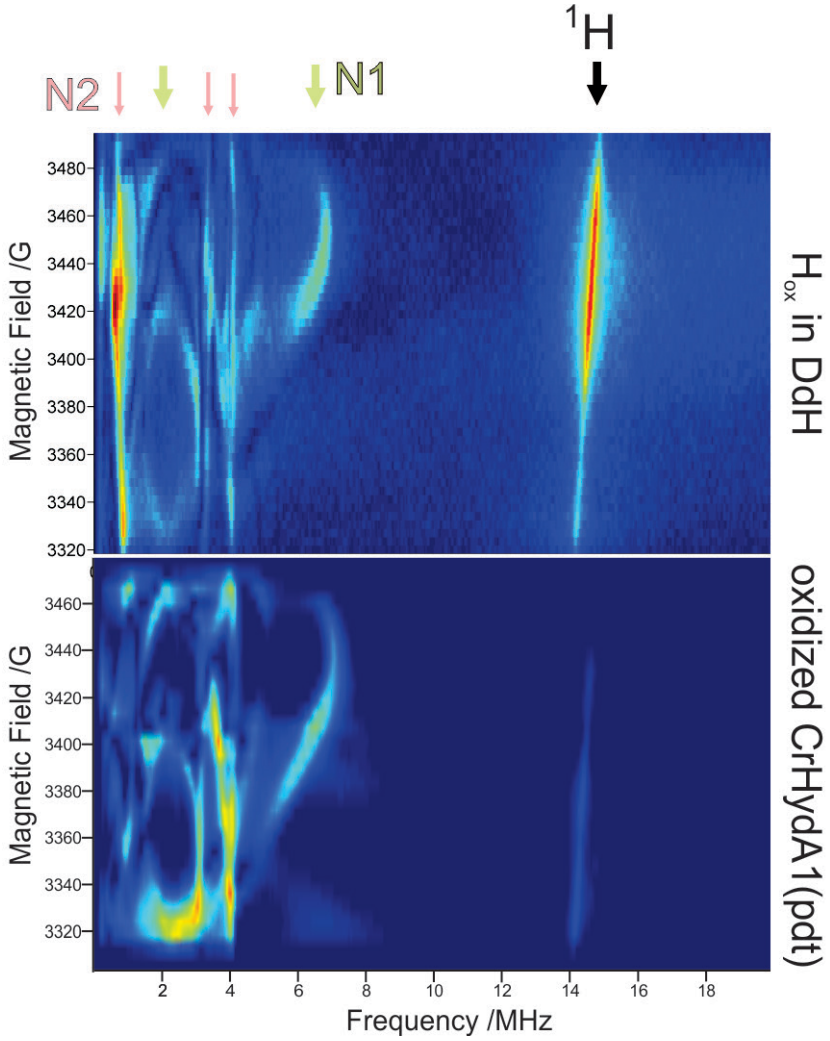


**Figure S4. Comparison of the X-band 3-pulse ESEEM vs magnetic field of oxidized CrHydA1(pdt) (bottom) with the previously published $H_{ox}$ state from DdH (top)[20]. Both spectra were measured under the same experimental conditions: temperature 15 K, length of microwave pulses π/2 = 8 ns, delay between first two pulses τ = 180 ns. Microwave frequency was 9.726 GHz (for the oxidized CrHydA1(pdt)) and 9.778 GHz (for the $H_{ox}$ state from DdH).**

The large difference in intensity between the $^1$H signals is most likely a result of the overlapping additional signal from $H_{ox}$-CO present in the native DdH preparation. In both spectra a $^{14}$N signal is present showing a strong field dependence; it is assigned to nitrogen from the $CN^-$ ligand.

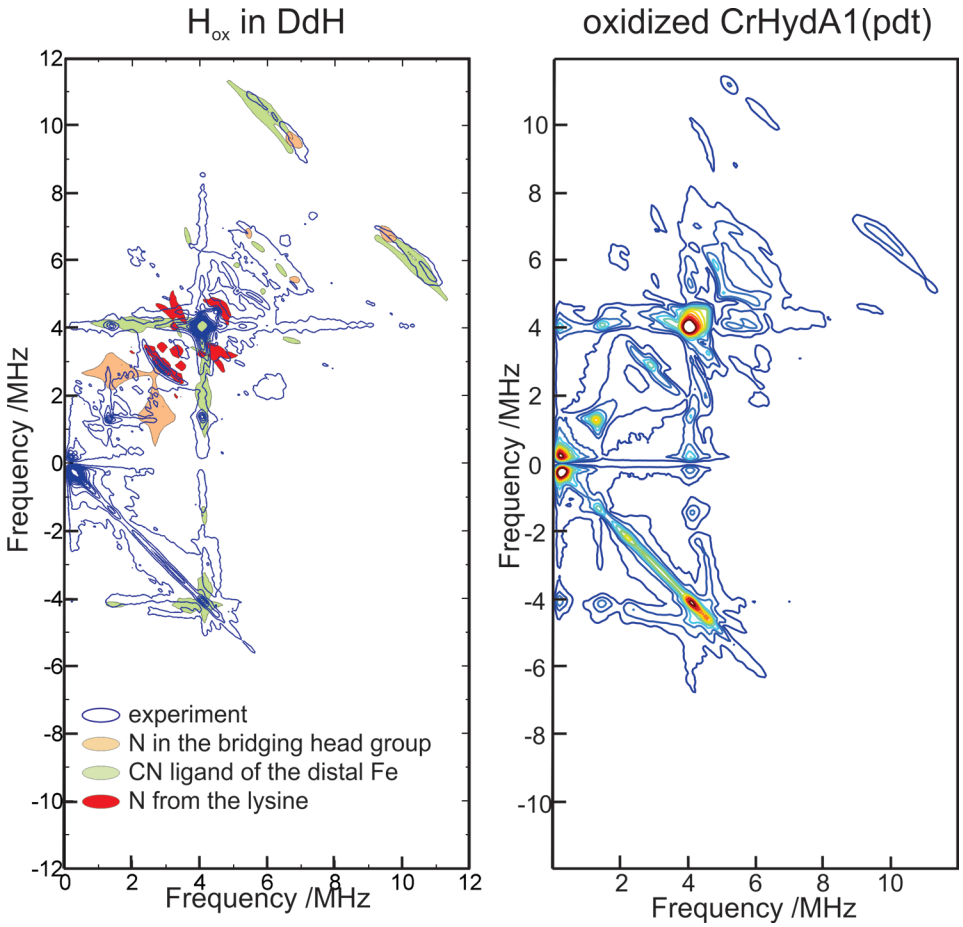


**Figure S5. Comparison of the Q-band HYSCORE spectra of oxidized CrHydA1(pdt) (right) with the previously published $H_{ox}$ state from DdH (left) measured at a field corresponding to the $g_2$ position[20]. Both spectra were measured under the same experimental conditions: temperature 20 K, $t_1$ and $t_2$ step 16 ns, shot repetition time 500 μs, delay between the two first microwave pulses (τ) 268 ns. Microwave frequency was 33.867 GHz (for the oxidized CrHydA1(pdt)) and 33.865 GHz (for the $H_{ox}$ state from DdH). The length of microwave pulses previously used was (π/2) 36 ns and 16 ns in the current measurements.**

A signal previously assigned to the nitrogen in the bridging head group is not present in the HYSCORE spectrum obtained for oxidized CrHydA1(pdt).

Reference List

(1) Silakov, A.; Wenk, B.; Reijerse, E.; Lubitz, W. *Physical Chemistry Chemical Physics* **2009**, *11*, 6592.

## *Curriculum Vitae*

**First name:** Agnieszka
**Surname:** Adamska-Venkatesh
**Family name:** Adamska
**Marital status:** married
**Born in:** 14th July 1986
**Nationality:** Polish

**Education:**

2003-2005 High school Liceum Ogólnokształcące im. Braci Śniadeckich w Żninie, Żnin, Poland
2005-2010 M.Sc. (Biophysics), Department of Biochemistry, Biophysics and Biotechnology, Jagiellonian University, Cracow, Poland.
2010- PhD student, Max Planck Institute for Chemical Energy Conversion, Mülheim an der Ruhr, Germany; Henrich-Heine Universitat, Düsseldorf, Germany

**List of publications:**

A. Adamska, A. Silakov, C. Lambertz, O. Rüdiger, T. Happe, E. Reijerse, W. Lubitz, "Identification and characterization of the "super-reduced" state of the H-cluster in [FeFe] hydrogenase: a new building block for the catalytic cycle?", ***Angew. Chem. Int. Ed.*** **2012,** *51* (46), 11458-11462.

G. Berggren, A. Adamska, C. Lambertz, T. R. Simmons, J. Esselborn, M. Atta, S. Gambarelli, J.M. Mouesca, E. Reijerse, W. Lubitz, T. Happe, V. Artero, M. Fontecave, "Biomimetic assembly and activation of [FeFe]-hydrogenases." ***Nature*** **2013,** *499* (7456), 66-69.

J. Esselborn, C. Lambertz, A. Adamska-Venkatesh, T. Simmons, G. Berggren, J. Noth, J. Siebel, A. Hemschemeier, V. Artero, E. Reijerse, M. Fontecave, W. Lubitz, T. Happe, "Spontaneous activation of [FeFe]-hydrogenases by an inorganic [2Fe] active site mimic." ***Nat. Chem. Biol.*** **2013**, 9 (10), 607-609.

A. Adamska-Venkatesh, D. Krawietz, J. Siebel, K. Weber, T. Happe, E. Reijerse, W. Lubitz, "New redox states observed in [FeFe] hydrogenases reveal redox coupling within the H-cluster." ***J. Am. Chem. Soc. 2014,*** 136 (32), 1139-11346.

A. Adamska-Venkatesh, T. Simmons, J. Siebel, V. Artero, M. Fontecave, E. Reijerse, W. Lubitz, "Artificially maturated [FeFe] hydrogenase from Chlamydomonas reinhardtii: A HYSCORE and ENDOR study of a non-natural H-cluster." ***Phys. Chem. Chem. Phys.*** **2015,** 17 (7), 5421-5430.

J. Siebel, A. Adamska-Venkatesh, K. Weber, S. Rumpel, E. Reijerse, W. Lubitz, "Synthesis and characterization of hybrid [FeFe]-hydrogenases containing an artificial active site." ***Biochemistry*** **2015,** 54 (7), 1474-1483.

**List of oral presentations:**

04.06.2012, Köln, Germany
BMBF Meeting Köln 2012 "$H_2$-Design Cells"
"Investigation of the super reduced state of [FeFe] hydrogenase from *C. reinhardtii*"

09.07.2013, Szeged, Hungary
10th International *Hydrogenase Conference*
"Maturation of [FeFe]-hydrogenases by inorganic [2Fe] active site mimics"

27.11.2013, Oxford, United Kingdom
Seminar at Inorganic Chemistry Laboratory, Department of Chemistry
"Maturation of [FeFe] hydrogenases by inorganic [2Fe] active site mimic"

05.03.2014, Mülheim an der Ruhr, Germany
Scientific Advisory Board Meeting 2014 at the MPI CEC (Fachbeirat)
"[FeFe] hydrogenases: the champions of (bio)hydrogen generation!"

22.05.2014, Maastricht, Nederland
22th Benelux EPR Society Meeting
"Pulsed EPR studies of an [FeFe] hydrogenase with a non-native cofactor"

**List of poster presentations:**

2011, Johannesbergs slot, Gottröra, Sweden
SOLAR-H2 Workshop 2011 in Sweden
"[FeFe]-Hydrogenase – In search of a super reduced state"

2012, Dublin, Ireland
EUROMAR 2012
"EPR investigation of the super reduced state of [FeFe] hydrogenase from *Chlamydomonas reinhardtii*"

2013, Rehovot, Israel
The 6th EFEPR School on Advanced Electron Paramagnetic Resonance (EPR) Spectroscopy
"EPR investigation of the super reduced state of [FeFe] hydrogenase from *Chlamydomonas reinhardtii*"

2013, Szeged, Hungary
10th International *Hydrogenase Conference*
"An improved mechanism of [FeFe] hydrogenases catalysis"

2013, Kraków, Poland
IX International Workshop on EPR in Biology and Medicine
"Spectroscopic investigation of the active site of [FeFe] hydrogenase from *Chlamydomonas reinhardtii* and related systems"

2014, Dundee, United Kingdom
The 47th Annual International Meeting of the ESR Spectroscopy Group of the Royal Society of Chemistry
“Artificially maturated [FeFe] hydrogenase from C. reinhardtii: A HYSCORE and ENDOR study of a non-natural H-cluster”

2014, Mülheim an der Ruhr, Germany
International Symposium: Catalytic Systems for Chemical Energy Conversion
“Artificially maturated [FeFe] hydrogenase from C. reinhardtii: A HYSCORE and ENDOR study of a non-natural H-cluster”

**Schools attended:**

The 6th EFEPR School on Advanced Electron Paramagnetic Resonance (EPR) Spectroscopy, 2013, Rehovot, Israel

Methods in Molecular Energy Research: Theory and Spectroscopy. Summer School, 2013, Essen, Germany

**Honors and prizes:**

Selected participant of the 64th Nobel Laureate Meeting in Lindau, 2014

Poster prize of the IES, International Symposium: Catalytic Systems for Chemical Energy Conversion, 2014